Hydraulic Fracturing in Particulate Materials

A Thesis
Presented To
The Academic Faculty

by

Hong Chang

In Partial Fulfillment
of the Requirements for the Degree
Doctor of Philosophy in the
School of Civil and Environmental Engineering

Georgia Institute of Technology
November 2004

Hydraulic Fracturing in Particulate Materials

Approved by:

Dr. Leonid N. Germanovich

Dr. Peter E. Van Dyke

Dr. Hermann Fritz

Dr. Robert Lowell

Dr. Larry C. Murdoch

Dr. Alexander M. Puzrin

Dr. J. Carlos Santamarina

November 22, 2004

ACKNOWLEDGEMENTS

I would like to express my sincere gratitude to my thesis advisor Dr. Leonid Germanovich for guiding and challenging me to a deeper understanding of knowledge and for his encouragement, support and trust at all levels.

I would like to thank my co-advisor, Dr. Peter Van Dyke, for his invaluable inspiration, encouragement and supports during the whole work with this dissertation.

I want to acknowledge my committee members: Dr. Hermann Fritz, Dr. Robert Lowell, Dr. Larry C. Murdoch, Dr. Alexander Puzrin, and Dr. Carlos Santamarina. Their useful comments and suggestions are greatly appreciated.

I thank Mr. Mike Sorenson, Mr. Seph Scott, and Mr. Kenneth Thomas, who provided timely assistance in conducting the experiments.

Also, I greatly appreciate the assistance and encouragement from past and present graduate students of the Rock and Fracture Mechanics Group at Georgia Institute of Technology: Andrew Schildmeyer, Rajesh Chanpura, Jongwon Choi, Chris Corrigan, Robert Hurt, Sheamus Kelleher, Sihyun Kim, Cem Ozan, Pierre Ramondenc, Chanin Ruangthaveekoon, Youngjong Sim, Kasemchart Sriwalai, and Ruiting Wu.

I am very grateful to my friends, Bin Cao, Liang Ge, Bo Gao, Dawei Shen, Tianyi Yi, Dongmei Yang, Xuan Yang and Jie Zheng, for their help and great friendship during years of my staying here.

Finally, I would like to thank my parents, Zongle Chang and Shulan Zhang, and my sister and brother, Lin Chang and Panfeng Chang, for their continuous encouragement

and support. Most importantly, I cannot fail to thank my husband, Quanzhan Zheng, for his endless love and support. Without them, this dissertation would not have been possible.

I appreciate the financial support that has been provided by Shell, Schlumberger, National Science Foundation (grants CMC-9896136, CMC-0421090, OCE-0242163), and Georgia Tech Foundation during the years of my Ph.D. study.

TABLE OF CONTENTS

LIST OF TABLES

LIST OF FIGURES

SUMMARY

Hydraulic fracturing is an important and prevalent process both in the natural environment and in industrial applications. For more than five decades, this technique has been widely used to enhance oil and gas production. Hydraulic fracturing in solid materials (e.g., rock) has been studied extensively. The main goal of this thesis is a comprehensive study of the physical mechanisms of hydraulic fracturing in cohesionless sediments. For this purpose, experimental techniques are developed, and used to quantify the initiation and propagation of hydraulic fractures in dry particulate materials.

Based on the developed experimental techniques, hydraulic fracturing has been directly observed in the laboratory. Hydraulic fractures at the different laboratory scales have been compared. We have conducted a comprehensive experimental series by varying such controlling parameters as the properties of particulate materials and fracturing fluids, boundary conditions, initial stress states, and injection volumes and rates. In this work, we suggest principal fundamental mechanisms of hydraulic fracturing in particulate materials and determine relevant scaling relationships (e.g., the interplay between elastic and plastic processes).

The main conclusion of this work is that hydraulic fracturing in particulate materials is not only possible, but even probable if the fluid leak-off is minimized (e.g., high flow rate, high viscosity, low permeability). Also, the scale effect (within the range of the laboratory scales) appears to be relatively insignificant, that is, the observed features of fractures of different sizes are similar. These results may be useful for the extrapolation of our conclusions to practical field scales.

For the fracture initiation at the peak pressure (i.e., following the initial cavity expansion), there exists a threshold value of cohesion that results in compressive stresses everywhere in the particulate material. For less cohesion, the cohesive materials can be considered to be effectively cohesionless.

The observed fracture geometry and the measured pressure injection curves suggest that hydraulic fracturing occurs in soft sediments in the following sequence:

(i) cavity expansion before the injection pressure reaches its peak;

(ii) fracture front initiation from the expanding cavity near the pressure peak; and

(iii) propagation of the developed fracture after the peak.

Another important conclusion of this work is that all parts of the particulate material are likely to be in compression. The compressive stress state is an important characteristic of hydraulic fracturing in particulate materials with low, or no, cohesion (such as were used in our experiments).

The fact that cavity expansion is observed before fracture initiation suggests that the new volume for the injected fluid is created primarily due to the elastic deformation of the undisturbed material outside of the plastic zone. The fact that the initial cavity is not preserved (and hence not observed) at the advanced stage of fracture propagation implies that the plastic deformation of the particulate material could be an important process resulting in the flattening ("squeezing)"of the initial cavity into a thin conduit. Such a flat shape is beneficial for creating a new volume for the injected fluid by the elastic opening of the thin fissure, so that a lower pressure is required, compared to expanding bubble-

like cavities. This may be a reason why the fairly thin shape has always been observed in our experiments during the advanced stage of fracture growth, and why the pressure is reduced after the peak.

Based on the cavity expansion mechanism we proposed the “pile driving” model of hydraulic fracturing in particulate materials. In this model, the fracturing fluid is viewed as a sheet pile (blade) that disjoints the host material and the cavity expansion process occurs at the fracture (blade) front. In this region, the host material is displaced (i.e., “pushed” away) by the advancing fracturing fluid. Accordingly, the stresses near the fracture tip are elevated (relative to the remote in-situ stresses), and so is the pressure of the fracturing liquid.

Based on the shear banding mechanism, we proposed an alternative model of hydraulic fracturing that is also consistent with a compressive stress state everywhere in the particulate material. In strain-softening materials, such as those used in our experiments, localized shear bands, inclined with respect to the fracture direction, may appear. The discontinuity of the shear displacements between the opposing sides of the shear band can also generate a fracture aperture that provides the necessary volume for the fluid inflow. This mechanism explains the commonly observed beveled fracture front.

The fingering at the fracture front that has been observed in some experiments may appear when an empty cavity (perhaps short-lived) is generated in the host material ahead of the fracture front, and the fracturing fluid enters this cavity. Such a cavity could be a fracture if the host material still has a small but non-zero cohesion (tensile strength). This cohesion could be inherent (e.g., due to electrostatic forces on clay platelets) or induced

by the fluid leak-off ahead of the fracture front. The induced cohesion may be caused by the tensile strain at the fracture tip zone (where the stress state is also compressive), which, in turn, induces the cavitation of the leaked-off fluid and capillary forces. Via this liquid cavitation mechanism, the cohesion may also be induced in fully-saturated particulate materials.

CHAPTER 1

INTRODUCTION

1.1 Motivation

Hydraulic fracturing is an important and prevalent process both in the natural environment and in industrial applications. It has been used in petroleum engineering for more than five decades to create deep-penetrating fractures in hydrocarbon reservoirs stimulating the production of oil and gas [*Howard and Fast*, 1970]. Hydraulic fracturing in solid, brittle materials (e.g., rock) has been studied extensively. Hence, a relatively good understanding of these brittle hydraulic fractures exists [*Hubbert and Willis*, 1957; *Haimson*, 1968; *Howard and Fast*, 1970].

The importance of hydraulic fracturing in geotechnical problems was identified when *in-situ* outflow permeability tests yielded false values that were higher than expected [*Bjerrum et al.*, 1972]. The false measurements were due to the hydraulic fractures that were generated under the high operation pressures. The Independent Panel to Review the Cause of the Failure of Teton Dam [*Jaworski*, 1981] defined the term "hydraulic fracture" as “the condition leading to the creation and propagation of a thin physical separation in a soil or rock mass due to high fluid pressure”.

Hydraulic fracturing in particulate materials has been widely observed. It can be either detrimental or useful, depending on the occurrence in the engineering applications.

Hydraulic fracturing is the known or suspected cause of the excessive leakage and

failure of many dams, such as Hyttejuvet Dam in Norway and Teton Dam in Idaho, USA [*Jaworski*, 1981]. These cases showed that the potential risk of hydraulic fracturing is an important issue in dam design.

Massarsch and Broms [1977] pointed out the significance of hydraulic fracturing in soils during the installation of a sand drain and pile driving in cohesive soils. Based on theoretical analysis and *in-situ* measurements, they concluded that the hydraulic fractures in the vicinity of the driven piles might have aided in the drainage and consolidation of the clay layers.

During pressure grouting, hydraulic fracturing has been observed and is believed to be responsible for soil foundation rupture and loss of grouting fluid [*Warner*, 1997], as shown in Figure 1.1. As hydraulic fracturing generally occurs under high grouting pressures, the ASCE Committee of Grouting recommends a maximum grouting pressure according to empirical experience [*Johnson*, 1958; *Klein and Polivka*, 1958; *Kravetz*, 1958]. On the other hand, fracture grouting is a common form of compensation grouting to offset subsidence caused during underground excavation and bored tunneling [*Soga et al.*, 2004].

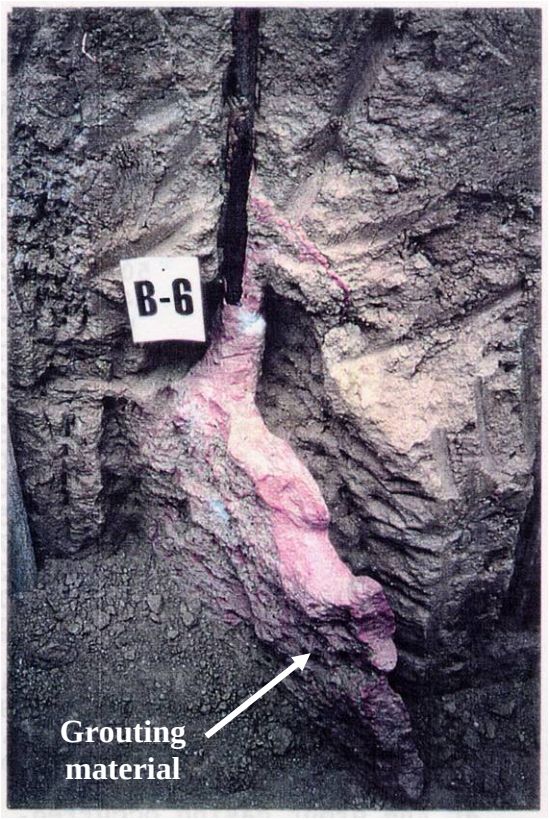

Figure 1.1 A hydraulic fracture caused by grouting [*Warner*, 1997].

Although the technique of hydraulic fracturing has been widely used in the oil industry, it can also happen undesirably during borehole drilling and cause a loss of drilling mud. One example is given by shallow-water flow (SWF) [*Ostermeier et al.*, 2000]. The SWF typically occurs while drilling in shallow over-pressured sand formations at deepwater sites (Figure 1.2). The existence of this over-pressured sand layer results in a pore pressure that is greater than the hydrostatic pore pressure. Formation drilling requires that a sufficiently high pressure be present in the borehole to prevent washout. However**,** hydraulic fracturing will occur when the pressure is too high. These sites generally have low formation strength and an elevated pore pressure. The combination of these factors makes drilling conditions extremely difficult. This is

referred to as narrow margin drilling. Figure 1.2 shows the effect of over-pressurized zones on the decrease of the pressure margin at a site in the Gulf of Mexico. The actual pressure is much closer to the fracture pressure in over-pressurized zones, thus decreasing the margin for acceptable borehole pressures. If the drilling pressure exceeds the fracturing pressure of the surrounding formations, SWF may occur.

A number of instabilities can occur as a result of SWF. These include large uncontrollable flows that manifest as violent eruptions on the seafloor, and the formation of large craters and trenches [*Ostermeier et al.*, 2000]. Figure 1.3 shows a trench formed on the sea floor at the URSA field of Gulf of Mexico located approximately 100 miles offshore of New Orleans. These instabilities can lead to the loss of drilled wells. They can also cause significant environmental pollution. SWF has been a common occurrence globally.

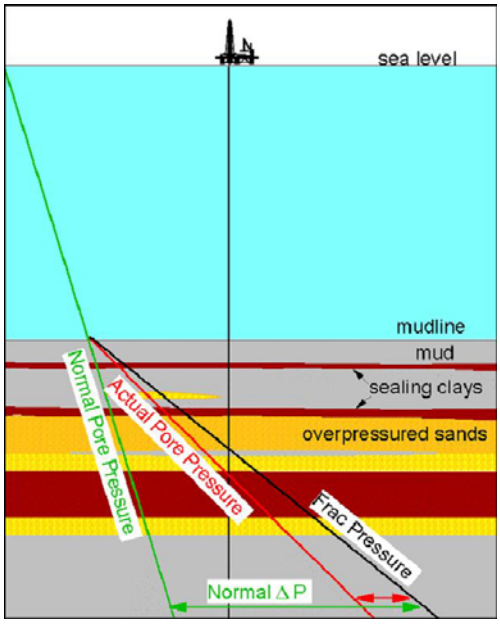

Figure 1.2 Effect of over-pressured zones on the decrease of the pressure margin at a site of the Gulf of Mexico [*Ostermeier et al.*, 2000].

Figure 1.3 Trench formed by SWF that damaged the ocean floor [*Ostermeier et al.*, 2000].

Hydraulic fracturing in particulate materials also has applications in environmental engineering. Slurry fracture injection has been used to dispose granular waste into deep ground formations such as clean 2-5 Darcy sands [*Dusseault et al.*, 1997]. In petroleum engineering, the cutting reinjection technique has been promoted and is being implemented in the field for injecting oil-based drilling cuttings and mud into underground strata [*Malachosky et al.*, 1991; *Nagel and Strachan*, 1998]. To enhance the efficiency of other *in-situ* remediation techniques (e.g., vapor extraction and bioremediation), hydraulic fracturing was designed by increasing the permeability of silty layers contaminated with organic compounds [*US EPA*, 1993]. It is also a novel technique, in contrast to the traditional trench technique, to construct subsurface permeable reactive barriers for groundwater remediation as shown in Figure 1.4 and Figure 1.5.

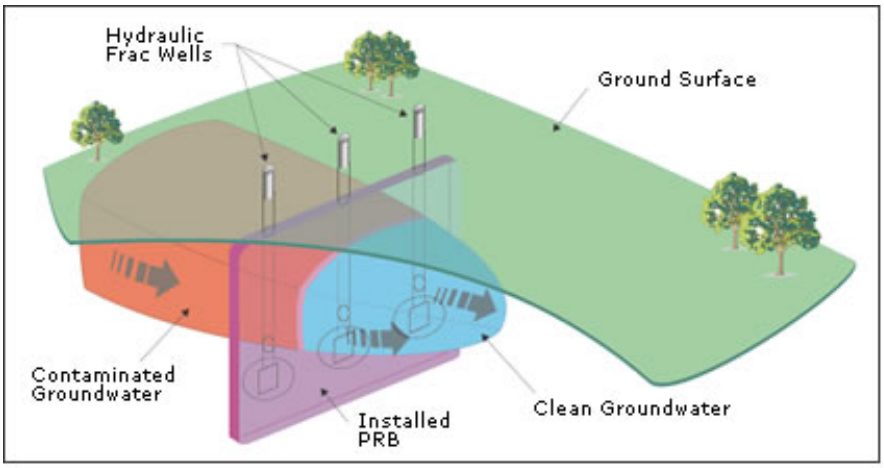

Figure 1.4 Permeable reactive barrier constructed by hydraulic fracturing for groundwater remediation [*Geoserria*, 2004].

Figure 1.5 A permeable reactive barrier [Courtesy of *Murdoch*, 2001].

Bjerrum and Andersen [1972] suggested using hydraulic fracturing to directly measure the *in-situ* minor principal stress in soils. Since then, it has been used due to its simplicity.

Despite the many applications of hydraulic fracturing in particulate materials, the risk of failure is still high due to the currently limited understanding about this phenomenon. The review of the literature has shown that at present, no fundamental and systematic research has been conducted to provide physical models of the hydraulic fracturing mechanisms. There are no fracture initiation and propagation criteria targeting hydraulic

fracturing in unconsolidated, cohesionless particulate materials. Almost all the research was conducted on cohesive particulate materials (see section 1.2). Currently, most of the criteria used for modeling fractures in cohesive particulate materials are based on conventional fracture mechanics that assumes non-zero tensile strength exhibited by the material in the fracture tip zone. In Chapter 6 it will be discussed that it is unlikely that fracturing cohesionless particulate materials can be described by this model. Therefore, a new physical model that is applicable to cohesionless particulate materials must be developed.

1.2 Literature Review

Studies on hydraulic fracturing in cohesive particulate materials have been performed since the 1970's. This includes laboratory experiments, field tests, analytical analyses, and numerical simulations. Currently, numerical simulations of these types of problems are very limited [*Vallejo*, 1993; *Andersen et al.*, 1993]. Most of the publications focus on laboratory experiments, field tests, and theoretical analyses.

1.2.1 Previous Laboratory Experiments and Field Tests

Bjerrum et al. [1972] proposed for first time that the results of the *in-situ* outflow permeability tests may be highly overestimated when applying excessive water pressure. Laboratory tests of permeability performed on models of soft silty clay confirmed that a sufficiently low water pressure was needed to ensure true permeability measurements. An analytical solution of the fracturing pressure indicated that the fracturing pressure is a function of the Poisson's ratio and the initial circumferential stress of the soil skeleton,

but is independent of the modulus of elasticity.

Since *Bjerrum et al.* [1972], laboratory experiments on hydraulic fracturing in particulate materials by pressurizing a borehole have been conducted by *Jaworski et al.* [1981], *Panah and Yanagisawa* [1989], *Mori et al.* [1987], *Lo and Kaniaru* [1990], *Murdoch* [1993], *Andersen et al.* [1993], *Vallejo* [1993], *Yanagisawa and Panah* [1994], *Reed* [1997], and *de Pater et al*. [2003]. *Soga et al.* [2004] performed fracturing grouting experiments by injecting liquid through single or multiple injection points. Figure 1.6 depicts a typical experimental setup.

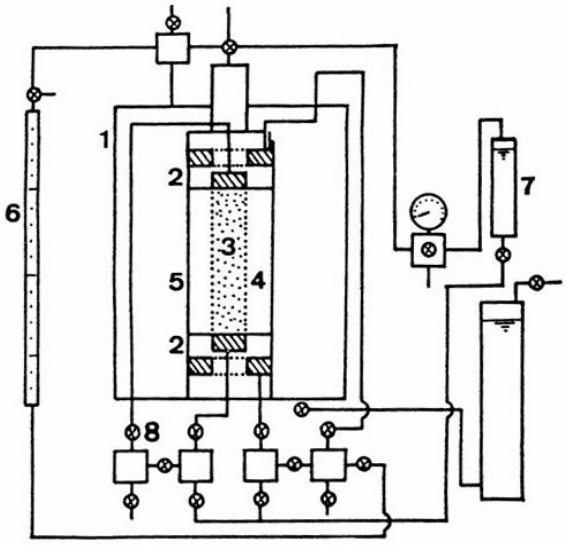

Figure 1.6 Tri-axial hydraulic fracturing apparatus [*Panah and Yanagisawa*, 1989].

Most of the experiments were performed on partially-saturated soils. A few studies [*Lo and Kaniaru*, 1990; *Murdoc*h, 1993; *de Pater et al.*, 2003; *Soga et al.*, 2004] used fully-saturated soils. These studies showed that hydraulic fractures can be created in partially-saturated as well as in fully-saturated soils. Figures 1.7a and 1.7b show

examples of typical hydraulic fractures generated in partially- and fully-saturated soils.

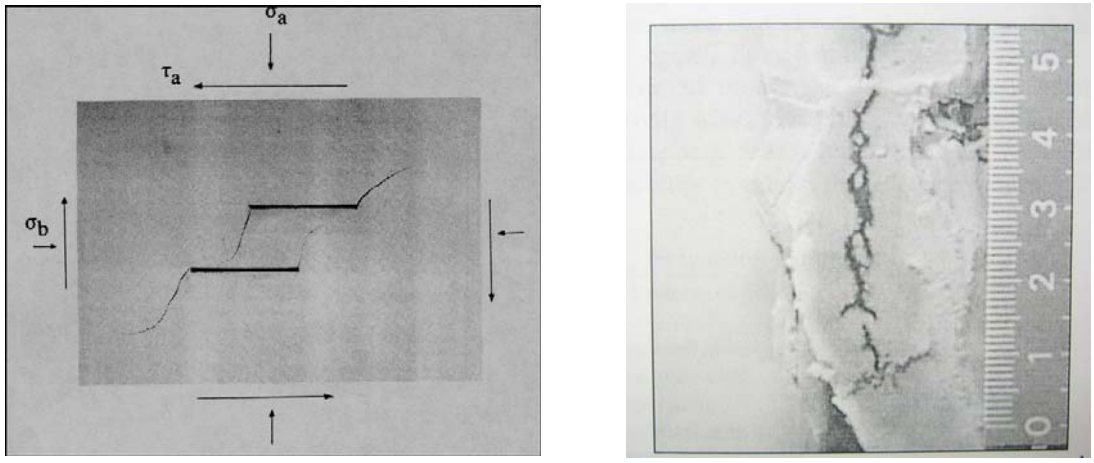

(a) (b)

Figure 1.7 Hydraulic fractures generated in (a) partially-saturated clay: consolidated kaolinite clay, 31% water content [*Vallejo*, 1993], and (b) fully-saturated sand [*de Pater et al.*, 2003] in laboratory experiments.

Field tests on hydraulic fracturing in soil have been performed by *Bjerrum et al.* [1972], *Lefebvre* [1991], *Reed* [1993], *Murdoc*h [1989, 1995; and 2002], and *Hocking* [1996]. Figure 1.8 is a photograph of a hydraulic fracture in a field test.

Figure 1.8 A hydraulic fracture generated in field test [*Hocking*, 1996].

1.2.2 Experimental Methodologies

Injection Patterns

The process of hydraulic fracturing is usually divided into two stages: fracture initiation and propagation [*Horsrud*, 1982; *Murdoch*, 1993]. The process is generally invisible unless some special techniques or tools are used to track it. Hence, the injection pressure is a very important index during hydraulic fracturing. A good understanding of the pressure response aids visualization of the fracturing process [*Murdoch*, 1993].

The initial goal of the investigation of hydraulic fracturing in soil was to prevent it from occurring in many engineering applications, such as pressure grouting, dam design, *in-situ* permeability testing, and pile driving. Consequently, most of the existing laboratory experiments and field tests focused on studying only the fracture initiation pressure [e.g., *Jaworski*, 1981; *Mori et al*., 1987; *Panah and Yanagisawa*, 1989; *Yanagisawa and Panah*, 1994; *Andersen et al.*, 1993]. The fracturing process was initiated by increasing the injection pressure while monitoring the flow rate (i.e., pressure-controlled injection method). The injection was stopped when the flow rate was observed to increase abruptly. This was attributed to the fracture initiation. After the hydraulic fracture initiated, it was difficult to continue the measurements because of the high, unstable fluid flow rates. As a result, these experiments were terminated after fracture initiation and did not produce information on fracture propagation.

In contrast to the pressure-controlled injection method, fluid injection with a constant injection rate was adopted by *Lo and Kaniaru* [1990], *Murdoch* [1993] and *de Pater et al.* [2003]. This method yields a more stable fracture propagation after the fracture initiates.

Hence, the pressure can be recorded during the entire fracturing process. A typical injection pressure curve of a hydraulic fracturing test is shown in Figure 1.9. The pressure curve can be interpreted to map the growth of hydraulic fractures.

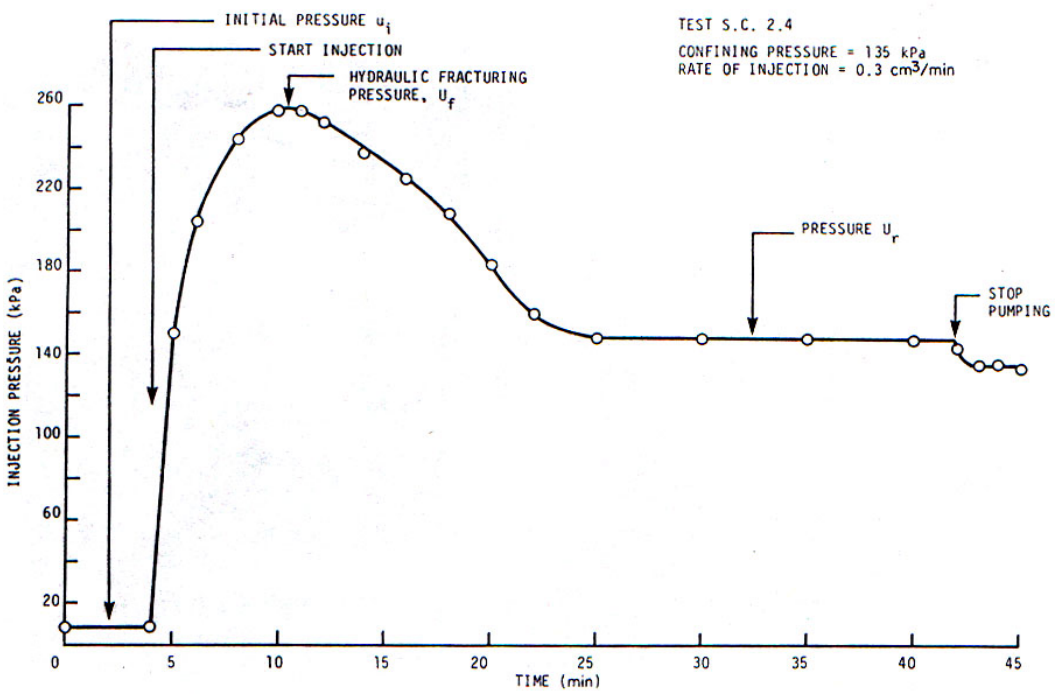

Figure 1.9 Injection pressure of a hydraulic fracturing test [*Lo and Kaniaru*, 1990].

Tracing and Exposing Fractures

To study the mechanisms of hydraulic fracturing, it is important to trace the fractures, and to reliably expose them intact. Generally, hydraulic fractures have been traced by using a dyed injection fluid [*Jaworski*, 1981; *Murdoch*, 1993; *de Pater et al.*, 2003] or by flushing a dyed fluid into the hydraulic fracture after creating it [*Yanagisawa and Panah*, 1994].

Hydraulic fractures were mapped by various methods such as breaking the intact material along the fracture plane [*Jaworski*, 1981], excavation [*Reed*, 1996], or cutting at

different cross-sections [*Lefebvre*, 1991]. These methods were not very reliable, because the quality of the trace of the fracture depends on how well the dyed fluid covers and dyes its surface. In some cases, fractures could not to be viewed due to the lack of proper preservation and exposure [*Lefebvre*, 1991].

X-ray computed tomograph (CT) scans were used by *de Pater et al.* [2003] to detect the geometry of fractures inside intact soil specimens.

Soga et al. [2004] used epoxy resin as the injection liquid to reveal fracture patterns through hardened epoxy.

The properties of the thickness and the tip of the fracture are very useful for understanding the hydraulic fracturing mechanisms. This study requires a reliable method that is capable of measuring these parameters.

1.2.3 Governing Parameters

Fracture Initiation Pressure

The previous studies mentioned above have shown that fracture initiation pressure depends on various parameters.

From the derived elastic solution of the fracture initiation pressure, *Bjerrum et al.* [1972] concluded that the pressure depends on the initial circumferential stress and the Poisson's ratio of the soil skeleton, and is independent of the modulus of elasticity.

The experimental results of *Jaworski et al.* [1981] showed that fracture pressure increases as the water content of the particulate material and injection rate decrease. The

presence of pre-existing cracks decreases the injection pressure.

Mori et al. [1987] experimentally studied the effect of balloon that was used to encase the injection fluid, specimen size, pre-existent wedge, and pressurizing rate on hydrofracture pressure. They concluded that these parameters have insignificant influence on the fracture pressure, provided that the pressurizing rate was sufficiently high to prevent the fluid from penetrating into the wedge.

Lo and Kaniaru [1990] concluded that the fracture initiation pressure is not a unique soil property, but depends on the degree of consolidation and saturation. The pressure increases with the decrease of water content and the increase of consolidation. The fracture initiation pressure has an upper limit according to the results from the saturated-consolidated tests. It has a lower limit according to the results from the saturated-unconsolidated tests. Murdoch's laboratory experiments [1993] also showed the importance of the degree of consolidation on fracture pressure. *Lo and Kaniaru* [1990] and *Murdoch* [1993] observed hydraulic fractures in both partially-saturated and fully-saturated clays.

Fracture Orientation

It is generally accepted in the literature that fractures propagate perpendicular to the direction of minimum principal stress [*Jaworski et al.*, 1981; *Andersen et al.*, 1993; *Murdoch*, 1993; *Reed*, 1997]. However, *Massarsch* [1978] stated that vertical fractures were likely to occur in soil with a maximum principal stress that is horizontal (i.e., $K_0 > 1$, where K_0 is the coefficient of lateral earth pressure at rest, expressed as the ratio of horizontal and vertical effective stresses). This conclusion was made based on a critical

ratio he derived for determining the direction of hydraulic fracturing in a plastic zone. In addition, *Lefebvre* [1991] observed vertical fractures for K_0 greater than unity in field tests.

1.2.4 Failure Criteria

Tensile and shear failure hypotheses of the hydraulic fracture criteria have been proposed in many publications.

Tensile failure

It is commonly accepted that hydraulic fracturing in particulate materials is associated with tensile failure. Two theories - the theory of the expansion of a cylindrical cavity and of a linear elastic fracture mechanics (LEFM) - were used in the literature to analyze tensile failure.

For the theory of expansion of a cylindrical cavity, a borehole is considered as a cylindrical cavity under the influence of hydraulic pressure. With an increasing pressure, the circumferential stress decreases and changes from compression to tension. The fracture is assumed to initiate when the tensile effective circumferential stress σ_θ' exceeds the tensile strength of the particulate media σ_t [*Bjerrum el at.*, 1972; *Massarsch*, 1978; *Jaworski,* 1981; *Lo and Kaniaru*, 1990; *Andersen et al.*, 1993; *Vallejo*, 1993; *Yanagisawa and Panah*, 1994]. That is,

$$\sigma_\theta'+\Delta\sigma_\theta'>\sigma_t \qquad (1.1)$$

where $\Delta\sigma_\theta'$ is the change of the tensile effective circumferential stress σ_θ'. It is generally agreed that for particulate media, the tensile strength is very low. In fact, tensile strength

is neglected in a number of investigations [*Bjerrum el at.*, 1972; *Massarsch*, 1978]. This corresponds to replacing the left hand side of Equation (1.1) by zero.

Bjerrum et al. [1972] explained that under the influence of the hydraulic pressure, particulates were displaced away from the borehole to produce hydraulic fractures. *Jaworski et al.* [1981] pointed out that the non-uniform changes in total stress, water pressure or both were necessary for the effective stress to become tensile, and to induce a tensile fracture. Hydraulic fracture may be induced by a wedging action formed by water pressure acting on pre-existing discontinuities on the wall of the borehole.

Fang [1989], *Harison et al.* [1994] and *Murdoc*h [1993] considered hydraulic fractures in partially-saturated soil as an analogy to tensile hydraulic fractures in brittle materials. Linear elastic fracture mechanics (LEFM) theory, in particular the concept of fracture toughness, was used to predict fracture initiation and propagation pressures. That is, a fracture initiates and propagates with the mode I stress intensity factor K_I equal to a critical value K_{Ic}, the fracture toughness, i.e.

$$K_I = K_{Ic} \tag{1.2}$$

Section 1.2.6 reviews in detail the work of *Murdoch* [1993 and 2002].

Shear failure

In contrast to the hypothesis of tensile fracturing, shear failure was suggested by *Mori et al.* [1987], *Panah* [1989], and *Lo and Kaniaru* [1990]. *Mori et al.* [1987] first proposed the shear failure mechanism for hydraulic fracturing in soils. They believed that the horizontal and inclined fractures observed in laboratory experiments indicated a shear

failure. *Panah* [1989] inferred that the fracture was due to shear failure rather than tensile failure based on analysis of the empirical formula of the fracturing pressure obtained from results of laboratory experiments. Both *Mori et al.* [1987] and *Panah* [1989] assumed that soil yields according to the Mohr-Coulomb criterion.

1.2.5 Prediction of Fracture Initiation Pressure

Prediction of fracture initiation pressure is critical to prevent the occurrence of hydraulic fractures in many engineering activities, such as pressure grouting, dam design, *in-situ* permeability testing and pile driving.

Empirical Formula

To predict the fracture initiation pressure P_f, empirical formulas were given by *Bjerrum et al.* [1972] and *Jaworski et al.* [1981] expressed as

$$P_f = m\sigma_{\min} + n \tag{1.3}$$

where σ_{min} is the minimum principle pressure, m and n are constants empirically obtained from laboratory experiments. The value of m generally ranges from 1 to 2. The value of n is related to the soil properties. The disadvantage of empirical formulas is that they cannot be used without performing tests to obtain the empirical constants. According to the experimental results of *de Pater et al*. [2002], initiation pressure was ~ 2 to 5 times greater than confining pressure.

Theoretical Modeling

Both *Panah* [1989] and *Lo and Kaniaru* [1990] developed elastic solutions of fracture

initiation pressure following the Mohr-Coulomb failure criterion. They both gave physical meanings to the empirical constants *m* and *n*. The only difference between the two solutions is that *Panah* [1989] assumed zero tensile strength of the soil. The derivation of the elastic solution by *Lo and Kaniaru* [1990] is presented below.

The stress state of a hydraulically pressurized borehole is modeled as shown in Figure 1.10.

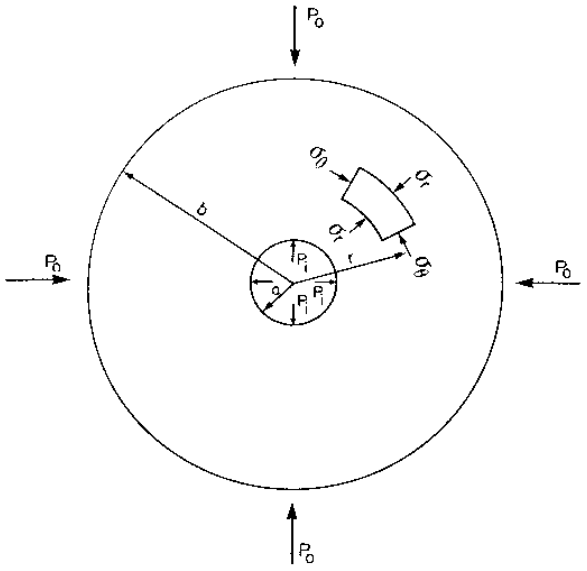

Figure 1.10 Stress condition in the vicinity of a borehole in hydraulic fracturing tests [*Lo and Kaniaru*, 1990].

A cylindrical sample containing a concentric cavity with internal and external radii *a* and *b*, respectively, is subjected to internal and external water pressure. The internal pressure P_i is increased until a fracture initiates. An elastic plane strain solution with the Mohr-Coulomb criterion and a non-associated flow rule gives the expression of the changes in radial $\Delta\sigma_r$ and tangential stresses $\Delta\sigma_\theta$

$$\Delta\sigma_r = \frac{3E}{2(1+\nu)(1-2\nu)}\left[c_1 + (1-2\nu)\left(\frac{c_2}{r^2}\right)\right] \tag{1.4}$$

$$\Delta\sigma_\theta = \frac{3E}{2(1+\nu)(1-2\nu)}\left[c_1 - (1-2\nu)\left(\frac{c_2}{r^2}\right)\right] \tag{1.5}$$

where E is Young's Modulus, ν is Poisson's ratio, r is the radial distance from the centre of the specimen and c_1 and c_2 are algebraic functions of material properties obtained from the boundary conditions.

The values of the radial stress σ_r and the tangential stress σ_θ are thereby obtained as

$$\sigma_r = P + \Delta\sigma_r = \frac{b^2}{b^2-a^2}\left(1-\frac{a^2}{r^2}\right)P_0 + \frac{a^2}{b^2-a^2}\left(\frac{b^2}{r^2}-1\right)P_i \tag{1.6}$$

$$\sigma_\theta = P + \Delta\sigma_\theta = \frac{b^2}{b^2-a^2}\left(1+\frac{a^2}{r^2}\right)P_0 - \frac{a^2}{b^2-a^2}\left(\frac{b^2}{r^2}+1\right)P_i \tag{1.7}$$

Examination of the radial and tangential stresses shows that the maximum radial stress and the minimum tangential stress occur at an inner radius a, where σ_r and σ_θ are

$$(\sigma_r)_{r=a} = P_i \tag{1.8}$$

$$(\sigma_\theta)_{r=a} = \frac{b^2}{b^2-a^2}\left(2P_0 - P_i - \frac{a^2}{b^2}P_i\right)_i \tag{1.9}$$

The material is assumed to yield following a liberalized Mohr-Coulomb failure criterion that is written in the following form:

$$(\sigma_1 - \sigma_3) - (\sigma_1 + \sigma_3)\sin\phi - 2C\cos\phi = 0 \tag{1.10}$$

where ϕ is the friction angle and C is the cohesion of the material. The Mohr-Coulomb failure criterion can be written in terms of σ_r, σ_θ and σ_t, where σ_t is the tensile strength and

$$\sigma_1 = \sigma_r \tag{1.11}$$

$$\sigma_3 = \sigma_\theta + \sigma_t \tag{1.12}$$

Equation (1.10) can be rewritten as

$$(\sigma_r - \sigma_\theta - \sigma_t) - (\sigma_r + \sigma_\theta + \sigma_t)\sin\phi - 2C\cos\phi = 0 \qquad (1.13)$$

Substituting Equations (1.11) and (1.12) into Equation (1.13) and solving for P_i (Equation (1.8)), which is the fracture initiation pressure u_f, Equation (1.13) becomes

$$u_f = \frac{b^2}{b^2 + a^2\sin\phi}\left\{\left(1 + \frac{a^2}{b^2}\right)\left[(1+\sin\phi)\frac{\sigma_t}{2} + C\cos\phi\right] + (1+\sin\phi)P_0\right\} \qquad (1.14)$$

If $b >> a$, and the value of P_0 is equal to the confining pressure σ_H, Equation (1.14) reduces to

$$u_f = (1+\sin\phi)\frac{\sigma_t}{2} + C\cos\phi + (1+\sin\phi)\sigma_H \qquad (1.15)$$

Equation (1.15) predicts a linear relationship between u_f and the total minor principal stress σ_H, with the interception and slope determined by strength parameters for a given soil. It indicates that fracture initiation pressure may be increased by increasing either the soil strength parameters or total minor principal stress.

Andersen et al. [1993] proposed an approach using finite element analysis to calculate the total stress state in the vicinity of the borehole. Unlike the previous solutions, this approach considered the non-linearity of the stress-strain properties of the soil, and the pore pressure changes in the soil due to changes in total normal stress and shearing of the soil.

1.2.6 Work by Murdoch [1993 and 2002]

Currently, the work by *Murdoch* [1993 and 2002] is probably the most comprehensive study on hydraulic fracturing in particulate materials. His work includes laboratory

experiments and theoretical analyses. Below, we present the work in detail to reflect the state of current understanding on hydraulic fracturing in particulate materials.

The objective of the work was to provide a method to analyze the growth of a hydraulic fracture in soil. The laboratory experiments were performed on specimens of clayey silt contained in a cubic fracture cell. Dyed glycerine was injected into a borehole in the specimen to fracture the soil. The principal stresses in three directions were controlled independently.

The fracturing fluid was injected with a constant flow rate. The experiments investigated different water contents and propagation stages. The injection pressure and pore pressure were measured. Hydraulic fractures were found to be readily created in silty clay (Figure 1.11) from partially-saturated to fully-saturated states. The propagation of fractures was normal to the direction of the least principle compressive stress.

The fracture surface was divided into four distinct zones as shown in Figure 1.12: (a) starter slot, (b) parent fracture, (c) lobes, and (d) leading edge. The appearance of the leading edge of a hydraulic fracture was found to depend on the pressure of the pore fluid.

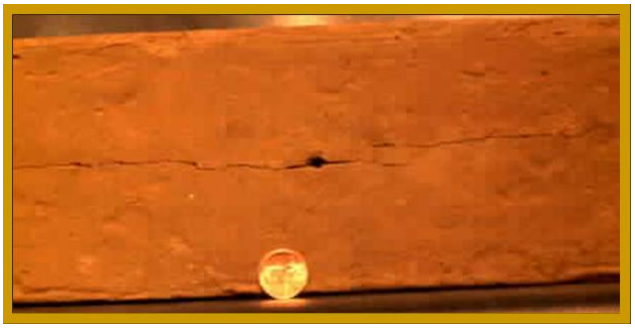

Figure 1.11 A hydraulic fracture generated in clayey silt [*Murdoch*, 1993].

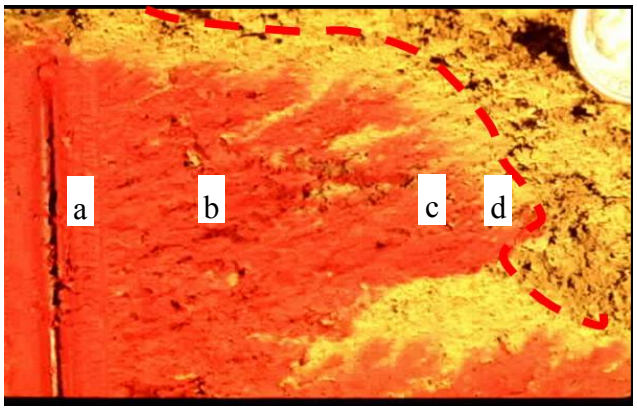

Figure 1.12 Surface of a hydraulic fracture: (a) starter slot, (b) parent fracture, (c) lobes, and (d) pristine leading edge [*Murdoch*, 1993].

The injection pressure as a function of time for a fracturing test is shown in Figure 1.13. The pressure curves were characterized by a period of nearly linear increase, a break in slope followed by a period of increasing pressure by decreasing slope, a maximum and then a period of decreasing pressure. Tests performed at different propagation stages indicated that the break in the slope marked the onset of hydraulic fracturing.

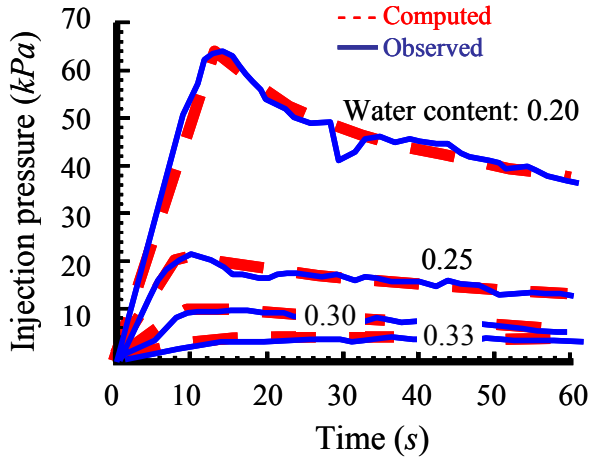

Figure 1.13 Pressure records from the laboratory (solid line) and from theoretical analysis (dashed line) for specimens with different water contents [*Murdoch*, 1993].

A theoretical analysis was conducted based on linear elastic fracture mechanics [*Murdoch*, 1993]. Laboratory experiments indicated that two fluids filled the fracture: one fluid is injected at a constant rate Q along the mid-line, and the other fluid infiltrates out of the soil pores and into the fracture tip. The driving pressure of the injection fluid P_d and the infiltrated pore fluid P_{dtip} were assumed to be uniform. Mathematically, the pressure distribution in the fracture can be considered as the superposition of the two loading conditions shown in Figure 1.14.

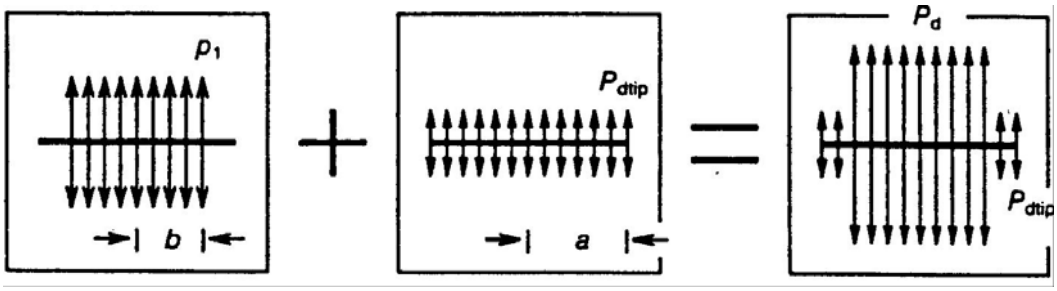

Figure 1.14 Loading conditions of a hydraulic fracture used to develop the analytical model [*Murdoch*, 1993].

Consequently, the mode I stress intensity factor K_I for the fracture was obtained by superposing those fractures under the two aforementioned loading conditions. Based on the elastic solution [*Tada et al.*, 1985], the driving pressure for propagating a fracture of half-length a was expressed as

$$P_d = \left\{K_i / [\sqrt{\pi a} - P_{dtip}(1-\theta)]\right\} / \theta \qquad (1.16)$$

where

$$\theta = (2/\pi)\sin^{-1}(b/a) \qquad (1.17)$$

b and a are the dimensions showed in Figure 1.14. The value of b / a is determined from laboratory measurements using the formula

$$b/a = [a + ma_i]/[a(m+1)] \qquad (1.18)$$

Here a_i is the initial half length of the fracture (i.e., of the starter slot) and m is the rate of growth of the tip zone.

To validate the theoretical analysis, the predicted pressure was compared with laboratory measurements. The parameters for predicting fracturing pressure were determined using a curve-fitting procedure to best fit the experimental pressure records. The computed injection pressure was compared with values measured in the laboratory.

An example of the theoretical prediction of pressure curves is shown in Figure 1.13. The theoretical prediction agrees with the experimental data.

According to *Murdoch* [1993], well-developed fractures were also observed in *fully*-saturated specimens. For fully-saturated materials, the fracture toughness is negligible.

The work concluded that K_{Ic} can be used as a material property to predict the driving pressure with the proposed analytical model. The value of K_{Ic} depends on water content and duration of consolidation.

Murdoch [2002] conducted a further analysis based on his experiments, elasticity theory and fracture mechanics. He considered that the ground over shallow hydraulic fracture flexed like a thin plate (Figure 1.15). He derived the closed-form expressions for the injection pressure p, fracture aperture δ, and length a of the hydraulic fracture as functions of fracture toughness K_{Ic}, elastic modulus E and time t. The values of the K_{Ic} and E were determined by fitting the analytical solutions with the field measurements, which resulted in excellent agreement between the Murdoch's [200] model and his field experiments (Figure 1.16).

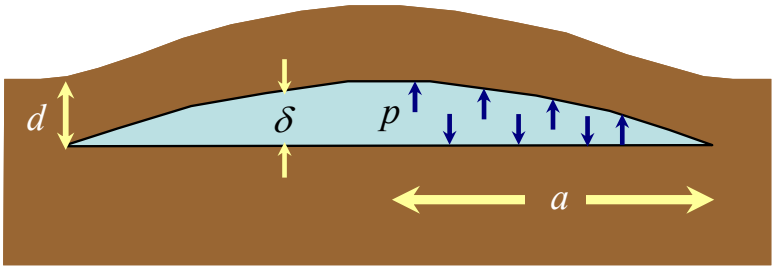

Figure 1.15 Section view of the loading with the ground over shallow hydraulic fracture flexed like a thin plate [*Murdoch*, 2002].

(a)

(b)

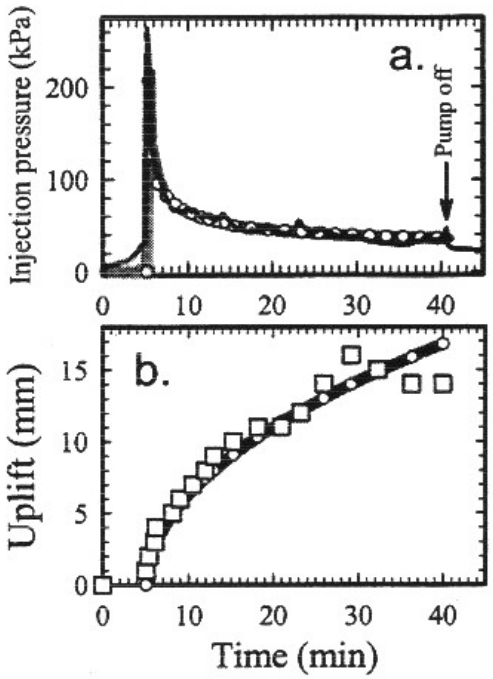

Figure 1.16 (a) Injection pressure as a function of time from field observation (black line) and theoretical analysis (gray line with dots); (b) uplift as a function of time from field observations (square symbols) and theoretical analysis (gray line with dots). [*Murdoch*, 2002].

1.2.7 Cavity Expansion Process

The typical process of hydraulic fracturing by pumping a fluid into a wellbore is considered to be an initial radial flow pattern (expansion of cavities) followed by the

formation of fractures after the fracture initiation pressure [*Department of Energy*, 2004]. The expansion of cavities in an ideal soil mass has been considered in various geotechnical applications such as pressuremeter tests [*Palmer and Mitchell*, 1972], cratering by explosives [*Vesic*, 1965], and breakout resistance of anchors [*Vesic*, 1971].

The theory of cavity expansion was first introduced by *Bishop et al.* [1949]. *Chadwick* [1959] derived a general solution for the expansion of a spherical cavity for an ideal soil with a friction angle $\phi = 0$. The effects of volume change in the plastic region were first considered by *Ladanyi* [1963]. However, this analysis was semi-empirical; it did not identify the significant controlling parameters of cavity expansion. *Vesic* [1972] developed general solutions of the expansion of spherical and cylindrical cavities in an ideal soil that is cohesive and frictional, taking into account the effects of volume change in the plastic region.

Cater et al. [1986] presented closed form solutions for the expansion of cylindrical cavities in an ideal, cohesive and frictional soil. An explicit expression for the pressure-expansion relation was derived for small strain deformation. The application of cavity expansion theory in their work is briefly described below.

The basic assumptions are:

(i) the cavity is expanded in an infinite medium with an initial hydrostatic stress state:

$$\sigma_1 = \sigma_2 = \sigma_3 = p_0 \tag{1.19}$$

where σ_1, σ_2 and σ_3 are the principal stress components and p_0 is a constant;

(ii) the medium is an isotropic, elastic, perfectly plastic solid that obeys Hooke's law before yielding;

(iii) the medium yields following the Mohr-Coulomb criterion,

$$\sigma_r = N\sigma_\theta \tag{1.20}$$

$$N = \frac{1+\sin\phi}{1-\sin\phi} \tag{1.21}$$

where σ_r are σ_θ are the radial and tangential stresses, respectively; and

(iv) during yielding the total strain increments consist of an elastic and a plastic components,

$$\dot{\varepsilon} = \dot{\varepsilon}_e + \dot{\varepsilon}_p \tag{1.22}$$

where $\dot{\varepsilon}_e$ and $\dot{\varepsilon}_p$ denote the elastic and plastic principal plastic strain rates, and the material dilates plastically at a constant rate.

The flow rule follows the general case proposed by *Davis* [1969]

$$\frac{\dot{\varepsilon}_1^p}{\dot{\varepsilon}_3^p} = -\frac{k}{M},\ \dot{\varepsilon}_2^{\ P} = 0 \tag{1.23}$$

where

$$M = \frac{1+\sin\psi}{1-\sin\psi} \tag{1.24}$$

and ψ is the dilatancy angle. $\dot{\varepsilon}_1$, $\dot{\varepsilon}_2$ and $\dot{\varepsilon}_3$ denote the major, intermediate and minor principal plastic strain rates, respectively. Parameter k is 1 for a cylindrical cavity.

Initially (at $t = 0$) the cavity had a radius a_0 and internal pressure p_0. At a later time t, the cavity enlarged to radius a and internal pressure increased to p. The equilibrium

equation was expressed as

$$\frac{\partial \sigma_r}{\partial r} + k\frac{\sigma_r - \sigma_\theta}{r} = 0 \tag{1.25}$$

The constitutive equation for the material of the continuum was written as

$$\dot{\sigma} = D\dot{\varepsilon} \tag{1.26}$$

where $\dot{\sigma}$, and $\dot{\varepsilon}$ denote the stress and strain rates, and D is given by

$$D_E = \begin{bmatrix} \lambda + 2G & \lambda \\ \lambda & \lambda + 2G/k \end{bmatrix} \tag{1.27}$$

for purely elastic deformations, and by

$$D = \frac{2G}{\chi}\begin{bmatrix} 1 & 1/M \\ 1/N & 1/MN \end{bmatrix} \tag{1.28}$$

for deformations which involve plastic yielding. The quantities in equations (1.27) and (1.28) are defined by

$$\lambda = \frac{v}{1-2v}2G \tag{1.29}$$

where λ is the Lame modulus and G and v are the elastic shear modulus and Poisson's ratio for the ideal material and,

$$\chi = \frac{k(1-v) - kv(M+N) + [(k-2)v+1]MN}{[(k-1)v+1]MN} \tag{1.30}$$

Consider the situation that plastic yield only occurs in the region $a \le r \le R$. The limiting internal pressure p_L can be derived as

$$\frac{2G}{p_0} = \frac{N-1}{N+k}\left[T\left(\frac{p_L}{\sigma_R}\right)^{\gamma} - Z\frac{p_L}{\sigma_R}\right] \tag{1.31}$$

$$\sigma_R = \frac{1+k}{N+k}Np_0 \tag{1.32}$$

The closed form solutions can be applied to practical problems such as the interpretation of pressuremeter tests and determination of end bearing capacity of deep foundations. Cavity expansion process also appears to be an important mechanism of hydraulic fracturing in particular materials (see Chapter 6).

1.2.8 Deformation Localization in Particulate Materials

To examine the initiation and propagation of localized and diffuse non-uniform deformation modes in geomaterials, laboratory and theoretical studies have been conducted [*Rudnicki and Rice*, 1975; *Desrues et al.*, 1985; *Han and Vardoulakis*, 1991; *Alsiny et al.*, 1992]. In most of the work, the Thomas-Hill-Mandel theory of equilibrium bifurcation in hardening materials [*Rice*, 1976] was used to mathematically analyze the deformation localization. Since it is relevant to fracture initiation in this work (see Chapter 6), the laboratory and theoretical study by *Alsiny et al.* [1992] is presented.

Alsiny et al. [1992] investigated the deformation localization due to cavity inflation in a finite domain. Laboratory experiments were performed on sand specimens and the experimental results were compared with theoretical results obtained from different theories in the literature.

According to *Alsiny et al.* [1992], the localized deformation mode is defined as a set of narrow bands undergoing large shear strains and possibly dilation (i.e., shear bands). The investigators conduct experiments on dry sand specimens with the shape of a thick-walled hollow cylinder. They wrapped all of the boundaries of the hollow cylinder with rubber membranes. They confined the specimen at the outer boundary and constrained boundary is applied in the direction of the vertical axis. Finally, they pressurized the

hollow cylinder with oil from the inside through the rubber membrane with a constant injection rate.

The variation of differential cavity pressure σ_c and radial diameter of the outer specimen surface as a function of the cavity radial displacement u_c for four experiments at different confining pressure are shown in Figures 1.17a and 1.17b.

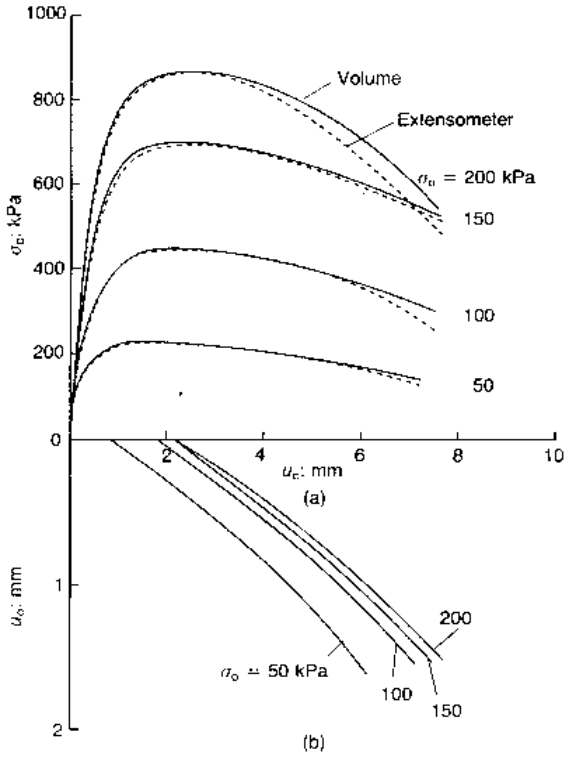

Figure 1.17 (a) Variation of differential cavity pressure σ_c and radial diameter of the outer specimen surface as a function of the cavity radial displacement u_c for four experiments at different confining pressures and (b) relationship of the radial displacement of the outer surface of the specimen and that of the cavity wall [*Alsiny et al.*, 1992].

All curves showed softening at a cavity volume change of ~ 20 to 30 cm^3. The authors attributed the delay in the growth of the outer surface displacement in Figure 1.17b to the initial contractancy of the sand and, possibly, to the insufficient sensitivity of the outer extensometer used for radial change measurement.

Deformation modes of the specimens were investigated by three different methods: visual inspection of the outer surface, radiograph of the specimen, and casting imprints of the deformed cavity.

A vertical fold observed in the outer surface rubber membrane indicated the localized deformation in the specimen. The fold was first detected after the peak differential cavity pressure.

Radiographs revealed acurved localized band of looser material extending from the cavity towards the outer surface of the specimen (Figure 1.18).

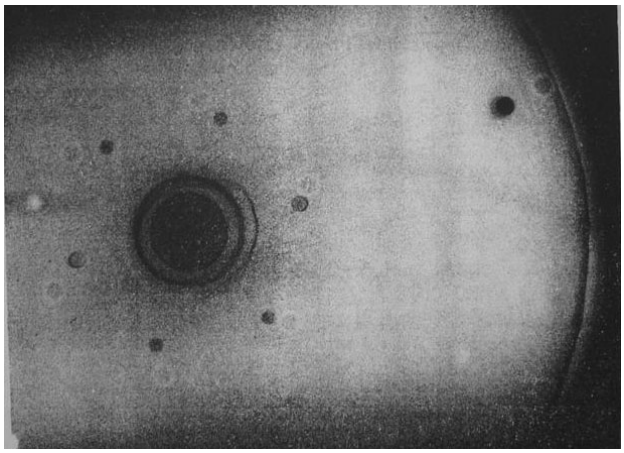

Figure 1.18 Radiograph of a specimen showing a curved localized band of looser material [*Alsiny et al.*, 1992].

Furthermore, cross-sections of hardened imprints of the cavities (Figure 1.19a) demonstrated shear bands induced distortion of the cavity wall, as well as cavity shape irregularities that occurred in all tests. The latter was interpreted as the manifestation of a diffuse deformation mode. Similarly, shear deformation from a pressurized borehole was also observed by *de Pater et al.* [2003] (Figure 1.19b). In this case, they injected bentonite slurry to the borehole without creating a clear fracture. However, the borehole

was significantly enlarged with shear deformations starting from the borehole as shown in Figure 1.19b.

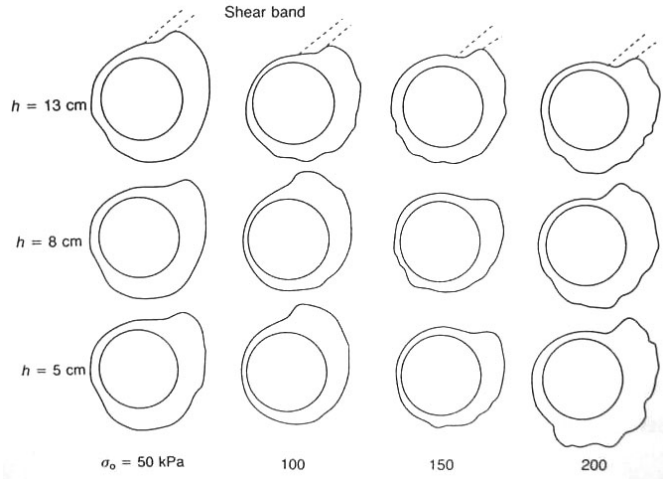

(a)

(b)

Figure 1.19 (a) Cross-sections of hardened imprints of cavities at different heights and at different confining pressures [*Alsiny et al.*, 1992] and (b) CT scan of cross-section a hydraulically pressurized borehole [*de Pater et al.,* 2003].

In addition to laboratory studies, they analyzed the stress and strains around a cylindrical cavity expanding axisymmetically in an elastoplastic material, based on incremental elastoplastic constitutive equations proposed by *Vardoulakis* [1988]. The results were then used for the local equilibrium bifurcations analysis by utilizing the methodology developed for investigating shear banding in the biaxial plain strain

compression tests [*Vardoulakis*, 1980; *Vardoulakis*, 1988]. The analytical results showed that deformation localization occurred when a hardening modulus reached a critical value. Consequently, the shear band inclination angle with respect to the direction of the algebraically greater principal stress was derived. This angle was predicted by several other formulas. Hence, they presented the predicted shapes of the shear banding for comparison with the laboratory observations (Figure 1.20). The comparison appeared to validate Coulomb's prediction that was given as

$$\Omega_c = \pm\left(45^o + \frac{\phi}{2}\right) \tag{1.33}$$

where Ω_c is the inclination angle of the shear banding and ϕ is the friction angle of the sand.

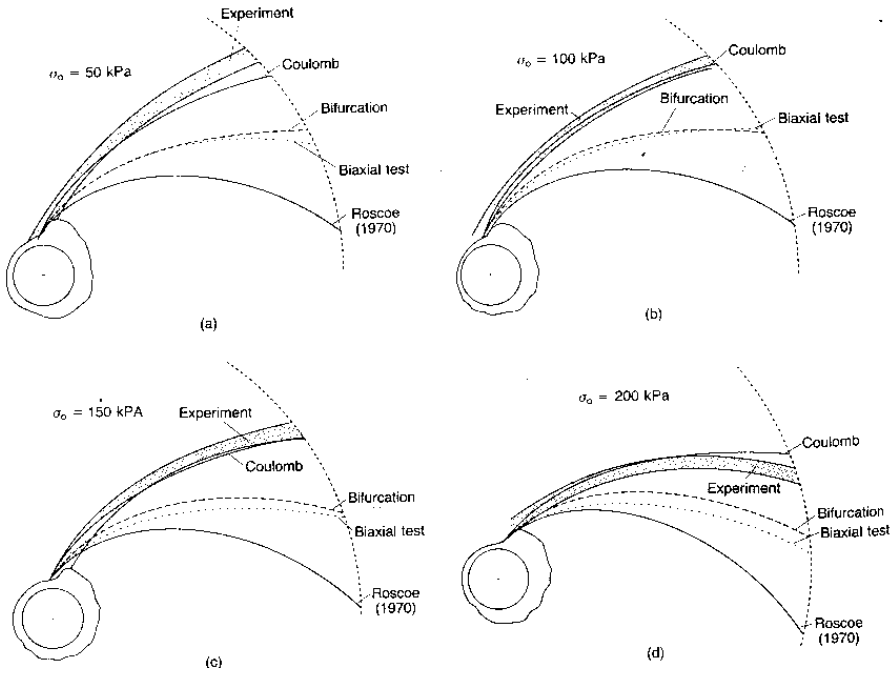

Figure 1.20 Shape of the shear bands at different confining pressures [*Alsiny et al.*, 1992].

1.3 Goal and Objectives

The main goal of this work is to determine whether hydraulic fracturing in uncemented sediments is possible, and if so, to study the relevant physical mechanisms. For this purpose, experimental laboratory techniques are developed and used to quantify the initiation and propagation of hydraulic fractures in dry particulate materials.

Dry particulate materials are used in this study as an extreme case. Dry materials are virtually cohesionless, as opposed to most solid materials. The study of this extreme case enables us to focus on the mechanisms of hydraulic fracturing due to the relevant properties of the particulate material itself. These properties are defined by the particle shape and size distribution, and the density and initial stress state of the specimen. In general, a complete understanding of hydraulic fracturing in particulate materials requires the consideration of other factors such as pressure diffusion, aqueous chemistry, and pressure solution. In this study, we attempt to minimize the effect of such complicating factors.

The principal objectives of this work include:

- Development of experimental techniques to directly observe hydraulic fracture initiation and propagation at laboratory scales.
- Comparison of hydraulic fracturing at different laboratory scales.
- Conducting a comprehensive experimental series with relevant values for the controlling parameters (e.g., properties of particulate materials and fracturing fluids, boundary conditions, initial stress states, injection volumes).

- Identification of principal fundamental mechanisms of hydraulic fracturing in particulate materials.

- Determining the relevant scaling relationships describing hydraulic fracturing in particulate materials (e.g., the interplay between elastic and plastic processes).

The detailed structure of this thesis is as follows:

Chapter 1 describes the background and motivation of this study.

Chapter 2 provides an overview of the laboratory experiments. It includes the principles, the parameters, the general procedures, and the setups of the developed experiments.

Chapter 3 presents the small-scale experiments, including the setup, and the procedures, and representative experimental results. The effects of the experimental parameters on the hydraulic fracturing behavior and the injection pressure are discussed.

Chapter 4 describes the experimental setup and procedures at the large scale for two extreme cases of the lateral boundary conditions: constrained and pressure-controlled lateral boundaries.

Chapter 5 presents the results of the large-scale experiments. The effects of the parameters on the fracturing behavior and the injection pressure are discussed. The correlation of different propagation stages with the injection pressure was examined. The results are compared between different sizes of the specimen and different lateral boundary conditions.

Chapter 6 identifies principal fundamental mechanisms of hydraulic fracturing in

cohesionless particulate materials based on the performed experimental study.

Chapter 7 summarizes important results obtained in this thesis, and provides recommendations for future work.

The experimental results of this work (Chapters 3 and 5) have been partly presented by *Chang et al*. [2003], *Van Dyke et al.* [2003] and *Germanovich et al.* [2002] while theoretical developments (Chapter 6) are discussed by *Germanovich et al.* [2005].

CHAPTER 2

EXPERIMENTAL DEVELOPMENTS AND TECHNIQUES

2.1 Introduction

In this chapter, an overview of the laboratory experiments will be provided, including the outline, the experimental setup, the parameters, and the general procedures. The properties of the particulate materials and the fracturing fluids will also be presented. The densification techniques for the particulate materials are discussed in the last section. More details of the experiments will be given in the subsequent chapters when relevant.

2.2 Experimental Outline

The general procedure of the experiments is to inject viscous fluids into dry particulate materials at a constant flow rate while the injection pressure is monitored. The injected fluid solidifies after the experiment, and is extracted from the particulate specimen.

A schematic of the experimental setup is shown in Figure 2.1.

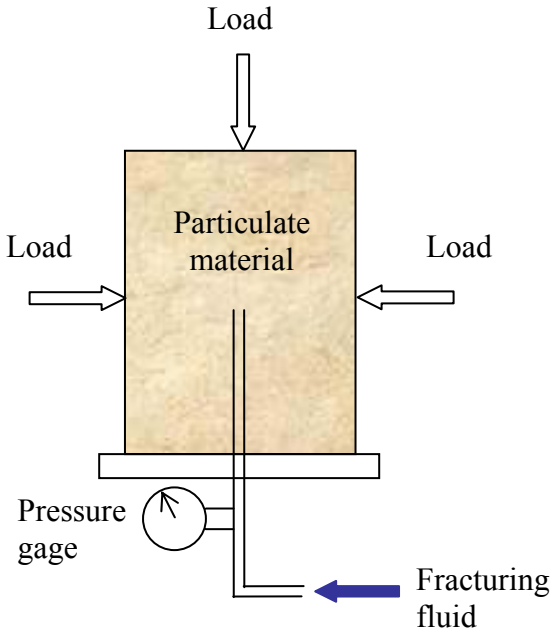

Figure 2.1 A schematic of the experimental setup.

Based on our preliminary experiments, the fluid flow appears to localize in discrete conduits. Often, these channels resemble cracks. By analogy they are called hydraulic fractures in this study. Also, non-fracturing phenomena (e.g., cavity expansion, leak-off) occur under certain conditions. However, in this study, the focus is on the thin, crack-like hydraulic fractures. In an attempt to concentrate on dry materials, leak-off of the injected fluid into the pore space is avoided as much as possible.

Dry particulate materials are used for the laboratory experiments as an extreme case. Dry materials are virtually cohesionless, as opposed to cohesive, solid materials. This extreme case study will aid us in examining the fundamental mechanisms of hydraulic fracturing in particulate materials. For the sake of brevity, "dry" is omitted in this thesis when mentioning particulate materials.

In reality (i.e., *in-situ*), the sediment conditions are usually very complicated. The

wide range of these conditions is probably bounded by two extreme lateral boundary conditions: constrained and pressure-controlled lateral boundaries. Hence, only these two extreme lateral boundary conditions are investigated in this study.

2.3 Experimental Parameters

The hypothesis is that the behavior of hydraulic fractures is influenced by the properties, the initial conditions and the boundary conditions of the particulate materials, and the properties and the injection conditions of the fracturing fluids. The principal influencing parameters studied are: (*i*) the type of particulate materials (i.e., the particle shape, size and particle size distribution), (*ii*) the density and (*iii*) the stress state (i.e., the stress ratio and mean stress) of the particulate materials; (*iv*) the flow rate, (*v*) the injection volume and (*vi*) the viscosity of the fracturing fluid; and (*vii*) the boundary conditions.

To show the effect of the particle size and particle size distribution, different types of particulate materials were used. Materials with similar particle geometry but different particle size distributions are most useful for this purpose.

The initial stress ratio of the particulate material is determined by the pressure applied to the specimen before the fluid injection. Since the specimen used in this study is cylindrical, the pressure applied to its boundaries is given by the vertical and horizontal (lateral) load components, p_v and p_h. At the boundaries,

$$p = \sigma \tag{2.1}$$

where p is the traction and σ is the normal stress inside the specimen. Due to the discrete properties of the particulate materials, the stresses inside the specimen fluctuate at the

particle scale. However, given the large dimensions of the specimens compared to the particle size used in this study, these fluctuations are ignored. The prepared specimen is assumed to be relatively uniform without significant stress concentration/fluctuations. In other words, at the specimen scale, the particulate material can be considered as continuous and homogeneous.

A Mohr-Coulomb material yields when the Mohr circle touches the failure envelope as shown in Figure 2.2. For cohesionless particulate materials, cohesion equals zero. At failure, the ratio between the maximum and minimum principal stresses, σ_1 and σ_3, is

$$\frac{\sigma_1}{\sigma_3} = \frac{1+\sin\phi}{1-\sin\phi} \tag{2.2}$$

where ϕ is the fracture angle of the particulate materials. Let

$$K = \frac{1+\sin\phi}{1-\sin\phi} \tag{2.3}$$

In the experiments of this study, either the horizontal stress p_h or vertical stress p_v can be the maximum principal stress σ_1. In order for Mohr-Coulomb materials not to yield (prior to the fracturing), the ratio p_v / p_h has to be such that

$$\frac{1}{K} < \frac{p_v}{p_h} < K \tag{2.4}$$

More accurately, the particulate material may yield even if p_v / p_h is within the range of (2.4) but it is not at plastic failure, which may be characterized, for example, by the appearance of the shear bands (say, in tri-axial tests).

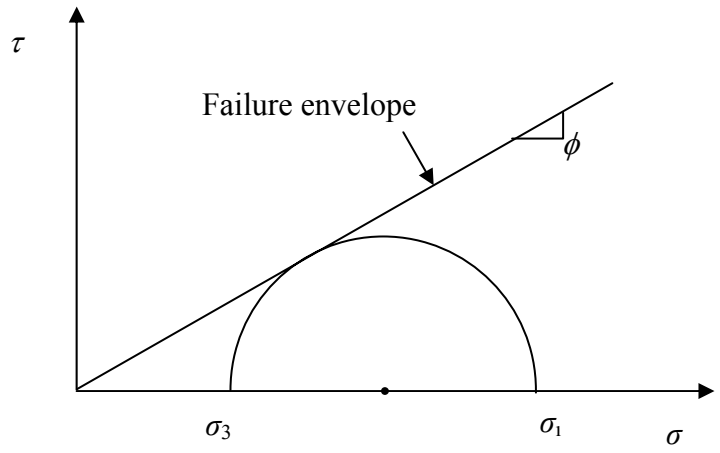

Figure 2.2 Mohr-Coulomb diagram for cohesionless materials. Here, σ represents normal stress, τ represents shear stress, and ϕ is the friction angle.

In this study, the following factors are varied in the experiments: (*i*) the ratio of the boundary loads p_v / p_h, (*ii*) the magnitude of the boundary loads p_v and p_h, (*iii*) the density and (*iv*) the type (the particle size and its distribution) of the particulate materials, (*v*) the viscosity and (*vii*) the injection volume of the fracturing fluid, (*vii*) the boundary condition, and (*viii*) the spatial and temporal scales.

The experiments with different temporal scales (i.e., different injection time, hence different injection volumes) are designed to examine the different stages of fracture propagation.

To study the boundary effect, experiments were performed at both small and large spatial scales.

2.4 General Procedures

The general procedures of the hydraulic fracturing experiments include the preparation of the particulate specimen, the injection of the fracturing fluid and the excavation of the

hydraulic fracture. A schematic view of the general procedures is shown in Figure 2.3a to Figure 2.3e.

To examine the fundamental mechanisms of hydraulic fracturing in the particulate materials, the testing material needs to be as cohesionless as possible. Because moisture could make the particles attach to each other, the particulate material is oven-dried before the experiments.

The specimen is prepared inside a cylindrical container. The injection tubing is mounted along the vertical, center axis of the container with an outflow hole at the half-height of the tubing. The outflow hole is temporarily sealed during specimen preparation to prevent the particulate materials from entering the tubing and clogging it. The density of the specimen is controlled by varying the preparation techniques and their parameters.

After the specimen is prepared, the experimental setup is assembled and the vertical and horizontal pressures (i.e., loads) are applied to the specimen as shown in Figure 2.1 and Figure 2.3b. Then, the seal of the outflow hole in the tubing is removed. The injection tubing is pre-filled with the fracturing fluid.

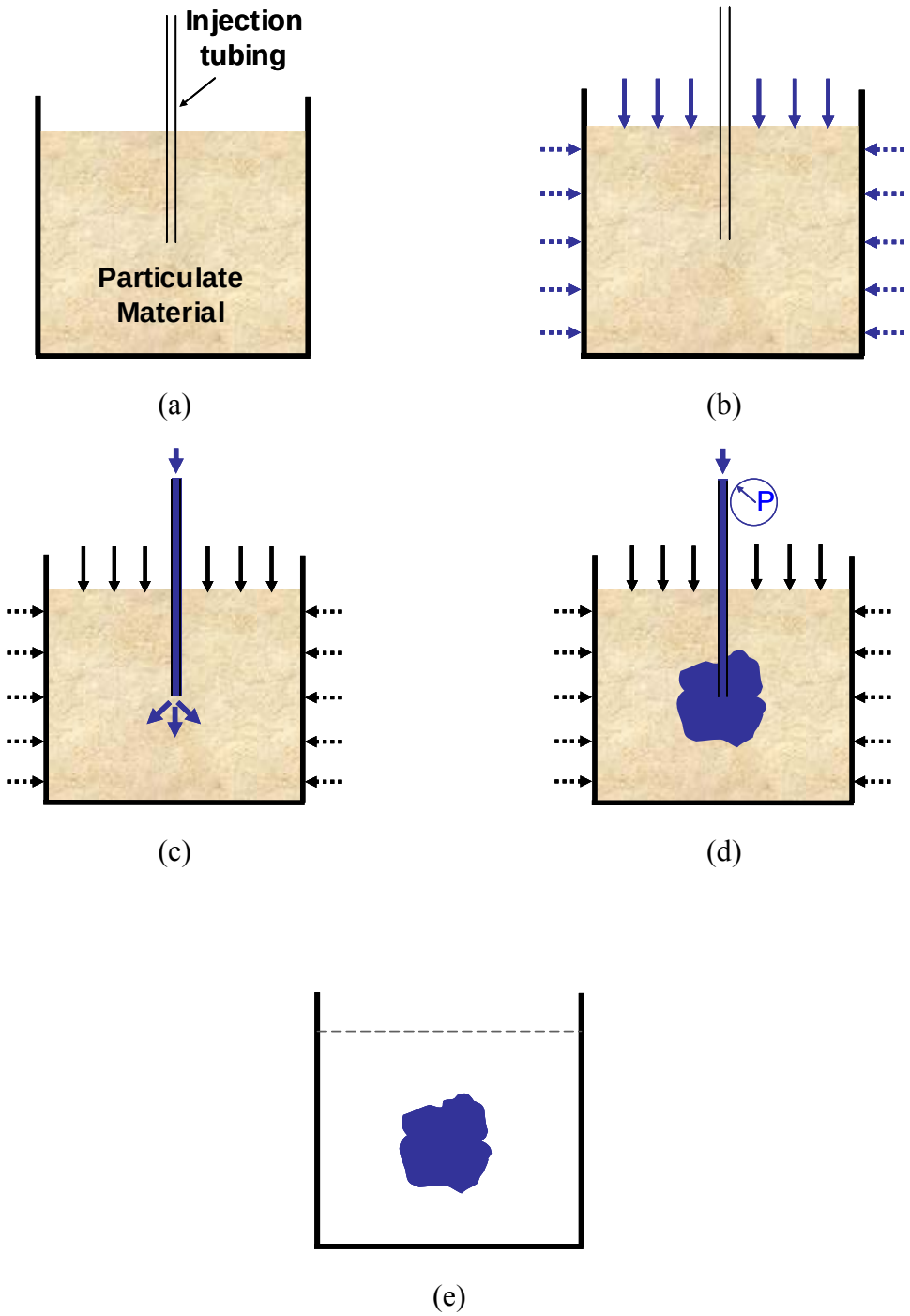

Figure 2.3 General procedures of hydraulic fracturing experiment: (a) preparing particulate specimen with injection tubing pre-mounted, (b) loading specimen, (c) injecting fracturing fluid through injection tubing, (d) fracturing particulate specimen with injection fluid and measuring the injection pressure, and (e) excavating solidified fracturing fluid from particulate specimen and exposing the fracture impression.

The fluid is injected by a pump at a constant flow rate. The pump is stopped at a certain target volume. After the pump stops, the fluid is sealed inside the specimen. A constant pump rate is used to simulate the *in-situ* fluid injection. In addition, this yields a stable fracture propagation to make data collecting easier.

The controlled parameters are the initial density, the initial loading condition of the particulate specimen, the viscosity of the fracturing fluid, the injection rate and the injected volume (i.e., the injection time). The change of volume of the specimen due to the fluid injection is measured. During and after the experiment, the fluid pressure near the outlet of the pump is recorded.

After the injection, the applied load on the specimen is maintained for at least 12 *hr*. This allows the fluid to solidify inside the specimen while maintaining the shape of the fracture until it is unloaded. After the solidification of the injection fluid, the loads are removed and the specimen container is opened to expose the specimen to the atmosphere. The impression of the hydraulic fracture is gradually excavated from the particulates while the fracturing "fluid" continues hardening. The excavation of a solidified hydraulic fracture in Georgia Red Clay is presented in Figure 2.4a and a fracture impression completely excavated from the particulate materials is shown in Figure 2.4b.

(a) (b)

Figure 2.4 Excavation of a solidified hydraulic fracture in Georgia Red Clay: (a) partially and (b) completely excavated.

2.5 Properties of Selected Particulate Materials

In this section, the principles used to select the particulate materials will be addressed. The physical properties, particle geometry and gradation, and the stress-strain relationship of the particulate materials are also presented.

2.5.1 Choice of Particulate Materials

To study the fundamental mechanisms of hydraulic fracturing in particulate materials, the inter-particle forces of the selected materials need to be dominated by skeletal, structural (mechanical) forces instead of physical-chemical surface electrical forces. The inter-particle forces acting on a particle as a function of the particle size are shown in Figure 2.5. Based on this graph, *Santamarina* [2001] states that when the particle size is ~ 10 μm the self-weight of the particle is of the same order of magnitude as the Van der Waals attraction. While we tried to minimize the content of particles that are finer than ~ 10 μm,

as will be shown in Chapter 6, such magnitudes of inter-particle forces (i.e., material cohesion) appear to not affect the hydraulic fracturing mechanism since all parts of the particulate material are in compression. This also ensures that the effect of the capillary forces that may appear even in a dry particulate material (due to the condensation of vapor from the atmosphere) is negligible for all practical purposes.

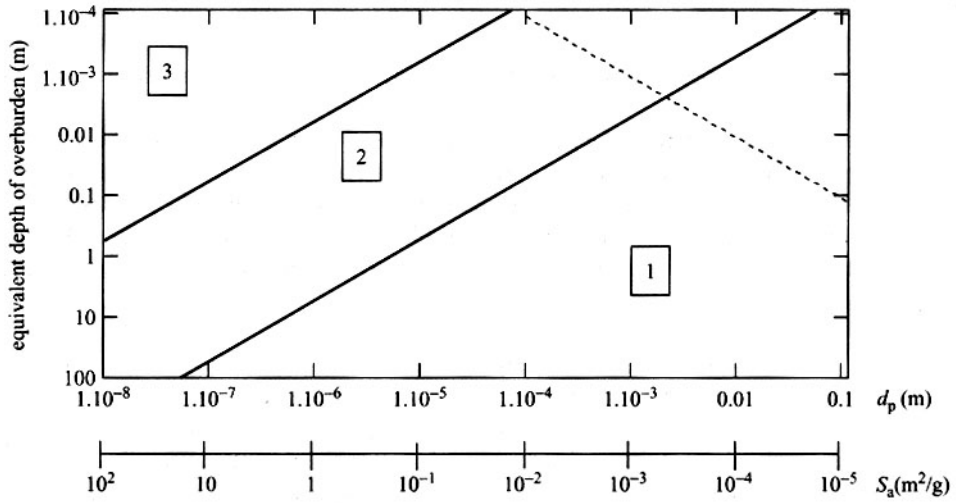

Figure 2.5 Forces acting on a particle as a function of the particle size. In Region 1, skeletal forces dominate. In Regions 2 and 3, capillary forces are greater than skeletal forces. In Region 3, electrical forces are greater than skeletal forces [*Santamarina*, 2001].

On the other hand, our preliminary experiments showed that coarse particulates with large void spaces allowed the fracturing fluid to leak-off into the voids. To ensure that leak-off does not dominates the hydraulic fracturing process, such coarse particles are generally avoided.

Based on these constraints, four dry particulate materials with mean particle sizes ranging from ~ 20 to 100 μm are analyzed for the hydraulic fracturing experiments: silica flour (silt-sized, ground sand), Georgia Red Clay (clayey-silt), Ottawa Sand (fine sand),

and a mixture of fine sand and silica flour with weight ratios of 93% and 7%, respectively. The material type is classified according to Unified Soil Classification System (USCS) [*U.S. Bureau of Reclamation*, 1974; *Army Engineer WES*, 1960].

The Georgia Red Clay is a clay-silt that was obtained locally in the field. The silica flour (SIL-CO-SIL® 106 from U.S. Silica) is produced by grinding high purity sand. The fine sand (Ottawa Sand F110 from U.S. Silica) is an unground foundry sand. The sand-silica flour mixture has a large fraction of sand and small fraction of silica flour so that it behaves cohesionless but has a reduced void ratio (i.e., the small particles partially fill the void spaces in between the large particles) compared to pure fine sand.

The preliminary experiments with fine sand showed that significant leak-off occurred. Hence, even the fine sand appears to be too coarse for the selected fluid viscosity and injection rate. Also, the mixture of fine sand and silica flour tends to segregate during the specimen preparation with vibration technique, and hence also appears to be not suitable. Therefore, Georgia Red Clay and silica flour were selected for the hydraulic fracturing experiments.

2.5.2 Typical Physical Properties

The index properties of the three particulate materials (Georgia Red Clay, silica flour and fine sand) are listed in Table 2.1. The specific gravity is determined by the standard of American Society for Testing and Materials (ASTM) D 854-00. The minimum and maximum void ratios are determined by ASTM D 4253-00 and D 4254-00, respectively.

Table 2.1 Index properties of particulate materials

Particulates		**Georgia Red Clay**	**Silica Flour (SIL-CO-SIL® 106)**	**Ottawa Sand F110**
Type		Clay-silt	Silt-sized ground sand	Fine sand
Mineral		Various	Quartz	Quartz
Color		Red / brown	White	White
Grain shape		Various	Angular and irregular	Round
Specific gravity		2.3[(1)]	2.65	2.65
Void ratio	Maximum	1.27	1.51	0.85
	Minimum	0.75	0.55	0.54
Porosity	Maximum	0.56	0.60	0.46
	Minimum	0.43	0.35	0.35
Dry density *(g/cm^3)*	Minimum	1.01	1.05	1.43
	Maximum	1.31	1.71	1.73
Angle of repose		41	50	27

Note: (1) Georgia Red Clay is not a commercial material but obtained locally in the field. The properties of the material may vary from site to site.

2.5.3 Particle Shape

Georgia Red Clay contains a wide range of particles (i.e., from sand to clay). Consequently, the particle shape is expected to vary widely from round to planar (Figure 2.6a). The particle shape of silica flour is irregular and angular as shown in Figure 2.6b since it has been produced by grinding. The strong frictional forces between the particles

and their interlocking may be one of the reasons for the high angle of repose (50º; see Table 2.1). Fine sand has round particles as shown in Figure 2.6c.

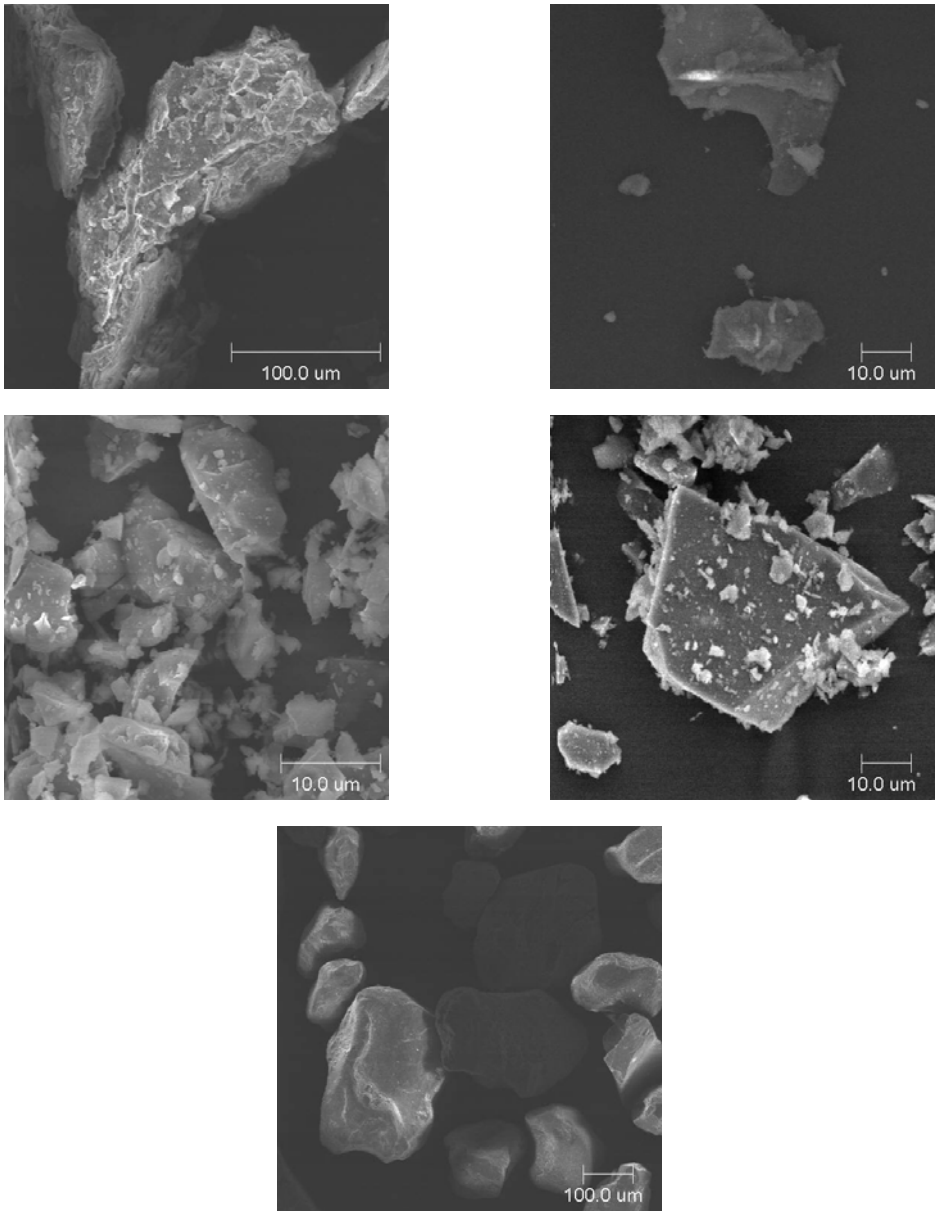

Figure 2.6 SEM microphotographs of particle shapes: (a) Georgia Red Clay, (b) silica flour, and (c) fine sand.

2.5.4 Grain Size Distribution

The grain size distribution curves of the three materials (i.e., Georgia Red Clay, silica

flour and fine sand), as determined by ASTM D 422-63, are shown in Figure 2.7. Grain size ranges are labeled in the figure. Please note that the tail of the curve of Georgia Red Clay with particle size from 1 to 0. 1 μm is extrapolated based on its trend. The main parameters of grain size distribution of the particulate materials are listed in Table 2.2.

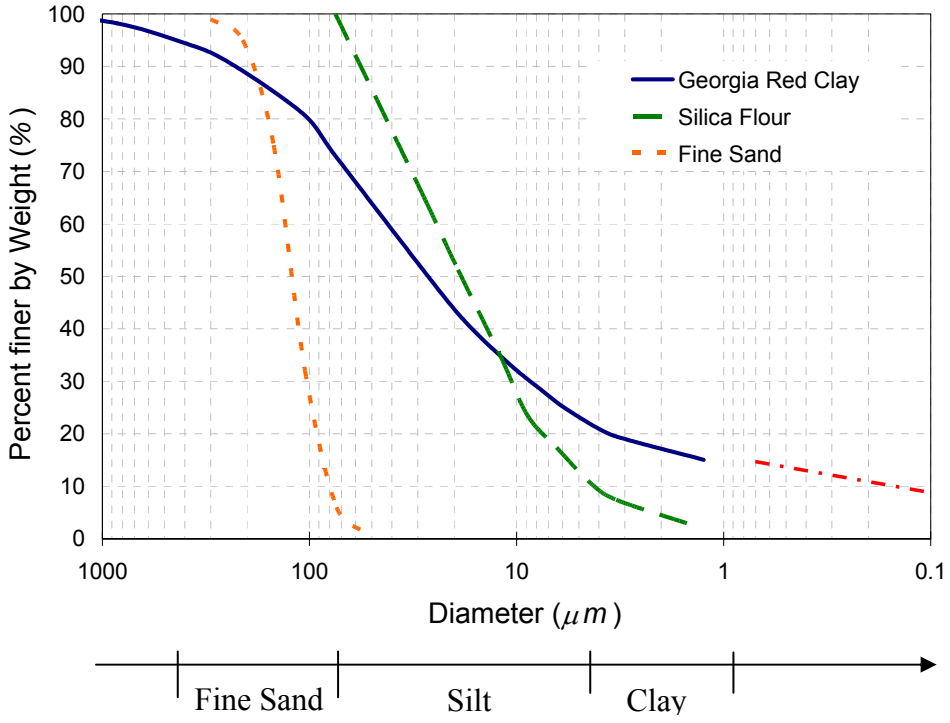

Figure 2.7 Grain size distributions of the particulates and the grain size range of tested particulate materials.

The particle size of Georgia Red Clay has a wide range from millimeters to microns. According to the ASTM D 422-63; D 653-97, it contains ~ 50% silt-size particles and ~ 22% clay-size particles. The high coefficient of uniformity indicates that it is well-graded. The Ottawa sand F110 contains ~ 95% of fine sand particles. The narrow particle size range and the low values of *Cu* and *Cc* indicate that it has a relatively uniform grain size and a poor gradation. Silica flour has ~ 88% silt-size particles. Its gradation falls in between Georgia Red Clay and fine sand.

In this study, the terms "coarse grain" and "fine grain" are used when referring to different particle sizes that are separated by U.S. standard sieve No. 200, according to the designation of USCS [*Holtz*, 1981].

Table 2.2 Parameters of grain size distribution of tested particulate materials

Particulates Media		**Georgia Red Clay**	**Silica Flour**	**Fine Sand**
Median particle size (D_{50})	μm	26	19	110
Coefficient of uniformity (Cu)		205	5.8	1.6
Coefficient of curvature (Cc)		9.9	1.3	1.0
Division according to USCS		Fine grain		Coarse grain

2.5.5 Critical State Parameters

The critical state parameters of silica flour were measured on dry specimens with standard tri-axial tests (ASTM 4767-02). Since global properties of a specimen are measured in this test, localization in the specimen needs to be avoided as much as possible. Therefore, the tests are performed on specimens with a density that is as low as possible under relatively high loads. Under these conditions, the specimen will more likely be contractive, implying that localization will be less likely [e.g., *Santamarina*, 2001]. The relative density of the specimen D_r used for the critical state parameter measurement is ~ 70%. The Relative density is defined [*Holtz and Kovacs*, 1981] as

$$D_r = \frac{e_{\max} - e}{e_{\max} - e_{\min}} \times 100(\%) \qquad (2.5)$$

where e_{max} and e_{min} are the maximum and minimum void ratios of the material, respectively. These two void ratios describe the loosest and densest possible conditions of

a soil.

The measured critical state line of silica flour plotted in v - p and q - p space is shown in Figures 2.8 and 2.9, respectively. The critical state parameters are listed in Table 2.3.

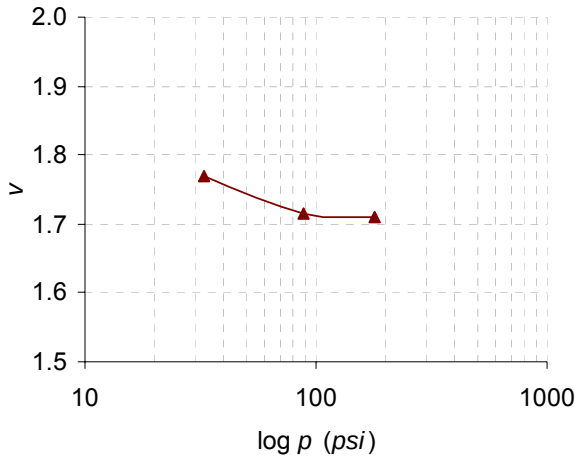

Figure 2.8 Critical state line of silica flour: specific volume v as a function of mean stress p.

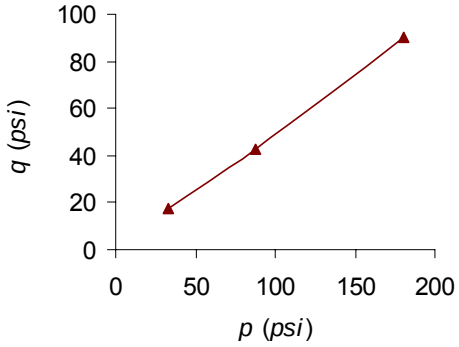

Figure 2.9 Critical state line of silica flour: deviatoric stress q as a function of mean stress p.

Table 2.3 Critical state parameters of silica flour

M	Γ	λ_{cs}	ϕ_{cs}
0.5	1.9	0.037	39°

Note: 1. Deviatoric stress $q = \sigma_1 - \sigma_3$.

2. Mean stress $p = (\sigma_1 + 2\sigma_3)/3$

3. Specific volume v = 1+e, where e is the void ratio of the material.

4. Parameter M is the slope of the critical state line on the q - p plane, i.e., $q = Mp$.

5. Parameter Γ is the value of v on the critical state line at a reference mean stress p_0, where $v = \Gamma - \lambda_{cs} \ln\left(\frac{p}{p_0}\right)$.

6. Parameter ϕ_{cs} is the friction angle at the critical state [*Santamarina*, 2001].

2.5.6 Stress - Displacement Behavior

The friction angles of Georgia Red Clay, silica flour and fine sand are determined by the ASTM standard method from direct shear test (ASTM D 3080 - 03) [*Lambe*, 1991]. The sketch of the testing apparatus is shown in Figure 2.10. The applied normal load on the specimen ranges from 5 to 40 *psi*. The initial relative density of the Georgia Red Clay, silica flour and fine sand are 90, 90 and 20%, respectively. The measured friction angles of Georgia Red Clay, silica flour and fine sand are listed in Table 2.4.

The relationship between shear stress and shear (horizontal) displacement, and the relationship between the vertical and horizontal displacements are shown in Figures 2.10 and 2.11 for Georgia Red Clay and silica flour, respectively.

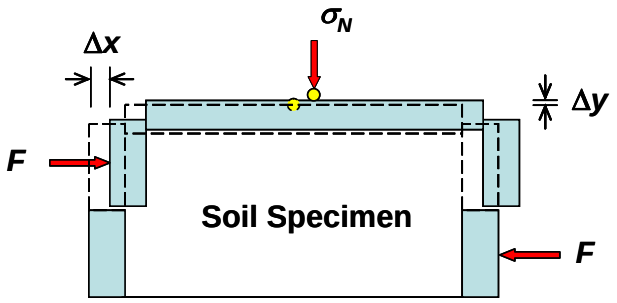

Figure 2.10 Sketch of direct shear test apparatus.

Table 2.4 Material properties from the direct shear test

Particulate Material		**Georgia Red Clay**	**Silica Flour**	**Fine Sand**
Peak friction angle	*degrees*	42	40	27
Residual friction angle		40	38	not observed
Shear Modulus	*MPa*	10	7	5

Both materials exhibit strain softening behavior as shown in Figures 2.11a and 2.12a. For the relationship of the vertical versus horizontal displacements, the change of the vertical displacement reflects the volume variation of the specimen during shear compared to its initial volume, given the fact that the diameter of the specimen is considered to be constant. During shear for both materials, the volume of the specimen decreases first, and then starts to increase.

The dilatancy angle ψ describes the volume change during pure shear of a particulate material. The maximum dilation angle ψ_{max} is the angle at the maximum slope, i.e., maximum value of dy/dx, of the vertical - horizontal displacement curve as shown in Figures 2.11b and 2.12b. The maximum dilation angles of Georgia red clay and silica

flour at different applied vertical loads are listed in Table 2.5.

(a)

(b)

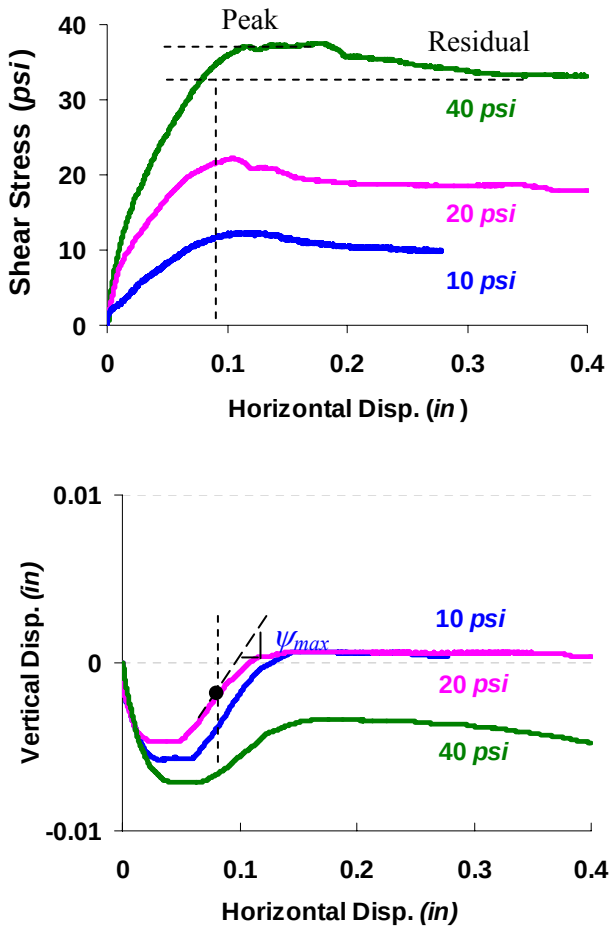

Figure 2.11 Silica flour: relationship of (a) shear stress versus horizontal displacement and (b) vertical displacement versus horizontal displacement. Here, ψ_{max} represents the maximum dilation angle.

(a)

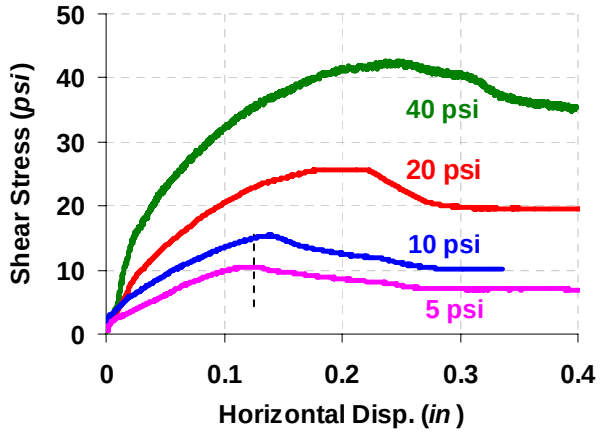

(b)

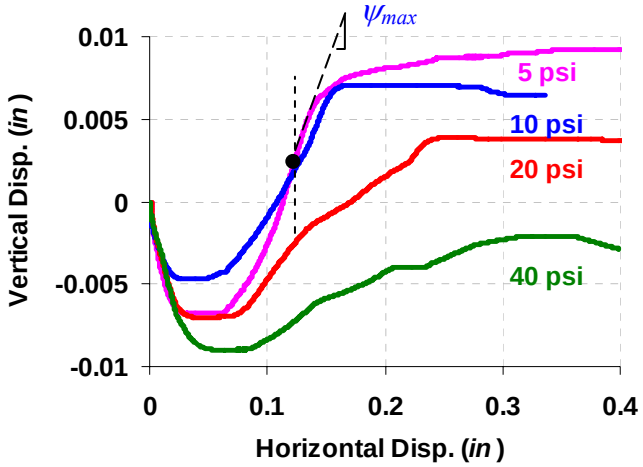

Figure 2.12 Georgia Red Clay: (a) Shear stress versus horizontal displacement and (b) vertical displacement versus horizontal displacement relationship of. Here, ψ_{max} represents maximum dilation angle.

Table 2.5 Maximum dilation angles of tested materials at different vertical loads

Vertical load	**Georgia Red Clay**		**Silica flour**	
	Void Ratio *e* / Porosity ϕ	**Maximum dilation angle ψ_{max}**	**Void Ratio *e* / Porosity ϕ**	**Maximum dilation angle ψ_{max}**
psi		°		°
5	0.80 / 0.44	14	0.68 / 0.40	not available
10		10		7
20		5		4
40		3		3

Generally, the maximum dilation angle decreases when the load increases [*Taylor*, 1948]. The measurements of the two materials demonstrate the same trend. This reflects the decrease of the dilation tendency with increasing the load level of the particulate materials.

2.5.7 Cohesion

Oven-dried Georgia Red Clay and fine sand cannot support vertical free surfaces. Hence, these two particulate materials behave cohesionless for all practical purposes.

Although silica flour contains ~ 88% silt-size particles, it does not behave completely cohesionlessly. Oven-dried silica flour can support vertical free surfaces. Apparently, inter-particle forces hold the silica flour together. However, these surface forces are very weak, even in dense silica four. That is, silica flour can bear almost no tension (no more than 0.1 *psi*), and it is considered to be virtually cohesionless, as far as the hydraulic fracturing experiments are concerned. A further discussion of the low cohesion of the

silica flour will be presented in section 6.4.4.

2.6 Properties of Selected Fracturing Fluids

To allow for excavation, the fracturing fluids need to solidify after the completion of the experiments. However, they should not solidify during or shortly after the experiments to enable the disassembly and cleaning of the equipment. Joint compound (Sheetrock all-purpose joint compound) and RTV silicone adhesive sealant (Dow Corning 734) are suitable fracturing fluids that are used in this study. The typical properties of these two fluids are listed in Table 2.6.

The apparent viscosities of joint compound and silicone sealant are measured by pumping the liquid through a long piece of tubing with different inner diameters and varying flow rates, and measuring the pressure drop. An apparent viscosity of a non-Newtonian fluid changes with the applied shear force or rate. As a result, non-Newtonian fluids do not have a well-defined viscosity [*Bird, 2002*]. In addition, the exact value of their apparent viscosity may depend on the measurement technique. Since both of the fracturing fluids are non-Newtonian, we use this pumping technique to obtain only the order of magnitude of the apparent viscosity of the two fluids. The m1easured magnitude of the apparent viscosity of the silicone sealant matches with the value from its product data sheet (Dow Corning Company).

Both fluids have a non-linear relationship between their apparent viscosity versus the shear force or rate. In particular, they are seemingly of the Bingham viscosity type with a finite strength at low shear force or rate. This may exert some (yet undetermined) control

on the fracture (front) shape at different injection rates.

Table 2.6 Properties of fracturing fluids

Fracturing fluid	**Dynamic Viscosity**	**Fluid Density at 25°C**	**Skin-over Time (~1 *mm* thickness)**	**Cure Time (see text)**
	cP	g/cm^3		
Joint compound	$\sim 10^{5(1)}$	1.6	does not skin	1 to 3 *days*
Silicone sealant	$4\times10^{4(2)}$	1.0	10 *minutes*	2 *hours* to 1 *day*

Note: (1) from laboratory measurement; (2) from the product data sheet (Dow Corning Company).

2.6.1 Joint compound

Joint compound is a water-based, viscous paste of gypsum particles that is grey-white, as shown in Figure 2.13. It resembles a thick slurry and has a dynamic viscosity of $\sim 10^5$ *cP*. The suspension is relatively stable and does not separate readily. Joint compound solidifies due to water evaporation. The cure time depends on the thickness and total mass of the joint compound body, and typically for our hydraulic fracturing experiments is ~ 1 *day*. A large fracture generally requires several days for complete solidification. Heating accelerates the solidification to occur in less than one day.

Solidified joint compound is hard and brittle. However, it is water soluble, that is, it loses its strength almost completely after soaking in water. For long-term preservation, encapsulation of the fracture sample in a transparent medium (e.g., epoxy resin) is recommended, as shown in Figure 2.14.

Figure 2.13 Consistency of joint compound.

Figure 2.14 A fracture sample encapsulated in a transparent epoxy resin.

Because the joint compound is water-based, the water may leak off from the paste and wet the surrounding dry particulate material during the hydraulic fracturing process. The wetting of the dry particulate material in the vicinity of the fracture tip is undesirable in this study since it may introduce apparent “cohesion” to the dry particulate materials due to capillary forces.

The leak-off consists of two processes: (*i*) the water in the joint compound dissipates from the joint compound first, and (*ii*) permeates into the surrounding particulate material. The dissipation of water from the joint compound resembles the consolidation process in

particulate materials. The consolidation rate is affected by the permeability of the joint compound and the hydraulic pressure gradient. The permeation rate is controlled by the permeability of the particulate material, the capillary forces and the hydraulic pressure gradient between the fracturing fluid and the void space of the surrounding particulate material. Of these two processes, the one that has the lower rate controls the rate of leak-off. The rate of fluid injection competes with that of the leak-off.

In this work, given the short period of injection and fast rate of fracture propagation, the leak-off can be considered to be negligible.

2.6.2 Silicone Sealant

The silicone sealant (Dow Corning 734) is a polymer-based and flowable silicone adhesive sealant. The color of the product used in this study is white. Since the silicone sealant is not a solution or a suspension, no water or other fluid will separate from the sealant over time. Hence, there is no wetting problem during fluid injection.

Silicone sealant solidifies due to the chemical reaction with the moisture from the atmosphere. The curing time of the silicone sealant depends on the thickness and the total mass of the body. For example, a layer with a 1/8 *in* thickness exposed to air will take a few *hours* to solidify. Hydraulic fractures with a thickness of ¼ *in* generated by the silicone sealant inside the specimen generally take 1 *day* to solidify sufficiently for handling.

2.7 Densification of Particulate Materials

For constrained lateral boundaries, the particulate specimen is prepared in a steel container. For pressure-controlled lateral boundary experiments, the particulate specimen is prepared in the split mold of a tri-axial cell. For both types of boundaries, experiments are performed in small and large cells.

The particulate specimens need to be prepared with an acceptable degree of repeatability and control of the target density.

The relative density is used as a measure of the densification of the particulate specimens. The terms such as "loose" and "dense" are used in this study to refer to the relative density as listed in Table 2.7.

Typical specimen preparation methods for dry particulate materials in laboratories include air pluviation, vibration compaction, one-dimensional static-load compaction, isotropic static-load compaction, rodding, spooning, tamping and tapping [*Frost*, 1994; *Paprocki*, 1971]. Each method has its advantages and disadvantages, depending on the type of particulate material and the target density.

In this study, spooning, vibration compaction, rodding, and one dimension static-load compaction are used for the specimen preparation. With each of the four methods, the particulate material is spooned into a container first before the densification.

Table 2.7 Designations based on relative density according to AS(1) 1726

Designation	Relative Density (%)
very loose	0 to 15
loose	15 to 35
medium dense	35 to 65
dense	65 to 85
very dense	85 to 100

Note: (1) AS –Australia Standard.

Vibration Compaction

With the vibration compaction method, the specimen is vibrated under a surcharge (i.e., dead weight). The specimen is usually prepared in bulk but can also be prepared in layers [*Mahmood et al.*, 1976].

The packing of the particles after vibration is influenced by the particle size distribution and the particle shape [*Paprocki and Hodge*, 1971]. For a given material, the densities can be controlled by varying the surcharge and the frequency, amplitude and duration of vibration.

This method is more effective for materials with angular particles than with round ones [*Paprocki and Hodge*, 1971]. It is typically used to prepare specimens ranging from medium to very dense [*Obrician*, 1969; *Mahmood et al.*, 1976]. In the ASTM test (ASTM D 4253), this method is specified for determining the maximum relative density of particulate materials.

This method is simple and has a good repeatability. With a fixed procedure, the

overall, average target density is easily achieved. The disadvantage of this method is that fine particles tend to migrate downward (and coarse particles upward) during vibration, which causes segregation. Since angular particles are typically less mobile than round particles, migration in particulate specimens with angular particles is expected to be less than that with round particles. *Mahmood et al.* [1996] showed that vibrated particulate materials do not have high locked-in lateral stresses, compared to air pluviation.

In this study, we use this method to prepare dense to very dense specimens of Georgia Red Clay and silica flour in steel containers for constrained lateral boundary experiments. The specimen is prepared in bulk at both small and large scale. It is not used in tri-axial cells for pressure-controlled lateral boundary experiments because it is likely to damage the tri-axial cells. The parameters of the vibration technique are listed in Table 2.8. More information about specimens prepared by this technique is presented in Appendix A.

Table 2.8 Parameters of vibration technique

Parameter			**Small**	**Large**
Diameter of specimen		*in*	6	12
Height of specimen		*in*	~ 5.5	~ 14
Surcharge		*psi*	1	
Vibration time		*min*	20	
Vibration frequency		*Hz*	60	
Obtained relative density	Silica flour	*%*	~ 100	~ 90
	Georgia Red Clay		~ 90	~ 70

Rodding

For the rodding method, the specimen is prepared in layers. This method is simple and no special apparatus is needed. From our experience in the laboratory, it is more efficient for particulates with angular shapes probably because the friction between the particles aids in locking the rodding energy. From our experience of densifying silica flour with rodding, this method is not effective for shallow loose material with a depth less than 2 *in*. Therefore, the first lower layer is less dense. In addition, an extra top layer is needed to densify the last upper layer of the specimen. With rodding, the surface of the densified layer increases gradually. After rodding on each layer, the upper part of each layer always remains very loose. Hence, scarification is not needed. Therefore, there is no distinguishable, sharp interface between the layers.

The rodding technique creates relatively uniform specimens at the scale of the specimen, but not at the scale of the rod diameter. To reduce the local non-uniformity, a large number of strokes are needed. The non-uniformity may not be critical if the scale of the hydraulic fracturing processes is greater than the scale of the non-uniformities. The repeatability depends mainly on operators.

We speculate that during rodding lateral stresses can be locked in the specimen, especially for specimens with a high density since it requires relatively large rodding forces. For pressure-controlled lateral boundaries, after the specimen is prepared, a low vacuum is applied to the specimen to maintain its shape and stability. Then the split mold is disassembled. Therefore, most of the large locked-in stresses, if there is any, are believed to be released at least near the boundary. In specimens with constrained lateral

boundaries, the locked-in stresses remain after specimen preparation. Therefore, the initial stress condition of the prepared specimen with constrained lateral boundaries is generally unknown. However, when the applied load level is much greater (e.g., at least one order of magnitude higher) than the expected locked-in stresses, we consider the effect of the locked-in stresses to be negligible.

The rodding technique has four main parameters: (*i*) the diameter of the rod, (*ii*) the thickness of each layer, (*iii*) the applied force of each stroke, and (*iv*) the number of strokes for each layer. The density can be controlled by varying these four parameters. A minimum layer thickness needs to be maintained for sufficient rodding efficiency. On the other hand, a layer thickness that is too large results in non-uniformities even within a layer. Therefore, there is an optimal thickness to achieve the highest efficiency. Similarly, the diameter of the rod needs to be much larger than the particle sizes, and on the other hand, sufficiently small to apply a high vertical pressure (i.e., otherwise, it becomes a tapping device). As mentioned before, the number of strokes for each layer needs to be as large as possible. Hence, the densities are controlled by varying the force applied to each stroke and the number of stokes per layer.

In this study, rodding is used to prepare silica flour specimen in layers for constrained lateral boundaries at large scale and pressure-controlled lateral boundaries at both small and large scales. The rodding parameters used in this study are listed in Table 2.9.

Table 2.9 Parameters of rodding technique

Parameter			Steel Container	Tri-axial cell	
			Large	Small	Large
specimen	Diameter	*in*	11	4	12
	Height	*in*	14	8	18
layer	thickness	*in*	1.8	~ 1.3	~ 1.8
	Number		8	6	12
Rod diameter		*in*	0.5		
Ratio of rodded area versus. specimen area per layer			2	3	2
Number of Strokes per layer			1,000	200	1,200
Average rodding force per stroke		*psi*	1to 50		
Obtained density for silica flour		*%*	45 to 100		

Static-load Compaction

With the static load compaction method, static loads are applied on the boundaries of the specimen to compact it. It can be either one-dimensioned or isotropic compaction. For one-dimensioned compaction, the specimen is placed in a rigid container and a static load is applied on the top boundary. The material is loaded until it stabilizes. The one-dimensioned compaction will produce an anisotropic grain structure which will be relevant to most geological consolidation situations. Isotropic compaction compresses a specimen equally from all three directions and will generate a more isotropic structure. This is the method that power metallurgists used to make uniformly dense components

[*Paprochi and Hodge*, 1971].

The densities can be controlled by adjusting the static loads. High compaction load is required to achieve high densities. This is one disadvantage of this method if it is used in this study. The reason is that the compaction load is limited by the target loading on the specimen, which cannot be unloaded; otherwise the specimen will be overconsolidated. On the other hand, from our laboratory experience with silica flour, increasing the applied load does not increase the achieved density much after a certain compaction load. More information about the method that is used in this study is available in Appendix B.

The other disadvantage is that very dense specimens are relatively difficult to obtain. For example, for the silica flour that we used in this study, the achieved relative density under an 80 *psi* vertical load is 72*%*. The main reason is that under static loads, particles are less likely to rearrange themselves to achieve higher densities compared to those under vibration.

In addition, when increasing the load level, the possibility of crushing grains increases. In sand, particle crushing occurs at a load level ranging from 1.5 to 15 *MPa* [*Terzaghi*, 1996]. The range depends on the material properties such as the strength and the shape of the grains.

In this study, we used this method to prepare a dense specimen of silica flour with a vertical load (e.g., 80 *psi*) in our 11 *in* diameter and 18 *in* height large-scale steel container. The prepared specimen is relatively uniform in the vertical direction. The difference of the relative density between the top and bottom halves is ~ 3*%*.

CHAPTER 3

SMALL-SCALE EXPERIMENTS

3.1 Introduction

The small-scale experiments focus on gaining principal understanding of fundamental processes of hydraulic fracturing in particulate materials. In this chapter, the experimental setup and procedures of the small-scale experiments are described. The representative experimental results are presented. The effects of the experimental parameters on the fracturing behavior and the injection pressure curves are discussed.

3.2 Devices

The laboratory experiments at the small scale are conducted with both constrained and pressure-controlled lateral boundaries. The experimental setup for the two lateral boundary conditions is presented in the following two sections.

3.2.1 Constrained Lateral Boundary

The experiments with constrained lateral boundaries are performed in a rigid, cylindrical steel container with a moving top lid. The particulate specimen is placed in the steel container. The specimen is densified to the designated density by vibration. Based on our calculation, the deformations of the container walls are negligible under the pressures applied in this study.

The experimental setup for constrained lateral boundaries is presented in Figure 3.1.

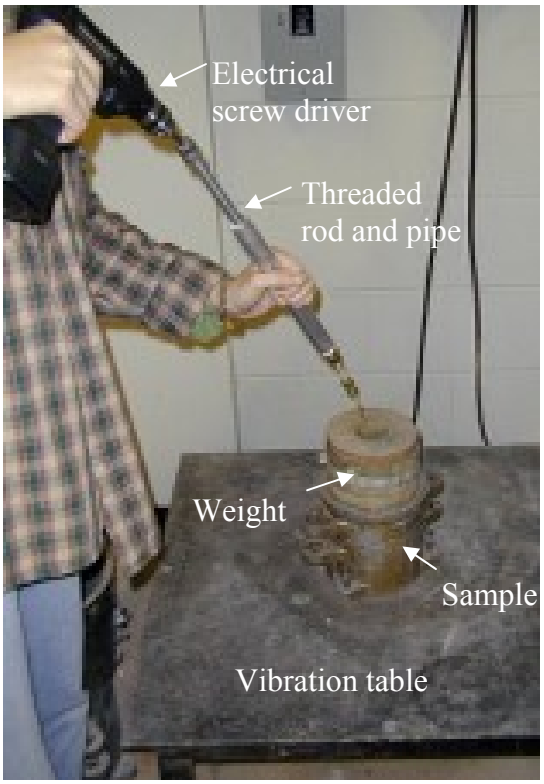

(a)

(b)

(c)

Figure 3.1 Experimental setup for small-scale constrained lateral boundary experiments: (a) entire setup, (b) steel container with top lid and injection tubing, and (c) screw injection pump.

A vertical load p_v is applied to the specimen by placing static weights on the top lid (Figure 3.1a). Consequently, the lateral and lower boundaries are constrained and the upper boundary is pressure-controlled.

The wall thickness of the steel container is 0.5 *in* (Figure 3.1b). Our calculations show that the deformations of the container walls under the pressures applied in the conducted experiments (up to 100 *psi*) are negligible. Therefore the steel container is considered to be sufficiently rigid to provide a constrained lateral boundary on the side and the bottom of the specimen.

Under applied vertical loads, particulate materials respond and exert lateral boundary load p_h to the container. Unfortunately, only a limited amount of data is available for the ratio of p_v / p_h for realistic particulate materials as the ones used in this study. Therefore, the initial stress state of the particulate material is unknown.

The fracturing fluid is injected through the top of the particulate specimen by a screw syringe pump. The screw pump consists of a threaded rod that is driven into a threaded pipe by an electric screw driver (Figure 3.1c).

3.2.2 Pressure-controlled Lateral Boundary

The experiments with pressure-controlled boundaries are conducted with a tri-axial cell. An example of an experimental setup for the small-scale experiments is shown in Figure 3.2.

A confining water pressure is applied to the specimen. Then, a vertical deviatoric load is added by a pneumatic load cylinder that is mounted inside a load frame. Thus, the vertical and horizontal loads are completely controlled, in contrast to the constrained lateral boundary experiments. In this study, the vertical stresses p_v are set to be greater than or equal to the horizontal stresses p_h and hence

$$\frac{p_v}{p_h} \geq 1 \qquad (3.1)$$

The fracturing fluid is injected through the bottom of the particulate specimen by a pump via a fluid displacement chamber (Figure 3.2b). The displacement chamber allows the transfer of pressure from the hydraulic fluid (driven by the pump) to the fracturing fluid via a flexible rubber membrane.

(b)

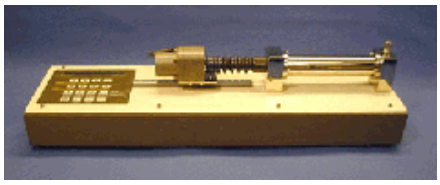

(a) (c)

Figure 3.2 Experimental setup for small-scale pressure-controlled experiments: (a) tri-axial cell with load frame, (b) tri-axial cell with fluid displacement chamber, and (c) GDS advanced 2*MPa* digital pressure/volume controller.

For experiments with relatively low injection pressures, a digital syringe pump (Figure 3.2c) is used. It pumps at a constant flow rate, and has a built-in pressure gauge. High-pressure pumps such as a manual screw pump are used for experiments with relatively high injection pressures.

The principal parameters of experiments with constrained and pressure-controlled lateral boundaries are listed in Table 3.1.

Table 3.1 Principal parameters of small-scale experiments with different lateral boundary conditions

Lateral Boundary			Constrained	Pressure-controlled
Specimen	**Diameter**	*in*	6	4
	Height	*in*	6	8
Maximum Injection	**Rate**	*ml/s*	3.5	1.7
	Volume	*ml*	80	100

3.3 Procedures

The principal procedures of the hydraulic fracturing experiments include the preparation of the particulate specimen, the injection of the fracturing fluid and the excavation of the hydraulic fracture.

The experiments with constrained and pressure-controlled lateral boundaries are executed following very similar procedures. Hence, the common procedures are described and the specific procedures for each boundary are explained separately.

3.3.1 Preparation of Specimen

The particulate material is oven-dried at 110°*C* for at least 24 *hr* before being used for the experiments.

The injection tubing is mounted along the vertical, central axis of the cylindrical container. It terminates at the center of the specimen with an open outflow hole. The fracturing fluid is injected into the specimen through the tubing.

For constrained lateral boundaries, the fracturing fluid is injected from the top of the

specimen. The top of the tubing is fixed in the center hole in the top plate, as shown in Figures 3.3a and 3.3b.

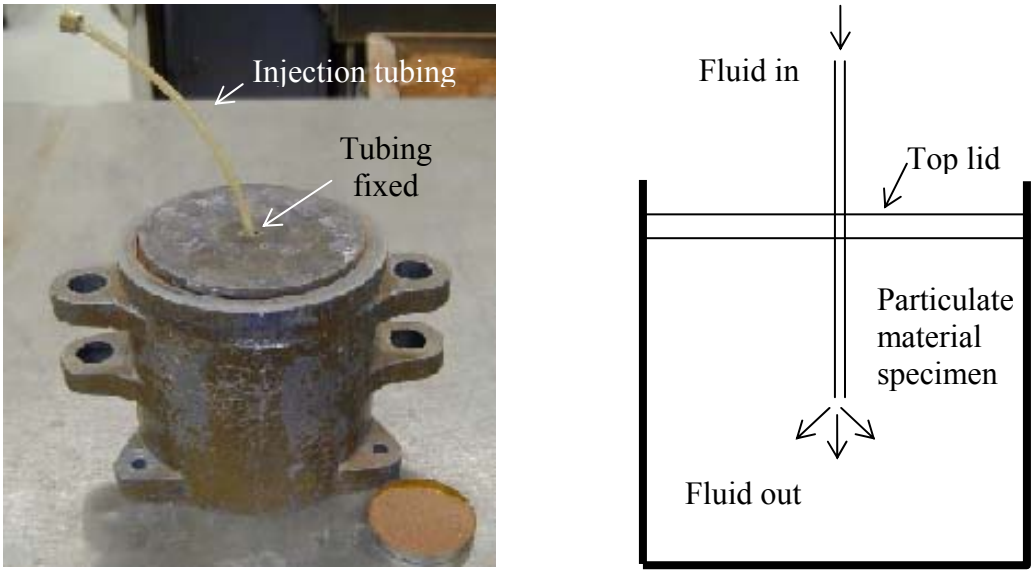

Figure 3.3 Fixed injection tubing in small steel container: (a) photograph and (b) diagram.

For pressure-controlled lateral boundaries, the fracturing fluid is injected from the bottom of the specimen. The bottom of the tubing is fixed in the center hole in the bottom base of the tri-axial cell as shown in Figure 3.4.

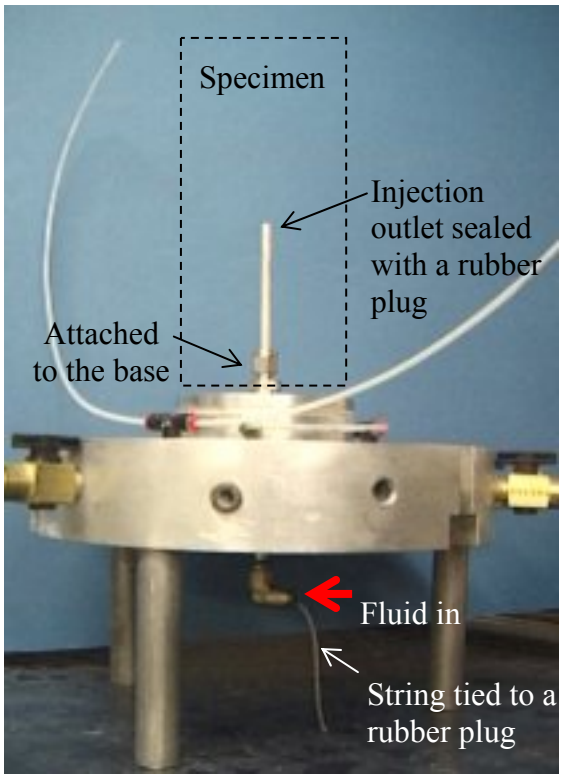

Figure 3.4 Fixed injection tubing in small tri-axial cell.

To prevent particulates from migrating into the injection hole and clogging it during specimen preparation, four types of plugs have been used: (*i*) a rubber plug attached to a string, (*ii*) an aluminum foil cap with a narrow slit, (*iii*) a rigid aluminum cap with a 0.04 *in* wide slotted opening, and (*iv*) a rigid aluminum cap with 0.03 *in* side openings. The last type of plug (Figure 3.5) is the one that was finally employed.

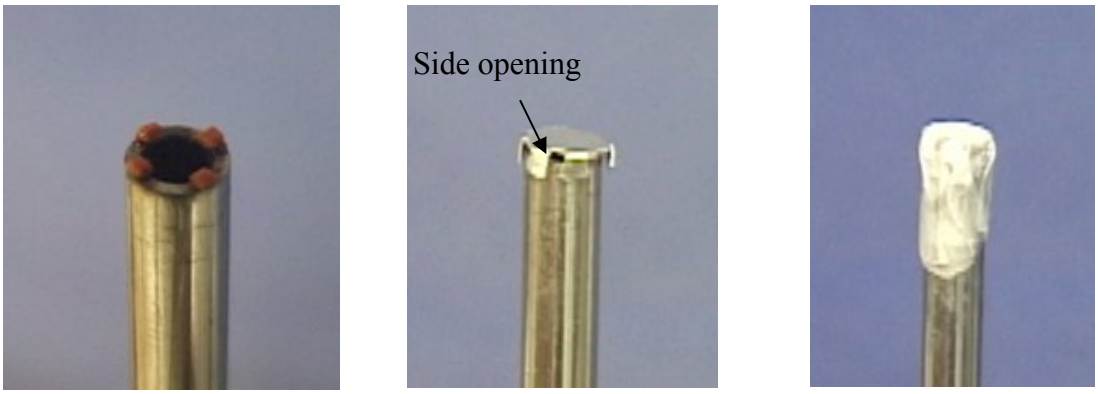

Figure 3.5 A rigid aluminum cap with side openings: (a) plastic spacers on top edge of tubing, (b) aluminum cap sitting on tubing top, and (c) cap secured with tissue.

The particulate materials are densified in the container using the appropriate preparation techniques. For constrained lateral boundaries, the specimen is vibrated (Figure 3.1) in a steel container. For pressure-controlled lateral boundaries, the specimen is rodded in a split mold. The split mold is lined with a latex membrane. Vacuum is applied between the membrane and the inner wall of the split mold to keep the membrane smoothly attached to the inner wall.

After the specimen is prepared, the experimental setup is assembled and the target loads are applied (see Figures 3.1a and 3.2a).

For constrained lateral boundaries, the height of the specimen is measured after loading to determine its initial volume and hence its initial density before carrying out the experiments.

For pressure-controlled lateral boundaries, a vacuum of 8 *psi* is applied before disassembling the split mold, because the dry particulate material may not have sufficient lateral support. The applied vacuum is sufficiently high to maintain the dimensions and

the stability of the specimen. On the other hand, it is lower than the target load of the specimen to avoid overconsolidaton of the specimen. The dimensions of the specimen are measured to determine the density. Then, the confining water pressure is increased while the vacuum is decreased simultaneously with increments of 2 *psi* to maintain a constant effective pressure on the boundaries of the specimen until the confining pressure reaches the target value.

Finally, the deviatoric vertical load is applied with the pneumatic cylinder (Figure 3.2a).

3.3.2 Injection of Fracturing Fluid

After loading, the fracturing fluid is pumped at 20% of the full injection rate to fill the injection tubing. Then, the fracturing fluid is injected into the specimen at a constant, full injection rate. For constrained lateral boundaries, the injection rate is ~ 4 *ml/s*. For pressure-controlled lateral boundaries, the injection rate is 0.5 or 1.7 *ml/s*, depending on the pump used. The pump is shut-off at a certain target volume. Then, the fracturing fluid is sealed inside the tubing and the specimen by closing a shut-off valve.

Nylon and thin-wall aluminum tubing was used for the low pressure experiments (i.e., < 250 *psi*), and stainless steel tubing was used for the high pressure experiments (i.e., > 250 *psi*).

In this study, a high-pressure pump is required to inject the fracturing fluid due to its relatively high viscosity (see Table 2.6) and, perhaps, due to the physical processes in particulate materials (see Chapter 6). However, most high-pressure pumps cannot handle

abrasive slurries and pastes. For pressure-controlled lateral boundaries, a fluid displacement chamber is used, as shown in Figure 3.2b. For constrained lateral boundaries, a screw pump is used to inject the viscous fluid directly into the specimen, and the fluid displacement chamber is not needed.

The injection pressure immediately downflow of the displacement chamber is recorded during and after the experiment. A video camera is used to record the pressure from analog dial pressure gages.

For constrained lateral boundaries, the height and hence the volume and density (from the measured mass of the particulate material) of the specimen are measured before and after injection. For pressure-controlled lateral boundaries, the density of the specimen is measured after the specimen is prepared and a vacuum is applied because it is difficult to access the specimen after the loads are applied with the tri-axial cell.

As mentioned previously, a constant pump rate is used to simulate the *in-situ* injection of the fracturing fluid and this also tends to yield a more stable fracture propagation process that allows easier data acquisition.

3.3.3 Excavation of Hydraulic Fractures

After the injection of the fracturing fluid into the particulate specimen, the applied loads are maintained for at least 12 *hr*. This allows the fluid to partially solidify inside the specimen and also helps to maintain the original shape of the fracture. After the fluid is partially solidified, the loads are removed and the specimen container is opened to expose the specimen to the atmosphere. The specimen is heated (e.g., the mold with the

specimen is placed in an oven) to accelerate the solidification of the fluid. The impression of the hydraulic fracture (the solidified fluid) is gradually excavated from the particulates while the fluid continued to solidify. An example of the excavation of a solidified hydraulic fracture of joint compound in Georgia Red Clay is presented in Figure 2.4.

3.4 Experimental Series

The objective of the small-scale experiments is to define the parameters that control the hydraulic fracturing processes. A parametric analysis was performed by varying four parameters: (*i*) the type of particulate materials (i.e., particle gradation and particle size), (*ii*) the density of the particulate materials, (*iii*) the ratio of the vertical and horizontal applied loads, and (*iv*) the viscosity of the fracturing fluid.

The experiments using different types of particulate materials were performed to select the proper materials for this study. In addition, these experiments are used to demonstrate the effect of the particle size and its distribution on the hydraulic fracturing processes. The experiments with different initial load ratios were performed to investigate the correlation between the orientation of hydraulic fractures and the initial stress state of the particulate specimen.

The experiment series performed at the small-scale with constrained and pressure-controlled lateral boundaries are summarized in Table 3.2.

Table 3.2 Experiment series at small scale

Lateral Boundary				Constrained	Pressure-controlled
Experimental Variables	**Particulate material**	**Type**		yes(1)	no(1)
		Density		yes	
		Load	**Magnitude**	no	
			Ratio	yes	
	Fracturing fluid	**Viscosity**		yes	
		Injection volume		no	
	Injection outlet type			no	yes

Note: (1) “yes” refers to the fact that the variable was varied in the series of the experiments, and "no" refers to the fact that the variable was not varied.

3.5 Results and Discussions

Seventy small-scale experiments were performed and fifteen representative tests are discussed in this thesis. This section presents the summary of the experimental results.

The experimental results with the aforementioned first four variables are presented as follows.

For constrained lateral boundary experiments, the cited specimen density refers to the density after the vertical load is applied. For pressure-controlled lateral boundary experiments, the cited specimen density refers to the density after the vacuum is applied but before the external pressures are applied. After the external pressures are applied to the specimen, the density is not measured because the specimen is enclosed inside the tri-axial apparatus.

3.5.1 Particulate Materials

The parameters of four experiments with different types of particulate materials (i.e., fine sand, mixture of fine sand and silica flour, Georgia Red Clay and silica flour) are listed in Table 3.3. The corresponding hydraulic fractures are presented in Figure 3.6.

Table 3.3 Parameters of experiments with different types of particulate material

Test		1	2	3	4
Particulate Material		*Fine sand*	*Sand and silica flour mixture*	*Georgia Red Clay*	*Silica flour*
Relative Density	*%*	90	95(1)	86	90
Densification		Vibration			
Lateral Boundary		Constrained			
Scale		Small			
Vertical Load	*psi*	1			
Ratio of p_v / p_h (2)		> 1			
Fracturing Fluid		Joint compound			
Injection Rate	*ml/s*	4			
Injection Volume	*ml*	15	18	15	15

Note: (1) the relative density is calculated based on the maximum and minimum void ratios of fine sand; and (2) here, p_v and p_h are the vertical and lateral applied loads, respectively.

(a) test 1

(b) test 2

(c) test 3

(d) test 4

Figure 3.6 Fractures with different types of particulate material: (a) fine sand, (b) mixture of sand and flour, (c) Georgia Red Clay, and (d) silica flour.

The solidified fracturing liquid in fine sand represents a bulb with depressions as shown in Figure 3.6a. The ratio of the mass of the sand and that of the fracturing fluid is ~ 1:2, which indicates significant leak-off of the fracturing fluid into the particulate materials dominates the hydraulic fracturing process. The exposed cross-section of the fracture shows that the body is a result of cavity expansion and leak-off on the surface.

The mixture of fine sand and silica flour has a ratio of 93% to 7% by weight. The large fraction of sand results in negligible cohesion, while the small fraction of silica flour reduces the leak-off during fluid injection by filling in the pores between the sand

particles. The solidified fracturing liquid generated in the sand-silica flour mixture (Figure 3.6b) is massive, thick and has angled edges. Because the mixture is not well graded, fine particles migrate downward through the voids of the fine sand during the vibration, which causes significant segregation.

Georgia Red Clay and silica flour have very similar mean particle sizes. The densities of the two specimens are also comparable. The main differences between these two types of particulate materials are the particle size distribution and particle geometry. The hydraulic fractures generated in both materials are vertical, thin and planar. The thickness of the fracture in silica flour is ~ 1/8 *in* as shown in Figure 3.6d. The fracture in Georgia Red Clay is ~ 50% thinner than that in silica flour. The fracture fronts are different. The fracture front in Georgia Red Clay has fingering characteristics (Figure 3.6c), while the fracture front in silica flour is beveled (Figure 3.6d) with minimal fingering. This comparison shows the important influence of the particle size distribution and particle geometry, and perhaps the void structure of the particulate materials, on the hydraulic fracturing behavior.

Summarizing, the solidified fracturing liquid in fine sand demonstrates significant leak-off of the fracturing fluid into the particulate specimen, and forms a bulb shape. The specimen of sand-silica flour mixture exhibits density non-uniformity in the vertical direction, probably due to the downward migration of the silica flour particles during specimen preparation by vibration. The fractures in both silica flour and Georgia Red Clay have a pronounced vertical orientation, and are planar and relatively thin. However, the fracture fronts of these two are different.

Based on these results, silica flour and Georgia Red Clay are selected for the majority of hydraulic fracturing experiments. Fine sand is not selected due to the cavity expansion and large leak-off. The sand-silica flour mixture is not used because of its segregation during vibration.

3.5.2 Density of Particulate Materials

Two series of experiments are performed to study the effect of varying the densities of the particulate materials. In the first series, joint compound is injected into Georgia Red Clay, and in the second series silicone sealant is injected into silica flour.

Joint compound in Georgia Red Clay

The parameters of the first series with joint compound injected into Georgia Red Clay with high and low densities are listed in Table 3.4. The corresponding hydraulic fractures are presented in Figure 3.7.

The fracture at a high density is thinner and has a smoother surface than that at a low density.

Table 3.4 Parameters of experiments with different densities

Test		3	5
Particulate Material		Georgia Red Clay	
Relative Density	***%***	*87*	*17*
Densification		Vibration	
Lateral Boundary		Constrained	
Scale		Small	
Vertical Load	*psi*	1	
Ratio of p_v / p_h		> 1	
Fracturing Fluid		Joint compound	
Injection Rate	*ml/s*	4	
Injection Volume	*ml*	15	

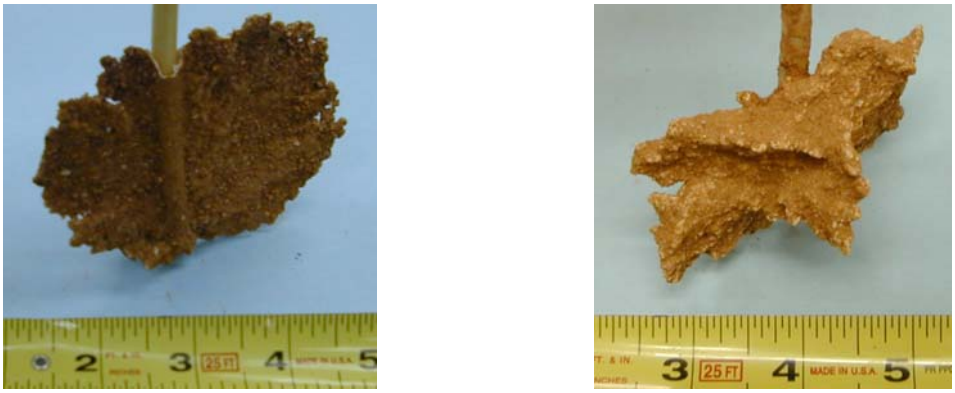

(a) test 3 (b) test 5

Figure 3.7 Fractures with different densities of particulate material: joint compound injected into Georgia Red Clay at (a) high density D_r = 87% and (b) low density D_r = 17%.

Silicone Sealant in Silica Flour

The parameters of the second series with silicone sealant injected into silica flour with high and low densities are listed in Table 3.5. The corresponding hydraulic fractures are

presented in Figure 3.8.

Again, the fracture at a high density is thinner and smoother than that at low density. Both fractures are highly multi-segmented though.

Table 3.5 Parameters of experiments with different densities

Test		6	7
Particulate Material		Silica flour	
***Relative Density*[(1)]**	***%***	*87*	*23*
Densification		Rodding	
Lateral Boundary		Pressure controlled	
Scale		Small	
Vertical Load	*psi*	5	20
Ratio of p_v / p_h		1	
Fracturing Fluid		Silicone sealant	
Injection Rate	*ml/s*	0.5	
Injection Volume	*ml*	29	25

Note: (1) the density is measured with only the 8 *psi* vacuum applied, which is lower than the full target load. Therefore, the density is considered to be lower than that during the fluid injection especially for the initially loose specimen.

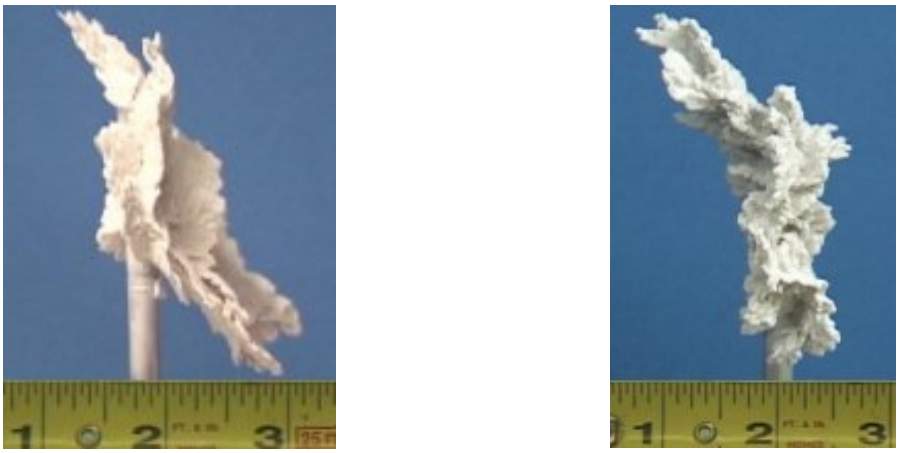

(a) test 6 (b) test 7

Figure 3.8 Fractures with different densities of particulate material: silicone sealant injected into silica flour at (a) high density D_r = 87% and (b) low density D_r = 23%.

3.5.3 Viscosity of Fracturing Fluid

The parameters of two experiments performed by injecting fracturing fluid with different viscosities into silica flour are listed in Table 3.6. The corresponding hydraulic fractures are presented in Figure 3.9.

For the two fractures, besides the viscosity of the fracturing fluid, the testing conditions are not very comparable. Therefore, the comparison here is qualitative. The fracture created at higher viscosity is thicker than the one created at lower viscosity. The fracture created at higher viscosity has a beveled fracture front. The front inclines at an angle of ~ 70° with respect to the direction of the fracture propagation. The fracture created at lower viscosity has a relatively sharp fracture front with fingering.

Table 3.6 Parameters of experiments with different viscosities of fracturing fluid

Test		4	6
Particulate Material		Silica flour	
Relative Density	*%*	97	87
Densification		Vibration	Rodding
Lateral Boundary		Constrained	Pressure controlled
Scale		Small	
Vertical Load	*psi*	1	5
Ratio of p_v / p_h		> 1	1
Fracturing Fluid		*Joint compound*	*Silicone sealant*
Injection Rate	*ml/s*	4	0.5
Injection Volume	*ml*	10	25

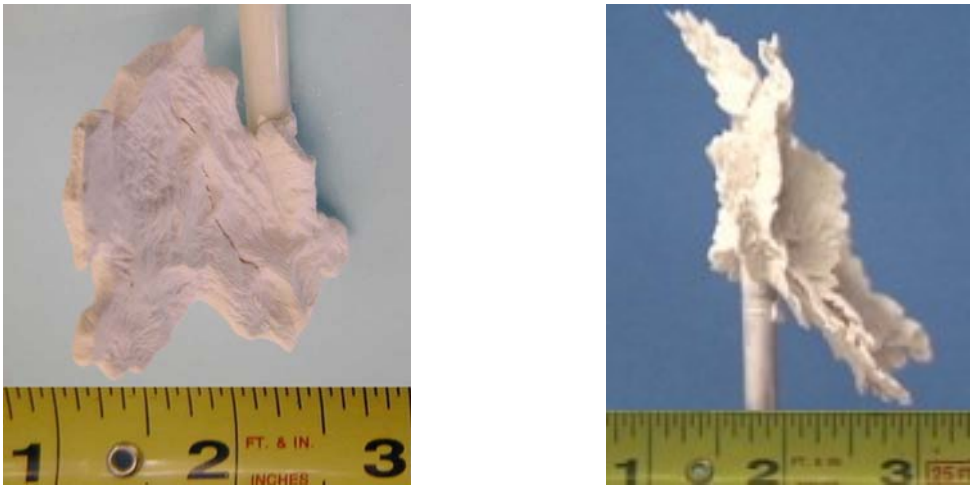

(a) test 4 (b) test 6

Figure 3.9 Fractures with different viscosities of fracturing fluid: (a) joint compound with high viscosity and (b) silicone sealant with low viscosity injected into dense silica flour.

3.5.4 Ratio of Applied Stresses

Generally, the orientation of the fracture is expected to vary with the minimum principal stress direction of the particulate specimens.

Two series of experiments are performed to study the effect of varying the ratio of the vertical and horizontal stresses (i.e., $p_v / p_h > 1$ or $p_v / p_h < 1$), and hence the minimum principal stress direction in the particulate specimens (vertical or horizontal). In the first series, joint compound is injected into Georgia Red Clay, and in the second series silicone sealant is injected into silica flour.

The first experiment is carried out on normally consolidated specimens, in which the vertical stress p_v is greater than the horizontal stress p_h (i.e., $p_v / p_h > 1$) in the central area of the specimen where the fracture is to be generated. The direction of the minimum principal stress is horizontal. The second experiment is performed on a heavily over-consolidated specimen. The specimen is vertically loaded at first. The vertical load is removed immediately before the injection of the fracturing fluid (see details below). Hence, the vertical stress p_v is smaller than the horizontal stress p_h (i.e., $p_v / p_h < 1$) in the central area of the specimen. The direction of the minimum principal stress is vertical.

Joint Compound in Georgia Red Clay

The parameters of the first series with joint compound injected into Georgia Red Clay with different ratios of the applied vertical and lateral loads are listed in Table 3.7. The corresponding hydraulic fractures are presented in Figure 3.10. To make the direction of the minimum principal stress to be vertical, the specimen is first loaded vertically to

create a minimum horizontal principal stress. Immediately before starting the experiment, the vertical load is removed so that horizontal stress (i.e., > 0) is greater than vertical stress (i.e., ~ 0) in the specimen.

The fracture with a horizontal minimum principal stress (i.e., $p_v / p_h > 1$) (Figure 3.10*a*) is orientated vertically, and the fracture with a vertical minimum principal stress (i.e., $p_v / p_h < 1$) (Figure 3.10*b*) tends to be orientated horizontally.

Table 3.7 Parameters of experiments with different ratios of applied stresses

Test		3	8
Particulate Material		Georgia Red Clay	
Relative Density	*%*	87	78
Densification		Vibration	
Lateral Boundary		Constrained	
Scale		Small	
Vertical Load	*psi*	1	1 → 0
Ratio of p_v / p_h		*> 1*	*< 1*
Fracturing Fluid		Joint compound	
Injection Rate	*ml/s*	4	0.5
Injection Volume	*ml*	30	25

(a) test 3 (b) test 8

Figure 3.10 Fractures with different directions of minimum principal stress: joint compound injected into Georgia Red Clay with (*a*) horizontal ($p_v / p_h > 1$) and (*b*) vertical ($p_v / p_h < 1$) minimum principal stresses.

Silicone Sealant in Silica Flour

The parameters of the second series with silicone sealant injected into silica flour with the different ratios of the applied vertical and lateral stresses are listed in Table 3.8. The stress ratios of the two specimens are equal to 2 and 1, respectively. That is, one specimen has a horizontal minimum principal stress and the other is under hydrostatic stresses. The corresponding hydraulic fractures are presented in Figure 3.11.

Table 3.8 Parameters of experiments with different ratios of applied stresses

Test		9	10
Particulate Material		Silica flour	
Relative Density	*%*	> 50[(1)]	~ 80
Densification		Rodding	
Lateral Boundary		Pressure controlled	
Scale		Small	
Vertical Load	*psi*	20	40
Ratio of p_v / p_h		2	1
Fracturing Fluid		Silicone sealant	
Injection Rate	*ml/s*	0.5	
Injection Volume	*ml*	22	20

Note: (1) the accurate measurement of the density of this specimen is not available.

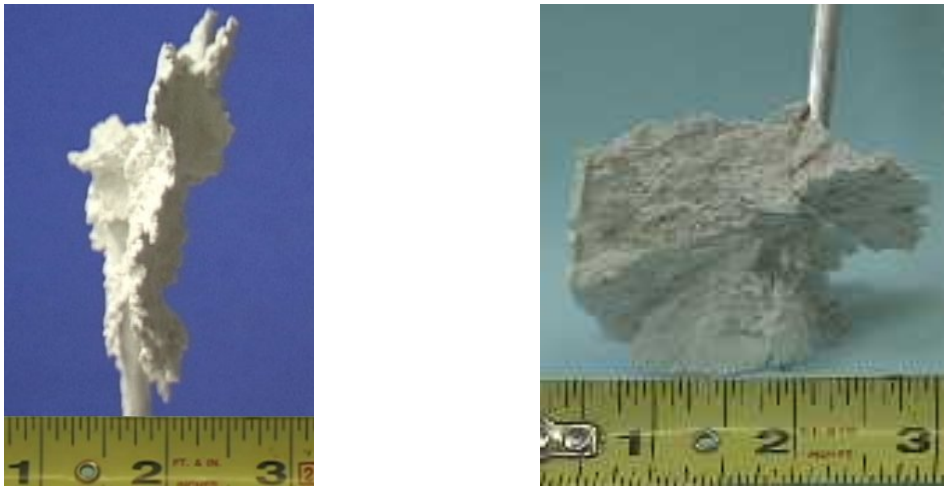

(a) test 9 (b) test 10

Figure 3.11 Fractures with different directions of minimum principal stress: silicone sealant injected into silica flour (a) with a horizontal minimum principal stress ($p_v / p_h > 1$), and (b) under hydrostatic stresses ($p_v / p_h = 1$).

Again, the fracture with the horizontal minimum principal stress (Figure 3.11a) is orientated vertically. The fracture under hydrostatic stresses (Figure 3.11b) has several

segments and is oriented randomly.

Summarizing, the hydraulic fractures in particulate materials tend to orientate perpendicular to the minimum principal stress direction. This is similar to the case of the hydraulic fracturing observed in cohesive, brittle rocks.

3.5.5 Fracture Geometry

From the small-scale experimental results, fractures demonstrate distinct characteristics in both fracture front and global features.

It appears that the hydraulic fracture fronts created in particulate materials have very different characteristics compared to those in solid, brittle materials. Three typical observed types of fracture fronts, beveled, fingered and round, are shown in Figure 3.12. Beveled and rounded fronts have been rarely observed in solid brittle materials. The parameters of the three experiments are listed in Table 3.6, Table 3.7, and Table 3.9, respectively.

(a) (b) (c)

Figure 3.12 Observed fracture fronts: (a) beveled (test 4), (b) fingered (test 8), and (c) beveled (test 11).

Beveled Front

As opposed to the sharp fracture fronts that are typically observed in solid, brittle materials, a beveled fracture front (Figure 3.12a) is common for the hydraulic fractures created in dense particulate materials. The front has a thickness of ~ 1/8 *in* for the given conditions of the small-scale experiments (e.g., in silica flour with relatively low loads and small injection volumes). The front is usually not perpendicular to the direction of fracture propagation, but inclined at an angle of ~ 70°. The front is either flat or curved. The occurrence of beveled fronts is more likely to be observed in silica flour specimens with high densities.

Fingered Front

With fingering, the fracture fronts are very rough and curved with small fingers along their edges, as shown in Figure 3.12b. Fingering is generally observed in particulate materials with high densities and relatively low loads. Fingered fracture fronts are more observed in Georgia Red Clay than in silica flour. More discussion about the fingered front is available in the later section 5.4.1.

Round Front

The round fronts are typically observed in silica flour specimens under a similar condition as that for beveled fronts, as shown in Figure 3.12c. The front has a thickness of ~ 1/6 *in.* The fracture surface is smoother that that with a beveled front. The parameters of the experiment are listed in Table 3.9.

Table 3.9 Parameters of experiments with different injection outlet types

Test		11
Particulate Materials		Silica flour
Relative Density	*%*	95
Densification Technique		Vibration
Lateral Boundary		Constrained
Scale		Small
Vertical Load	*psi*	1
Ratio of p_v / p_h		>1
Injection Outlet Type		*Tubing opening*
Fracturing Fluid		Joint compound
Injection Rate	*ml/s*	4
Injection Volume	*ml*	15

Besides the phenomena observed at the fracture fronts, some fractures demonstrate overall multiple wings and multiple segments patterns.

Multiple Wings

The observed fracture have two wings (planar) (Figure 3.7a) or three wings (Figure 3.7b). The parameters of the experiment are listed in Table 3.4.

Multiple Segments

Fractures do not always consist of a single segment, but can split into multiple segments during propagation, as shown in Figure 3.8. The segments grow from a host fracture and slightly deviate from its host fracture plane. The parameters of the fracture are listed in Table 3.5 (test 6).

Non-planar Features

A few samples of hydraulic fractures that were generated in the small-scale experiment setup are shown in Figure 3.13. From these samples, it is difficult to identify whether they are fractures or bulb shape volumes. From the fractures in Figures 3.13a and 3.13b, it is hard to predict whether the process of fracturing or cavity expansion (i.e., the bulb increases its volume) will dominate if a larger volume of the fracture fluid is injected.

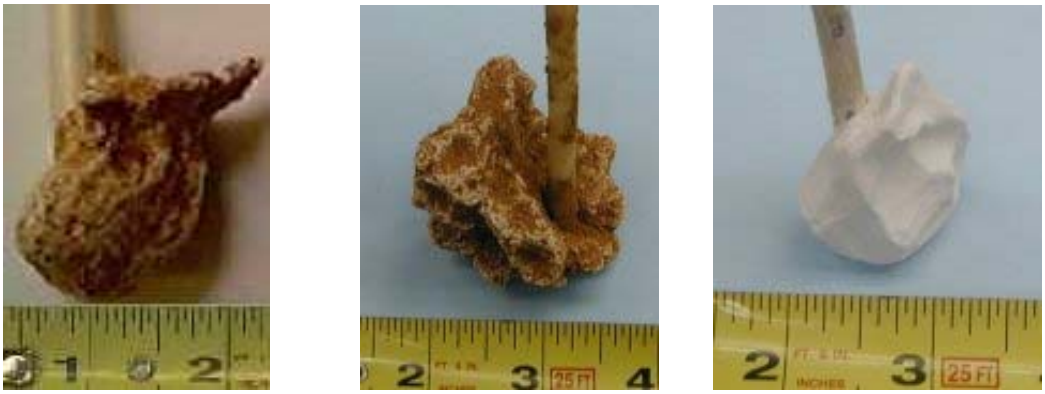

(a) test 12 (b) test 13 (c) test 15

Figure 3.13 Fractures – bubbles that are generated with the small-scale experimental setup.

The small fractures and "bubbles" are more likely to be at the initial stage of fracture propagation. This has been demonstrated in the comparison between the fractures that are generated with the small- and the large scale experimental setups (see section 5.6). One pair of fracture examples generated at small and large scales is shown in Figure 3.14. The detailed information of these two tests is listed in Table 5.24. Although the two fractures demonstrate similarity in geometry, it is difficult to predict the growth of the developed fracture (Figure 3.14b) based on the fracture at the initial stage (Figure 3.14a).

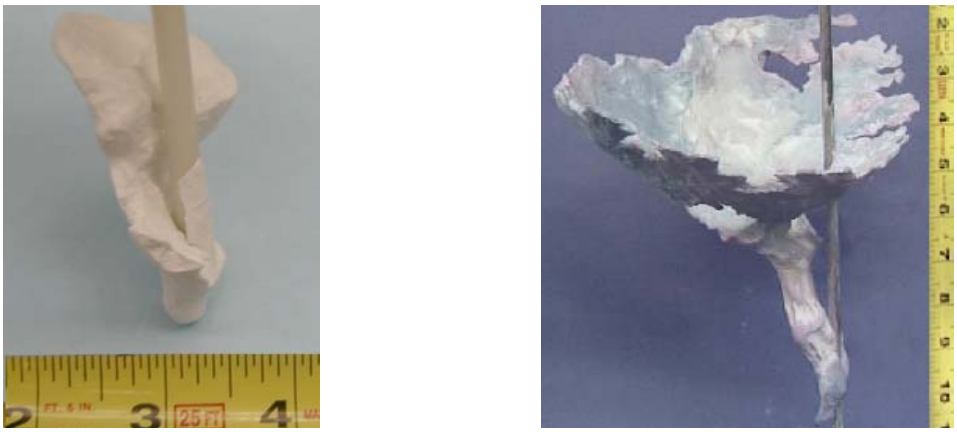

(a) test 15 (b) test 19

Figure 3.14 Similar fractures generated at: (a) small scale (white) and (b) large scale (red → blue → white).

Finally, the dimensions of some fractures approach the dimensions of the specimens. In some experiments, the injected fluid deformed the boundary of the specimen significantly. Therefore, boundary effects in the small-scale experiments are expected to be important. To study the scale effects and attempt to reduce the boundary effects, laboratory experiments at a larger scale are required.

3.6 Summary

The small-scale laboratory experiments show that hydraulic fracturing in dry particulate materials is possible, if the fluid is injected at an adequately high flow rate or has a sufficient high viscosity (i.e., the leak-off is minimized).

In addition to fracturing phenomena, non-fracturing (i.e., leak-off and cavity expansion) phenomena were also observed. The different phenomena were observed in different regimes that are defined by the experimental parameters (e.g., the properties of

the particulate materials and the fracturing fluids, and the initial conditions of the particulate specimens).

Figures 3.15a and 3.15b present a summary of the fracture appearance versus the density of the particulate materials and the viscosity of the fracturing fluids for Georgia Red Clay and silica flour.

In Georgia Red Clay and silica flour, the thickness of the fracture increases with the decrease of the density of the particulate materials and increase of the viscosity of the fracturing fluids.

Although the particle size distribution and the density of the particulate materials expect to be important with respect to the fracture behavior, it is not yet obvious how they control the fracturing behavior based on the current laboratory experiments since these properties were not studied separately in this work.

It appears that the orientation of the fracture propagation is perpendicular to the direction of the minimum principal stress. The observed fracture fronts include fingered, beveled and round fronts.

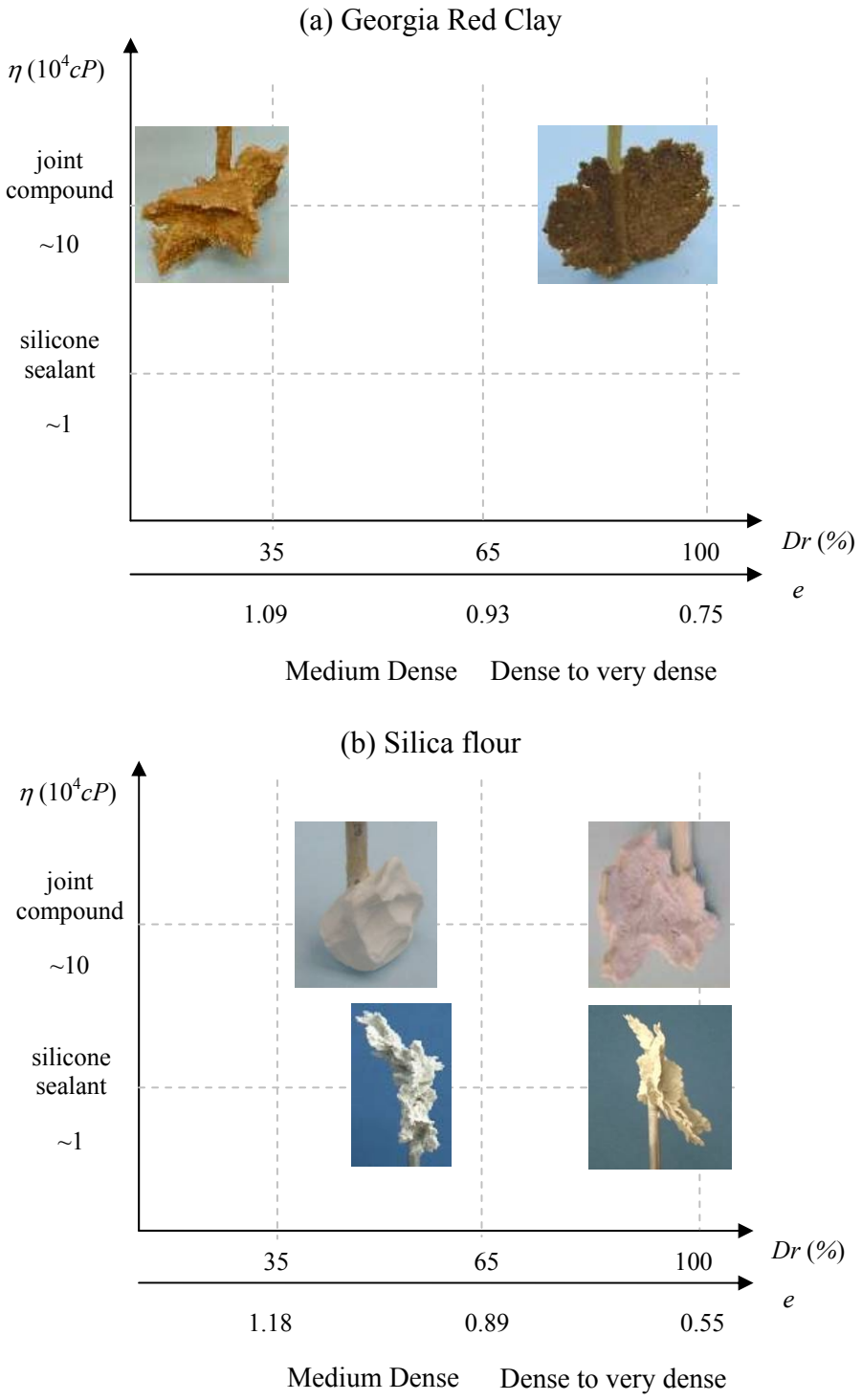

Figure 3.15 Fracture appearance versus specimen density and viscosity of fracturing fluid in (a) Georgia Red Clay and (b) silica flour. Here, η is the dynamic viscosity of the injection fluid, and D_r and e are the relative density and void ratio of the particulate material, respectively.

The observations of the small-scale experiments provide a significant insight into the understanding of hydraulic fracturing in dry particulate materials. Yet, there are shortcomings associated with the limited size of the experimental setup. The dimensions of specimens limit the injection volumes, and therefore, the dimensions of the hydraulic fractures.

CHAPTER 4

LARGE-SCALE EXPERIMENTAL SETUP

4.1 Introduction

The large-scale experiments are designed to study the scale effect and to minimize the boundary effect. The principle, experimental setup and procedures of the large-scale experiments are very similar to those of the small-scale experiments that are presented in Chapter 3. However, the large-scale experiments are better controlled and monitored.

This chapter describes the large-scale experimental setup and procedures for two extreme lateral boundary conditions: constrained and pressure-controlled. The design of the experimental apparatus is briefly discussed, and the main parameters of the apparatus are listed. Finally, an overview of the experiment series is presented.

4.2 Devices

The large-scale experimental setup for the two extreme lateral boundary conditions (i.e., constrained and pressure-controlled) is discussed.

4.2.1 Constrained Lateral Boundary

A typical experimental setup of the large-scale, constrained lateral boundary experiments is shown in Figure 4.1.

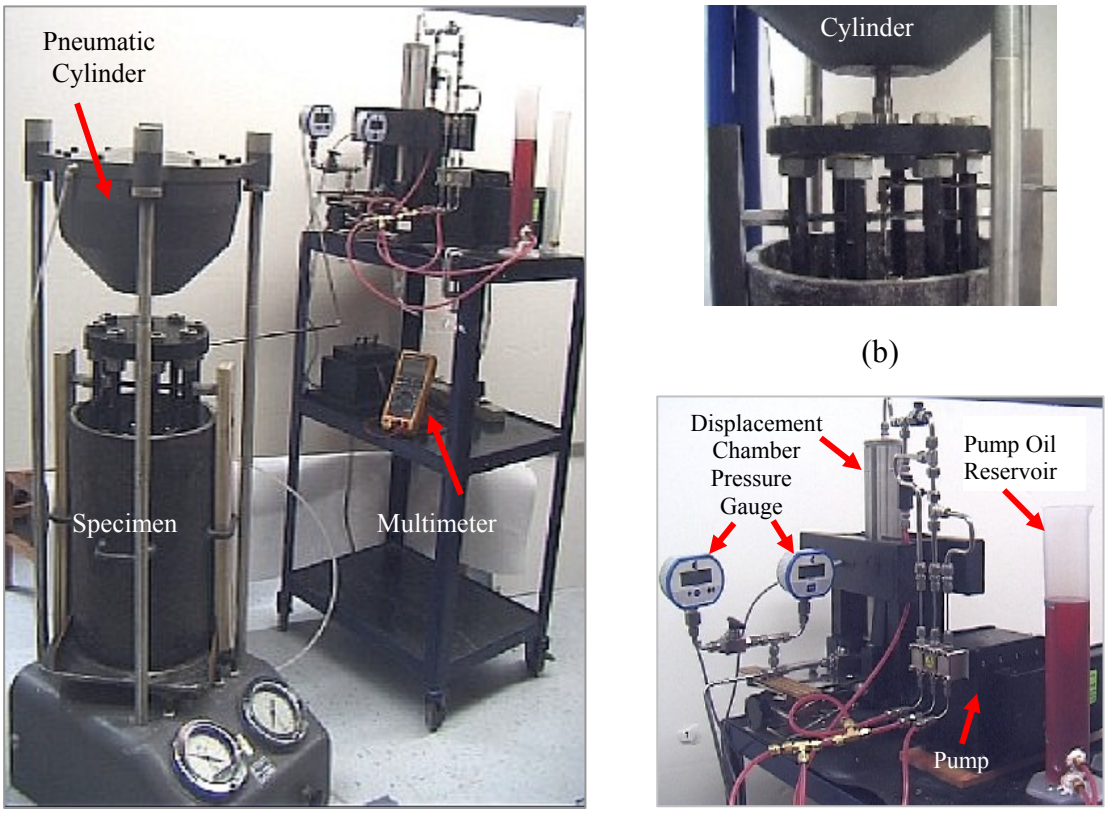

Figure 4.1 Experimental setup for the large-scale, constrained lateral boundary experiments: (a) entire setup, (b) application of the vertical load and the injection tubing through the top of the particulate specimen, and (c) high-pressure piston pump, fluid displacement chamber and pressure gauges.

In this setup, the particulate specimen is prepared in a large-scale steel container (Figure 4.1a). The load is applied to the specimen by a pneumatic cylinder that is mounted inside a load frame (Figures 4.1a and 4.1b). Dyed fracturing fluid is pumped into the particulate specimen by a high-pressure piston pump via a fluid displacement chamber (Figure 4.1c). The chamber transfers the pressure from the hydraulic fluid to the fracturing fluid. A moving piston in the chamber separates the two fluids. Subsequent layers of the fracturing fluid are dyed with different color codes to indicate the injection sequence.

The steel container has a 0.5 *in* thick wall. Based on the calculation of the rigidity of the container, the deformations of the container walls are negligible for all internal pressures used in this work (up to 100 *psi*). It is concluded that the rigidity is sufficiently high to provide a constrained lateral boundary on the side and the bottom of the specimen.

Depending on the experimental conditions, a variety of experimental equipment components is used. For example, for relatively low applied vertical loads, a weight table is used instead of the pneumatic cylinder, and the specimen is prepared with vibration instead of rodding (Figure 4.2).

Figure 4.2 Specimen in steel container with a static load on a vibration table.

4.2.2 Pressure-controlled Lateral Boundary

The experimental setup for large-scale, pressure-controlled lateral boundaries is presented in Figure 4.3.

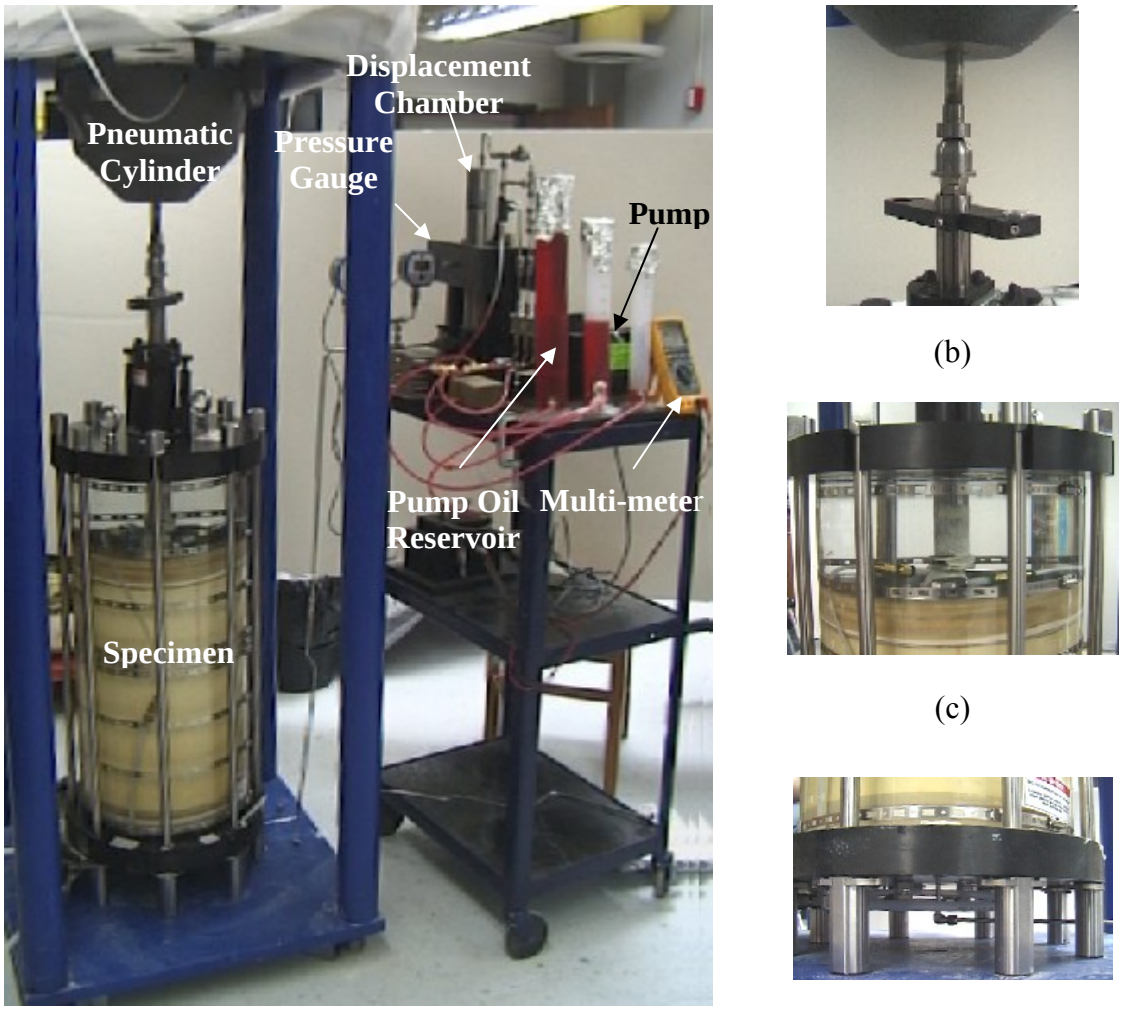

Figure 4.3 Experimental setup for the large-scale, pressure-controlled experiments: (a) tri-axial cell mounted inside a load frame with injection tubing connected to a displacement chamber and a high-pressure piston pump, (b) tri-axial cell loaded by a pneumatic cylinder, (c) a particulate specimen loaded inside the tri-axial cell, and (d) injection tubing through the bottom of the particulate specimen.

The principal parameters of the large-scale experiments for both lateral boundaries are listed in Table 4.1.

Table 4.1 Principal parameters of large-scale experiments

Lateral Boundary	Specimen Dimension		Injection Rate	Maximum Injection Volume	Diameter of Injection Hole
	Diameter	Height			
	in	*in*	*ml/s*	*ml*	*in*
Constrained	11	~ 14	1.7	600	0.13 or 0.18
Pressure-controlled	12	18			

The large-scale tri-axial cell can sustain a water pressure of 100 *psi*. The maximum deviatoric pressure that can be applied to the specimen is limited by the available pressurized air source.

4.3 Procedures

The large-scale experiments are executed following very similar procedures as those of the small-scale experiment. However, the quality of the large-scale experiments has been improved considerably. Hence, the procedures that are similar to those of the small-scale experiments are described briefly. Then, the specific procedures for the large-scale experiments are explained in greater detail.

Similar to those of the small-scale experiments, the principal procedures include the preparation of the particulate specimen, the injection of the fracturing fluid, and the excavation of the hydraulic fracture.

4.3.1 Preparation of Specimen

The particulate material is oven-dried for at least 24 *hr* before being used for the

experiments.

For constrained lateral boundaries, the fracturing fluid is injected from the top of the specimen. A stainless steel injection tubing is mounted along the vertical, central axis of the container as shown in Figure 4.4. The open end of the tubing is mounted at the top of the mold with an extendable rod and a thumb screw. The closed end of the tubing is fixed at the bottom of the mold with a thumb screw. The outflow hole located at half-height of the tubing. The surface of the tubing is roughened by sand paper. Then, a layer of particulates is affixed to the surface with epoxy adhesive. This ensures the stability of the tubing during specimen preparation, and hence good contact between the tubing and the particulate material, especially in the vicinity of the injection hole. The fracturing fluid is injected into the open top end of the tubing and is ejected from the injection hole (with a diameter of 1/8 *in*) into the specimen.

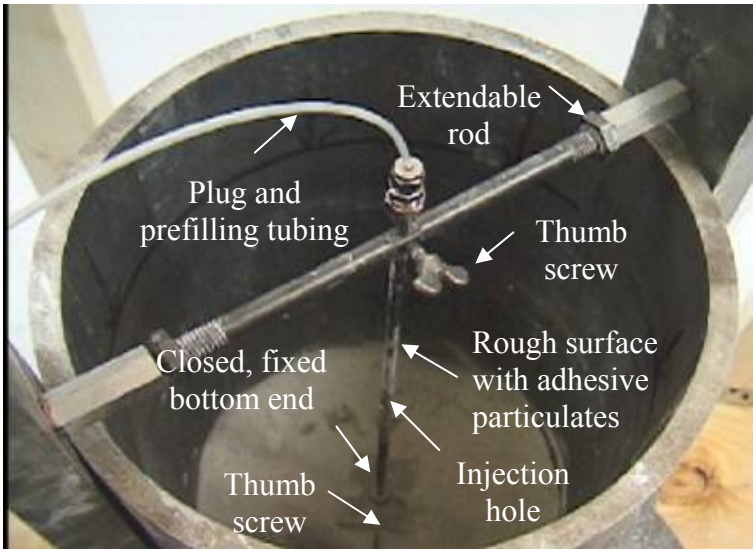

Figure 4.4 Injection tubing in large steel container.

For pressure-controlled lateral boundaries, the fracturing fluid is injected from the

bottom of the specimen. Therefore, the injection tubing is reversed in the vertical direction, compared to that for constrained lateral boundaries. The open bottom end of the tubing is attached to the base of the tri-axial cell. The closed top end of the tubing is terminated in the center of the tri-axial cell. The injection hole is right below the closed end of the tubing, in the center of the specimen. The fracturing fluid is injected into the open bottom end of the tubing (Figure 4.5).

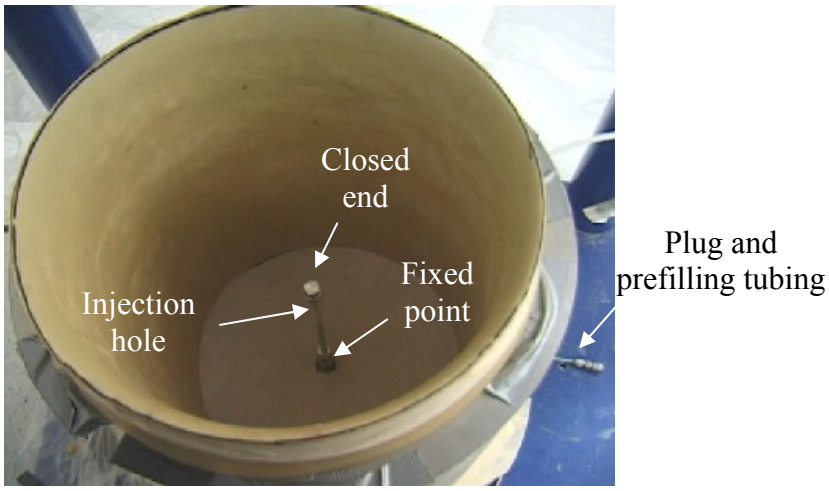

Figure 4.5 Injection tubing in split mold of large-scale tri-axial cell.

To prevent particulates from migrating into the injection hole and clogging it during specimen preparation, two types of plugs have been used: (*i*) a wax plug and (*ii*) a piece of flexible plastic tubing that is inserted snugly into the injection tubing (Figures 4.4 and 4.5). For the wax plug, wax is compacted into the section of the tubing adjacent to the injection hole. Before the injection of the fracturing fluid, the wax plug is punctured with a rigid steel wire. For the plastic tubing plug, the outer diameter of the plastic tubing matches the inner diameter of the injection tubing. Hence, it plugs the hole from the inside. In addition, a small amount of wax is used to seal the hole from the outside. The plastic tubing is filled with injection fluid and therefore, also functions as a pre-filling

tubing. Both types of plugs are very efficient. However, the wax plug requires more operational space (due to the puncturing with the rigid steel wire) which is not available underneath the tri-axial cell, and is prone to malfunction. Therefore, the plastic plug is used as the final design for the experiments.

The particulate materials are densified in the container using the appropriate preparation techniques. For constrained lateral boundaries, the specimen is rodded or vibrated (Figure 4.2) directly in the steel container. For pressure-controlled lateral boundaries, the specimen is rodded in a split mold, as is typical for tri-axial tests, as shown in Figure 4.6. The split mold is lined with a latex membrane. Vacuum is applied between the membrane and the inner wall of the split mold to keep the membrane smoothly attached to the inner wall.

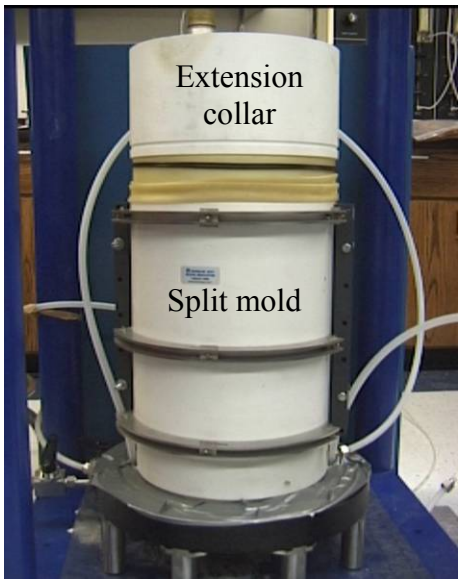

Figure 4.6 Specimen in split mold of large tri-axial cell with an extension collar on top.

After the specimen is prepared, the experimental setup is assembled and the target loads are applied. The vertical load is applied in small increments with a pneumatic

cylinder mounted on a load frame (Figures 4.1a and 4.3a). The procedures of loading and the density measurement are the same as for the small-scale experiments.

4.3.2 Injection of Fracturing Fluid

After loading, the plastic plug tubing is slowly pulled out of the injection tubing. Simultaneously, the fracturing fluid is pumped at ~ 20% of the full injection rate to fill the injection tubing. Then, the fracturing fluid is injected into the specimen by a high-pressure piston pump at a constant flow rate of 1.7 *ml/s*. Hydraulic fluid is pumped into a fluid displacement chamber to displace the fracturing fluid, as shown in Figures 4.1c and 4.3a. The pump is shut-off at a certain target volume. Then, the fracturing fluid is sealed inside the tubing and the specimen by closing a shut-off valve.

Due to the high pressures (up to thousands of *psi*) in the large-scale experiments, stainless steel injection tubing with a maximum pressure rating of ~ 6,000 *psi* is used with two different wall thicknesses. The inner diameter of the tubing is either 0.13 or 0.18 *in*.

The injection pressure immediately downflow of the displacement chamber is recorded during and after the experiment. A multi-meter is used for automatic data acquisition from digital pressure gages. The accuracy of the digital gages is better than 1 *psi*. Typically, the multi-meter records data every second. When there is a dramatic change of the data, it records twice per second.

For constrained lateral boundaries, the height and hence the density of the specimen are measured before and after the experiment. For pressure-controlled lateral boundaries,

the global volume change of the specimen (including injected fracturing fluid) is monitored during and after the experiment via the water level change in the pipette of the pressure panel.

4.3.3 Excavation of Hydraulic Fracture

The procedures for the excavation of the hydraulic fractures are the same as those for the small-scale experiments, except for the fact that the specimen is heated with four halogen work lights to accelerate the solidification of the fracturing fluid.

Summarizing, compared to the small-scale experiments, the large-scale experiments allow for: (*i*) a larger dimension of the specimen, and (*ii*) a larger injection volume for the study of the later propagation stages; (*iii*) a better monitoring of the volume change of the particulate specimen due to the injection of the fracturing fluid; (*iv*) a higher sustainable pressure because the injection system (including the piston pump, the fluid displacement chamber, and the injection tubing) can withstand higher pressures; (*v*) more accurately controlled injection rates, and (*vi*) a more accurate data acquisition system.

4.4 Pressure Calibration

The injection pressure is measured at the outlet of the fluid displacement chamber. During the injection of the fracturing fluid, the friction between the viscous fracturing fluid and the wall of the injection tubing results in a pressure gradient along the tubing. It depends on the dimensions (i.e., length and inner diameter) and the roughness of the inner surface of the tubing, and the viscosity and the flow rate of the fracturing fluid. The pressure drop between the outlet of the displacement chamber and the injection hole is

calibrated for various flow rates. For the relevant injection rates (i.e., from 0.5 to 4 *ml/s*), the pressure drop is ~ 5 *psi*/*in* for the thin wall tubing and ~ 10 *psi*/*in* for the thick wall tubing.

Because the details of the injection systems varied before the final design was determined, only rough estimation of the pressure drop for most of the experiments is available. To avoid losing any valuable information of the pressure curve before we well understand the fracturing process, the pressure curves that will be presented as part of the experimental results are not calibrated according to this pressure calibration.

4.5 Experimental Series

Summarizing, the controlled parameters that we control in the experiment are the initial density, the applied vertical load and the confining pressure of the particulate specimen (for pressure-controlled lateral boundaries); and the viscosity, the injection rate and the total injection volume of the fracturing fluid. The measurements include the injection pressure and the volume change of the particulate specimen, at different stages of the experiments.

The parameters of the experiment series performed at the large scales with constrained and pressure-controlled lateral boundaries are listed in Table 4.2. In the table, the notation "yes" means that experiments are conducted by varying the variables.

Table 4.2 Experiment series at large-scale

Lateral Boundary	Experimental Variables					
	Particulate				Fluid	
	Media type	Density	Load		Viscosity	Injection volume
			Magnitude	Ratio		
Constrained	yes	no	yes	no	no	yes
Pressure-controlled	no	yes				

Different types of particulate materials were used for the experiments to select the proper materials for this study. In addition, these experiments are conducted to show the effect of the particle size and its distribution on the hydraulic fracturing behaviors. The experiments with different initial load ratios were performed to investigate the correlation between the orientation of hydraulic fractures and the initial stress conditions of specimens. The experiments with different injection volumes were intended to demonstrate the different fracture propagation stages.

The boundary effect can be studied by comparing the experimental results between two lateral boundary conditions (i.e., constrained and pressure-controlled) and the scale effect can be investigated by comparing the experimental results between the small and large scales.

CHAPTER 5

LARGE-SCALE EXPERIMENTAL RESULTS

5.1 Introduction

In this chapter the results of the large-scale experiments are summarized. The effects of the parameters on the fracturing behavior and injection pressure curves are discussed. The results for two lateral boundary conditions will be presented and compared. We will also compare the results between the small- and large-scale experiments.

The main injection fluid used in large-scale experiments is joint compound because of the similarity of its properties with the injection fluids used in the field.

Forty experiments were performed and eighteen are presented.

5.2 Constrained Lateral Boundary

A parametric analysis was performed by varying five parameters: the type of the particulate materials (in terms of the particle gradation and mean particle size), the vertical load, the stress ratio, the injection volume, and the density of the particulate materials.

5.2.1 Type of Particulate Materials

To determine the effects of different types of particulate materials, a series of experiments are performed in three different particulate materials (i.e., mixture of fine

sand and silica flour, Georgia Red Clay and silica flour), similar to the small-scale experiments. The main difference is that a larger volume of fracturing fluid is injected into a larger particulate specimen.

The parameters of the three experiments are listed Table 5.1. The corresponding hydraulic fractures are presented in Figure 5.1. The pressure curves are shown in Figure 5.2. The results of the experiments are listed in Table 5.2.

Table 5.1 Parameters of experiments with different particulate materials

Test		**2**	**4**	**3**
Particulate Materials		*Sand and flour mixture (93% : 7%)*	*Silica flour*	*Georgia Red Clay*
Density	*%*	92	73	68
Void Ratio		< 0.56	0.84	0.92
Densification		Vibration		
Lateral Boundary		Constrained		
Scale		Large		
Vertical Load	*psi*	1		
Ratio of p_v / p_h		> 1		
Fracturing Fluid		Joint compound		
Injection Rate	*ml/s*	1.7		
Injection volume	*ml*	360	200	85

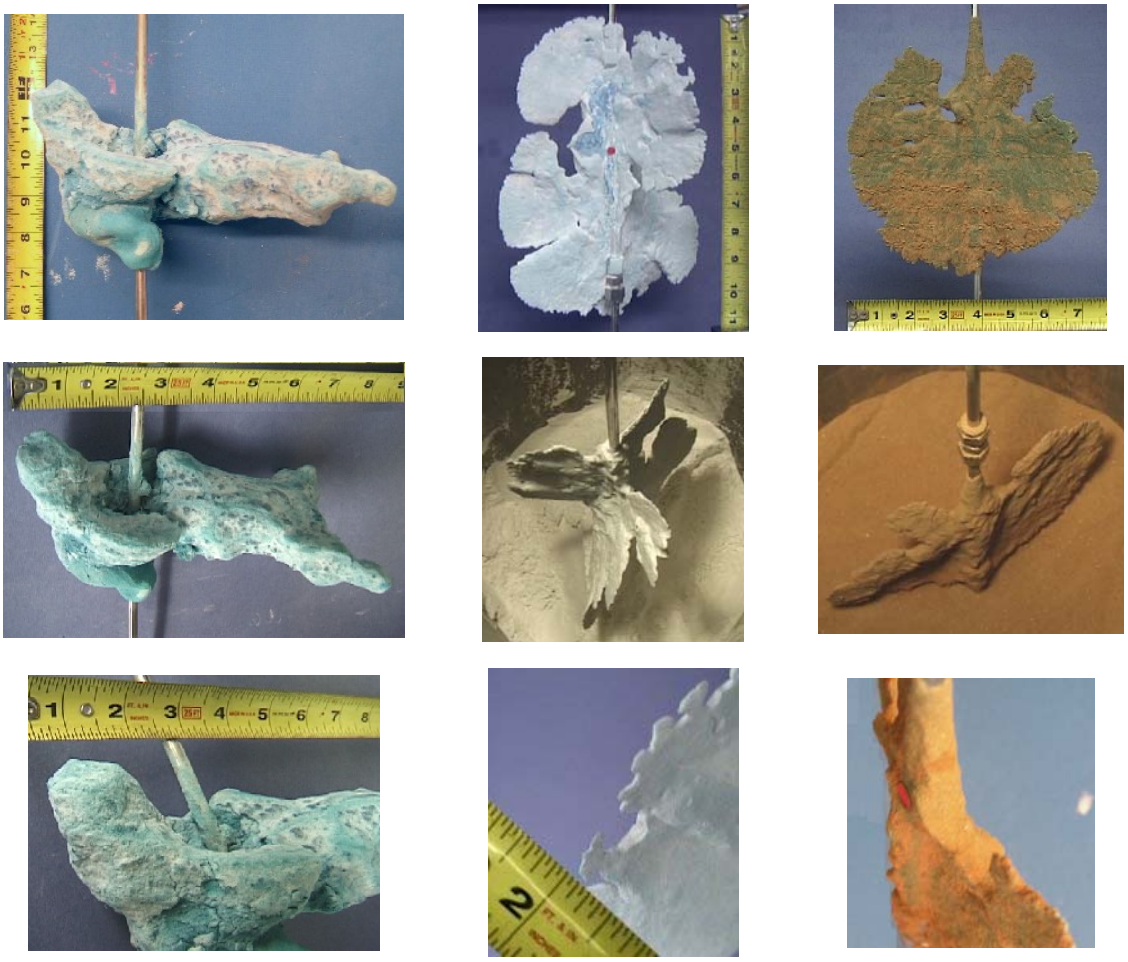

(a) test 2 (b) test 4 (c) test 3

Figure 5.1 Fractures in different types of particulate materials: (a) mixture of fine sand and silica flour, (b) silica flour, and (c) Georgia Red Clay.

Note: when visible, the dot in the photographs indicates the position of the injection hole.

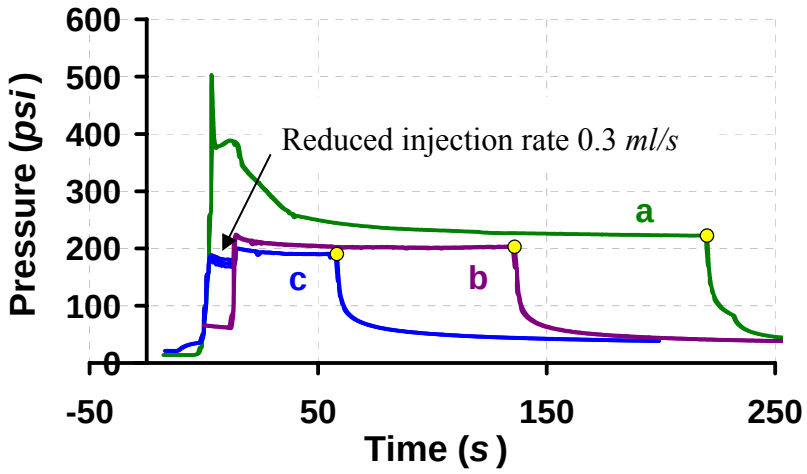

Figure 5.2 Injection pressure curves for three types of particulate materials: (a) mixture of sand and flour, (b) silica flour, and (c) Georgia Red Clay.

Note: for curve c, the injection rate during the first 15 seconds was accidentally set to a low value (i.e., 0.3 *ml/s*) compared to its set point value (i.e., 1.7 *ml/s*). This caused the first segment in the pressure curve with low pressures.

Table 5.2 Results of experiments with different types of particulate materials

Test		**2**	**4**	**3**
Peak Pressure	*psi*	498	224	200
Relative Volume Change	*%*	n/a	n/a	n/a
Average Density after Injection	*%*	n/a	n/a	n/a

The average relative density after injection listed in Table 5.2 is the relative density of the particulate material (excluding the volume of the injected fracturing fluid) measured immediately after the experiment. The application of this quantity assumes that the water leak-off from the joint compound to the particulate material is negligible during the injection of the fracturing fluid.

The relative volume change of the particulate material is defined as

$$\frac{\Delta V_{specimen}}{V_{injection}} \times 100\% \qquad (5.1)$$

where $\Delta V_{specimen}$ is the volume change of the entire specimen (including the injected fluid inside) and $V_{injection}$ is the injected volume of fracturing fluid. The relative volume change is a measure of the degree of the volume change of the specimen compared to the injection volume. Positive values indicate that the volume of the specimen increases and negatives values indicate the volume decreases.

The relative volume change and the average relative density after the injection were not measured for these three experiments.

In the sand-silica flour mixture, the hydraulic fracture is thick and massive (Figure 5.1a). A certain degree of leak-off of the fracturing fluid into the sand-silica flour mixture is observed from the thin layer (i.e., ~ 2 *mm*) of the mixture of joint compound and particulates that peeled off the fracture surface.

In silica flour (Figure 5.1b), the fracture is also thin and vertical. However, it has three vertical wings. On each wing, multiple segments are visible. The fracture thickness decreases from the fracture center (~ 1 *cm*) to the fracture front (~ 1 *mm*). The fracture front demonstrates both beveled and fingered features.

In Georgia Red Clay (Figure 5.1c), the hydraulic fracture is thin and vertical. It is planar, which is in contrast to the three-wing fracture in silica flour. Similar to the fracture in silica flour, the fracture thickness decreases from the center area (~ 7 *mm*) to to the fracture front (~ 2 *mm*). The thick front in the vicinity of the center area is clearly

beveled. The thin front that is far away from the center area has many small fingers. Compared to the fracture in silica flour, the size of the fingers is smaller, and consequently, they display more details. An exposed cross-section of the fracture, as shown in Figure 5.3, indicates that the leak-off of the fracturing fluid into Georgia Red Clay is negligible.

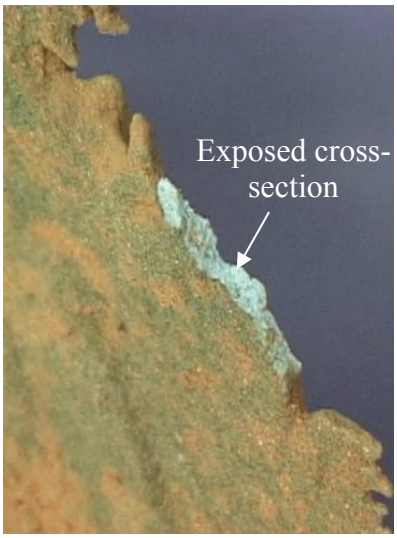

Figure 5.3 Exposed cross-section of the fracture created by injecting joint compound into Georgia Red Clay. The light color is solidified joint compound (test 3).

Summarizing, both beveled and fingered fronts are observed in Georgia Red Clay and silica flour. Due to the leak-off of the fluid into the formation and the massive fractures observed in the fine sand and the sand-silica flour mixture, and the fine particle migration in the mixture, these two materials are not used for the large-scale experiments. Although Georgia Red Clay yields feasible fractures, the properties of Georgia Red Clay are difficult to quantify accurately, since they may vary with its local origin. Therefore, silica flour is the main particulate material used for the large-scale experiments.

During hydraulic fracturing, the pressure curves typically increase monotonically until

they reach a peak pressure. After this peak, the injection pressure decreases abruptly. Then, the injection pressure does not decrease continuously as would be expected for thin fractures in solid, brittle materials. The pressure either stays almost constant or gradually approaches an asymptotic value.

The pressure at the peak is referred to as fracture initiation pressure, since it likely corresponds to the initiation of the hydraulic fracture (the experimental series with different injection volumes supports this hypothesis; see section 5.2.4). The pressure after the peak is referred to as fracture propagation pressure, since it likely corresponds to the propagation of the hydraulic fracture after its initiation. For the pressure curves with increasing fracture propagation pressure, the minimum pressure after the peak and before increasing is referred to as a pressure minimum.

Typically, the peak pressure is two orders of magnitude higher than the confining pressure. The peak pressure for the sand-silica flour mixture is almost twice as great as that in Georgia Red Clay and silica flour under similar conditions.

5.2.2 Vertical Load

Two series of experiments are performed in particulate specimens with different vertical loads. The first series is performed on specimens densified by vibration and the second series on specimens densified by rodding.

Particulate Specimen Prepared by Vibration

The experiments are conducted using dense silica flour with vertical loads ranging from 1 to 11 *psi*. The parameters of the experiments are listed in Table 5.3. The corresponding

fractures are presented in Figure 5.4. The pressure curves are shown in Figure 5.5. The results of the experiments are listed in Table 5.4.

Table 5.3 Results of experiments with different types of particulate materials

Test	4	5	6
Particulate materials	Silica flour		
Relative Density *%*	73	76	81
Densification Technique	Vibration		
Lateral Boundary	Constrained		
Scale	Large		
Vertical Load *psi*	*1*	*6*	*11*
Ratio of p_v / p_h	> 1		
Fracturing Fluid	Joint compound		
Injection Rate *ml/s*	1.7		
Injection Volume *ml*	200		

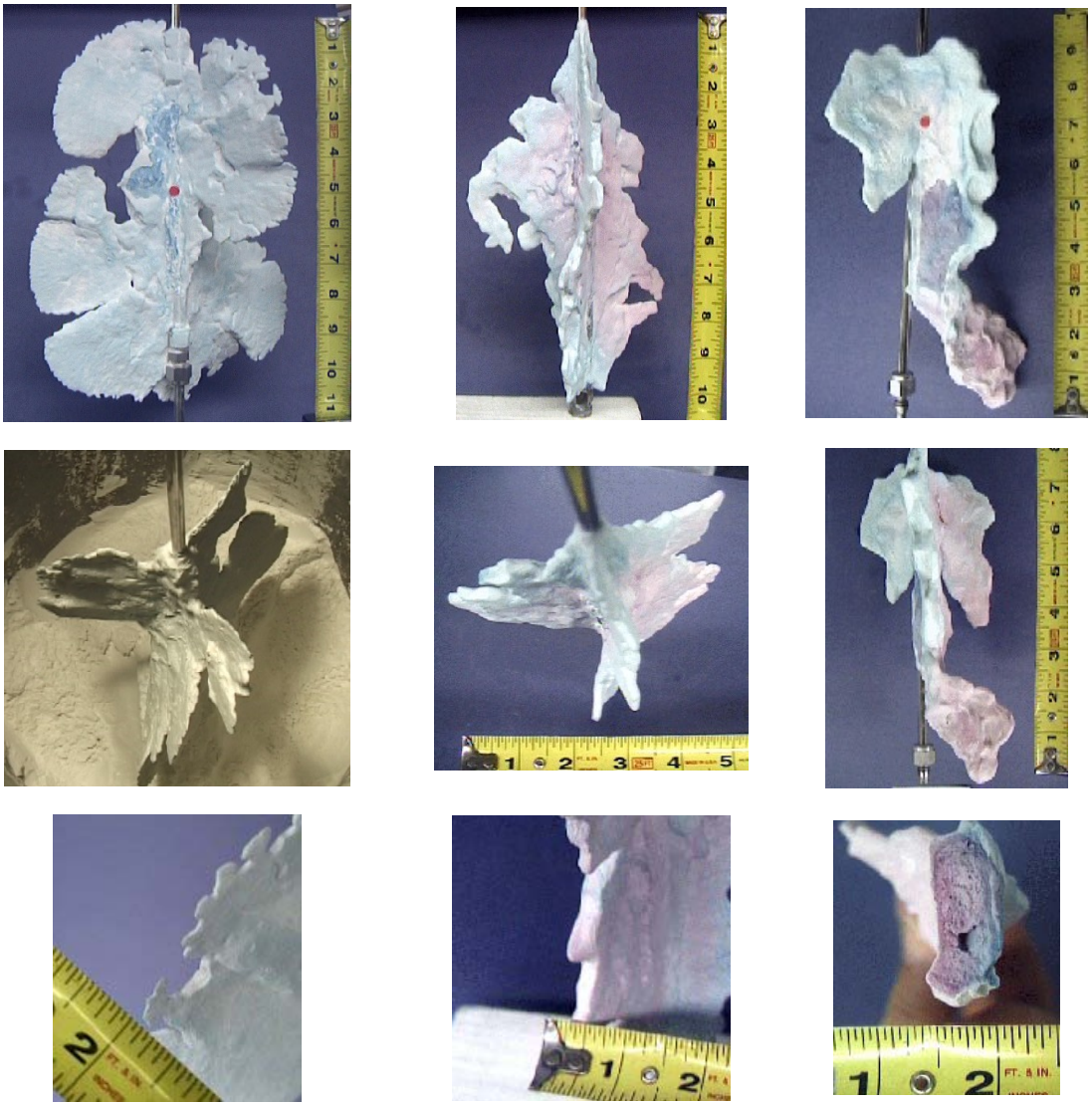

(a) test 4 (b) test 5 (c) test 6

Figure 5.4 Fractures with different vertical loads: (a) 1 *psi* (blue), (b) 6 *psi* (blue → red) [(1)], (c) 11 *psi* (blue → red)[(1)].

Note: (1) the colors indicate the color code of the injection fluid with the sequence of the injection.

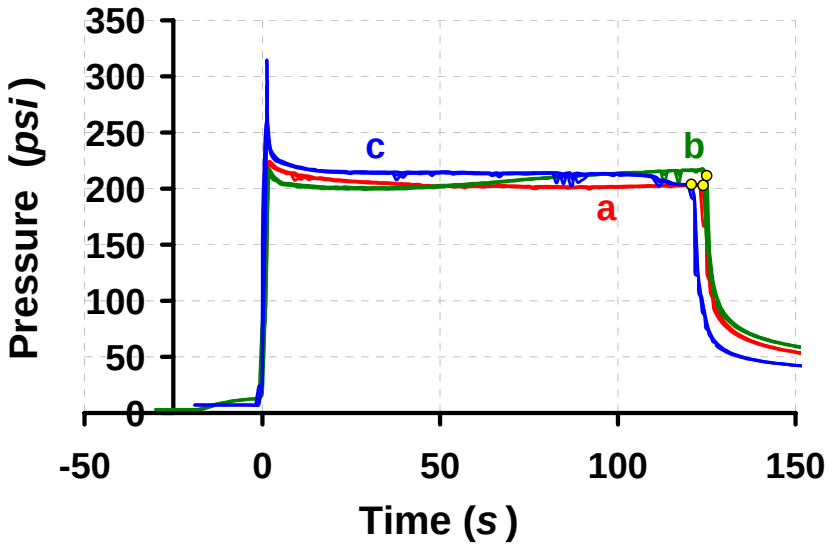

Figure 5.5 Injection pressure curves for different vertical loads: (a) 1 *psi*, (b) 6 *psi*, and (c) 11 *psi*.

Table 5.4 Results of experiments with different vertical loads

Test		4	5	6
Peak Pressure	*psi*	224	218	315
Relative Volume Change	*%*	n/a	n/a	n/a
Average Density after Injection	*%*	n/a	n/a	n/a

All three fractures are vertical and have beveled fronts and multiple wings. The wings tend to have an axial rotational translation with respect to the injection tubing.

With similar injection volumes, the length and width of the fractures decrease (hence, the thickness increases), with increasing vertical load. The thickness of the fracture front varies from ~ 1 *mm* to ~ 1.5 *cm*. The fracture with a low vertical load shows more fingering at the front. As the vertical load increases, the fracture front is thicker and its fingering characteristic disappears. When increasing the vertical load to 10 *psi*, the

roughness of the fracture surface increases.

The propagation of the three fractures is not symmetric in the vertical direction with respect to the injection hole. All the fractures propagate mainly downwards. This is probably due to the fact that the particulate specimens are prepared by vibration. During vibration, the fine particles migrate downwards, which results in a vertical density gradient.

The three injection pressure curves have similar trends. The peak pressure of the experiment with a vertical load of 11 *psi* is about 30% higher than the peak pressures of the other two experiments with lower vertical loads. The fracture propagation pressure is either constant or decreases slightly.

Particulate Specimen Prepared by Rodding

The experiments are conducted using very dense silica flour with vertical loads ranging from 1 to 83 *psi*. The parameters of the experiments are listed in Table 5.5. The corresponding fractures are presented in Figure 5.6. The pressure curves are shown in Figure 5.7. The results of the experiments are listed in Table 5.6.

Table 5.5 Parameters of experiments with different vertical loads

Test		17	8	15	16
Particulate materials		Silica flour			
Relative Density	***%***	91	89	92	96
Densification Technique		Rodding			
Lateral Boundary		Constrained			
Scale		Large			
Vertical Load	***psi***	*1*	*11*	*11*	*83*
Ratio of p_v / p_h		> 1			
Fracturing Fluid		Joint compound			
Injection Rate	***ml/s***	1.7			
Injection Volume	***ml***	180	200	350	390

(a) test 17

(b) test 8

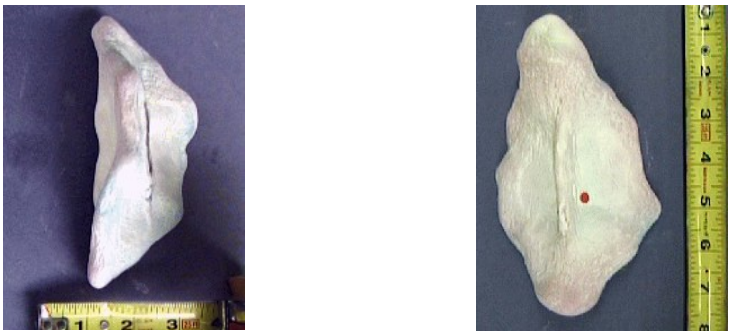

(c) test 15

(d) test 16

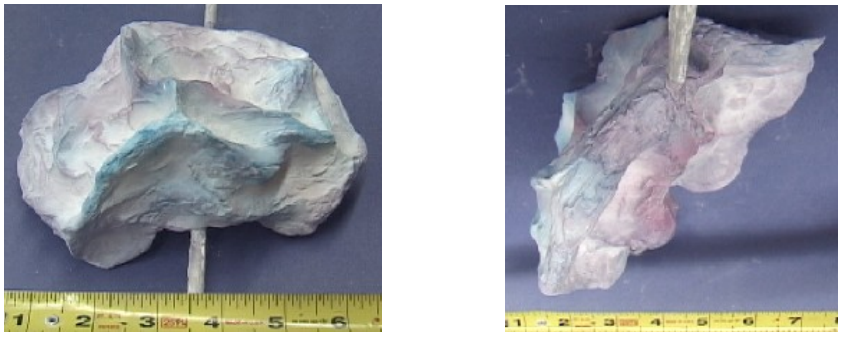

Figure 5.6 Fractures with different vertical loads: (a) 1 *psi* (blue → red), (b) 11 *psi* (blue → red → green), (c) 11 *psi* (white → green → red), (d) 83 *psi* (red → blue → white).

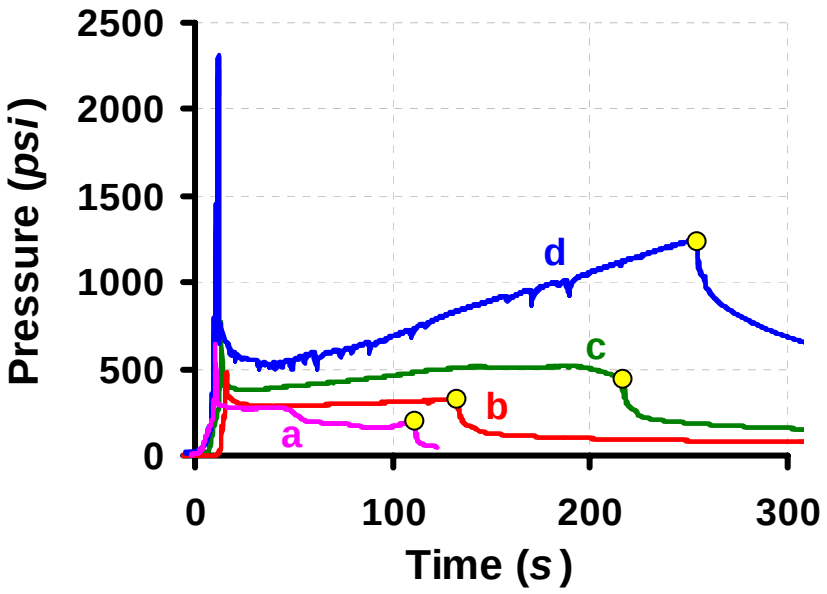

Figure 5.7 Injection pressure curves for different vertical loads: (a) 1 *psi*, (b) 11 *psi*, (c) 11 *psi*, and (d) 83 *psi*.

Table 5.6 Results of experiments with different vertical loads

Test		17	8	15	16
Peak Pressure	*psi*	651	479	770	2,311
Relative Volume Change	*%*	38	-4	36	3
Average Density after Injection	*%*	92	93	94	99

The fractures generated at a vertical load of 1 *psi* (the lower section in Figure 5.6a) and 11 *psi* have a similar appearance. They are vertical and have three wings. The surfaces of the fractures are smooth. The fracture at 1 *psi* (Figure 5.6a) has a beveled front. In contrast, at 11 *psi*, the fracture front (Figures 5.6b and 5.6c) is rounder and does not show a clear beveled feature. For the fracture at a same vertical load of 11 *psi* but a

larger injection volume of 350 *ml*, the front is round. Many annular ridge lines appear around the injection holes on the surface of the fracture and increases its roughness. The comparison of the fractures in Figures 5.6a and 5.6b shows that the thickness of the fractures increases with increasing vertical load. This is consistent with the results in the vibrated specimens.

However, when the vertical load increases to 83 *psi*, the appearance of the fracture is very different (Figure 5.6d). It is thick and massive with two developed and one underdeveloped wing (in contrast to three equally developed wings at lower vertical loads). Its surface is very rough with many sharp off-shoots at different scales. The size of the off-shoots ranges from ~ 1 *mm* to ~ 1 *cm*. A number of the small off-shoots are aligned. Its thickness is about twice as great as that of the fractures at lower vertical loads. The fracture front is sharp and angular.

The fractures are approximately symmetric in the vertical direction with respect to the injection hole (except for the fracture at 1 *psi*). This is probably due to the uniform density at the global scale of the rodded specimens.

The fracture at 1 *psi* has an unusual shape (Figure 5.6a). It has two segments. The lower one is vertical and the upper one is oblique. The two segments may be caused by the discontinuity of the density around the center of the specimen due to switching rodding operators. Based on the observations of the small-scale experiments, fractures tend to be perpendicular with respect to the direction of the minimum principal stress. The oblique upper segment may be an indication of locked-in lateral stresses due to rodding (on average ~ 50 *psi* is applied for each stroke of the rod for the preparation of a

very dense specimen) that are greater than the 1 *psi* externally applied vertical load. Similarly, the top part of the fracture at 11 *psi* (Figure 5.6b) is also slightly curved towards the horizontal direction. From these observations, an estimate of the order of the locked-in lateral stress due to rodding for these specimens is ~ 10 *psi*.

The pressure curves for vertical loads of 1 and 11 *psi* have almost constant fracture propagation pressures (Figure 5.7). For the pressure curve at 1 *psi*, the pressure drop at ~ 50 *s* occurs concurrently with the narrow transition of the two segments (based on an estimate of the injected volume). At a vertical load of 83 *psi*, the fracture propagation pressure increases almost linearly with increasing injection volume at a rate of 2 *psi/ml* (Figure 5.7).

It appears that peak and fracture propagation pressures increase with increasing vertical loads. The peak pressure is approximately three times greater than that of the fractures at 1 and 11 *psi*. The fracture propagation pressure is also significantly greater. The unusual low peak pressure of the test 8 (i.e., vertical load of 11 *psi* and injection volume of 200 *ml*) is most likely due to the fact that the surface of the injection tubing was not treated to increase its roughness like other experiments in this series.

Summarizing, the thickness and surface roughness of the fractures, and the peak pressure increase with increasing vertical load. The fracture surface characteristics and its corresponding injection pressure pattern can vary dramatically with different loads applied on the particulate materials.

5.2.3 Ratio of Applied Stresses

A series of two experiments with different ratios of the applied loads are performed. The first experiment is conducted on a normally consolidated specimen, in which the vertical stress is greater than the horizontal. The second experiment is performed on a heavily over-consolidated specimen. To prepare such a specimen, the specimen is vertically loaded with 83 *psi* initially. The vertical load is removed immediately before the injection of the fracturing fluid. Hence, the vertical stress (≈ 0) is less than the horizontal (> 0). The parameters of the experiments are listed in Table 5.7. The corresponding fractures are presented in Figure 5.8. The pressure curves are shown in Figure 5.9.The results of the experiments are listed in Table 5.8.

Table 5.7 Parameters of experiments with different ratios of applied stresses

Test		4	19
Particulate materials		Silica flour	
Relative Density	*%*	73	98
Densification Technique		Vibration	Rodding
Lateral Boundary		Constrained	
Scale		Large	
Vertical Load	*psi*	1	83 → 0
Ratio of p_v / p_h		*> 1*	*< 1*
Fracturing Fluid		Joint compound	
Injection Rate	*ml/s*	1.7	
Injection Volume	*ml*	200	450

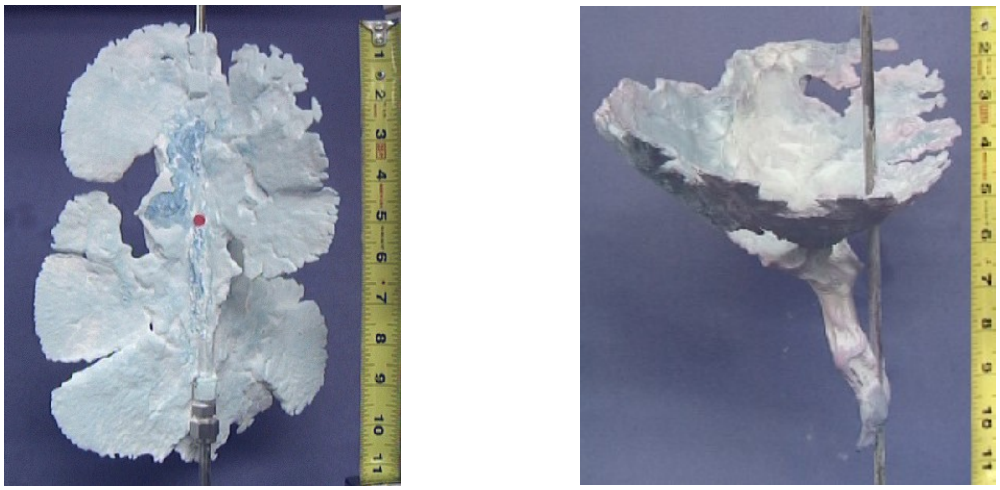

(a) test 4 (b) test 19

Figure 5.8 Fractures with different ratios of applied stresses: (a) $p_v / p_h > 1$ (blue) and (b) $p_v / p_h < 1$ (red → blue → yellow).

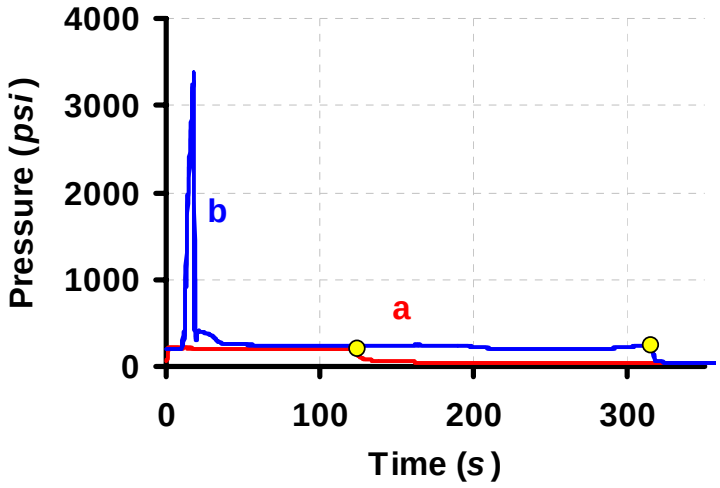

Figure 5.9 Injection pressure curves for different ratios of applied stresses: (a) $p_v / p_h > 1$ and (b) $p_v / p_h < 1$.

Table 5.8 Results of experiments with different ratios of applied stresses

Test		4	19
Peak Pressure	*psi*	224	3,364
Relative Volume Change	*%*	n/a	n/a
Average Density after Injection	*%*	n/a	n/a

The two fractures are generated under similar vertical loads but different load ratios (i.e., p_v / p_h). The fracture for $p_v / p_h > 1$ is vertical with three wings while the fracture for $p_v / p_h < 1$ is inclined and has a conical shape as shown in Figure 5.8b. The fronts of both fractures are thin (~ 1 *mm*) and beveled.

The conical shape is unique, which is rarely observed for hydraulic fractures in brittle, solid materials. Cone-shaped cracks in Champlain clays were reported to be observed in the field hydraulic fracturing tests by *Lefebvre et al.* [1991].

The fracture for $p_v / p_h > 1$ is oriented perpendicular to the direction of the minimum principal stress. This is consistent with the results of the small-scale experiments (section 3.5.4).

The two fractures have very similar pressure curves and fracture propagation pressures. However, their peak pressures differ. The peak pressure of the fracture for $p_v / p_h < 1$ is 14 times as great as that of the other fracture. This is likely due to the memory of the material in one specimen about the high over-consolidation pressure (i.e., 83 *psi*) it experienced.

The dimensions of the cone shape fracture (for $p_v / p_h < 1$) is close to those of the

specimen. The top edge of the cone even touches the side wall of the container.

The two fractures have very similar pressure curves and fracture propagation pressures. However, their peak pressures differ. The peak pressure of the fracture for $p_v / p_h < 1$ is 14 times as great as that of the other fracture. This is likely due to the memory of the material in one specimen about the high over-consolidation pressure (i.e., 83 *psi*) that it experienced.

5.2.4 Injection Volume

Two series of experiments are performed with different injection volumes to demonstrate the different propagation stages of the hydraulic fracturing process. The first series is performed on specimens with a vertical load of 11 *psi* and the second series at a vertical load of 83 *psi*. These two different vertical loads are studied because they produce very different fracture properties.

11 *psi* Vertical Load

The parameters of the experiments are listed in Table 5.9. The corresponding fractures are presented in Figure 5.10. The pressure curves are shown in Figure 5.11. The results of the experiments are listed in Table 5.10.

Table 5.9 Parameters of experiments with different injection volumes

Test		10	13	8	15
Particulate materials		Silica flour			
Relative Density	*%*	93	94	89	92
Densification Technique		Rodding			
Lateral Boundary		Constrained			
Scale		Large			
Vertical Load	*psi*	11			
Ratio of p_v / p_h		> 1			
Fracturing Fluid		Joint compound			
Injection Rate	*ml/s*	1.7			
Injection Volume	*ml*	*10*	*40*	*200*	*350*

(a) test 10

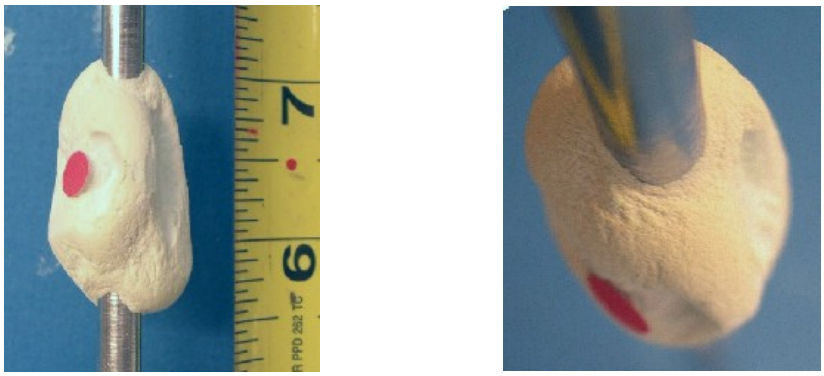

(b) test 13

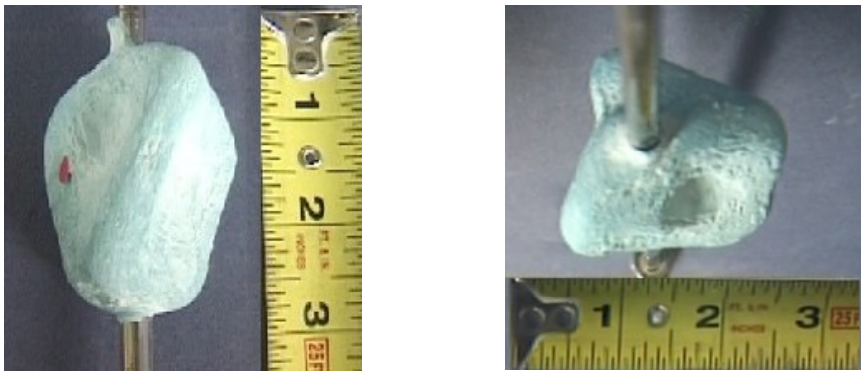

(c) test 8

(d) test 15

Figure 5.10 Fractures with different injection volumes: (a) 10 *ml* (green), (b) 40 *ml* (blue), (c) 200 *ml* (red → blue → green), and (d) 350 *ml* (white → green → red).

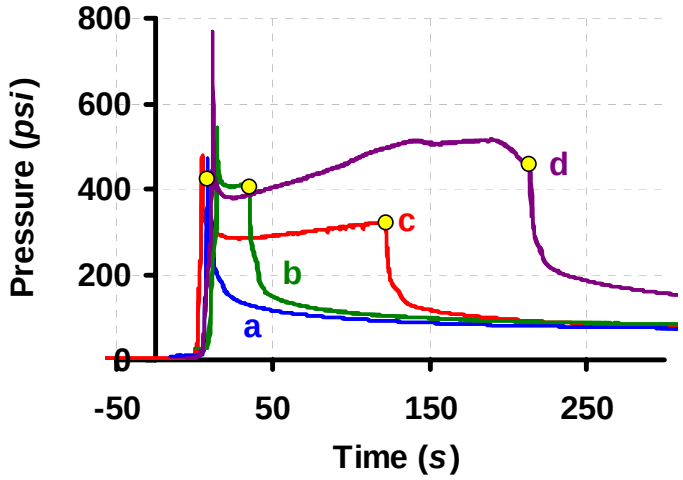

Figure 5.11 Injection pressure curves for different injection volumes: (a) 10 *ml*, (b) 40 *ml*, (c) 200 *ml*, and (d) 350 *ml*.

Table 5.10 Results of experiments with different injection volumes

Test		10	13	8	15
Peak Pressure	*psi*	471	540	479	770
Pressure Minimum	*psi*	351(1)	407	285	380
Relative Volume Change	*%*	0	-7	-4	36
Average Density after Injection	*%*	93	95	93	94

Note: (1) due to the small volume of the fracturing fluid, the pressure minimum has not been reached. The pressure listed here is the value when pump stops.

From Figures 5.10and 5.11, it appears that the injected fracturing fluid forms a small bubble shape volume first. Immediately following the peak pressure, a small wing-like vertical fracture is developed (Figure 5.11a) from this bubble shape volume. The injection pressure drops dramatically after the peak pressure. With continuous injection, three wings grow and becomes longer and thicker (Figures 5.10b, 5.10c, and 5.10d).

During the fracture growth, the pressure either remains constant or increases almost linearly with a small slope. After injecting ~ 200 *ml*, the length and width of fracture barely increase, but its thickness increases significantly. The fracture fronts during the fracturing propagation (see Figures 5.10b, 5.10c, and 5.10d) are all round rather than beveled.

The pressure curves of the four experiments have similar trends. The fracture propagation pressure tends to increase with increasing injection volume. The four experiments are performed under similar conditions. The higher propagation pressures of the fractures for 40 and 350 *ml* are likely due to the improved design of the injection hole, with a better contact between the injection tubing and the particulate material, compared to the other two experiments.

Among the four experiments, only the test with 350 *ml* has an increase in total specimen volume. The relative volume change is less than 100%. It indicates that the total volume change of the specimen is less than the injection volume.

83 *psi* Vertical Load

The parameters of the experiments are listed in Table 5.11. The corresponding fractures are presented in Figure 5.12. The pressure curves are shown in Figure 5.13. The results of the experiments are listed in Table 5.12.

Table 5.11 Parameters of experiments with different injection volumes

Test		18	16
Particulate materials		Silica flour	
Relative Density	*%*	99	96
Densification Technique		Rodding	
Lateral Boundary		Constrained	
Scale		Large	
Vertical Load	*psi*	83	
Ratio of p_v / p_h		> 1	
Fracturing Fluid		Joint compound	
Injection Rate	*ml/s*	1.7	
Injection volume	*ml*	*43*	*375*

(a) test 18 (b) test 16

Figure 5.12 Fractures with different injection volumes: (a) 43 *ml* (blue → red) and (b) 375 *ml* (blue → red → white).

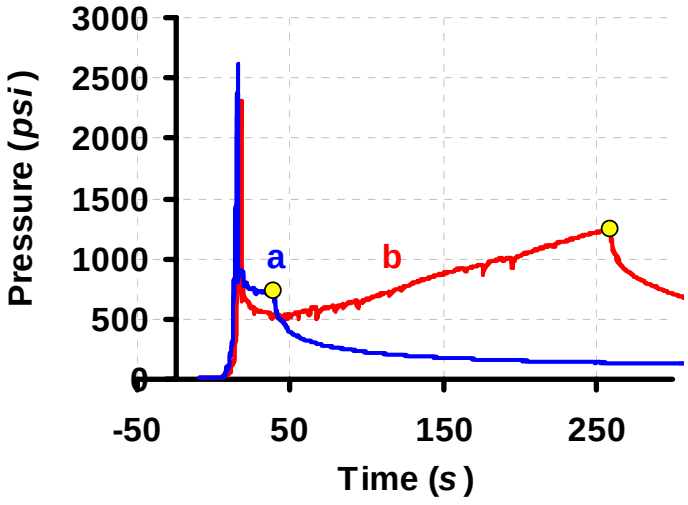

Figure 5.13 Injection pressure curves for different injection volumes: (a) 43 *ml* and (b) 375 *ml*.

Table 5.12 Results of experiments with different injection volumes

Test		18	16
Peak Pressure	*psi*	2,605	2,311
Relative Volume Change	*%*	0	3
Average Density after Injection	*%*	99	99

The fracture with 43 *ml* of the injection volume orients approximately vertically. The fracture front consists of multiple thin wings. Each wing is composed of a single or multiple petals (Figure 5.12a). The surface of the petals is smooth and shows ridge lines along the propagation direction. The features of the petals resemble those of brittle fractures. Each petal seems to propagate in a short time and appears sequentially. The petals are thin (1 to 2 *mm* thickness) with round fronts. The pressure after the peak pressure decreases asymptotically before the pump is stopped.

The fracture with 375 *ml* is massive. It has multiple, arbitrarily oriented, sharp off-shoots of varying sizes on its surface. The fracture front is sharp. No petals are observed. After the pressure reaches its minimum value, it increases almost linearly.

Both of the pressure curves have multiple downward spikes during the fracture growth process (Figure 5.13). They are believed to be related to the sharp off-shoots. The sharp offshoots on the fracture with the large injection volume may be the exposed fronts of the petals that developed during the earlier injection stages.

Summarizing, the abrupt pressure drop after the peak pressure appears to be related to the fracture initiation. The propagation pressure remains constant or increases when the fracture thickness increases.

5.2.5 Density of Particulate Materials

A series of fractures with different densities of the particulate materials are performed. The parameters of the experiments are listed in Table 5.13. The corresponding fractures are presented in Figure 5.14. The pressure curves are shown in Figure 5.15. The results of the experiments are listed in Table 5.14.

Table 5.13 Parameters of experiments with different densities of the particulate materials

Test		21	16
Particulate materials		Silica flour	
Relative Density	*%*	*74*	*96*
Densification Technique		Rodding	Static loading
Lateral Boundary		Constrained	
Scale		Large	
Vertical Load	*psi*	83	
Ratio of p_v / p_h		> 1	
Fracturing Fluid		Joint compound	
Injection Rate	*ml/s*	1.7	
Injection Volume	*ml*	185	375

(a) test 21 (b) test 16

Figure 5.14 Fractures with different densities of particulate material: (a) $D_r = 74\%$ (red → blue) and (b) $D_r = 96\%$ (blue → red → white).

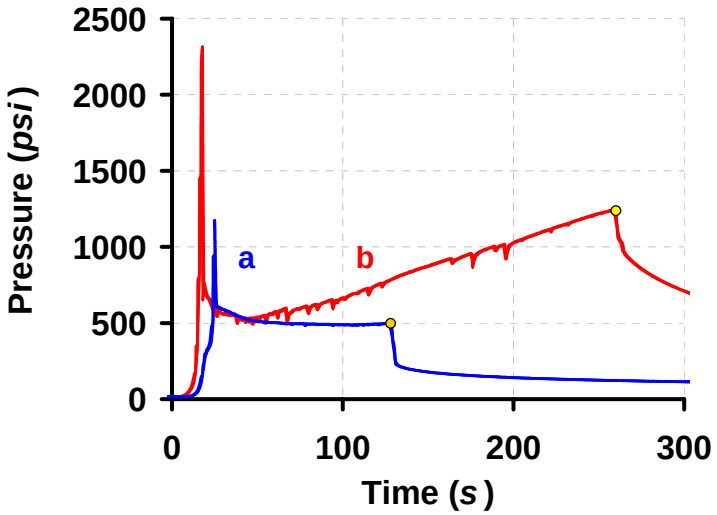

Figure 5.15 Injection pressure curves for different densities of particulate material: (a) $D_r = 74\%$ and (b) $D_r = 96\%$.

Table 5.14 Results of experiments with different densities of particulate material

Test		21	16
Peak Pressure	*psi*	1,168	2,311
Relative Volume Change	*%*	6	3
Average Density after Injection	*%*	75	99

The two fractures have very different appearances. The fracture with a density of 74% has three thick, vertical wings. The surface of the fracture is rough with parallel ridge lines. The fracture front is round and rough. It behaves similar to the fracture generated under lower vertical loads with high density (e.g. test 15: under 10 *psi* with relative density 92%), except that the fracture surface is rougher. The fracture with a density of 96% has two developed wings while the third wing is underdeveloped. It is massive, thick and vertical with many randomly oriented sharp off-shoots with different sizes on its surface. The fracture demonstrates features that are similar to that of brittle fractures. This is probably due to the fact that under the conditions of a high applied load and a high density, leak-off becomes more significant and wets the particulate material in the vicinity of the fracture front. This may introduce capillary forces, and make brittle fractures possible.

The fracture at a vertical load of 83 *psi* and a density of 96% is believed to be generated by mechanisms that are different from those at lower densities and vertical loads.

5.3 Pressure-controlled Lateral Boundary

One reason to perform the large-scale experiments is intended to minimize the boundary effect. With the pressure-controlled lateral boundary, the measurements of the specimen volume change in very dense specimens (Figures 5.18 and 5.19) show that the volume starts to increase immediately following the peak pressure. This indicates that the lateral boundary is not sufficiently remote from the hydraulic fracture, even for the large-scale experiments Therefore, for very dense particulate specimens, the boundary effects are inevitable with the available experimental setup.

A parametric analysis was performed by varying four parameters: the magnitude and the ratio of the applied loads, the density of the particulate materials, and the injection volume. The particulate specimens are prepared by rodding.

5.3.1 Applied Loads

A series of fractures with different magnitudes of the applied loads are performed. The specimen is loaded by vertical and horizontal boundary stresses with the ratio of 2. The parameters of the experiments are listed in Table 5.15. The corresponding fractures are presented in Figure 5.16. The pressure curves are shown in Figure 5.17.The results of the experiments are listed in Table 5.16. The measured volume changes of the specimens during injection are presented in Figures 5.18 and 5.19.

Table 5.15 Parameters of experiments with different applied loads

Test		P10	P11
Particulate materials		Silica flour	
Relative Density	*%*	96.2	95.9
Densification Technique		Rodding	
Lateral Boundary		Pressure-controlled	
Scale		Large	
Vertical Load	*psi*	*25*	*40*
Ratio of p_v / p_h		2	
Fracturing Fluid		Joint compound	
Injection Rate	*ml/s*	1.7	
Injection Volume	*ml*	200	300

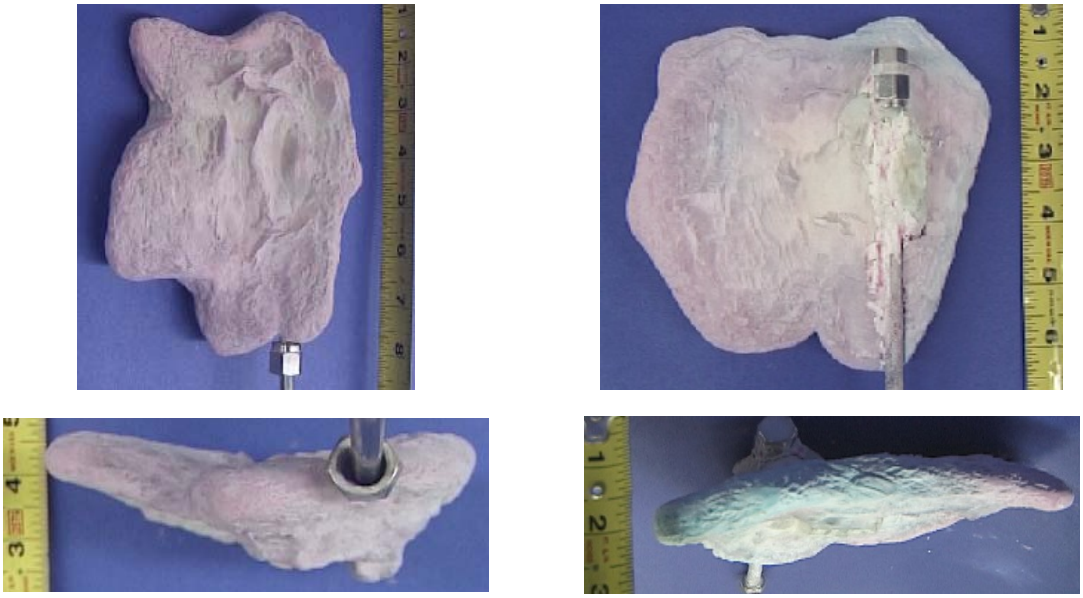

(a) test P10 (b) test P11

Figure 5.16 Fractures with different applied loads: (a) $\sigma_v = 25$ *psi* (blue → red) and (b) $\sigma_v = 40$ *psi* (blue → red → yellow).

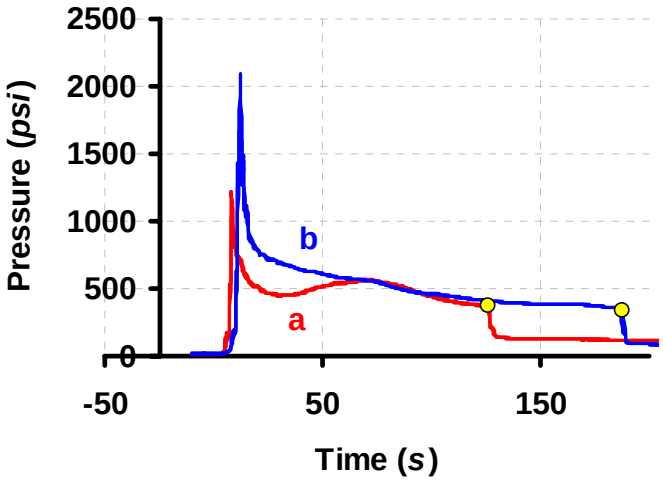

Figure 5.17 Injection pressure curves for different applied loads: (a) $\sigma_v = 25$ *psi* and (b) $\sigma_v = 40$ *psi*.

Table 5.16 Results of experiments with different applied loads

Test		P10	P11
Peak Pressure	*psi*	1,212	2,088
Relative Volume Change	*%*	142	141
Average Density after Injection	*%*	95.7	95.3

Both fractures are thick, vertical and planar. Both have round fracture fronts. Their surfaces have sharp off-shoots in the vicinity of the injection hole, and become smoother farther away from the injection hole. For the constrained lateral boundaries, the off-shoots are observed for fractures generated in a dense specimen under a high vertical load (i.e., 83 *psi*). For the pressure-controlled lateral boundaries, similar phenomena are observed for the dense specimen under lower vertical loads (i.e., 25 and 40 *psi*).

The thicknesses of the two fractures at different vertical loads are not significantly different.

The fracture at a vertical load of 25 *psi* is shaped as a five-pointed star. The contour of the fracture front is jagged. The fracture at a vertical load of 40 *psi* does not display a very jagged fracture front, but it is also angled. The difference of the fronts between the two fractures is likely due to the fact that the shapes of the two fractures represent two different propagation stages, since the injection volume of the latter fracture is ~ 50% greater than that of the former. The jagged fracture contour is very different from the smooth and round contours of most of the fractures under the similar conditions with constrained lateral boundaries. However, a few fractures with constrained lateral boundaries demonstrate similar angled contour, as shown in Figure 5.4c (test 6) and Figure 5.6a (test 17).

Overall, the injection pressure increases with increasing the magnitude of applied loads. For a vertical load of 40 *psi*, the fracture propagation pressure decreases monotonically. At a vertical load of 25 *psi*, it decreases non-monotonically, as shown in Figure 5.17.

For pressure-controlled lateral boundaries, the change of the volume of the specimen is monitored during fluid injection. Seen from Figures 5.18 and 5.19, the boundary begins to translate at the peak injection pressure. The delay of the increase of the specimen volume is probably due to the initial contraction of the particulate material and the insufficient sensitivity of the gages used for pressure measurement.

Then, the volumes of the specimen increase at almost constant rates that are slightly

higher compared to the injection rate. With the injection rate of 1.7 *ml/s* for these two experiments, the average rate of increase of the specimen volume (i.e., the ratio of the increase of the overall volume of the specimen versus the injection time) is ~ 2.2 *ml/s*. This indicates that for pressure-controlled lateral boundaries, initially the increase of the overall specimen volume is less than the injection volume. However, given a sufficiently high injection volume, the increase of the specimen volume can exceed the injection volume.

For both tests, the relative change of the volume of the specimen (see Table 5.16) is greater than 100%. That is, the increase of the volume of the particulate material in the specimen (excluding the volume of the injected fluid) is greater than the injection volume. This indicates that at least part of the particulate material in the specimen dilates. Dilation in particulate materials is associated with plastic deformation.

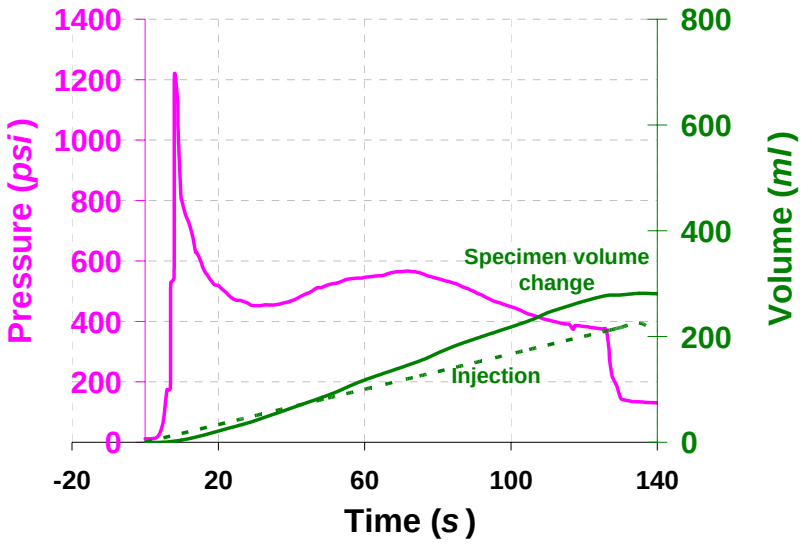

Figure 5.18 Injection pressure, injection volume and change of specimen volume versus injection time for test P10.

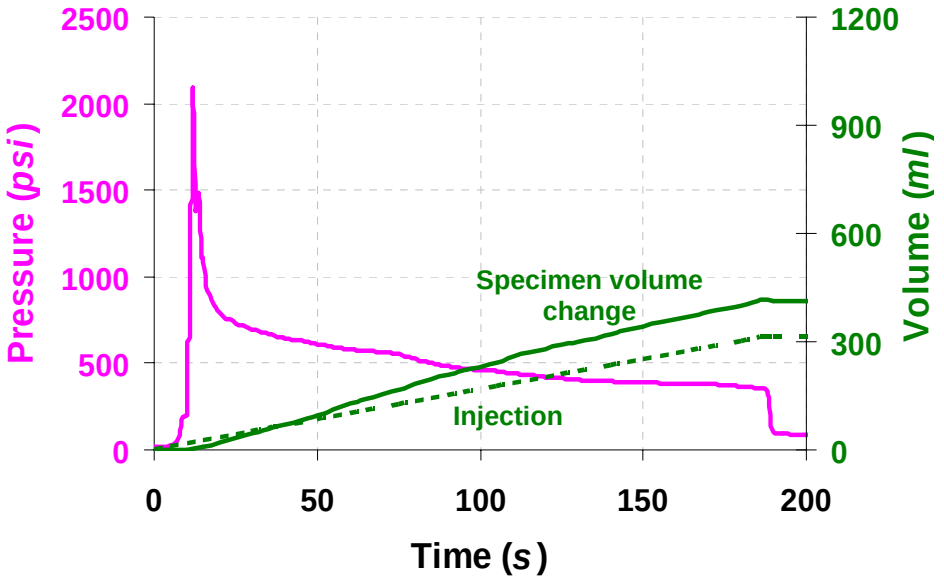

Figure 5.19 Injection pressure, injection volume and change of specimen volume versus injection time for test P11.

5.3.2 Injection Volume

A series of experiments with different injection volumes are performed to demonstrate the different propagation stages. The parameters of the experiments are listed in Table 5.17. The corresponding fractures are presented in Figure 5.20. The pressure curves are shown in Figure 5.21.The results of the experiments are listed in Table 5.18.

Table 5.17 Parameters of experiments with different injection volumes

Test		P12	P11
Particulate Materials		Silica flour	
Relative Density	*%*	96	96
Densification Technique		Rodding	
Lateral Boundary		Pressure-controlled	
Scale		Large	
Vertical Load	*psi*	40	39
Ratio of p_v / p_h		2	
Fracturing Fluid		Joint compound	
Injection Rate	*ml/s*	1.7	
Injection volume	*ml*	*65*	*300*

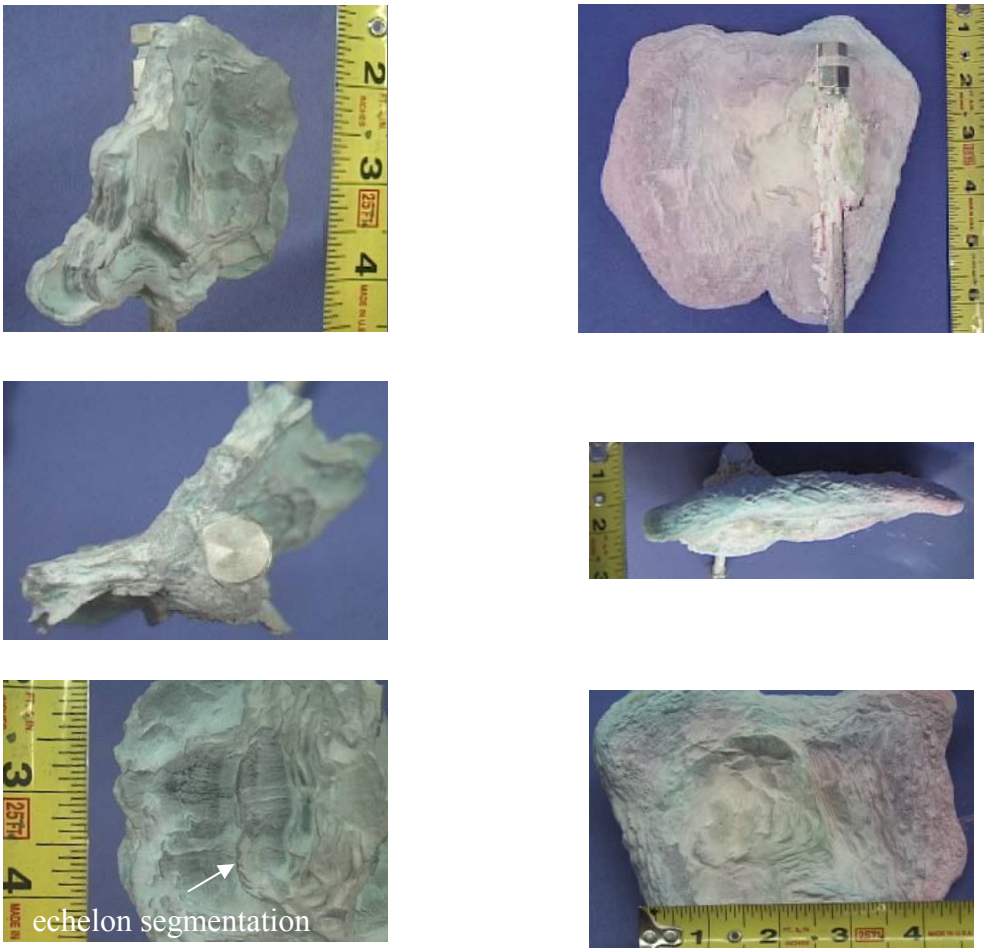

(a) test P12 (b) test P11

Figure 5.20 Fractures with different injection volumes: (a) 65 *ml* (blue) and (b) 300 *ml* (blue → red → yellow).

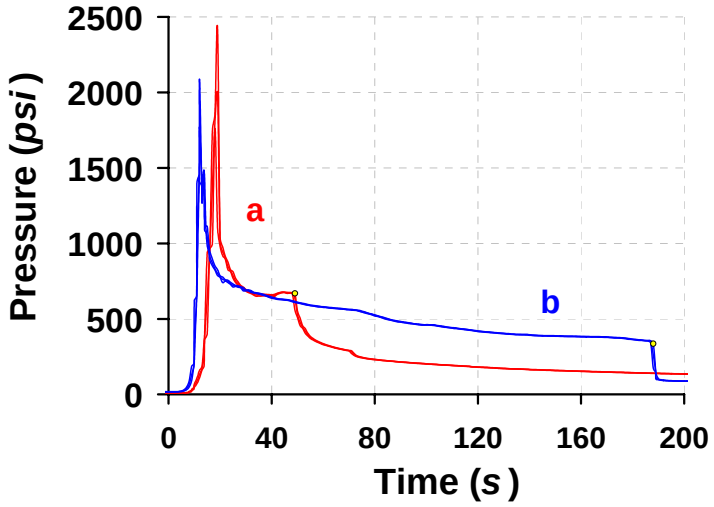

Figure 5.21 Injection pressure curves with injection volumes: (a) test P12: 43 *ml* and (b) test P11: 375 *ml*.

Table 5.18 Results of experiments with different injection volumes

Test		P12	P11
Peak Pressure	*psi*	2,423	2,088
Relative Volume Change	*%*	88	141
Average Density after Injection	*%*	96.1	95.3

The fractures at the two propagation stages display commonalities as well as differences. Both fractures are planar, vertical and thick, with thick fracture fronts. Their thickness is relatively uniform over the entire fracture, typically ~ 1/4 *in* for the early stage (test P12) and ~ 5/8 *in* (test P11) for the late stage. The fracture at the early stage has an undeveloped third wing. The pressures curves have very similar trends and magnitudes.

The fracture at the early stage (Figure 5.20a) has a mixture of beveled and multiple,

parallel, sharp fracture fronts. The surface of the fracture has small sharp offshoots. Petals are visible on the surface along the main stream of the front propagation. The residual ridge lines of the multiple petals that developed earlier are visible. These petals are very similar to those observation in test 18 (Figure 5.12a) with constrained lateral boundaries. This indicates that the fracture propagates in increments.

The fracture at the late stage (Figure 5.20b) has a round front. Most of the fracture surface is rough but relatively flat. In the vicinity of the injection hole, small and scattered sharp off-shoots are observed. They resemble a lot to the residual ridge lines of the petals on the fracture at early propagation stage (Figure 5.20a). A reasonable inference is that they are the residual marks of the sharp fracture fronts in the earlier propagation stages.

If we approximate the shape of the two fractures as a round disk, the diameter and thickness of the fracture are 3 and 1/4 *in* at the early stage, and 5 and 5/8 *in* at the late stage, respectively. With increasing the injection volume, the diameter of the fractures increases ~ 70% while the thickness increases ~ 150%. This means that after the pressure minimum, the fracture grows more in the aperture direction than in the fracture plane direction.

Summarizing, with increasing the injection volume (i.e., at different propagation stages), fracture front can change from beveled or sharp to round. This may indicate that different mechanisms are dominating at different propagation stages.

5.3.3 Ratio of Applied Stresses

A series of experiments with different ratios of the applied vertical and horizontal applied stresses has been performed. The ratios of the vertical and horizontal pressures used are 2 and 1. The parameters of the two experiments are listed in Table 5.19.

Unfortunately, the experiment with a ratio of 1 (i.e., under a hydrostatic confining pressure) did not succeed. The reason was that the peak pressure exceeded the pressure capacity of the pump (~ 4,000 *psi*) and the specimen could not be fractured. After the particulate material was excavated and the injection tubing was exposed, only a tiny amount (< 1 *ml*) of the fracturing fluid was found in the vicinity of the injection hole. The results of the experiments are listed in Table 5.20.

Table 5.19 Parameters of experiments with different ratios of applied stresses

Test		P11	P13
Particulate materials		Silica Flour	
Relative Density	*%*	96	100
Densification Technique		Rodding	
Lateral Boundary		Pressure-controlled	
Scale		Large	
Vertical Load	*psi*	40	30
Ratio of p_v / p_h		*2*	*1*
Fracturing Fluid		Joint compound	
Injection Rate	*ml/s*	1.7	
Injection volume	*ml*	300	~ 0

Table 5.20 Results of experiments with different applied stresses

Test		P11	P13
Peak Pressure	*psi*	2,088	> 4,000
Relative Volume Change	*%*	141	n/a
Average Density after Injection	*%*	95.3	n/a

The high peak pressures of these experiments are possibly the result of the high densities of the specimens (because the peak pressure is sensitive to the material density).

5.3.4 Fracture Behavior and Critical State Line

To study the correlation of the fracture behavior with the contractive and dilative properties of the material, the initial stress states of the two experiments with pressure-controlled lateral boundaries are plotted in the v - p space (Figure 5.22), where v is the specific volume and p is the mean stress (see section 2.5.5). The center point of the photograph of each fracture indicates the point of the initial stress state. The critical state line (CSL) of the particulate material, i.e., silica flour, is plotted in the same figure.

It appears that fractures are observed on the dilative side of or almost on the critical state line. However, no clear experiment has been conducted for the contractive material.

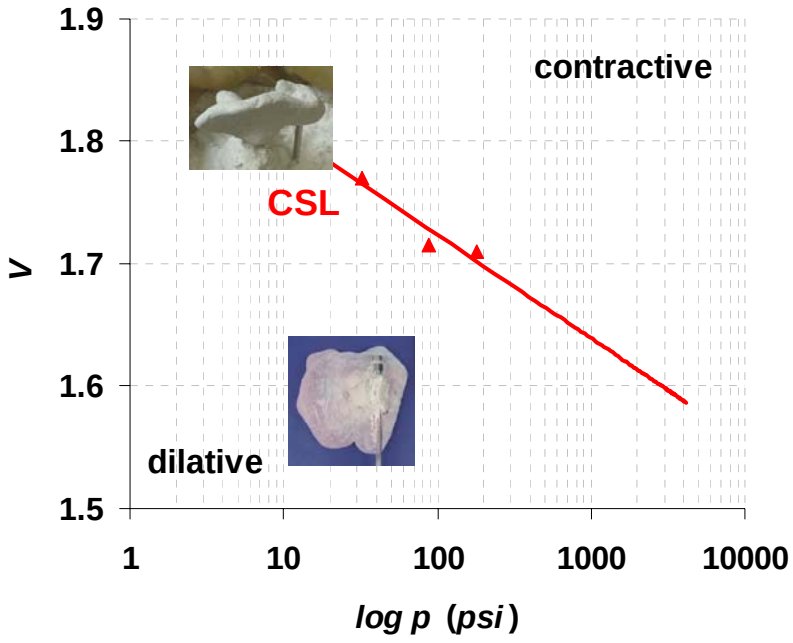

Figure 5.22 Initial stress state of fractures for pressure-controlled lateral boundary in v - p space.

5.4 Fracture Characteristics

In this study, the fracture geometry is described in terms of the fracture front, the fracture surface, the overall fracture geometry, and the fluid flow pattern during fracturing.

5.4.1 Fracture Front

For the large-scale experiments, the observed main fracture fronts (e.g., beveled, fingered and round) are similar to those for the small-scale experiments (Figure 5.23). In addition, at the large scale, multiple-fracture front is observed that are not evident at the small scale.

(a) test 5

(b) test 3

(c) test 15

Figure 5.23 Observed fracture fronts: (a) beveled, (b) fingered, and (c) round.

Beveled Front

A beveled front is frequently observed at low applied vertical loads (< 10 *psi*), as shown in Figure 5.23a. The parameters of the experiment are available in Table 5.3.

Fingered Front

A fingered front is observed at very low vertical loads (~ 1 *psi*).

It is commonly observed in Georgia Red Clay, as shown in Figure 5.23b. Fingered front is also observed in some fractures that are generated in silica flour and one example is shown in Figure 5.24. However, the fingered front of this fracture also demonstrates beveled features (see Figure 5.4a). The fingers in the upper part of the fracture (Figure 5.24a) are larger and have more details than that of the lower part (Figure 5.24b). The fracture surface is smooth with ridge lines along the fracture propagation direction, which seem to be the track lines of the finger growth. The fingers in the lower part of the fracture are less visible. The surface of the fracture is rough without significant ridge

lines. The difference between the fingers at different locations was correlated to the different densities. The lower part of the specimen tends to be denser (i.e., has a lower void ratio) than the upper part due to the downward migration of fine particles during vibration.

(a) (b)

Figure 5.24 Fingering of (a) upper part and (b) lower part of the fracture (test 4).

By comparing two fractures in Georgia Red Clay (GRC) and silica flour in Figures 5.1b and 5.1c, it is noticed that fingering feature is more distinct in Georgia Red Clay than in silica flour. Since the test conditions for both experiments are exactly the same, the difference in the fingering feature is attributed to the different properties of the materials. Beside the difference in the particle geometry, the void ratio of specimen of GRC (e = 0.92) is larger than that of silica flour (e =0.80).

Due to the limited experimental results on the fingering phenomenon, the mechanism of the fingered front is not quite clear yet, although an interpretation is offered in Chapter 6.

Round Fronts

The round front is observed at vertical loads greater than 10 *psi*, as shown in Figure 5.23c.

For the constrained lateral boundary with fingering and beveled fronts, the propagation pressure typically remains almost constant or decreases slightly (see Figures 5.2 and 5.5). For round fronts, the propagation pressure generally increases slightly with the injection volume (see Figures 5.7 and 5.10). It appears that the propagation of the round front is associated with a gradually increasing injection pressure.

Multiple Fronts

The multiple sharp fracture fronts (Figure 5.20a) are observed at the early stage of the fracture propagation. As the fracture continues to propagate, the multiple sharp fronts become a single, round fracture front, as shown in Figure 5.20b.

5.4.2 Fracture Surface

At the large scale, surface features such as, sharp off-shoots and semi-spherical expansion, are observed that are not evident at the small scale.

Sharp Off-shoots

At high applied loads for both lateral boundary conditions, sharp off-shoots protrude from the fracture surface, as showed in Figures 5.14b, 5.16, and 5.20. The size of these off-shoots varies from ~ 1 *mm* to the size of the fracture. They are oriented randomly.

Some of the off-shoots are aligned parallel to each other, and form echelon segmentations (Figure 5.20a). In the pressure curve of the fracture with the off-shoots with the constrained lateral boundary, many small downward pressure spikes (i.e., drops) during fracture propagation are visible (Figure 5.13).

Semi-spherical Expansion

Semi-spherical expansion has been observed in two fractures. The expansion appears in the vicinity of the injection holes, as shown in Figure 5.25. The expansion has a smooth surface. Its diameter ranges from ½ to ¾ *in*. The parameters of the two experiments can be found in Table 5.3 and Table 5.5. These features may be an indication of the initial cavity expansion prior to the fracture initiation (see Chapter 6).

(a) test 5

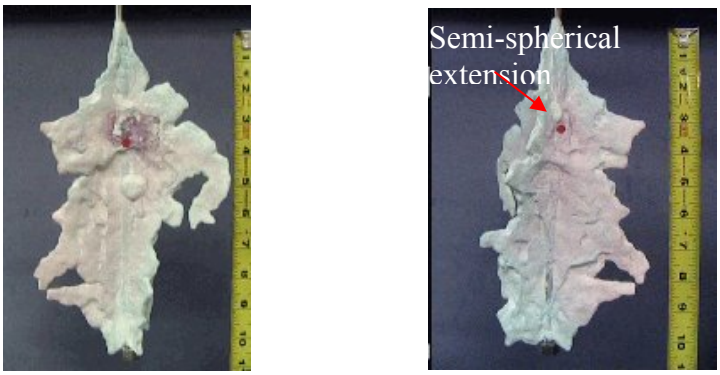

(b) test 16

Figure 5.25 Semi-spherical expansion observed in (a) 6 *psi* and 200 *ml* (blue → red) and (b) 83 *psi* and 375 *ml* (blue → red → white).

5.4.3 Fracture and Front Thickness

For the three typically observed fracture fronts, fractures with fingered and beveled fronts are thin and long. The thickness of the fractures attenuates from the center to the front with a ratio of ~10 (see Figures 5.1b and 5.1c). Fractures with round fronts are typically thick and short. The thickness of the entire fracture is relatively uniform. The thickness ratio between the center and the front is generally less than 2 (e.g., Figure 5.10). The fingered or beveled front can be as thin as 1 *mm*, and no larger than 10 *mm*. Round front is typically thicker than 5 *mm*.

The thickness of the fracture fronts of representative large-scale experiments for the two lateral boundary conditions are plotted with respect to the injection volume and applied vertical loads in Figure 5.26. The different colors of the data points indicate different levels of the applied vertical loads. A darker color denotes a higher load. The different shapes of the data points indicate different fracture front types. The numbers beside the data points represent the test number.

With greater injection volumes, the front thickness increases while the front maintains its round shape as shown by the test series 10-13-8-15 (see Table 5.9 and Figure 5.10) in Figure 5.26a. This may be interpreted as the front thickness increase during fracture growth. It also appears that for the applied vertical loads that are greater than 10 *psi*, and with an increasing injection volume, the shape of the fracture front may become round, as shown in test series 6-7 (Figure 5.26a) and test series P12-P11 (Figure 5.26b). Detailed information about the first series is available in Table 5.3, Table 5.21, Figure 5.30 and Figure 5.4 and about second series in Table 5.17 and Figure 5.20.

For greater applied vertical loads, the front thickness increases, as shown in the test series 4-5-6 (see Table 5.3 and Figure 5.4) in Figure 5.26a. For applied vertical loads less than 5 *psi*, all three fractures have beveled fronts.

As a result of greater injection volumes in combination with greater applied vertical loads, the fracture thickness increases (see test series P10-P11 in Figure 5.26b; detailed information about the two tests is available in Table 5.15 and Figure 5.16). All round fronts are observed with an applied vertical load greater than 10 *psi*.

Summarizing, the laboratory experiments show that the thickness of the fracture fronts increases with increasing injection volume and increasing applied loads. For vertical applied loads that are greater than 10 *ps*i, with increasing injection volume, the fracture front tends to become round. Beveled fronts are generally observed under lower vertical applied loads (i.e., less than 10 *psi*) while round fronts are observed under higher vertical applied loads (i.e., greater than10 *psi*).

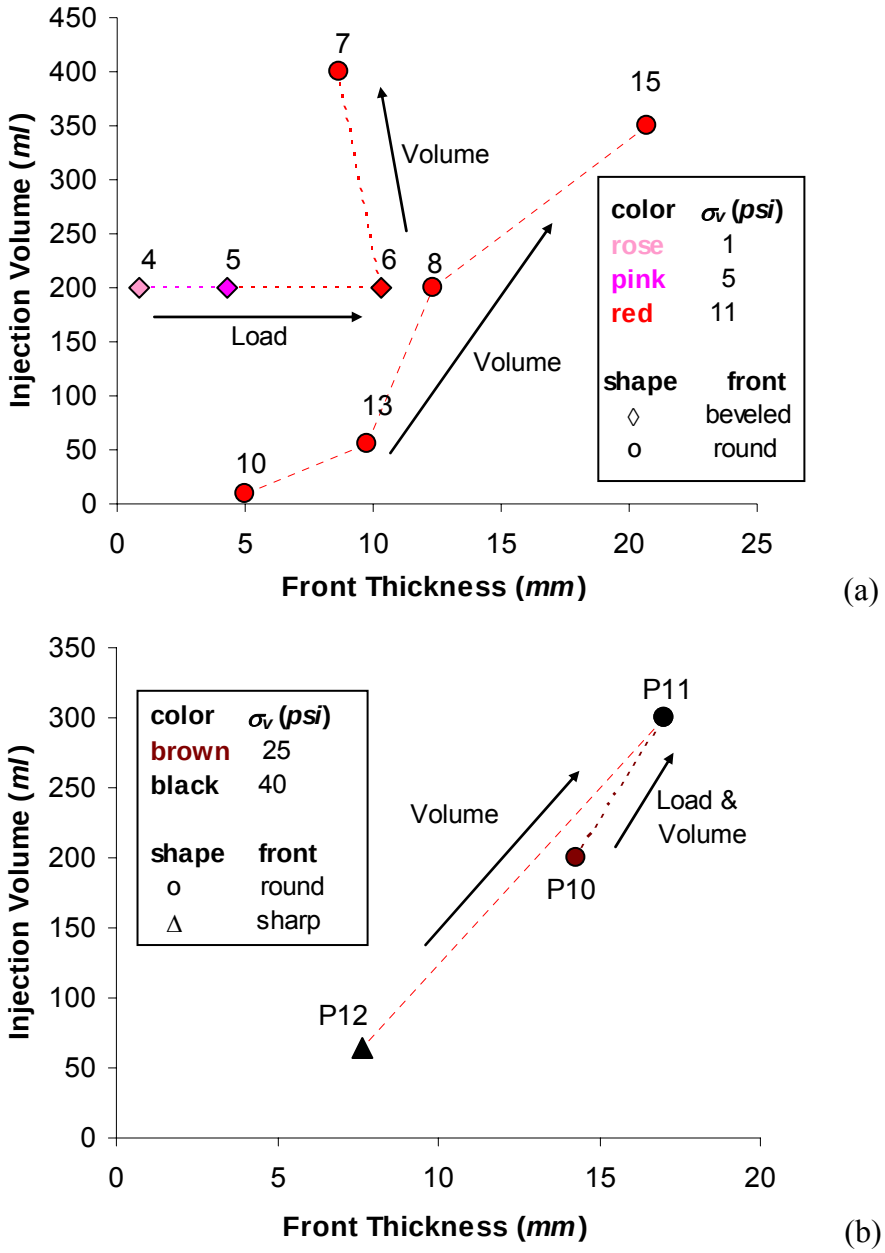

Figure 5.26 Fracture front thickness with respect to injection volume and vertical applied load (a) constrained and (b) pressure-controlled lateral boundaries. Arrows indicate the increase of the corresponding quantities.

Note: (1) different colors of the data points indicate different levels of applied vertical loads. A darker color denotes a higher load;

(2) different shapes of the data points indicate different fracture front types; and

(3) numbers beside the data points represent test numbers.

5.4.4 Overall Geometry

The overall geometry of the fractures demonstrates multi-wing (Figures 5.4a, 5.4b, and 5.4c) and multi-segment patterns (Figures 5.4a and 5.4b) that are similar to those of the small-scale experiments.

Multiple Wings

The fracture geometry is based on either a single section as shown in Figures 5.1b, 5.16a, and 5.16b, or three equi-distant (that is, at an angle of ~ 120°) wings as shown in Figures 5.4 and 5.10.

Multiple Segments

Each wing of a fracture can have multiple segments, as shown in Figures 5.4a and 5.4b. These segments were generally observed at low applied loads (e.g., 1 and 5 *psi* for the fractures in Figures 5.4a and 5.4b, respectively). Similar to multi-segmented hydraulic fractures in cohesive materials [*Germanovich and Astakhov*, 2004a and 2004b], closely spaced segments appear to interact with each other, locally changing their orientations.

5.4.5 Fluid Flow Pattern inside Fractures

The fracturing fluid that flows during the fracture propagation demonstrates fingering and layering pattern. Figure 5.27 (test 19) shows a fracture generated by injecting fracturing fluid with a red color, followed by a blue color. The information of the test is listed in Table 5.7. The photograph shows that the blue (i.e., later) fracturing fluid fingers into the

red (i.e., earlier) fracturing fluid and pushes it away. This demonstrates one feature of the fluid flow pattern with the sequence of injection.

Figure 5.27 Fluid flow in a fingering pattern: fluid in read is injected first and followed by fluid in blue (test 19).

In addition, sometimes the later fracturing fluid flows on the side of the earlier fracturing fluid. It forms a secondary layer on the surface of the initial fracture plane. This layering phenomenon is frequently observed. One example is shown in Figure 5.28. The parameters of this experiment can be found in Table 5.3.

Summarizing, the localized fluid flow (i.e., the formation of a hydraulic fracture) in the particulate materials attempts to flow either through the earlier injected fluid or alongside the layer of the earlier injected fluid (i.e., between the earlier fluid layer and the particulate material).

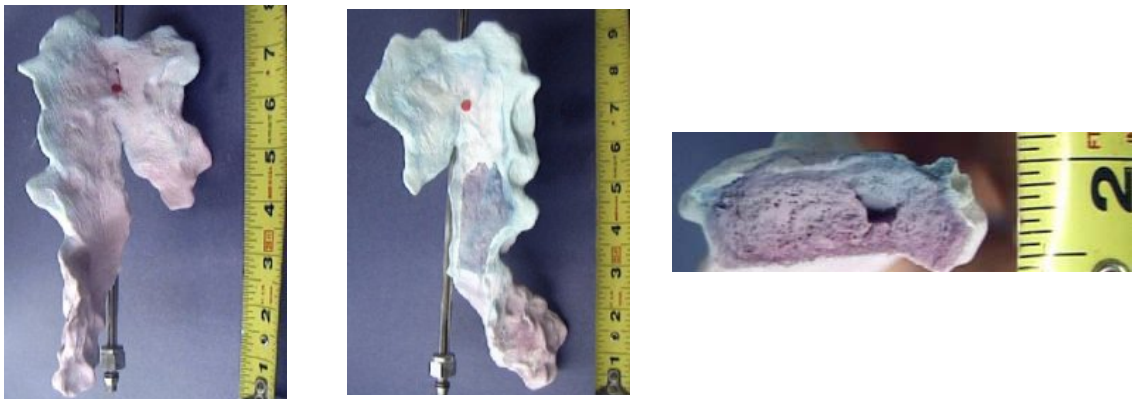

(a) (b) (c)

Figure 5.28 Fluid flow in layers during fracture propagation (test 6): (a) red side and (b) blue side and (c) cross section of the fracture (blue→ red).

5.5 Boundary Effect

The fractures generated with constrained and pressure-controlled lateral boundaries exhibit differences in overall geometry, fracture front, pressure response and volume change of specimens. The differences for the two boundary condition types will be discussed and compared in this section. Due to the limited number of performed experiments, especially with pressure-controlled lateral boundaries, the comparison may not represent all the possible cases.

5.5.1 Overall Geometry

With constrained lateral boundaries, most generated fractures have three wings under vertical loads up to 83 *psi* (see Figures 5.4 and 5.10). The wings developed away from the injection tubing, separated by a similar angle (~ 120°). A few fractures that have two wings include the fracture generated under an 83 *psi* vertical load (Figure 5.6d) and the

fracture in heavily over-consolidated particulate materials (Figure 5.8b). With pressure-controlled lateral boundaries, the fractures are typically planar (see Figure 5.29b).

Initially, the planar fracture could have been a triple-wing fracture. However, the third wing does not propagate further at the later growth stage as shown in Figure 5.29. Another example is test 7 with a constrained lateral boundary (Figure 5.30). The information of the experiment is listed in Table 5.21.

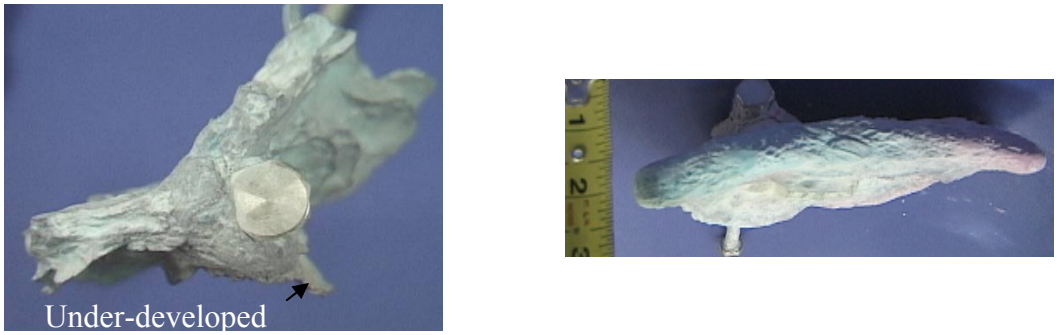

(a) test P12 (b) test P11

Figure 5.29 Top views of fractures at: (a) early stage and (b) late stage of fracture propagation.

(a) test 7 (b) test 7

Figure 5.30 Planar fracture with an undeveloped wing (a) side view and (b) top view.

Table 5.21 Parameters of test 7

Test		7
Particulate materials		Silica flour
Relative Density	*%*	84
Densification Technique		Vibration
Lateral Boundary		Constrained
Scale		Large
Vertical Load	*psi*	11
Ratio of p_v / p_h		*> 1*
Fracturing Fluid		Joint compound
Injection Rate	*ml/s*	1.7
Injection volume	*ml*	400

5.5.2 Fracture Front

For the constrained lateral boundaries at low loads, the fracture front is beveled for a small injection volume with low loads (< 10 *psi*). With continued fracture propagation, the beveled front becomes round. At high loads (80 *psi*), and at both small and large injection volumes, the fracture front is sharp and consists of extruded petals (Figure 5.12).

For the pressure-controlled lateral boundaries, the fracture front has multiple sharp fronts at a small injection volume with a vertical load of 40 *psi* (Figure 5.20a). As the fracture propagates, the fronts become round and smooth (Figure 5.20b). However, in the vicinity of the injection hole, the scattered sharp off-shoots are visible on the fracture surface. These off-shoots and the sharp fronts at the initial growth stage are very similar to the observation at a high load (83 *psi*) for the constrained lateral boundary, but at lower

applied loads. Since an insufficient number of experiments have been performed at vertical loads less than 40 *psi*, the comparison with the experiments at low loads for the constrained lateral boundary is not available.

5.5.3 Peak Pressure

The peak pressures of representative experiments under different applied loads for the two lateral boundary conditions are plotted in Figure 5.31. For these experiments, the densities range from 91 to 99%. It appears that at similar applied loads, the peak pressure for the pressure-controlled lateral boundaries is higher than that for the constrained lateral boundaries, although the pressures are within the same order of magnitude.

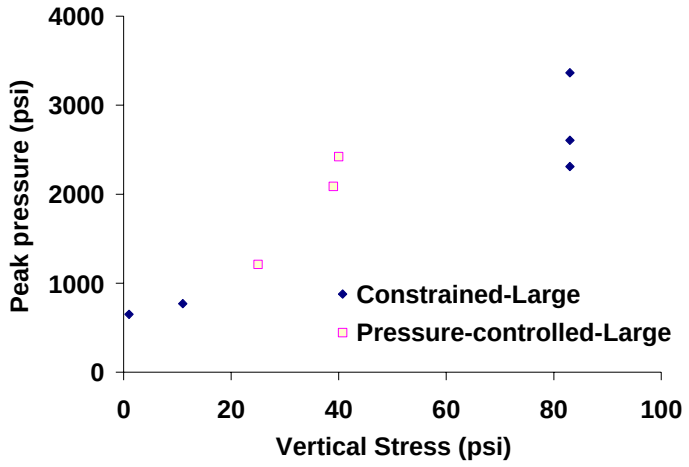

Figure 5.31 Peak pressures of large-scale experiments versus vertical applied loads , with two lateral boundary conditions.

5.5.4 Volume of Particulate Specimen

For both lateral boundary types, the overall specimen volume (including the volume of the injected fracturing fluid) increases during injection.

The pressure-controlled lateral boundary translates during injection, while maintaining the constant external water pressure. As discussed in section 5.3.1, given a sufficient injection volume, the volume increase of the particulate material in the specimen (excluding the injected fluid) can exceed the injection volume (see Figures 5.18 and 5.19).

For the constrained lateral boundary, only the top boundary can move (pressure controlled) and the other boundaries have zero-lateral strains. With the applied experimental setup and injection volumes, the final volume of the particulate material (excluding the injected fluid) is less than its initial volume (i.e., before the injection). This may indicate that the particulate material contracts. It may also dilate partially and locally, but that the dilation does not exceed the contraction. The trend of the volume change during the injection is not monitored (i.e., it is only monitored before and after the injection). Therefore, the information about the volume change trend at a larger volume is not available.

5.6 Scale Effect

To demonstrate the effect of the spatial scale, two series of experiments with different spatial scales are performed. The first series is performed on normally consolidated specimens (i.e., the ratio of vertical and horizontal applied stresses larger than the unity, $p_v / p_h > 1$). The second series is performed on over-consolidated specimens (i.e., the ratio of vertical and horizontal applied stresses less than the unity, $p_v / p_h < 1$).

5.6.1 Vertical Load Greater than Horizontal Load

The parameters of the two representative experiments are listed in Table 5.22. The

corresponding fractures are presented in Figure 5.32. The pressure curves are shown in Figure 5.33. The results of the experiments are listed in Table 5.23.

Table 5.22 Parameters of experiments with different scales

Test		$11^{(1)}$	$17^{(2)}$
Particulate materials		Silica flour	
Relative Density	*%*	95	91
Densification Technique		Vibration	Rodding
Lateral Boundary		Constrained	
Scale		*Small*	*Large*
Vertical Load	*psi*	1	
Ratio of p_v / p_h		> 1	
Fracturing Fluid		Joint compound	
Injection Rate	*ml/s*	~ 4	1.7
Injection Volume	*ml*	12	~ $60^{(3)}$

Note: (1) test number in small-scale experiment series; (2) test number in large-scale experiment series; and (3) it refers to the volume of the fracture section shown in Figure 5.32b.

(a) test 11 (b) test 17

Figure 5.32 Fractures generated at: (a) small scale (blue) and (b) large scale (blue → red → yellow).

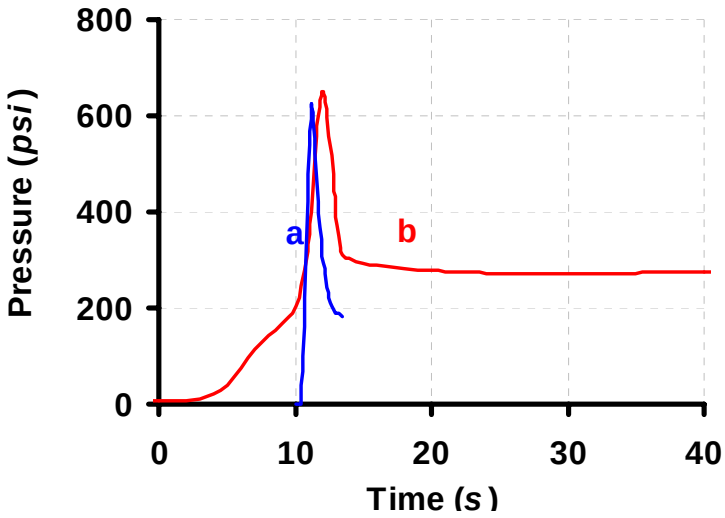

Figure 5.33 Injection pressure curves for (a) small scale and (b) large scale. The pressure curve a shows the pressure before the pump is stopped. The pressure curve b is the part that is corresponding to the section of the fracture shown in the Figure 5.32b.

Table 5.23 Results of experiments with different scales

Test		11	17
Peak Pressure	*psi*	623	651
Relative Volume Change	*%*	n/a	38
Average Density after Injection	*%*	n/a	92

Two fractures have similar geometry and features. Both of them are vertical, three wing fractures with mixed beveled and round fronts. The contours of the fractures are slightly jagged. The surfaces of the fractures are smooth with annular marks around the injection holes. Besides the dimensions, the two fractures do not show fundamental differences.

5.6.2 Vertical Load Smaller than Horizontal Load

The parameters of the two representative experiments are listed in Table 5.24. The corresponding fractures are presented in Figure 5.34.

Table 5.24 Parameters of experiments with different scales

Test		15[(1)]	19[(2)]
Particulate materials		Silica flour	
Relative Density	*%*	86	91
Densification Technique		Vibration	Rodding
Lateral Boundary		Constrained	
Scale		*Small*	*Large*
Vertical Load	*psi*	1 → 0	83 → 0
Ratio of p_v / p_h		< 1	
Fracturing Fluid		Joint compound	
Injection Rate	*ml/s*	4	1.7
Injection Volume	*ml*	12	450

Note: (1) test number in small-scale experiment series; and (2) test number in large-scale experiment series.

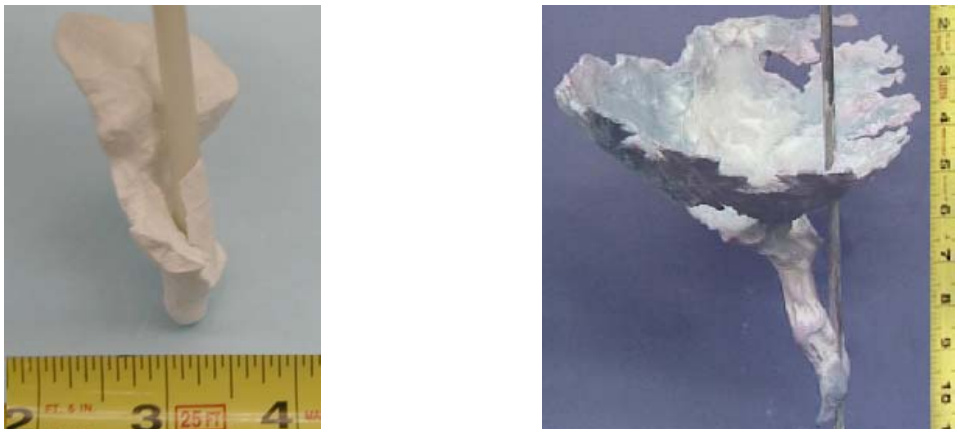

(a) test 15 (b) test 19

Figure 5.34 Similar fractures generated at: (a) small scale (white) and (b) large scale (red → blue → white).

The two experiments propagate inclined. The fracture at the small scale resembles the initial stage of the fracture at the large scale.

Summarizing, fractures at small- and large-scales behavior similarly. Small-scale experiments demonstrate the initial stage of the fracture propagation.

5.7 Summary

The fracturing behavior (including the shape, thickness, characteristics of the front, specimen volume, etc.) varies with the properties of the particulate materials (in terms of the particle gradation and mean particle size), the viscosity and the injection volume of the fracturing fluid, and the initial stress condition (i.e., stress ratio and magnitude), and the type of the lateral boundary condition of the particulate specimen.

Our observations suggest that the fracture thickness increases with decreasing void ratio, increasing fluid viscosity and applied loads. The fracture geometry also varies at different propagation stages. With the propagation of a fracture, its thickness increases and the fracture front can change from beveled or sharp to round. This may be an indication that different mechanisms dominate at different propagation stages.

Similar to the small-scale tests, three main fracture front types, beveled, fingered and round, are observed in the large-scale experiments. More than one front type can be observed on a single fracture. This also indicates that multiple mechanisms can coexist during the fracturing process.

Our observations suggest that hydraulic fracturing occurs in the following sequence:

(i) cavity expansion (before the injection pressure reaches its peak);

(ii) fracture front initiation from this cavity (near the pressure peak); and

(iii) growth of the developed fracture (after the pressure peak).

The observed features of fractures of different sizes appear to be similar. The small-scale experiments resemble the initial stage of the fracture propagation during the large-scale experiments. This may be an indication that the scale effect is relatively insignificant within the range of the laboratory scales.

Fractures in specimens with constrained and pressure-controlled lateral boundaries exhibit differences in the geometry and the front type, the pressure curves, and the change of the specimen volume due to the fluid injection. The fracture propagation pressure generally remains almost constant or increases for constrained and decreases for pressure-controlled lateral boundaries (sometimes with oscillations). For a given injection rate and fracturing fluid, both the peak and propagation pressures increase with the increase of the density and the applied loads.

Fractures generated in specimens prepared by different techniques exhibits minor difference in the behavior. A discussion of the effect of different techniques is presented in Appendix D.

CHAPTER 6

THEORETICAL MODELING

6.1 Fracture in Cohesive Materials

Different propagation criteria for fracturing in soft sediments, which include cohesive (Figure 6.1a) and cohesionless (Figure 6.1b) particulate materials, have been proposed in the literature. In all publications available to us these criteria are based on conventional linear or nonlinear fracture mechanics. *Saada et al.* [1985], *Lim et al.* [1988], *Fang et al.* [1989], *Morris et al.* [1994a], and *Murdoch* [1993] used fracture toughness K_{Ic} as a propagation criterion. *Vallejo* [1994] and *Morris et al.* [1994] employed the maximum tangential tension criterion [e.g., *Anderson*, 1995] to determine the fracture propagation direction. *Papanastasiou* [1997] and *Saada et al.* [1994] studied plastic yield at the fracture tip. In all these (and other) works, it is assumed (either explicitly or implicitly) that a tensile stress field exists near the fracture tip.

(a) (b)

Figure 6.1 (a) Saturated clay (Kaolin) and (b) dry coarse sand.

In general, solid materials fracture when the tensile stress at the fracture tip is sufficient to break the material bonds, (i.e., it exceeds the tensile strength). The conventional model of hydraulic fracturing in a solid material is presented in Figure 6.2. The stress distribution ahead of the fracture tip is shown schematically. Material representative volume elements are shown as small squares. The remote element 1 is in ambient compression, σ_1 and σ_3 ($0 < \sigma_3 < \sigma_1$). In contrast, element 3 in the fracture process zone is in tension, as is required to actually separate the two surfaces and to break the material bonds. Accordingly, the following assumptions (based on conventional fracture mechanics) are commonly used:

- tensile stress state near the fracture tip;
- non-zero tensile strength;
- a criterion of material failure based on fracture in tension, e.g., $\sigma_{yy} = -\sigma_t$, where σ_t is the tensile strength of the material (compression is positive in this chapter).

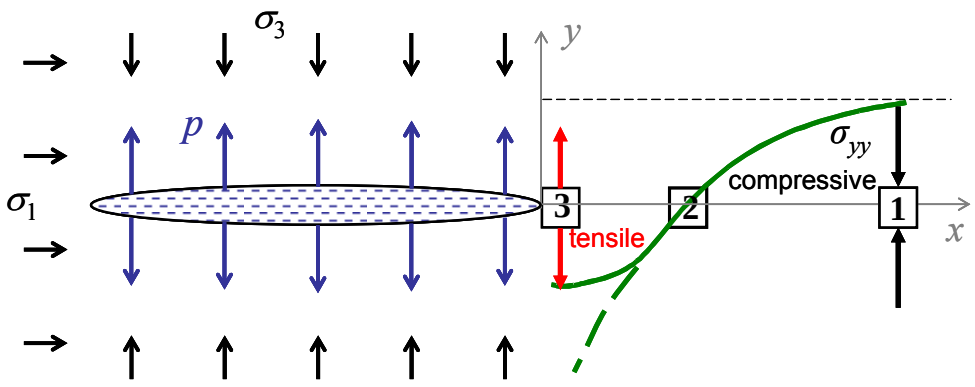

Figure 6.2 Stress distribution at the fracture tip in cohesive material with a non-zero tensile strength, σ_t. The dashed line indicates the singular stress distribution for a discontinuity in ideally elastic material.

Linear elastic fracture mechanics (LEFM) specifies the above postulates, assuming

that [e.g., *Anderson*, 1995]:

- material is elastic everywhere except at the process zone near the fracture tip, which is small compared to the fracture size;
- fracture is infinitesimally thin and can be modeled by a discontinuity;
- tensile stresses near the tip of this discontinuity in the elastic material can be described as the elastic singular stress distribution (shown as a dashed line in Figure 6.2) given by

$$\sigma_{yy} = -\frac{K_I}{\sqrt{2\pi r}} \qquad (x > 0, y = 0) \tag{6.1}$$

- in plane strain, the fracture aperture in the vicinity of the fracture tip is given by

$$w = \frac{4(1-\nu^2)}{\sqrt{2\pi}E} K_I \sqrt{r} \tag{6.2}$$

- the fracture growth criterion is

$$K_I^{elastic} = K_{Ic} \tag{6.3}$$

Here $K_I^{elastic}$ is the elastic stress intensity factor, that depends upon the body and fracture geometry, and the applied loads; K_{Ic} is the fracture toughness that, in LEFM, is a material property characterizing the resistance to the fracture growth; r is a *small* distance from the origin along the x-axis in the coordinate system shown in Figure 6.2 (i.e., $r = |x|$), and E and ν are Young's modulus and Poisson's ratio of the material, respectively.

Consider a classic example to illustrate how these ideas can be applied to the modeling of a hydraulic fracture. Below we follow an approach based on an analysis of the process zone according to the Dugdale-Barenblatt model. For our purposes, we ignore the lag

zone between the fluid and the process zone (Figure 6.3a).

In conventional fracture mechanics, a process zone is assumed to exist at the fracture tip. The existence of this process zone removes the elastic stress singularity at the fracture tip. It also provides a finite displacement opening at the end of the process zone for the fluid flow in the fracture, since viscous fluid cannot readily flow into an infinitesimally thin opening [*Detournay*, 2004]. According to the Dugdale-Barenblatt model, this process zone is treated as a localized linear cohesive zone with a tensile stress distribution $\sigma(x)$ inside [e.g., *Broek*, 1978]. This is depicted as the grey area shown in Figure 6.3. This model provides the conditions for fracture propagation in terms of either critical crack opening displacement δ_c or fracture toughness K_{Ic}.

The length d of the localized cohesive zone is determined from the condition of finite stresses at the fracture tip. This yields that the total stress intensity factor K_I is equal to zero:

$$K_I = 0 \tag{6.4}$$

where K_I is at the tip of the process zone (i.e., the superposition of the stress intensity factor due to remotely applied loads, fluid pressure, and plastic closure).

The closing stress $\sigma(x)$ is determined by the softening behavior that the material exhibits in the post-peak region during a displacement control tensile test. A simplified stress-displacement curve $\sigma(\delta)$ is shown in Figure 6.3c. The closing stress σ reduces to zero at the critical opening δ_c.

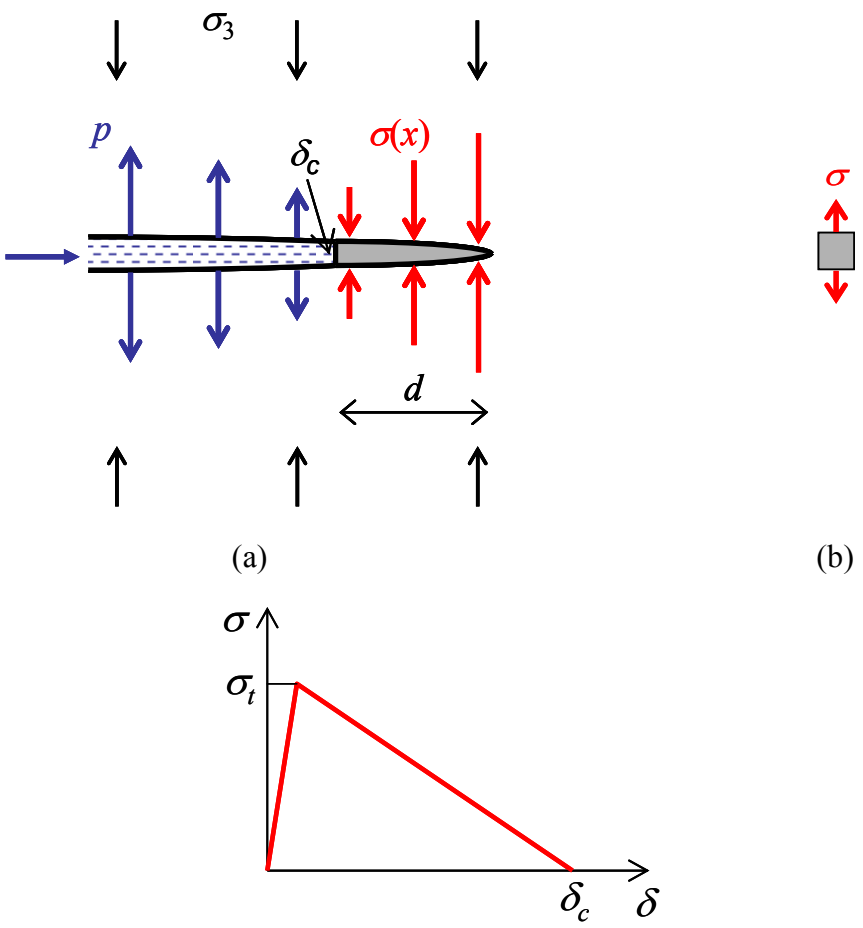

Figure 6.3 (a) Localized cohesive zone, (b) its representative element in a state of tension, and (c) a simplified stress-displacement relationship in a tensile test of a strain-softening material.

In practice, it is difficult to execute such a tensile test. However, δ_c can be calculated. In particular, if the linearly increasing section in Figure 6.3c is steep, it can be neglected. Then [e.g., *Papanastasiou*, 1997]

$$\delta_c = \frac{2K_{Ic}{}^2\left(1-\nu^2\right)}{E\sigma_t} \tag{6.5}$$

where K_{Ic} and σ_t are material properties obtained from independent experiments.

With this approach, the fluid pressure p can be obtained from the fluid flow equation

inside the fracture and elastic relations for the host material. The fracture is visualized as a flexible conduit, although, according to (6.2), its width δ_c always remains constant at its end and the pressure is zero in this location. While highly oversimplified [e.g., *Detournay*, 2004], this scenario illustrates modeling of hydraulic fracturing.

6.2 Cohesionless Particulate Materials

The goal of this work is to study cohesionless particulate materials. However, we recognize that ideally cohesionless materials (i.e., with a true absence of cohesion) are merely an extreme case and may not actually exist. A quantitative measure to determine whether a material can be considered effectively cohesionless (such as dry sand in Figure 6.1b) is desirable.

The physical nature of cohesion in particulate materials may be due to different reasons, including:

(i) cementation (as in some marine sediments);

(ii) partial saturation for materials with a considerable fraction of fine particles (e.g. clay); and

(iii) sintering processes (as in silica flour).

The threshold value of the Mohr-Coulomb cohesion, c, below which a particulate material behaves cohesionless (for all practical purposes), will be specified later in section 6.4.4. Until then we consider $c = 0$ and assume that the material possesses zero tensile strength. Below we argue that during hydraulic fracturing in soft sediments the stresses are compressive everywhere (at lease, in most cased considered in this work).

Therefore, if tensile stresses do not ever appear, the assumption of zero tensile strength in merely used for convenience and will not affect our conclusions.

As opposed to fracturing in cohesive solids, cohesionless particulate materials are already "fractured". Hence, no material bonds are broken and, accordingly, no new surfaces are created at the grain/particle (i.e., micro) scale. Furthermore, all material parts are in compression (e.g., since the material cannot bear any tension) and no fracturing process per se is involved. Rather, the liquid flow is localized in thin propagating crack-like conduits. By analogy, we call them "cracks" or "hydraulic fractures". The walls of these conduits are well defined at the macroscale. While these "fractures" resemble displacement discontinuities typical for cracks in solids, the conventional fracture mechanics principles cannot be applied directly without modification.

As an example, consider the Dugdale-Barenblatt model applied to the case of fracture in cohesionless particular materials (Figure 6.4). As in the case of fracture in solids (e.g., section 6.1), this model is appealing due to its simplicity and since all expressions can be derived in the closed form. Similar to the case of cohesive materials (Figure 6.2), the remote part of the material is in ambient compression, σ_3. The material adjacent to the fracture sides is assumed to be elastic (e.g., the corresponding plastic layer is small compared to the fracture size). Then, the fluid pressure tends to open the fracture and, as shown below, the stress $\sigma_{yy}(x, 0)$ reduces towards the fracture tip (solid curve in Figure 6.4). However, in the fracture process zone (shown in grey), material is in compression as well. Therefore, the stress in the vicinity of the fracture tip deviates from the elastic stress (dashed curve in Figure 6.4) and is less than the ambient value, σ_3. Fracture growth (i.e., the separation of the two fracture surfaces) occurs because the fluid is forced to flow into

the unloaded (relative to σ_3) material (although the details are left unspecified in this model; see below).

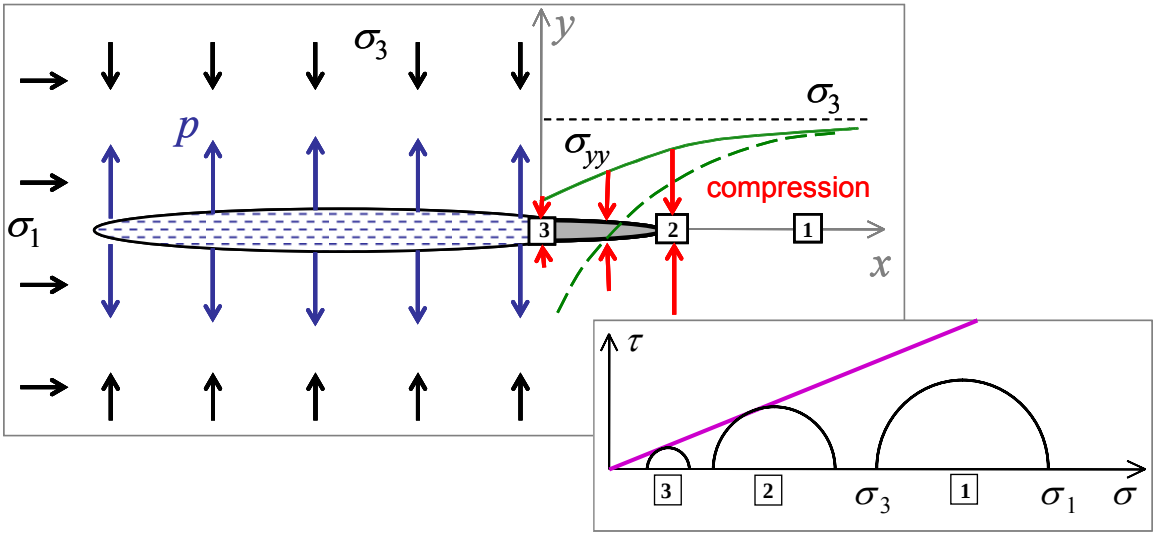

Figure 6.4 Stress distribution at fracture tip in cohesionless material with zero tensile strength, $\sigma_t = 0$. In the shown case, the stress near the fracture tip is less than the ambient value. The Mohr-Coulomb diagram illustrates that yielding near the fracture front occurs as a result of unloading of the material.

As in the Dugdale-Barenblatt model, a localized linear process zone is assumed to exist at the fracture tip. In our case, however, we also made the following assumptions for the fracture process:

- compressive state of stress everywhere in the material including the vicinity of the fracture tip;
- material is yielding in the process zone as a result of the stress decrease near the fracture tip (Figure 6.5a);
- material yielding can be described by the simplest Mohr-Coulomb yielding criterion, $\tau_f = \sigma_N \tan\phi$ ($\sigma_N > 0$), i.e., at failure

$$\sigma_{\min} = \kappa\sigma_{\max}, \qquad \kappa = \frac{1-\sin\phi}{1+\sin\phi} < 1 \tag{6.6}$$

where τ_f is the shear strength of the material, σ_N is the applied normal stress, ϕ is the angle of internal friction, and σ_{max} and σ_{min} are the maximum and minimum principal stresses, respectively;

- the fracture opening (i.e., thickness) in the process zone is significantly greater than the internal, micro-mechanical scales that are characteristic of yielding processes (e.g., grain scale, arching scale, or small-scale shear band spacing); and
- after the fracture tip passes through, the layer of yielded material adjacent to the fracture sides is thin relative to the fracture size, and does not have to be considered in the fracturing process.

Consider a fracture with a length of a, pressure distribution $p(x)$ (Figure 6.5a) and the length d of the process zone at the fracture tip. The boundary conditions on the two fracture surfaces can be written as

$$\sigma_{yy}(x, \pm 0) = p(x) \qquad (x \in \text{crack}) \tag{6.7}$$

In the remote stress field (Figure 6.5), σ_{xx} and σ_{yy} are equal to σ_1 and σ_3, respectively.

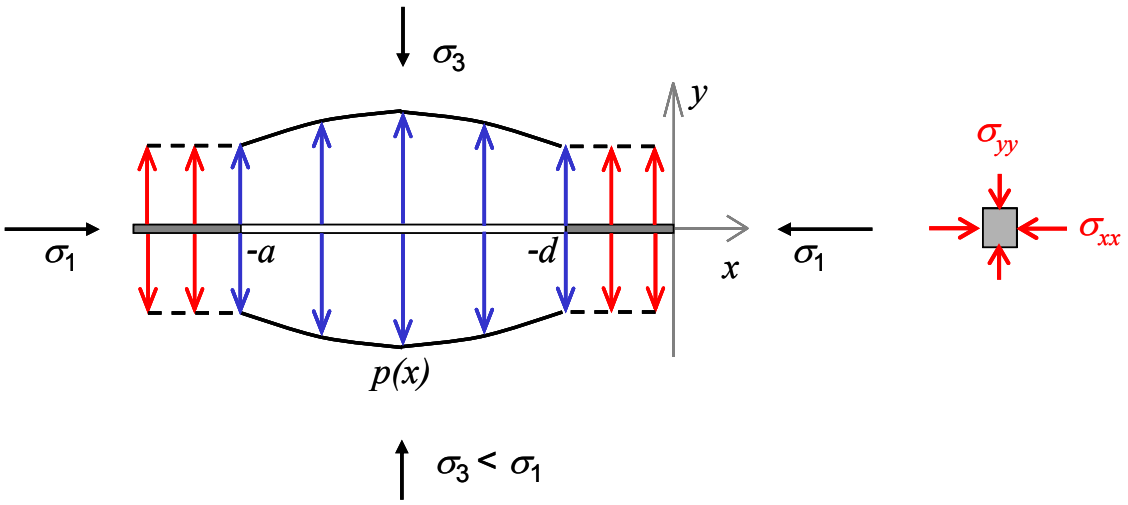

Figure 6.5 (a) Dugdale-Barenblatt model applied to cohesionless material, and (b) a representative element in the process zone in a state of compression.

To complete the formulation of the boundary value problems, we further note that according to (6.6), in the process zone

$$\sigma_{yy} = \begin{cases} \kappa\sigma_{xx} & \text{if} \quad \sigma_{yy} < \sigma_{xx} \\ \dfrac{1}{\kappa}\sigma_{xx} & \text{if} \quad \sigma_{yy} < \sigma_{xx} \end{cases} \qquad (x \in \text{process zones}) \tag{6.8}$$

As in cohesive material (see (6.4)), there is no stress singularity at the tip of the process zone:

$$K_I = 0 \tag{6.9}$$

Due to the symmetry of the problem about the x-axis,

$$\tau_{xy} = 0 \qquad (-\infty < x < +\infty, \quad y = 0) \tag{6.10}$$

and the x-displacement is continuous along the x-axis, while the y-displacement is continuous outside of the fracture, i.e.,

$$\begin{cases} u(x,+0)-u(x,-0)=0 & (-\infty < x < +\infty) \\ v(x,+0)-v(x,-0)=0 & (x<-a-d \ \ and \ \ x>0) \end{cases} \tag{6.11}$$

The solution of this problem is given by *Wu* [2005]. In the process zone, stresses

$$\sigma_{xx}(x)=\frac{1}{1-\kappa}(\sigma_1-\sigma_3), \qquad \sigma_{yy}(x)=\frac{\kappa}{1-\kappa}(\sigma_1-\sigma_3) \tag{6.12}$$

are constant, and as long as $\sigma_3 < \sigma_1$, only the first condition in (6.8) is possible. Therefore, the stresses ahead of the fracture tip are indeed reduced compared to those at infinity which justifies the assumption that was made above (Figure 6.4).

In the case of small scale yielding (i.e., $d << a$), the size of the process zone is given by

$$d=\frac{\pi}{8}\frac{(K_I^{\ elastic})^2}{{\sigma_0}^2} \qquad (d << a) \tag{6.13}$$

where

$$\sigma_0=\left|\frac{\kappa(\sigma_1-\sigma_3)}{1-\kappa}-\sigma_3\right| \tag{6.14}$$

and $K_I^{elastic}$ is the "elastic" stress intensity factor obtained from taking into account only the pressure $p(x)$ inside the fracture (i.e., considering $\sigma_{yy} = 0$ in the process zone). The fracture width at the beginning of the process zone is

$$\delta_c=\frac{(K_I^{\ elastic})^2(1-\nu^2)}{E\sigma_0} \qquad (d << a) \tag{6.15}$$

It appears from (6.12) that the stresses inside the process zone are not only uniform but also independent of the fluid pressure. They are determined only by the remote stresses and the friction angle of the material (see (6.12) and (6.6)). Therefore, the stresses inside the process zone are fully defined. According to (6.13), the length of the

process zone d is a function of the remote stresses, material properties (e.g., friction angle), fracture dimension, and fluid pressure.

The condition for fluid pressure at the end of the process zone can now be expressed as

$$p(-d) = \sigma_{yy}(-d, 0) = \frac{\kappa}{1-\kappa}(\sigma_1 - \sigma_3) \tag{6.16}$$

and, similar to the case of cohesive materials, the fluid pressure distribution $p(x)$ can be calculated from fluid flow equations inside the fracture and elastic theory outside.

However, now the value of δ_c cannot be determined (even in principle) from independent experimental measurements. The only available approach is to use controlled experimental results from hydraulic fracturing (e.g., our results) to calibrate K_{Ic} based on the considered model (see the next section). Then, the idea would be to employ K_{Ic} with criterion (6.3) of fracture growth.

It is important to emphasize that while this simple model yields a convenient approach for modeling fracture propagation in cohesionless materials, it suffers from serious deficiencies, including:

- The physical nature of the thin, localized process zone appearing in compression is not clear. Moreover, whether this process zone actually exists has not yet been determined.

- This model does not address the mechanism of localized fluid in-flow in cohesionless materials (which is simply postulated based on conditions (6.3) and (6.16)). In other words, it remains unclear how the fluid is forced into the

particulate material that is under compressive stresses everywhere.

6.3 Apparent Fracture Toughness

In conventional fracture mechanics for solid materials, the fracture toughness is directly related to the energy that is required to open a new surface and propagate a fracture. This energy is needed to overcome the tensile strength of the cohesive material.

Similarly, the term "fracture toughness" is used here for cohesionless materials to refer to the energy that is required to create a new surface. However, this energy originates from different sources compared to those in solid materials. Cohesionless material is already fractured at the scale of individual particles. Hence, no energy is required to separate the particles from each other. Rather, at the fracture scale, the energy is needed to overcome the shear (yielding) strength of the material due to the compressive stress state. Therefore, we use the concept of the *apparent* fracture toughness that would correspond to this energy in elastic material. We further omit the term "apparent" when this is not confusing.

In this section, the apparent fracture toughness K_{Ic} is determined for the studied particulate materials. While it is the basis of the conventional approach, employing this K_{Ic} for the analysis of hydraulic fracturing in cohesionless media may not be legitimate and requires a great deal of caution (see the previous section). Yet, the obtained values of K_{Ic} for cohesionless materials provide an interesting basis for comparison with solid materials.

6.3.1 Constrained Lateral Boundaries

For constrained lateral boundaries, the calculation is conducted via numerical simulations with the finite element code FRANC2D [*Wawrzynek and Ingraffea*, 1987]. The two-dimensional, plane strain model, shown in Figure 6.6, simulates a thin fracture with a length of $2a$ in the center of a circular elastic disk with a radius of R and a fixed boundary.

A uniform internal pressure p is applied to the fracture surface. The stress intensity factor is calculated for various fracture lengths. The results are presented in Figure 6.7 in dimensionless form, convenient for computing K_I for specific values of R, a, and p.

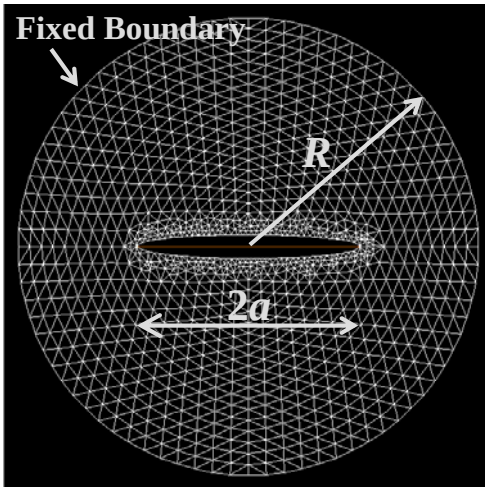

Figure 6.6 FRANC2D finite element model of a pressurized fracture in a circular disk.

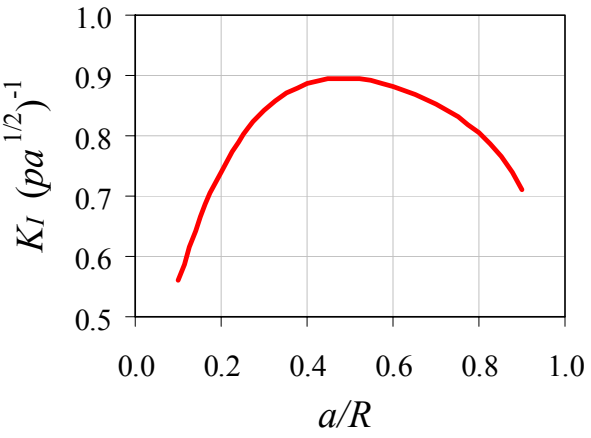

Figure 6.7 Dimensionless relationship between the stress intensity factor K_I and fracture half-length a.

To calculate the fracture toughness for each observed fracture, the values of R and the material properties are taken directly from the laboratory experiments at the final state of propagating fractures. The half-length of the fracture a is taken as the average width of the fracture wings. The fluid pressure inside the fracture is assumed to be uniform. The value of the pressure p is taken for the point in time when the pump was stopped and is calibrated for the pressure drop of the injection system (Appendix C). This pressure p is taken as an approximation of the fluid pressure inside the fracture. Since the pressure is measured during fracture propagation, the calculated stress intensity factor is considered to be an estimate of the apparent fracture toughness K_{Ic}.

The obtained K_{Ic} for representative fractures is summarized in Figure 6.8. The photographs of the corresponding fractures are shown in Figure 6.9.

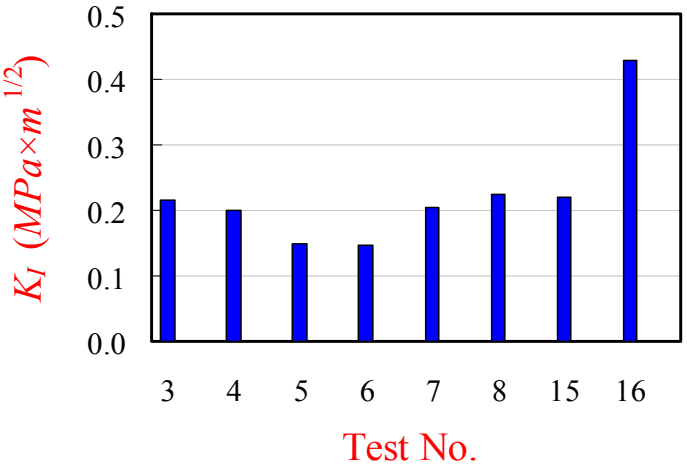

Figure 6.8 Apparent fracture toughness (experiments with a constrained lateral boundary).

Test#	**3**	**4**	**5**	**6**
				
Test#	**7**	**8**	**15**	**16**
				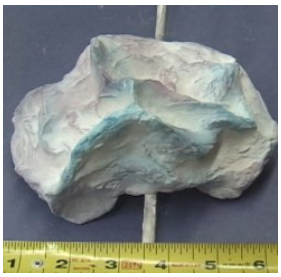

Figure 6.9 Hydraulic fractures used for estimation of the apparent fracture toughness (Figure 6.8) (experiments with a constrained lateral boundary).

6.3.2 Pressure-controlled Lateral Boundaries

For pressure-controlled lateral boundaries, the fracture toughness is approximated based on the analytical solution by *Yarema* [1979] for a thin fracture with a length of $2a$ in the center of a circular elastic disk with a radius of R (Figure 6.10). A normal pressure p is applied to the boundary of the disk, which is in the plane strain condition. Similar to the previous section, the values of R, p and a are taken from the laboratory experiments. The calculated K_{Ic} for representative fracture samples is given in Figure 6.11. The photographs of the corresponding fractures are shown in Figure 6.12 (information about test P7 is summarized in Appendix E).

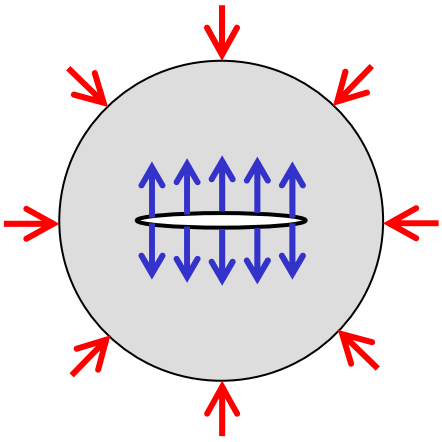

Figure 6.10 A pressurized fracture in a circular disk with a pressure-controlled lateral boundary.

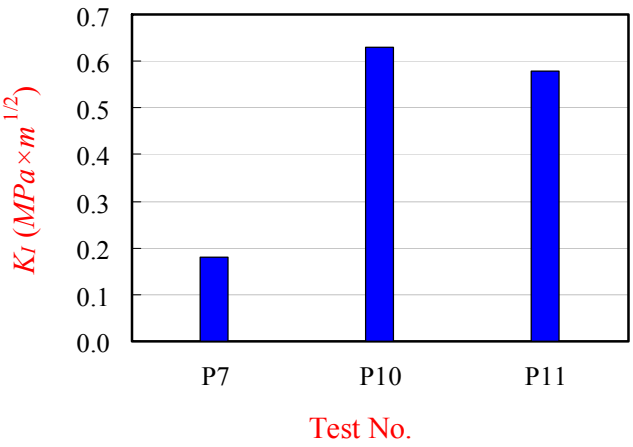

Figure 6.11 Apparent fracture toughness (experiments with a pressure-controlled lateral boundary).

Test#	P7	P10	P11
			

Figure 6.12 Hydraulic fractures used for estimation of the apparent fracture toughness (experiments with a pressure-controlled lateral boundary).

The estimated values of the fracture toughness of silica flour for both lateral boundary conditions are of the same order of magnitude (Figures 6.9 and 6.11). They range from 0.2 to 0.6 $MPa \times m^{1/2}$, and appear to be only slightly less than those of rock [e.g., *Bertram and Kalthoff*, 2003]. Unfortunately, the usefulness of this peculiar result is obviously limited by the lack of a physical basis for the apparent fracture toughness of cohesionless materials (we are not concerned with such trivial cases as hydraulic fracturing by fluid injection between two half spaces that are pressed together).

6.4 Observed Physical Processes

As can be seen from the discussion in the previous sections, even when a consistent model can be formulated and all the required parameters can be determined, it still may not be trustworthy if the key physical mechanisms remain unclear. Consequently, our next step is to explicitly use the experimental results as the basis for the modeling.

6.4.1 Fracturing Stages

The main conclusion of our experimental work is that hydraulic fracturing in particulate materials is not only possible, but even probable. The observed fracture geometries and the measured injection pressures suggest that hydraulic fracturing occurs in the following sequence:

(i) cavity expansion (e.g., Figures 6.13a and 6.16a) before the injection pressure reaches its peak (e.g., Figure 6.16b);

(ii) fracture front initiation from this cavity near the pressure peak (e.g., Figure 6.13a); and

(iii) growth of the developed fracture (e.g., Figures 6.13b and 6.16a) after the peak pressure (e.g., Figures 6.14 and 6.16b).

In essence, stages (*i*) and (*ii*) together constitute the fracture initiation process, while stage (*iii*) is the subsequent process of fracture propagation.

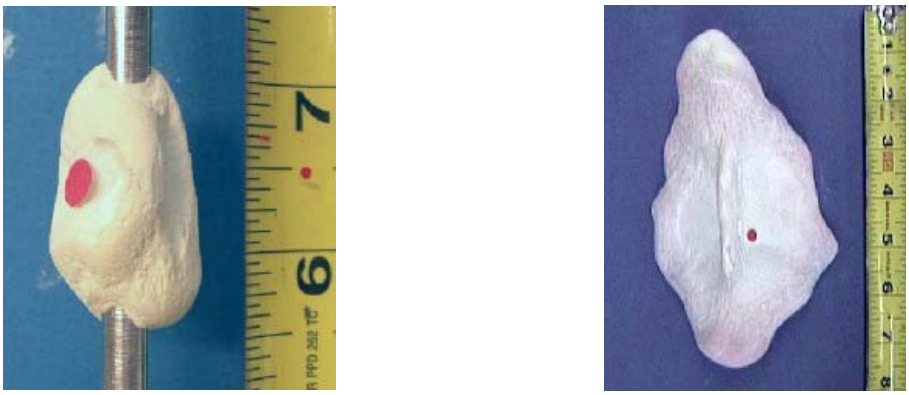

(a) (b)

Figure 6.13 Two hydraulic fractures with different injection volumes (a) 10 *ml* and (b) 200 *ml* (tests 10 and 8, respectively; see Table 5.9). The small wing-like vertical feature in (a) (that has a volume of approximately 3 *ml*) indicates the stage of fracture initiation from the expanding cavity (see also Figure 5.10a where this wing is shown from a different direction and Figure 5.10b where the stage of fracture initiation has probably been completed).

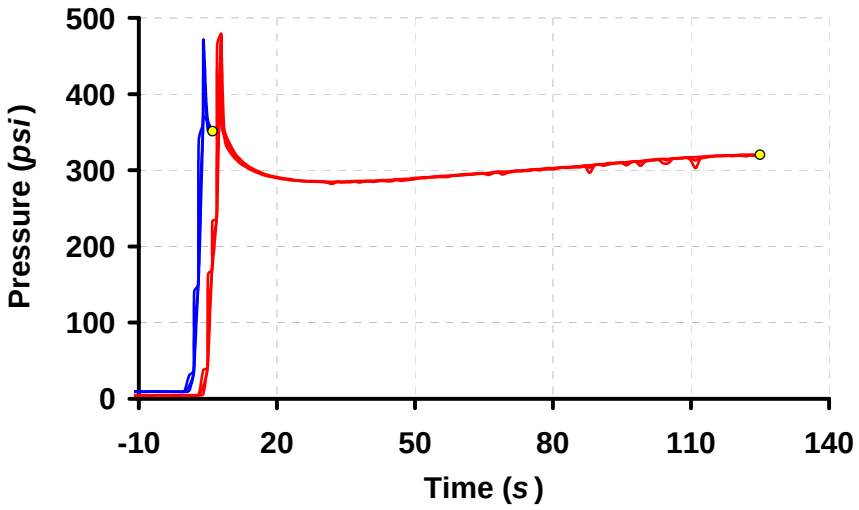

Figure 6.14 Injection pressure curves for hydraulic fractures shown in Figure 6.13. The shorter line on the left refers to Figure 6.13a, and longer line on the right to Figure 6.13b. The circles indicate the end of the experiments.

6.4.2 Fracture Initiation

As mentioned above, the fracture initiation process begins as cavity expansion in the

material surrounding the injection source. The fact that cavity expansion is indeed observed suggests that at the initial stage (*i*) a relatively large plastic zone is formed in the particulate material (Figure 6.15) before the pressure reaches its peak. Accordingly, the new volume that is created for the injected fluid is primarily due to the deformation of the undisturbed material outside of the plastic zone (for contracting materials, their inherent contraction may also contribute to this volume).

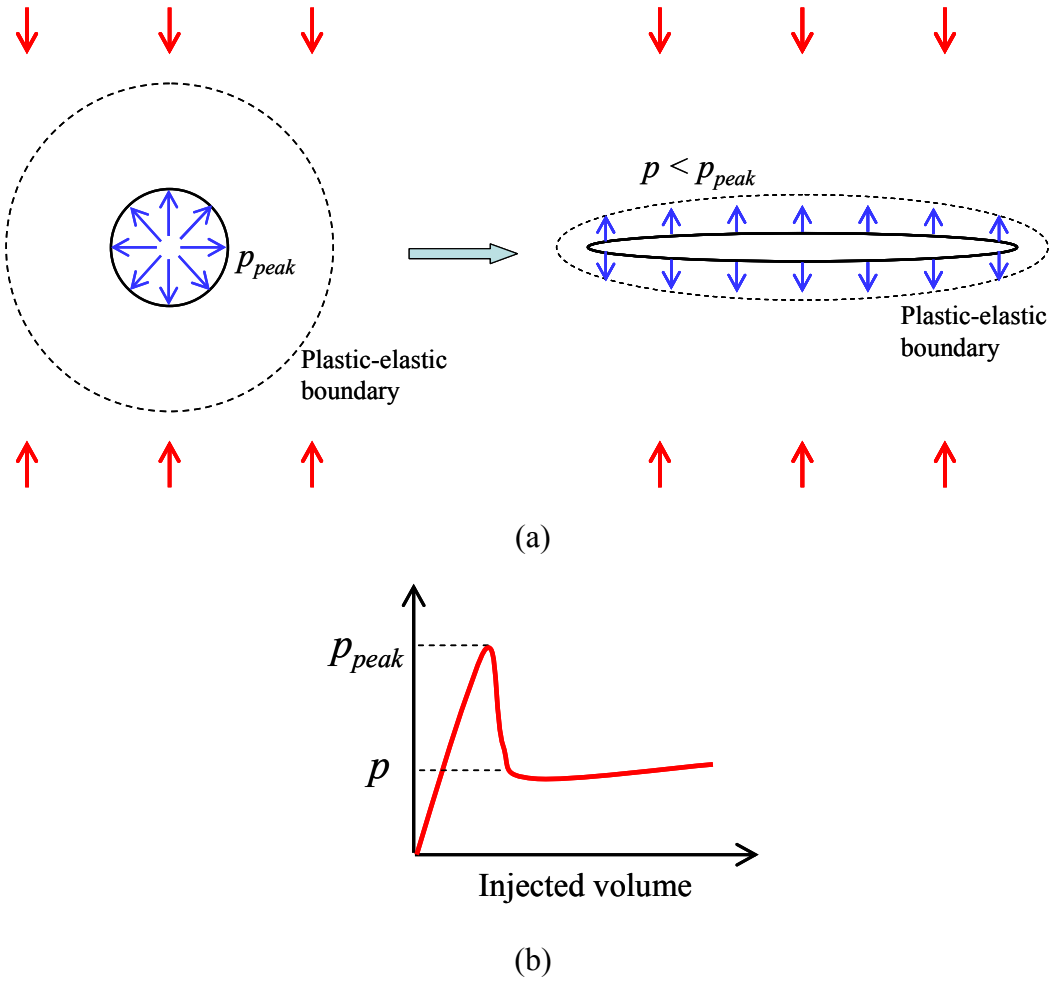

Figure 6.15 (a) Transition between the cavity expansion and the advanced stage of fracture growth, and (b) the corresponding decrease of the injection pressure. Here, p_{peak} is the peak pressure at the final stage of the initial cavity expansion, and p is the pressure at the end of the fracture initiation stage.

Probably, a small-scale boundary instability of the initial cavity expansion results in the initiation of the fracture front at stage (*ii*) of the fracture evolution. The exact mechanism of this instability is not clear at this point in time. However, before detailed modeling is conducted, the physical nature of this instability may perhaps be attributed to phenomena such as: large-scale shear banding that abruptly deforms the cavity shape (Figure 6.16); liquefaction-like effects induced by the inflation of the pressurized fluid into the dry material (Figure 6.17a); or off-shoots from the main cavity, also driven by the cavity expansion mechanism but at a smaller dimension and smaller pressure (Figure 6.17b).

There could be other possible phenomena that trigger fracture initiation. However, further study supported with experimental and theoretical analysis is required to identify the actual physical mechanisms. Here we only note that the shear band concept is consistent with the experimental observations by *Alsiny et al.* [1992] (Figures 1.19a and 1.20) and by *de Pater* [2003] (Figure 6.16b; see also Figure 1.19b) of a deformation around a borehole during hydraulic fracturing in soft sediments. It is also supported by *Kim*'s [2005] numerical calculations, who considered the cavity expansion problem in strain-softening material (Figure 6.18). He observed the formation of shear bands (Figures 6.19a and 6.19c) and the shearing of the borehole boundary (Figures 6.19b and 6.19d). This resembles the observations by *Alsiny et al.* [1992] and *de Pater* [2003] surprisingly well. Both in the experiments (Figures 1.19a, 1.20, 1.19b, and 6.16b) and in the simulation (Figure 6.19), the shear displacement at the hole boundary along the shear bands is clearly visible.

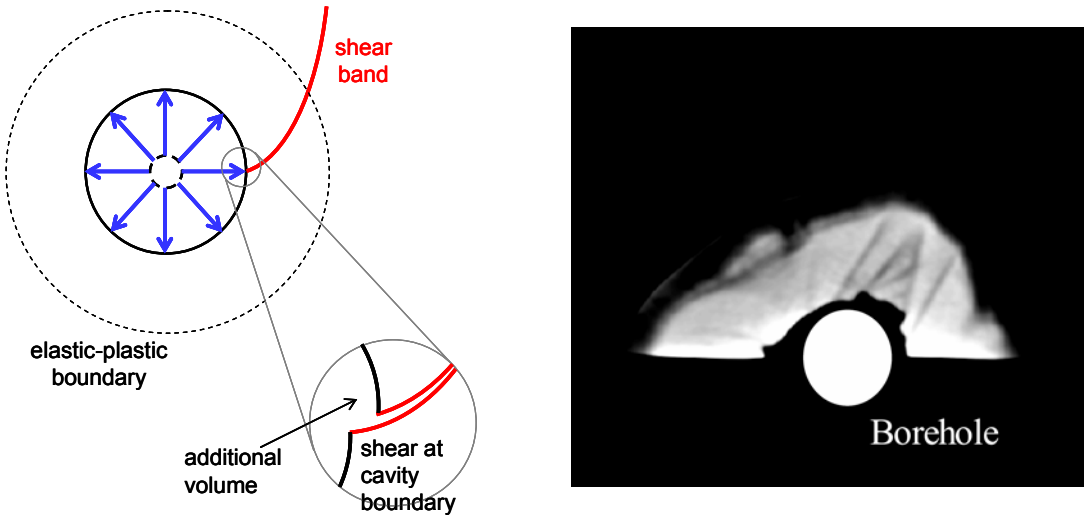

(a) (b)

Figure 6.16 (a) Mechanism of fracture initiation by a shear band induced at the boundary of the expanding cavity, and (b) CT scan of a cross-section of a hydraulically pressurized borehole [*de Pater et al.,* 2003].

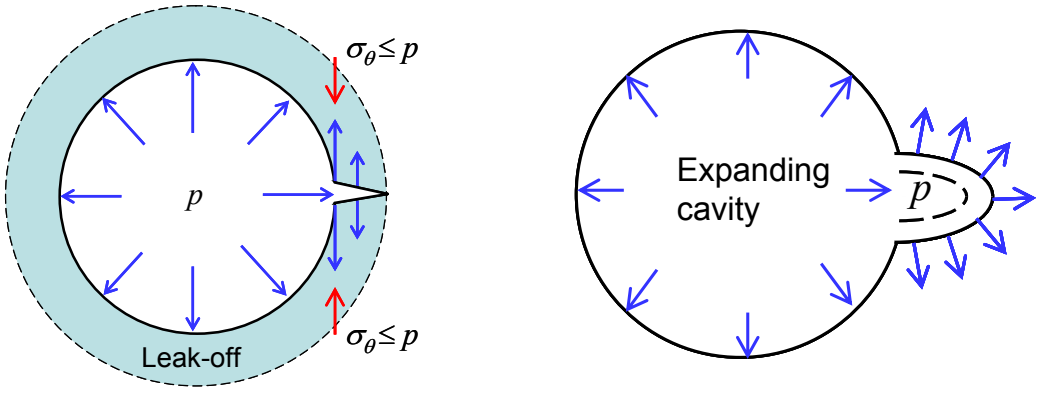

(a) (b)

Figure 6.17 Hypothesized mechanisms of fracture initiation. From the expanding cavity during the pressure build-up stage (Figure 6.15a). (a) Decrease of the effective stress to zero as a result of the fluid leak-off into the material surrounding the expanding cavity. Here, p is the injection pressure inside the cavity, and σ_θ is the total circumferential stress. (b) A small cavity originating from the expanding cavity. This may occur if the pressure that is required for the expansion of the small cavity in the stress-strain field of the large cavity is less than the current pressure in the large cavity (leading to the pressure drop after the peak; see Figure 6.15b.)

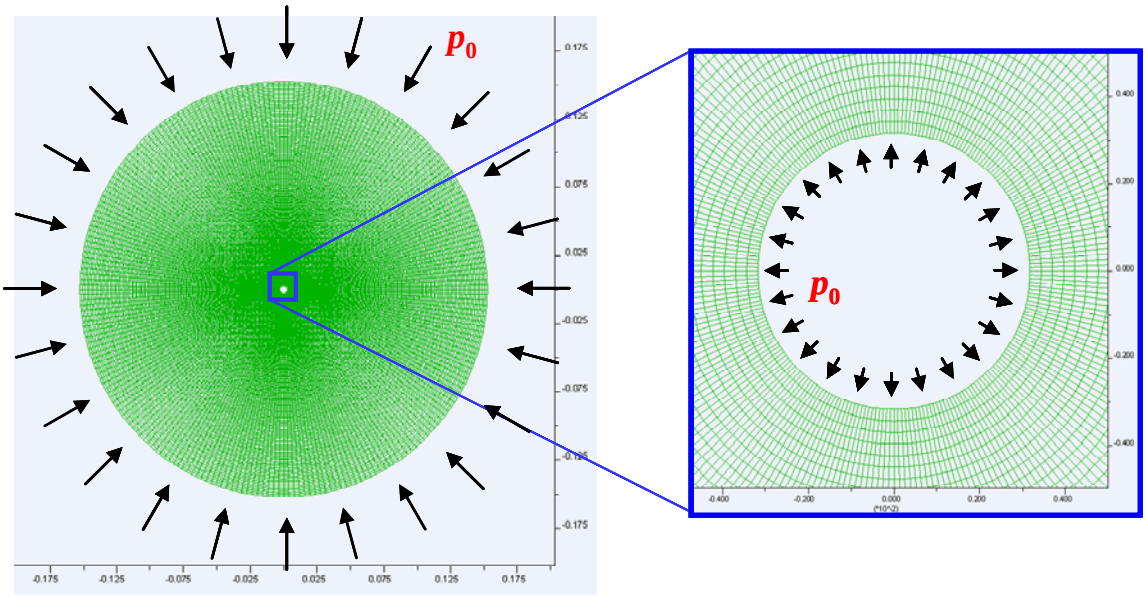

Figure 6.18 FLAC model of cavity expansion in strain-softening material. (a) Overview of the grid and (b) magnified part of the grid in the vicinity of the circular cavity. In the simulations, the shear modulus $G = 10$ *MPa*, Poisson's ratio $\nu = 0.3$, the peak friction angle $\varphi = 39°$ decreasing linearly to 20° in softening, the peak dilation angle $\psi = 7°$ reducing linearly to 0° as a result of softening (a bi-linear model without an ascent and with residual values attained at the plastic strain of 1% was used). These parameters resemble properties obtained for our experimental materials (see section 2.5). The external and internal radii of the hollow cylinder are 3.175 *mm* and 152.4 *mm*, respectively (which is similar to the small-scale experimental setup; see Chapter 3). The outer confining pressure $p_0 = 10$ *psi* (69 *kPa*) is constant, while the internal pressure increases from this value to 49.5 *psi* (341 *kPa*) with increments of 0.5 *psi* (3.45 *kPa*). The simulation results for this moment are shown in Figure 6.19.

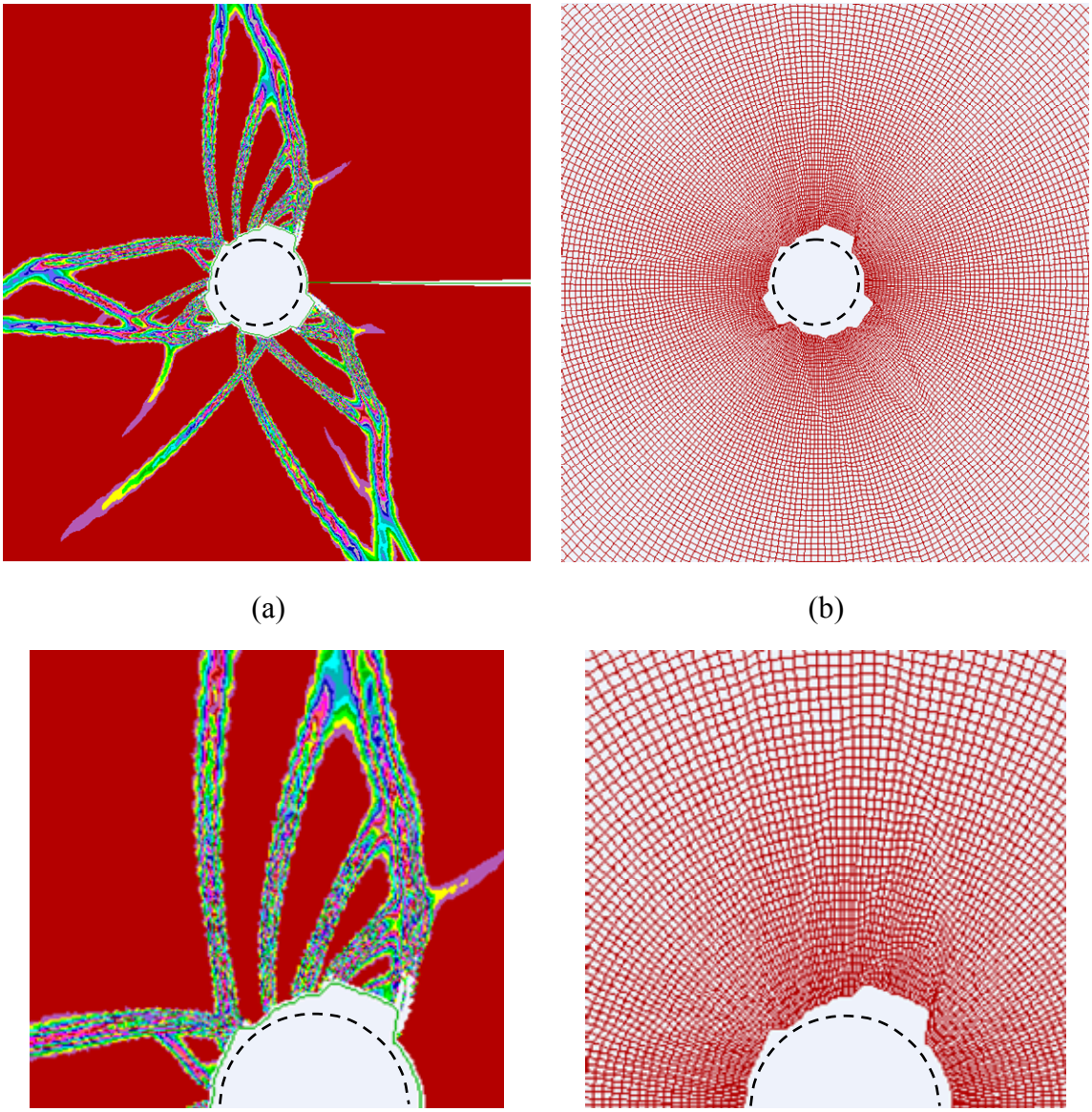

Figure 6.19 Cavity expansion in strain-softening material simulated with the FLAC model shown in Figure 6.18: (a), (c) shear strain increments and (b), (d) the corresponding deformed mesh; (c) and (d) are the magnified views of (a) and (b), respectively. Shear strain increments represent the developed shear bands. The shear displacements along the bands are clearly seen from the deformed mesh. The mesh consists of 192 radial by 240 tangential elements. The internal pressure is 49.5 *psi* (341 *kPa*). The dashed circle shows the original location of the expanding cavity.

6.4.3 Fracture Propagation

In any case, the initial cavity is almost never preserved (and hence not observed) at the developed stage (*iii*) of the fracture propagation (e.g., Figure 6.13b). This implies that the plastic deformation of the particulate material that surrounds the initial cavity could be an important process that results in the flattening of the cavity by "squeezing" the fracturing fluid into a thin conduit (Figure 6.15a). Similar to hydraulic fractures in cohesive materials, this flat shape is beneficial for creating a space for the injected volume by elastic opening of such thin cavities. In other words, generally, a lower pressure is required to create a new volume by opening thin fissures than compared to pressurizing bubble-like cavities (Figure 6.20). Although the details need to be resolved, this may be an indication of why the fairly thin shape has been always observed in our experiments at stage (*iii*) of the advanced fracture growth, and why the pressure is reduced after the pressure peak (e.g., Figures 6.14 and 6.15b). This may also imply that the size of the plastic zone around the well-developed fracture is not very large (Figure 6.15a). Finally, the "squeezing" mechanism is consistent with the thinning of the middle parts of some fractures (e.g., Figure 5.6c; see also Figure 6.22a)

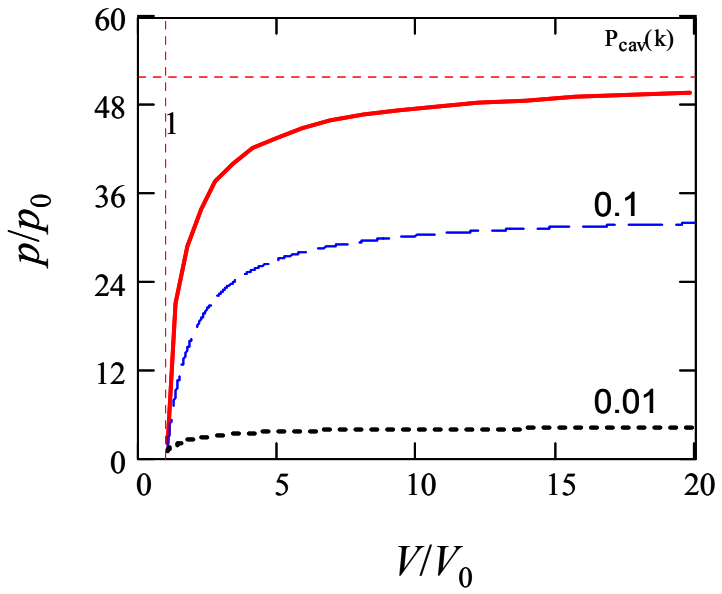

Figure 6.20 Normalized pressure versus normalized injection volume for a cavity (solid line), and an elastic crack (dashed lines for two indicated crack aspect ratios). The pressure curve for cavity expansion was plotted based on the model by *Yu and Houlsby* [1991]) for a spherical cavity in an infinite, ideally plastic Mohr-Coulomb material (the parameters are presented in the next section 6.6.1). The crack pressures were computed for a penny-shaped crack in an elastic medium (e.g., *Germanovich and Lowell*, 1995). Even for a not very thin (from an elastic perspective) cavity (with an aspect ratio 0.1), a considerably lower pressure is required to attain the same injection volume. With increasing remote stress p_0, this difference increases.

6.4.4 Cohesionless versus Cohesive Materials

Another important conclusion of this work is that all parts of cohesionless particulate materials are likely to be in compression. For the fracture initiation at the peak pressure (i.e., following the cavity expansion prior to the pressure peak), the maximum value of the cohesion that results in compressive stresses everywhere in the particulate material determines the transition from relatively cohesionless to cohesive materials (Figure 6.21). If the cohesion of the material is greater than the critical value, the material experiences tensile stresses and should possess some tensile strength to resist this tension. When the

cohesion of the material is less than the critical value (such as in our experiments; see Figure 6.21b), all material parts are in compression and no tensile strength is required. The compressive stress state is an important characteristic of hydraulic fracturing in particulate materials with low or no cohesion. Yet, even if cohesion is rather high, as long as it is below the threshold value (Figure 6.21a), the material can be considered to be effectively cohesionless (since it does not "sense" any tensile stress).

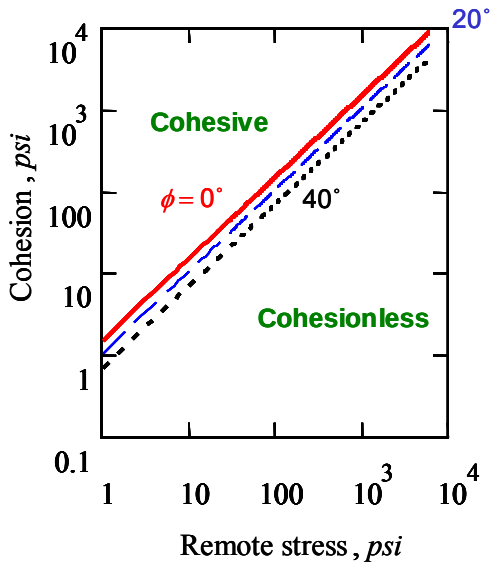

(a) (b)

Figure 6.21 (a) The critical cohesion versus the remote stress, based on the model by *Yu and Houlsby* [1991] for a spherical cavity in an infinite, ideally plastic Mohr-Coulomb material (the parameters are presented in section 6.6.1). Solid, dashed, and dotted lines correspond to friction angles of 0º, 20º, and 40º, respectively. If cohesion is higher than the critical value, the material experiences tensile stresses and should possess some tensile strength to hold this tension. For cohesion smaller than the critical value, all material parts are in compression, so that no tensile strength is required. (b) Free vertical walls and fissures that are commonly observed in oven-dried silica flour in both loose and dense states. The cohesion that is sufficient to maintain this fissure does not exceed ~0.1 *psi*.

6.5 Mechanisms of Fracture Propagation

As discussed in Chapter 3 and Chapter 5, different types of the observed fronts of fractures (Figure 6.22) indicate different underlying mechanisms of fracture propagation in cohesionless particulate materials. In this section we suggest three possible mechanisms that are in agreement with our observations (e.g., Figure 6.22). These are "pile driving" or cavity expansion, shear banding, and induced cohesion, which appear to be consistent with round, beveled, and fingered fracture fronts (Figure 6.22), respectively. These mechanisms are probably not exclusive. The observation of fractures with both fingered and beveled fronts (e.g., Figures 5.1b and 5.1c), or with both beveled and round fronts (e.g., Figures 5.32a and 5.32b) indicates that multiple mechanisms may coexist during the fracturing process. Although further verification of these mechanisms is certainly required, the discussion in this section may provide a framework for more accurate experimental and theoretical modeling.

(a) (b) (c)

Figure 6.22 Different types of observed fracture fronts: (a) round (test 15 in Figure 5.10), (b) beveled (test 4 in Figure 3.6), and (c) fingered (test 8 in Figure 3.11).

6.5.1 "Pile Driving" or Cavity Expansion

For the round fracture fronts (e.g., Figure 6.22a), the corresponding physical mechanism of fracture propagation could be similar to the "sheet pile driving" in industrial applications (Figure 6.23). In this extreme case, the fracturing fluid is viewed as a sheet pile (or blade) that disjoints the host material (see the magnified view of the fracture tip in Figure 6.23). The plastic zone adjacent to the fracture (i.e., pile) may be relatively thin, compared to the fracture dimensions (Figures 6.15a and 6.23). Again, it is likely that at this stage of the fracture development, the elastic deformation of the host material primarily creates a new volume for the injected fluid (see Figure 6.20). Near the fracture front, the cavity expansion process is still important (Figure 6.23). In this region, the host material is displaced (i.e., "pushed") away from the advancing fracturing fluid. Accordingly, the pressure of the fracturing liquid near the fracture front is elevated (relative to the remote in-situ stresses), and so are the stresses near the front (Figure 6.23).

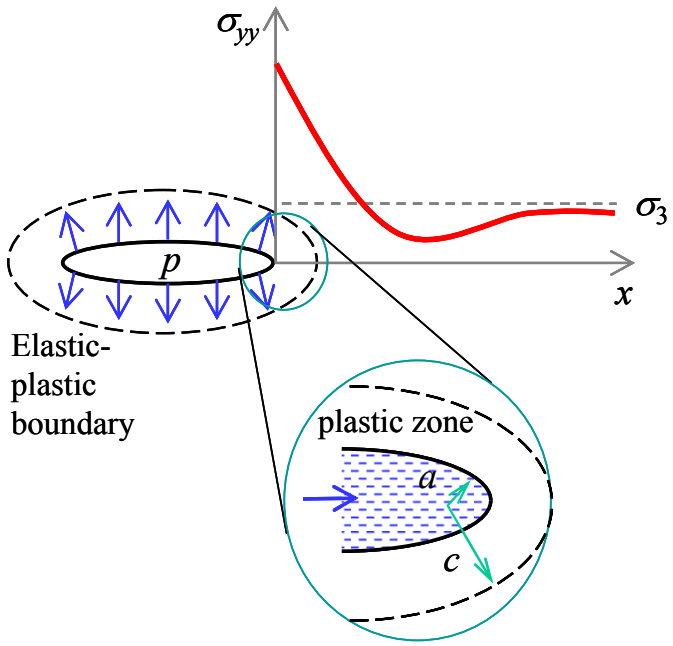

Figure 6.23 "Sheet pile driving" model of fracture propagation based on the cavity expansion mechanism at the fracture front. Here, p is the injection pressure inside the fracture, a is the radius of the fracture front, c is the radius of the plastic zone around the fracture front, σ_{yy} is the stress in the y-direction, and σ_3 is the minimum principal stress (remote stress). In the simplest case, a and c can be computed based on the cylindrical/spherical cavity expansion in the inifite medium (see section 6.6).

Another extreme case may correspond to a plastic zone that is large compared to the fracture dimensions (Figure 6.24). While a lower pressure is required in thin cavities with small and thin adjacent plastic regions (Figure 6.20), the existence of a large plastic zone cannot be ruled out at present (before the details of the transition (Figure 6.15a) between the initial and advanced stages of fracture growth are understood). The existence of such a large plastic region may also be consistent with an elongated oval fracture shape, round fracture front, and the plastic deformation of the particulate material that allows the inflow of the fracturing fluid into the material by the cavity expansion mechanism. That would likely be the case if the pressure of the expansion of the elliptical cavity were smaller than that for a circular cavity (see also section 6.4.3).

A quantitative example of the "pile driving" (cavity expansion) model will be given in section 6.6.

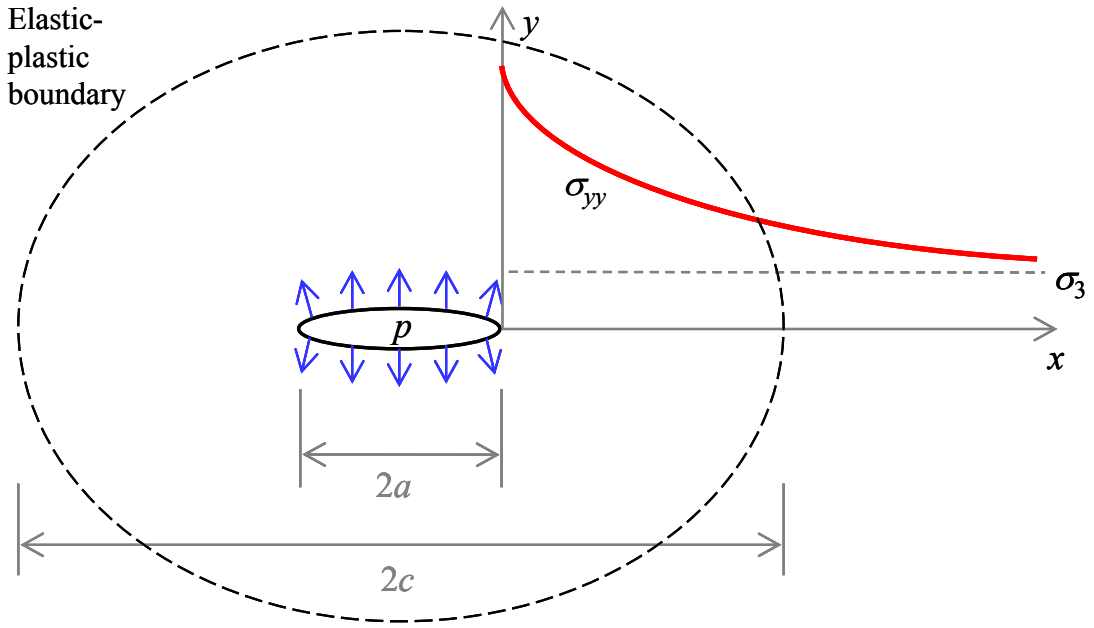

Figure 6.24 Advanced stage of fracture propagation with a large plastic zone compared to the fracture size ($c >> a$). Here, p is the injection pressure inside the fracture, a is the half-length of the fracture, c is the size of the plastic zone, σ_{yy} is the stress in the y-direction, and σ_3 is the minimum principle remote stress.

6.5.2 Shear Banding

The observed beveled fracture front (e.g., Figure 6.22b) consists of a distinct flat plane that is inclined with respect to the direction of fracture propagation. This geometry seems to be consistent with both an elevated or reduced pressure at the fracture tip (i.e., less or greater than the remote confining stresses). In this case, the host material adjacent to the fracture front may yield not only because of the increased stresses near the fracture tip, but also due to the considerably decreased stresses (i.e., smaller than the remote loads). In

strain-softening materials (as were used in our experiments), both elevated and reduced stresses may have resulted in the localized shear bands that are inclined with respect to the fracture direction (Figure 6.25). The discontinuity of the shear displacements between the opposing sides of a shear band can also generate a fracture aperture (i.e., an opening normal to the fracture plane) that provides the necessary volume for the fluid inflow (Figure 6.25). Therefore, contrary to the cavity expansion model, in this scenario, the fracture can propagate also due to the *decrease* of the stresses from the remote in-situ values to a smaller magnitude near the fracture front.

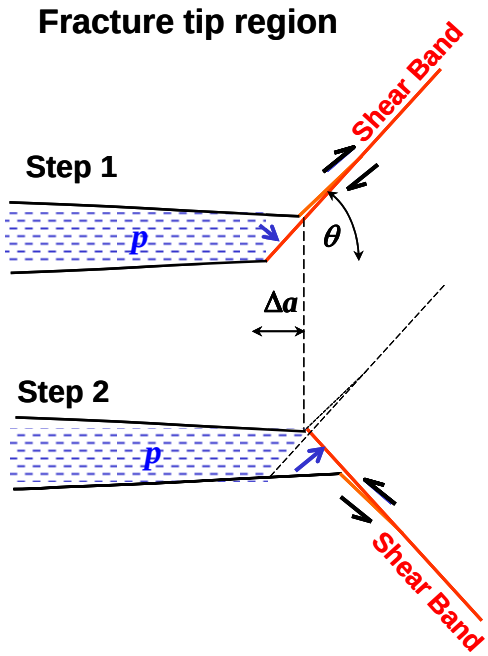

Figure 6.25 Shear band model. Here, p is the injection pressure inside the fracture, θ is the angle of the shear band with respect to the fracturing direction, and Δa is the incremental advance of the fracture in the fracturing direction.

The shear band hypothesis is consistent with the results of numerical simulations by *Wu* [2005]. She studied a thin fracture inside a rectangular body that is pressurized by the internal fluid pressure. Her formulation is somewhat similar to the finite element

modeling conducted by *Papanastasiou* [1997], although she was simulating shear bands in a strain-softening material.

Figure 6.26a shows a FLAC grid fragment near the fracture (that is modeled by a thin slot) in a strain-softening material. Because of the symmetry about the *y*-axis, only one half of the fracture was simulated. The full dimensions of the rectangular body that contains the half-fracture are 70 *cm* wide by 60 *cm* high. The half-fracture has a length of 4.8 *cm* and a width of 0.48 *cm*. The fracture aspect ratio (i.e., aperture / half-length) is 0.1. The grid used for this simulation was 120 units wide by 141 units high. The mesh in the vicinity of the fracture front is denser than that of the surrounding area. The fracture thickness is 3 elements allowing sufficient resolution at the fracture tip. The material properties used in the FLAC analysis are given in the caption to Figure 6.18 (except that the values of ϕ and ψ should be replaced by 40° to 35° and 5° to 0°, respectively). The applied remote stresses are σ_{xx} = 0.552 *MPa* and σ_{yy} = 0.276 *MPa*. The internal fracture pressure has a uniform distribution along the fracture length, which increases from p_0 = σ_{yy} = 0.276 *MPa* with an increment of Δp = 0.0138 *MPa* for each loading step.

The plastic zone and the contour of the maximum shear strain increment are given in Figures 6.26b and 6.26c, and correspond to the internal fracture pressure p = 0.59 *MPa*. As can be seen, the developed plastic zone has two localized bands that are inclined with respect to the fracture plane in agreement with the shear band model hypothesized in Figure 6.25. Therefore, while the shear band appearance is currently rather difficult to detect in physical experiments, they manifested themselves quite noticeably in numerical experiments, as describe above.

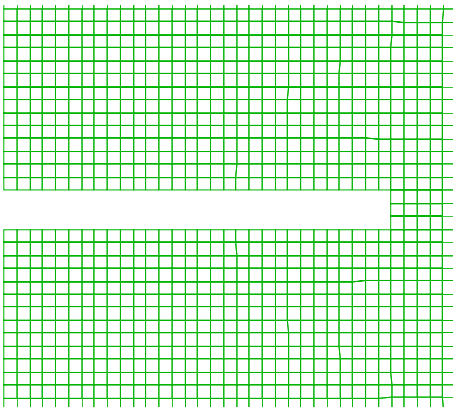

(a)

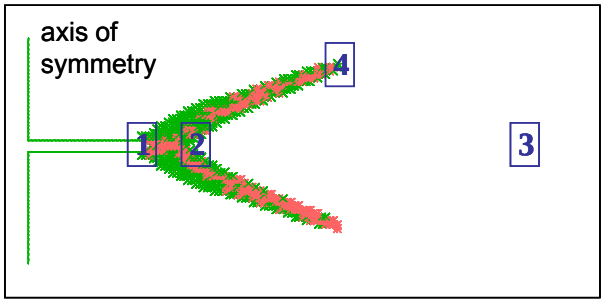

(b)

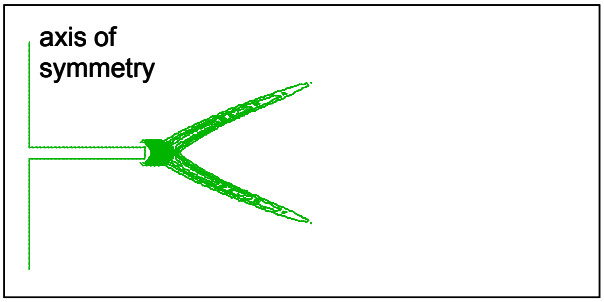

(c)

Figure 6.26 (a) A FLAC grid fragment in the vicinity of the fracture front, (b) plastic zone (red color; green color shows elements that are currently elastic, but were plastic in the past), and (3) contour of maximum shear strain increment. See text and Figure 6.27 for elements 1, 2, 3, and 4.

The distributions of the stresses σ_{xx} and σ_{yy} ahead of the fracture tip at this stage are plotted in Figure 6.27a. In the vicinity of the right boundary, σ_{xx} is equal to the applied boundary pressure. Closer towards the fracture, both σ_{xx} and σ_{yy} first decrease

(compressive stress is positive), and then increase near the fracture tip (in the process zone). The decrease of the stress from element 3 to 2 can be attributed to the elastic strain far from the fracture tip. At the fracture tip (i.e., at the end of the process zone), σ_{xx} is equal to the applied pressure.

The Mohr circles for all three elements as well as for element 4 (Figure 6.26b) are plotted in a σ_N - τ space in Figure 6.27b. The schematic location of the elements 1, 2, and 3 can also be seen in Figure 6.27a. For elements 1 and 2 in the plastic zone, the material yield corresponds to the residual friction angle (i.e., in Figure 6.27b the Mohr circles touch the failure envelopes for $\phi = 35°$). The stresses at the very end of the upper localized plastic zone in Figure 6.26a (i.e., at the last upper, right red element 4) are $\sigma_{xx} = 0.5113\ MPa$, $\sigma_{yy} = 0.1357\ MPa$, and $\tau_{xy} = 0.08143\ MPa$. That element 4 is at peak load (Figure 6.27b) and element 2 at the base of the localized plastic zone is at the residual friction state (Figure 6.27b) is consistent with *Palmer and Rices*'s [1973] shear band model (e.g., see also *Puzrin and Germanovich*, 2005).

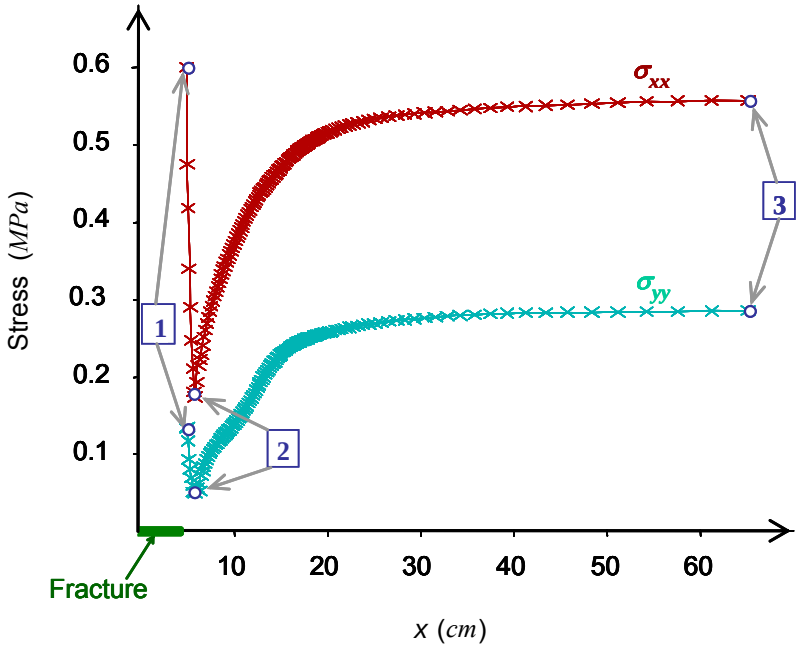

(a)

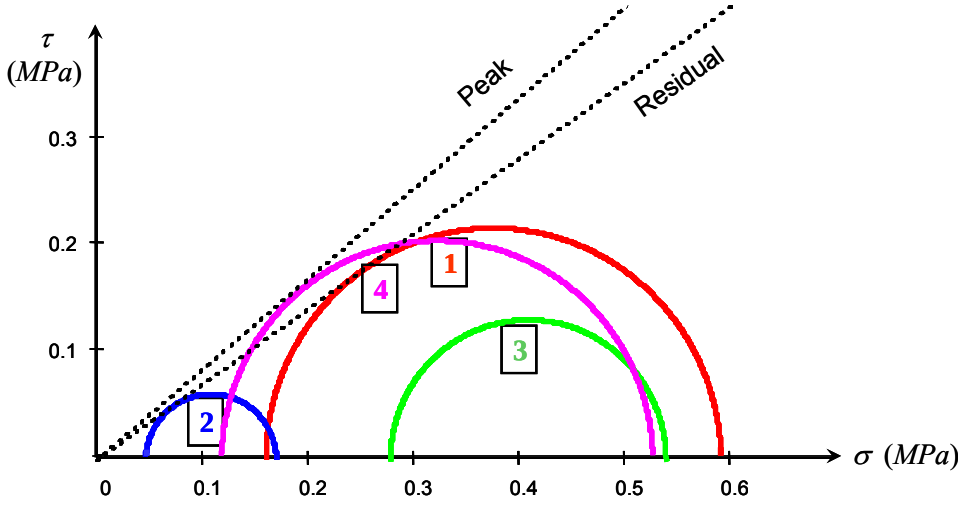

(b)

Figure 6.27 (a) Stress distribution of σ_{xx} and σ_{yy} ahead of the fracture tip, and (b) Mohr circles for elements 1, 2, 3, and 4 (see Figure 6.26b).

6.5.3 Induced Cohesion

We notice the remarkable similarity of the observed fingered front with the front that was

reported by *Murdoch* [1993] in cohesive clay (Figure 6.28). He observed a fluid lag at the fracture tip (see dashed curve in Figure 6.28a), which is not filled with the fracturing liquid. The fingering in Figure 6.28a may perhaps be attributed to the contraction of the fracturing liquid near the fracture front, which results in "breaking" the continuous liquid sheet into distinct fingers separated by the capillary menisci. The similarity between Figures 6.28a and 6.28b may be an indication that the fingered front observed in our experiments (e.g., Figure 6.28b) with dry particulate materials could also be due to a similar mechanism.

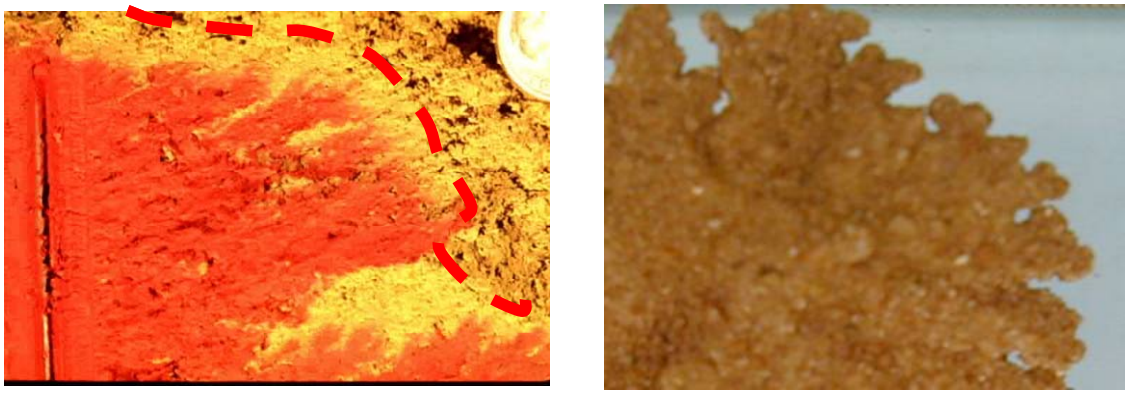

(a) (b)

Figure 6.28 Fingered fracture front in (a) partially-saturated clay [*Murdoch*, 1993] and (b) dry Georgia Red Clay.

More specifically, in the case of hydraulic fracturing in particulate materials, this type of front may appear when the host material perhaps has a small but non-zero cohesion (tensile strength). This cohesion could be inherent (e.g., due to electrostatic forces on clay platelets), or induced by the fluid leak-off ahead of the fracture front (see Appendix F). The latter type of cohesion may be caused by the *tensile strain* near the fracture tip (where the stress state is still compressive), which induces fluid cavitations and, hence, capillary forces (Figure 6.29). By this liquid cavitation mechanism, the cohesion may

also be induced in fully-saturated materials (see Appendix F).

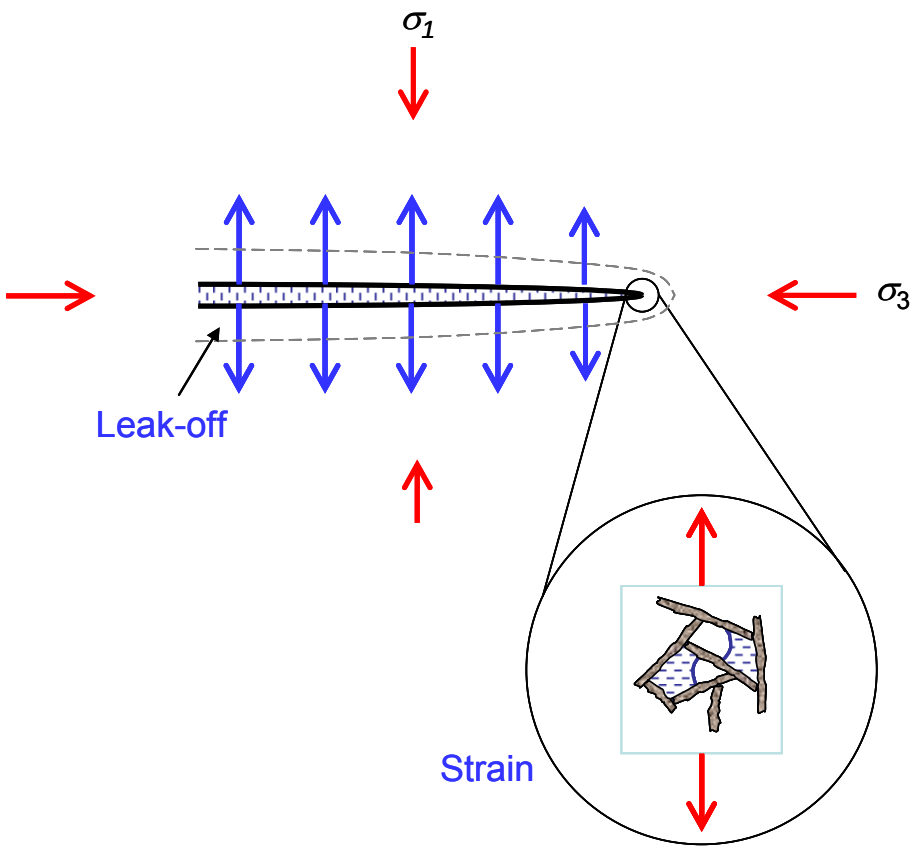

Figure 6.29 Induced cohesion (tensile strength) due to the cavitation caused by the tensile strain generated by the leak-off from the propagating fracture ahead of its front. In Appendix F, the fluid leak-off region manifests itself as a bubbly layer around the fracture, which thins towards the fracture tip (similar to brittle fractures).

6.6 Cavity Expansion Model of Hydraulic Fracturing

We now illustrate the "pile driving" or cavity expansion mechanism described above by using, as an example, hydraulic fracture tests 10 and 8 (see Table 5.9). Both tests were performed under similar conditions (see details in section 5.2.4), but with different injection volumes (i.e., 10 and 200 *ml*, respectively). These two fractures represent different stages of the hydraulic fracturing process. The photographs of these fractures

are shown in Figures 6.13a and 6.13b. In test 10, the injection was stopped shortly after the peak pressure. The small wing-like vertical features with a volume of ~ 3 *ml* (see also Figure 5.10a) probably correspond to the stage of fracture initiation from the expanding cavity. Test 8 represents the advanced stage of fracture propagation.

6.6.1 A Model of Cavity Expansion and Its Main Parameters

Our cavity expansion model of hydraulic fracturing is based on the cavity expansion in an ideally plastic Mohr-Coulomb material. The properties of the particulate material (silica flour; see details in section 2.5), loading conditions, and the geometrical parameters of the fracture samples are summarized in Table 6.1. While the values of these parameters should be viewed as approximate, this is sufficient for our purposes (see the end of this section 6.6).

Table 6.1 Experimental parameters (tests 10 and 8; see Table 5.9)

Properties of particulate material

Shear modulus	$G = 10\ MPa$
Poisson's ratio	$v = 0.3$
Cohesion	$C = 0$
Friction angle	$\phi = 40^{\circ}$
Dilation angle	$\psi = 6^{\circ}$

Loading condition

Remote stress	$p_0 = 11\ psi$
Peak pressure for tests 10 and 8	$p_{peak} = 480\ psi$
Propagation pressure for test 8	$p_{prop}^{(1)} = 120\ psi$

Geometrical parameters

Initial cavity radius	$a_0 = 1/8\ in$
Final radius of spherical cavity (at fracture initiation) for test 10	$a_{exp} = 0.4\ in$
Radius of cylindrical cavity at the propagating fracture front for test 8	$a_{exp} < 0.4\ in$

Note: (1) the pressure is calibrated for the pressure drop along the injection system.

We estimate the relationship between the cavity pressure p and the cavity radius a using the cavity expansion model by *Yu and Houlsby* [1991]. Although many such models are available, this simple case allows for consideration of basic scaling relationships that are relevant to the physical mechanisms discussed above. While *Yu and Houlsby*'s [1991] choice of the logarithmic strain to account for the effect of large strain in the plastic zone may require further justification, their closed form solution is convenient for estimating the pressure-expansion dependence $p(a)$, which is shown in

Figure 6.30. That the obtained cavitation pressure p_{cav} = 514 *psi* is greater than the measured peak pressure p_{peak} = 480 *psi* (which is practically equal for both tests; see Figure 6.14b) is consistent with the choice of parameters in Table 6.1.

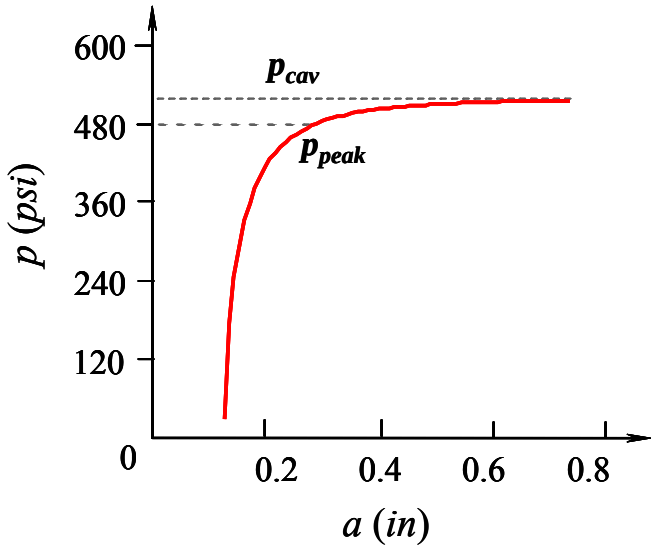

Figure 6.30 Cavity expansion pressure versus cavity radius for silica flour.

For simplicity, below we assume zero cohesion (the results can be easily generalized for non-zero cohesion that if below the threshold shown in Figure 6.21a). Then, the relationship between the radius of the plastic zone and that of the cavity is given by [*Yu* and *Houlsby*, 1991]

$$c = a\left[\frac{p}{p_0}\frac{k+\alpha}{(k+1)\alpha}\right]^{\frac{\alpha}{k(\alpha-1)}} \tag{6.17}$$

Hence, the radius of the plastic zone can be easily expressed as a function of the cavity volume:

$$c = a_0\left(\frac{V}{V_0}\right)^{\frac{1}{k+1}}\left[\frac{p}{p_0}\frac{k+\alpha}{(k+1)\alpha}\right]^{\frac{\alpha}{k(\alpha-1)}} \tag{6.18}$$

where $\alpha = (1+\sin\phi)/(1-\sin\phi)$, $k = 1$ for cylindrical symmetry and the plane strain condition (σ_z should be an intermediate principle maximum principal stress, which is guaranteed if $2\nu \geq 1$- $\sin\phi$), $k = 2$ for spherical symmetry,

$$V_0 = \left(\frac{4}{3}\right)^{k-1} \pi H^{2-k} a_0^{k+1} \qquad (6.19)$$

is the initial cavity volume, and H is the height of the initial cylindrical cavity ($H >> a_0$; obviously, H does not appear for the spherical cavity).

6.6.2 Cavity Expansion at Fracture Initiation

For the initial stage of fracture propagation (test 10), we use expressions (6.17) and (6.18) to calculate the radius, c, of the plastic zone. Since the final radius of the cavity is difficult to evaluate based on the observed cavity shape (Figure 6.13a), we first used the dependence $p(a)$ in Figure 6.30 to obtain a value of $a = a_{peak} = 0.35$ *in* that corresponds to the measured peak pressure $p_{peak} = 480$ *psi* (Table 6.1). We then compute $c = 2.1$ *in* from expression (6.17). Since the measured cavity volume $V = 7$ *ml* (10 *ml* injection volume minus 3 *ml* wing volume; see preface of this section) is a more reliable parameter, we also used (6.18) with $p = p_{peak}$ to obtain $c = 3.5$ *in* directly. These two results have a similar magnitude and, hence, are consistent. The size of the plastic zone compared to that of the initial cavity is shown schematically according to scale in Figure 6.31.

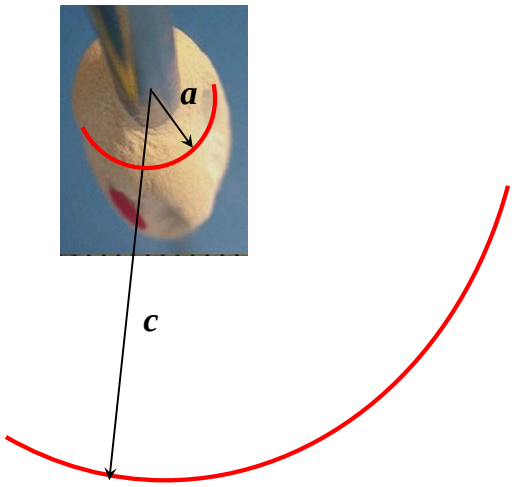

Figure 6.31 Schematic to scale of the size of the plastic zone c compared to that of the cavity a in test 10.

Thus, the dimension of the plastic zone ($\sim 2c \approx 4$ to 7 *in*) appears to be only a factor of two less than the diameter 11 *in* of the test container with the specimen of particulate material (Figure 4.1a). While in principle the external boundary could be incorporated in our estimates, this will not change the conclusion that at the peak pressure, a considerable part of the specimen (which is an order of magnitude greater than the initial cavity size $\sim 2a_0 \approx 0.25$ *in*) is occupied by the yielded particulate material. This is because the employed model of the cavity expansion in the infinite space gives the lower bound for the size of the plastic zone. Note that for hydraulic fracturing in the field, the assumption of the infinite space is likely to be adequate. See, however, the end of this section 6.6.

6.6.3 Unloading after Fracture Initiation

At the peak pressure, the magnitude of the radial stress is greater than that of the tangential stress, i.e., $\sigma_r > \sigma_\theta$ (recall that compressive stresses are positive). The pressure decreases abruptly after it reaches the peak (e.g., Figure 6.14). Consequently, as noted by

Yu and Houlsby [1995], the plastic material around the expanded cavity begins to unload elastically. The magnitude of the radial stress σ_r decreases because all of the stresses are compressive while the magnitude of the tangential stress σ_θ increases. Therefore, when the pressure decreases, the magnitude of σ_r may become less than that of σ_θ. This will induce a reversed plasticity. The occurrence of this reversed plasticity is determined by the condition that the pressure at the peak should be greater than

$$p_2 = \frac{\alpha \cdot (1 + k\alpha)}{k + \alpha} \cdot p_0 \qquad (6.20)$$

where α, k and p_0 have been defined earlier. In other words, if $p_{peak} < p_2$, the plastic zone cannot form during the pressure decrease from p_{peak} to p_0. As is seen from (6.20), It appears that p_2 is a function of the frictional angle and the remote stress rather than of the elastic properties of the material.

For test 8 (Figure 6.13a), the calculations with (6.20) show that $p_2 = 67$ *psi*, i.e., $p_{peak} >> p_2$. This indicates that in principle, the reversed plastic zone may exist if the pressure decrease is sufficient. To evaluate whether the decrease of the pressure for test 10 (Figures 6.13b and 6.14) is indeed sufficient to generate a reversed plastic zone, we need to compare the final pressure magnitude $p_{prop} = 120$ *psi* (Table 6.1) to another critical pressure [*Yu and Houlsby*, 1995]

$$p_3 = \left[1 - \frac{k \cdot (1 + \alpha) \cdot (\alpha - 1)}{\alpha \cdot (1 + k\alpha)}\right] \cdot p_{peak} \qquad (6.21)$$

If $p_{peak} > p > p_3$, the unloading is purely elastic while the reversed plasticity occurs if $p_3 > p > p_0$. In our case, $p_3 = 74$ *psi* for $k = 2$, and $p_3 = 114$ *psi* for $k = 1$. In any event, the final pressure $p_{prop} = 120$ *psi* for test 8 is greater than p_3, so that the material unloads

elastically with a considerable “factor of safety”.

Note that this result assumes that the appearance of the fracture during the stage of the pressure decrease does not change the stress state. Yet, by the end of the pressure drop, this fracture may have developed rather significantly (e.g., Figure 5.10b). Also, while the transition period (Figure 6.15) is short (Figure 6.14), some fracturing fluid is still injected into the developing fracture-cavity during this period. All this may result in plastic deformation. This suggests that the ideal cavity expansion model may not be fully applicable to the entire duration of the fracture initiation stage. As mentioned in section 6.4.3, the transition from the initial to the advanced stage of fracture growth (Figure 6.15) may require a plastic deformation, at least at some scale. The elastic unloading may be favorable compared to the small scale yielding, although due to the residual stresses, the details remain to be determined [*Wu*, 2005].

6.6.4 Cavity Expansion Model of Fracture Propagation

At the advanced stage of fracture propagation (test 8), the discussed cavity expansion model (“sheet pile driving” model; see section 6.5.1) can be used to consider two extreme cases: small and large plastic zones (Figures 6.23 and 6.24, respectively).

The small plastic zone corresponds to the “sheet pile driving” model (see Figure 6.23 and the discussion in section 6.5.1). In this case, the cylindrical symmetry analysis seems more appropriate to describe the cavity expansion along the fracture front. Similar to the industrial pile driving, the cavity expansion process at the pile end serves as a mechanism of displacement of the particulate material away from the fracture tip.

To the first order, we estimate the radius of the plastic zone from (6.18) (again, this is similar to certain pile driving applications). From the experimental observation, the radius of the round fracture front for test 8 (Figure 6.13b) is $a \approx 0.2$ *in*. The pressure in the tubing at the end of the test is $p_{prop} = 120$ *psi*. Then, for $k = 1$ (cylindrical symmetry) and $a = 0.2$ *in*, we find from (6.18) that the radius of the plastic zone surrounding the fracture front (Figure 6.23) is $c = 2.6$ *in*. The dimension of the plastic zone compared to the size of the initial cavity is shown schematically according to scale in Figure 6.32. Although the size of the plastic zone is one order of magnitude greater than the radius of the cavity at the fracture front, it is still less than the overall dimension of the fracture.

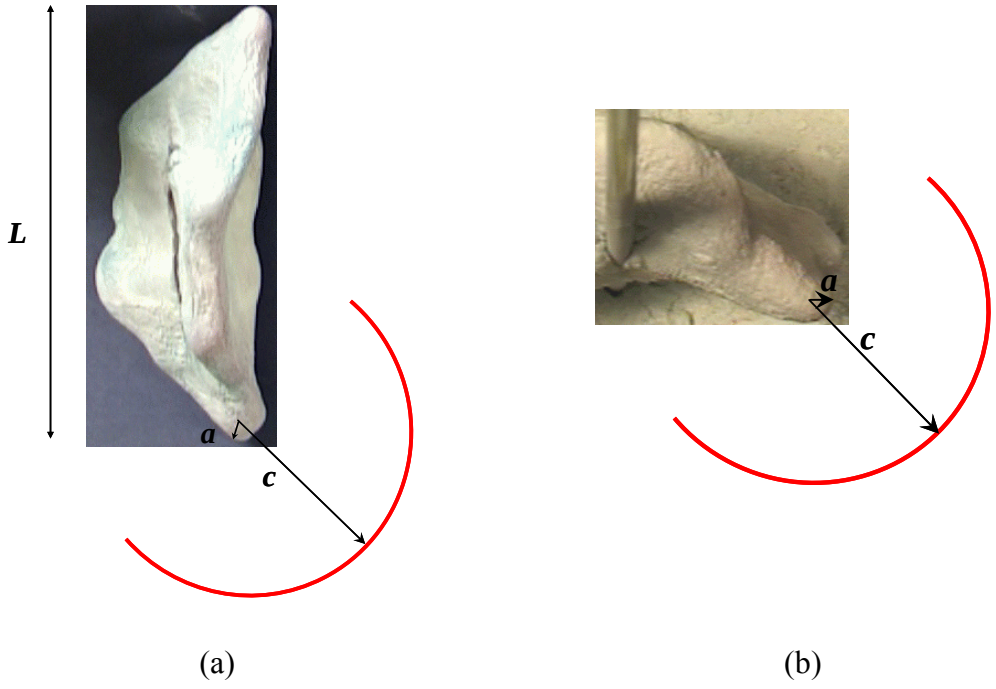

(a) (b)

Figure 6.32 Schematic (to scale) of the size of the plastic zone *c* compared to the size of the cavity *a* in test 8: (a) side and (b) top views of the same fracture (also shown in Figure 6.14b).

Strictly speaking, this conclusion neither confirms nor disproves the "pile driving" model (at least, for the used values of the parameters). Indeed, if the radius of the fracture

tip of $a = 0.2$ *in* remains approximately constant for another order of magnitude of the fracture propagation (as would be expected if the process were self-similar), then the plastic zone with a radius of $c = 2.6$ *in* could be considered reasonably thin for the pile model to be applicable. However, an alternative model of fracture propagation, when the plastic zone is significantly greater than the fracture dimension (Figure 6.24), cannot be excluded either.

In this case, we use again the spherically symmetrical model. If $c >> a$, the exact cavity shape is, probably, not very important and we can use the equivalent cavity volume assuming that it has a spherical shape. Then expression (6.18) can once more be applied to estimate the size of the plastic zone. For the fracture volume $V = 200$ *ml* (Figure 6.13b) and the propagation pressure $p_{prop} = 120$ *psi*, the plastic zone has a size of $2c = 9$ *in*, which is similar to the fracture length of $L = 7$ *in*. Therefore, in principle, this case is not consistent with the assumption of the large plastic zone.

With the "sheet pile" mechanism, the size of the plastic zone ($2c \approx 5$ *in*) is less than half of the specimen size. This is probably consistent with the laboratory observation that the specimen volume practically did not change during test 10 (Table 5.10).

Concluding, the "pile driving" model and the corresponding cavity expansion mechanism at the fracture front may be more realistic for test 10 (at least, with the chosen parameter values in Table 6.1) than the model of the large plastic zone (Figure 6.25).

Finally, it is worth mentioning, that the strain-softening material is probably far more realistic than the ideal-plastic material considered in this section (e.g., see section 2.5). One important difference in the behavior of the two materials is that the loading of the

strain-softening material produces shear bands, which are likely to appear at rather low injections pressure (only a factor of two or three greater than the initial pressure, according to the numerical experiments as shown in Figures 6.19 and 6.20). Because the peak pressure is much higher, i.e., the pressure continues to grow after the appearance of the shear bands, this indicates that the shear bands are stable (although they may be quite large; see Figures 1.19 and 1.20). Therefore, the cavity expansion may continue even after the shear bands appear and accompany their propagation. In other words, the processes of shear banding and cavity expansion may, in fact, co-exist before the pressure peak is reached. Similarly, shear banding and cavity expansion may co-exist at the tip of the propagating fracture when the pressure already is less than the peak value but still much greater than the initial pressure. Since these "details" are essentially ignored if the assumption of the ideal-plastic material is adopted, the corresponding model produces, at best, order-of-magnitude estimates. Consequently, more accurate computations and more complex models based on the ideal-plastic material are, probably, not warranted, and the inaccuracy of such assumptions as infinite space or plane strain becomes of secondary concern.

6.7 Summary

In this chapter, we outlined the principle fundamental mechanisms and suggested models of hydraulic fracturing in particulate materials based on our experimental results. The observed geometry of the hydraulic fractures and the injection pressure suggests that hydraulic fracturing occurs in the following sequence:

(i) cavity expansion before the injection pressure reaches its peak;

(ii) fracture front initiation from the expanding cavity near the pressure peak; and

(iii) propagation of the developed fracture after the peak.

The fact that cavity expansion is indeed observed, suggests that at the initial stage (*i*), a relatively large plastic zone is formed in the particulate material before the pressure reaches its peak. Accordingly, the new volume that is created for the injected fluid is primarily due to the elastic deformation of the undisturbed material outside of the plastic zone (for contracting materials, their inherent contraction may also contribute to this volume).

Probably, a small-scale boundary instability of the initial cavity expansion results in the initiation of the fracture front at stage (*ii*) of the fracture evolution. The exact mechanism of this instability is not yet clear and, before detailed modeling is conducted, the physical nature of this instability can be attributed to different phenomena. One example is given as large-scale shear banding that abruptly deforms the cavity shape, and is consistent with numerical simulations. In any case, the initial cavity is not preserved (and hence not observed) at the developed stage (*iii*) of the fracture propagation. This implies that the plastic deformation of the particulate material that surrounds the initial cavity could be an important process that results in the flattening of the cavity by "squeezing" the fracturing fluid into a thin conduit. Similar to hydraulic fractures in cohesive materials, the elastic opening of such flat cavities is beneficial for creating space for the injected volume. That is, generally, a lower pressure is required to create a new volume by opening thin fissures, than to expand bubble-like cavities. Although the details need to be resolved, this may be a reason why the fairly thin shape has been commonly

observed in our experiments at stage (*iii*) of the advanced fracture propagation, and why the pressure is reduced after the pressure peak. Then, this may also imply that the size of the plastic zone around the well-developed fracture is not very large compared to the dimensions of the fracture.

Another important conclusion of this work is that all parts of cohesionless particulate materials are likely to be in compression. The compressive stress state is an important characteristic of hydraulic fracturing in particulate materials with extremely low, if any, cohesion (such as used in our experiments). For the fracture initiation at the peak pressure (i.e., following the initial cavity expansion), there exists is a threshold value of cohesion that results in compressive stresses everywhere in the particulate material. For less cohesion, the cohesive materials can be considered to be effectively cohesionless.

Three main types of fracture fronts were observed in our laboratory experiments: round, beveled and fingered. Accordingly, three physical mechanisms of fracture propagation corresponding to the three observed front types were suggested. These are "pile driving" or cavity expansion, shear banding, and induced cohesion, which appear to be consistent with round, beveled, and fingered fracture fronts, respectively.

For the round fracture fronts, the corresponding physical mechanism of fracture propagation could be similar to the "pile driving" in industrial applications. In this case, the fracturing fluid is viewed as a sheet pile (or blade) that disjoints the host material. The plastic zone adjacent to the fracture (i.e., pile) may be relatively thin, compared to the fracture dimensions. Again, it is likely that at this stage of the fracture development, the elastic deformation of the host material primarily creates a new volume for the injected

fluid. Near the fracture front, however, the cavity expansion process is still important. In this region, the host material is displaced (i.e., "pushed") away from the advancing fracturing fluid. This displacement is modeled as a cavity expansion at the end of the propagating fracture ("pile"). Accordingly, the pressure of the fracturing liquid near the fracture tip is elevated (relative to the remote in-situ stresses), and so are the stresses near the tip.

The observed beveled fracture front consists of a distinct flat plane that is inclined with respect to the direction of fracture propagation. This geometry seems to be consistent with both an elevated or reduced pressure at the fracture tip (i.e., less or greater than the remote confining stresses), respectively. In this case, the host material adjacent to the fracture front may yield not only because of the increased stresses near the fracture tip, but also due to the considerably decreased stresses (i.e., smaller than the remote loads). In strain-softening materials (as were used in our experiments), either elevated or reduced stresses may have caused the localized shear bands that are inclined with respect to the fracture direction. The discontinuity of the shear displacements between the opposing sides of a shear band can also generate a fracture aperture (i.e., an opening normal to the fracture plane) that provides the necessary volume for the fluid inflow. Therefore, contrary to the cavity expansion model, in this scenario, the fracture can also propagate due to the *decrease* of the stresses from the remote in-situ values to a smaller magnitude near the fracture front.

The fingering at the fracture front has been observed in some experiments with Georgia Red Clay. We argue that this type of the fracture front may be due to the small but non-zero cohesion (tensile strength) of the host material. This cohesion could be

inherent (i.e., due to electrostatic forces on clay platelets), or induced by the fluid leak-off ahead of the fracture front. The latter type of cohesion may be caused by the *tensile strain* at the fracture tip zone (where the stress state is still compressive), which induces the cavitation of the leaked-off fluid and capillary forces. Via this liquid cavitation mechanism, the cohesion may also be induced in fully-saturated materials.

CHAPTER 7

CONCLUSIONS AND RECOMMENDATIONS

7.1 Conclusions

Hydraulic fracturing is an important and prevalent process both in the natural environment and in industrial applications. For more than five decades, this technique has been widely used to enhance oil and gas production from petroleum reservoirs.

The main conclusion of this work is that our laboratory experiment results show that hydraulic fracturing in particulate materials is not only possible, but even probable if the leak-off is minimized (e.g., high flow rate, high viscosities, low permeability). Also, it appears that the scale effect (within the range of the laboratory scales) is relatively insignificant (the observed features of fractures of different sizes appear similar). These results may be useful for the extrapolation of our conclusions to the practical field scales.

We arrived at these conclusions using reliable experimental techniques that have been designed and implemented. The laboratory experiments are based on injecting solidifying fluids into particulate materials while observing the injection pressure, and removal of the particulate material to observe the shape of the excavated hydraulic fractures (i.e., solidified fracturing fluids). The principle of these experiments is simple. However, in essence, the localization of the fluid flow is an unstable phenomenon, especially in particulate materials, which exhibit complex and inherently non-linear behavior. Hence, to quantify the relevant processes and the underlying mechanisms reproducibly and accurately, the development of specialized and novel equipment and procedures was

required.

The observed geometry of the hydraulic fractures and the injection pressure suggests that hydraulic fracturing occurs in the following sequence:

(i) cavity expansion before the injection pressure reaches its peak;

(ii) fracture front initiation from the expanding cavity near the pressure peak; and

(iii) propagation of the developed fracture after the peak.

The fact that cavity expansion is indeed observed, suggests that at the initial stage (*i*), a relatively large plastic zone is formed in the particulate material before the pressure reaches its peak. Accordingly, the new volume that is created for the injected fluid is primarily due to the elastic deformation of the undisturbed material outside of the plastic zone (for contracting materials, their inherent contraction may also contribute to this volume).

Probably, a small-scale boundary instability of the initial cavity expansion results in the initiation of the fracture front at stage (*ii*) of the fracture evolution. The exact mechanism of this instability is not yet clear and, before detailed modeling is conducted, the physical nature of this instability can be attributed to different phenomena. One example is given as large-scale shear banding that abruptly deforms the cavity shape, and is consistent with numerical simulations. In any case, the initial cavity is not preserved (and hence not observed) at the developed stage (*iii*) of the fracture propagation. This implies that the plastic deformation of the particulate material that surrounds the initial cavity could be an important process that results in the flattening of the cavity by

"squeezing" the fracturing fluid into a thin conduit. Similar to hydraulic fractures in cohesive materials, the elastic opening of such flat cavities is beneficial for creating space for the injected volume. That is, generally, a lower pressure is required to create a new volume by opening thin fissures, than to expand bubble-like cavities. Although the details need to be resolved, this may be a reason why the fairly thin shape has been commonly observed in our experiments at stage (*iii*) of the advanced fracture propagation, and why the pressure is reduced after the pressure peak. Then, this may also imply that the size of the plastic zone around the well-developed fracture is not very large compared to the dimensions of the fracture.

Another important conclusion of this work is that all parts of cohesionless particulate materials are likely to be in compression. The compressive stress state is an important characteristic of hydraulic fracturing in particulate materials with extremely low, if any, cohesion (such as used in our experiments). For the fracture initiation at the peak pressure (i.e., following the initial cavity expansion), there exists is a threshold value of cohesion that results in compressive stresses everywhere in the particulate material. For less cohesion, the cohesive materials can be considered to be effectively cohesionless.

Three main types of fracture fronts were observed in our laboratory experiments: round, beveled and fingered. Accordingly, three physical mechanisms of fracture propagation corresponding to the three observed front types were suggested. These are "pile driving" or cavity expansion, shear banding, and induced cohesion, which appear to be consistent with round, beveled, and fingered fracture fronts, respectively.

For the round fracture fronts, the corresponding physical mechanism of fracture

propagation could be similar to the "pile driving" in industrial applications. In this case, the fracturing fluid is viewed as a sheet pile (or blade) that disjoints the host material. The plastic zone adjacent to the fracture (i.e., pile) may be relatively thin, compared to the fracture dimensions. Again, it is likely that at this stage of the fracture development, the elastic deformation of the host material primarily creates a new volume for the injected fluid. Near the fracture front, however, the cavity expansion process is still important. In this region, the host material is displaced (i.e., "pushed") away from the advancing fracturing fluid. This displacement is modeled as a cavity expansion at the end of the propagating fracture ("pile"). Accordingly, the pressure of the fracturing liquid near the fracture tip is elevated (relative to the remote in-situ stresses), and so are the stresses near the tip.

The observed beveled fracture front consists of a distinct flat plane that is inclined with respect to the direction of fracture propagation. This geometry seems to be consistent with both an elevated or reduced pressure at the fracture tip (i.e., less or greater than the remote confining stresses), respectively. In this case, the host material adjacent to the fracture front may yield not only because of the increased stresses near the fracture tip, but also due to the considerably decreased stresses (i.e., smaller than the remote loads). In strain-softening materials (as were used in our experiments), either elevated or reduced stresses may have caused the localized shear bands that are inclined with respect to the fracture direction. The discontinuity of the shear displacements between the opposing sides of a shear band can also generate a fracture aperture (i.e., an opening normal to the fracture plane) that provides the necessary volume for the fluid inflow. Therefore, contrary to the cavity expansion model, in this scenario, the fracture can also

propagate due to the *decrease* of the stresses from the remote in-situ values to a smaller magnitude near the fracture front.

The fingering at the fracture front has been observed in some experiments with Georgia Red Clay. We argue that this type of the fracture front may be due to the small but non-zero cohesion (tensile strength) of the host material. This cohesion could be inherent (i.e., due to electrostatic forces on clay platelets), or induced by the fluid leak-off ahead of the fracture front. The latter type of cohesion may be caused by the *tensile strain* at the fracture tip zone (where the stress state is still compressive), which induces the cavitation of the leaked-off fluid and capillary forces. Via this liquid cavitation mechanism, the cohesion may also be induced in fully-saturated materials.

In summary, based on the developed experimental techniques, hydraulic fracture initiation and propagation has been directly observed in the laboratory. Hydraulic fractures at the different laboratory scales used in this study have been compared. Comprehensive experimental series with relevant ranges of values of the controlling parameters (e.g., properties of particulate materials and fracturing fluids, boundary conditions, initial stress states, injection volumes) have been conducted. The outline of the principal fundamental mechanisms of hydraulic fracturing in particulate materials was suggested. Relevant scaling relationships describing hydraulic fracturing in particulate materials (e.g., the interplay between elastic and plastic processes) were also tested against the experiments.

7.2 Recommendations for Future Work

Our recommendations for future studies include:

- Experimental modeling of
    - saturated particulate materials (see Appendix F)
    - multiple layers of particulate materials
    - more realistic fracturing fluids
    - more realistic particulate materials
    - considerably (i.e., orders of magnitude) higher applied loads and pressures
    - Initial stress state close to sediment failure (see Appendix G)
- Executing detailed experimental modeling of transition stage (i.e., between fracture initiation and propagation)
- Developing detailed theoretical modeling of proposed fracture initiation and propagation mechanisms
- Performing numerical simulations using programs that are based on discrete particles (e.g., PFC) instead of continua
- Testing industrial applications of
    - multiple injection holes
    - pre-consolidation of cohesionless particulate materials
    - multiple well bores and interacting hydraulic fractures
- Considerably increasing the size of the experimental setup for constrained lateral boundary considerably (e.g., twofold)

- Performing controlled field tests

APPENDIX A

EFFECT OF VIBRATION ON SPECIMEN DENSITY

Vibration is one of the methods used in this study to prepare silica flour specimens for the hydraulic fracturing tests. The setting of the vibration table, i.e., the frequency and the amplitude, is fixed. The dry silica flour is spooned into the steel container. The surcharge on the specimen during the vibration is 1 *psi*. After loading with the surcharge of 1 *psi*, the relative density becomes 50%.

The reacting density of the specimen increases with the vibration time. Figure A.1 shows the relationship of the relative density and the vibration time for the specimen prepared in the large-scale steel mold with an inner diameter of 11 *in* diameter.

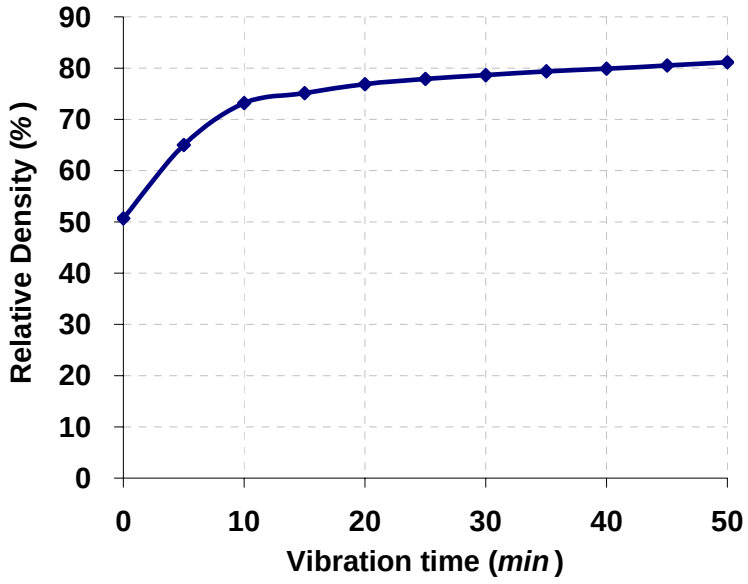

Figure A.1 Increase of density of silica flour specimen in the large steel mold with vibration time.

The density increases significantly during the first 10 *min*. After 10 *min*, the density

increases only slightly and approaches an asymptotic value of ~80%.

To maximum the density, the vibration time should to be maximized. However, this may cause the segregation of the particles. Practically, an optimum vibration time of 20 *min* is selected to prepare dense silica flour specimens.

APPENDIX B

EFFECT OF STATIC LOADING ON SPECIMEN DENSITY

Static loading is used to prepare dense silica flour specimens. The dependency of the relative density of the specimen on the applied static vertical load (up to 83 *psi*) in the large-scale steel mold with an inner diameter of 11 *in* is shown in Figure B.1.

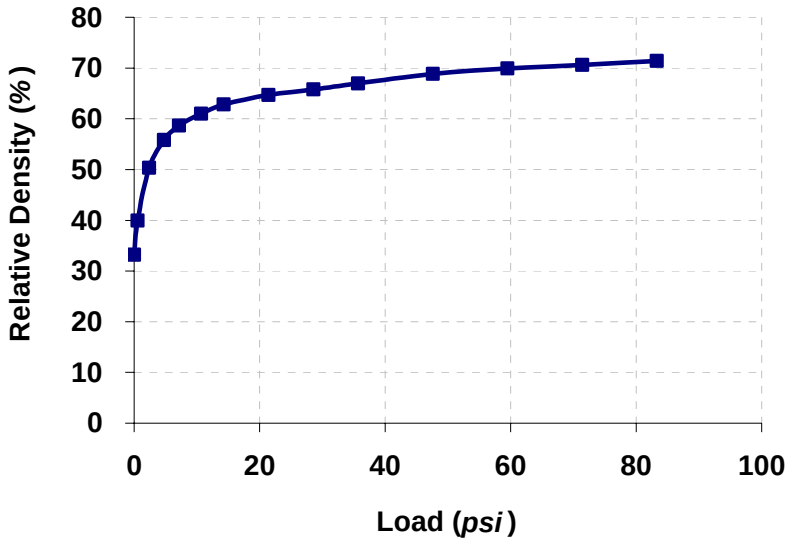

Figure B.1 Density of silica flour specimen in steel mold versus static load.

The density increases with increasing static load. Under the static vertical load of 83 *psi*, the achieved density is 72%. From extrapolating the trend of the curve, the density may not increase significantly after the load reaches a certain value (~ 100 *psi*)., the relative density at 10 *psi* is only 10% greater than at 80 *psi* (Figure B.1).

The density at a certain static load is measured after a consolidation of 15 *min*. Loading the specimen for 24 *hr*, the increase of the density is very small (< 1%). This indicates the packing of the particle becomes relatively static a short time after the load is

applied (i.e., ~10 *min*).

The prepared specimen has a non-uniform density along the vertical direction. The vertical non-uniformity is probably mainly due to frictions between the specimen side and the non-lubricated container wall which hampers particles from moving downward along the wall. Since the specimen is loaded from the top, the density is greater in the upper part than in the lower part of the specimen. The experimental results show that the non-uniformity decreases with an increasing static load level, as shown in Table B.1. When increasing the applied load from 10 *psi* to 80 *psi*, the vertical non-uniformity of the specimen reduces from 9% to 3%.

Table B.1 Density of a silica flour specimen prepared with one-dimensioned static-load compaction.

Vertical Load	**Relative Density *Dr***	**Density Increase after loading 24 *hr***	**Density difference Δ*Dr* between upper and lower halves**
(psi)	**(%)**	**(%)**	**(%)**
10	62	1	9
80	72	1	3

The vertical non-uniformity is expected to be further reduced by lubricating the wall of the container. In this case, the efficiency of the densification may also improve.

APPENDIX C

SOME PARAMETERS OF EXPERIMENTAL SETUP

The small- and large-scale tri-axial cells are designed to perform pressure-controlled lateral boundaries experiments. The large-scale tri-axial cell and the split mold used for the preparation of the specimen are shown in Figure C.1. The parameters of the tri-axial cells are listed in Table C.1.

(a)

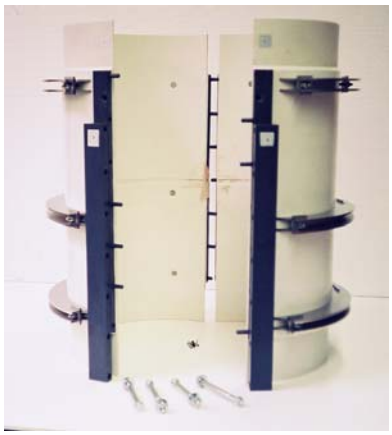

(b)

Figure C.1 (a) Large-scale tri-axial cell and (b) split mold.

Table C.1 Parameters of tri-axial cells

Scale	Specimen Dimension		Maximum Confining Water Pressure
	Diameter	Height	
	in	*in*	*psi*
Small	4	8	60
Large	12	18	100

The applied maximum confining pressure of the tri-axial cells is limited by the available pressurized air source and the strength of the plexi-glass walls of the confining cylinder.

The fluid injection system consists of a pump, a fluid displacement chamber and injection tubing. A number of different pumps were used to establish a range of different experimental conditions. The parameters of the four pumps that were used for the experiments are listed in Table C.2.

Table C.2 Parameters of the four pumps

Type	**Injection Rate**	**Maximum Pressure**	**Maximum Injection Volume**	**Need for displacement chamber**
	ml/s	*psi*	*ml*	
screw pump	4	> 1,000	15 or 55	no
digital syringe pump	0 to 0.5	290	1000	yes
manual piston pump	0 to 0.5	3,000	unlimited	yes
electric piston pump	0 to 1.7	5,000	unlimited	yes

The parameters of the three fluid displacement chambers of different sizes used are listed in Table C.3.

Table C.3 Parameters of the fluid displacement chambers

Scale	**Volume**	**Maximum Pressure**
	ml	*psi*
Small	110	1,000
Medium	450	4,000
Large	630	4,000

The small chamber contains an elastic membrane. The medium and large chambers contain a sliding stainless steel piston with an O-ring that separates the hydraulic from the fracturing fluid, while transferring the hydraulic pressure. The small chamber is used for small injection volumes and low pressures. The medium and large chambers are used for large injection volumes and high pressures.

Three types of injection tubing with different maximum pressures were used for the experiments: nylon, aluminum, stainless steel. The stainless steel tubing has two different wall thicknesses. The parameters of the tubing are listed in Table C.4. The liquid is either pumped out of the open end of the tubing or from injection holes on the side of the tubing.

Table C.4 Parameters of the injection tubing

Type		**Inner Diameter**	**Maximum Pressure at 22°C**	**Diameter of Injection Hole**
		in	*psi*	*in*
Nylon		0.18	250	0.18 (tubing opening)
Aluminum		0.22	> 500	0.22 (tubing opening)
Stainless Steel	Thin-wall	0.18	4,400	0.1 (dilled hole)
	Thick-wall	0.12	8,100	

The data acquisition system includes components for the data measurement and the data collection. In this study, the main measured parameter is the injection pressure.

Analog dial and digital pressure gages are used for the measurement of the pressure for the experiments. A digital video camera and a digital multi-meter are used to collect data from the two types of the pressure gages, respectively. The main parameters of the pressure gages are listed in Table C.5.

During the experiments, a high- and a low-pressure gage are mounted together to the injection system to measure the pressure. The low range pressure gage is separated from the injection tubing by a switch to protect it from high pressure, when relevant.

Table C.5 Parameters of the pressure gages

Type	**Maximum Pressure**	**Accuracy**	**Data Collection Apparatus**
	psi	*psi*	
Analog dial	300	5	Video camera
	3,000	50	
Digital	1,000	1	Multi-meter
	5,000		

Typically, the multi-meter records data at a rate of 1/*s*. When it detects a dramatic change of the data, it records at a rate of 2/*s*. Its own memory records data automatically in, and does not require a connected computer or recorder.

The injection pressure is measured at the outlet of the fluid displacement chamber. During the injection of the fracturing fluid, the friction between the viscous fracturing fluid and the wall of the injection tubing results in a pressure gradient along the length of the tubing. The calibration of the pressure gradient for the stainless steel injection tubing (which is used most frequently) is listed in Table C.6.

Table C.6 Pressure Drop Calibration of Stainless Steel Injection Tubing

Wall Thickness	**Inner Diameter**	**Injection Rate**	**Pressure Gradient**
	in	*ml/s*	*psi/in*
Thin	0.18	1.7	5
Thick	0.12		10

APPENDIX D

EFFECT OF SPECIMEN PREPARATION TECHNIQUE

A series of fractures generated in specimens prepared by different techniques are compared to study their effect on the fracture properties. Two series of experiments are compared for specimens prepared by vibration and rodding, respectively. For these two series, the applied vertical load is 1 and 10 *psi*, respectively. The four fractures are compared in Table D.1. The parameters of the experiments can be found in Table 5.3 and Table 5.5

The fractures generated in the specimen that is densified by vibration tend to be symmetric with respect to the injection tubing. In contrast, the fracture generated in the specimen that is densified by rodding tends to be asymmetric. This indicates that the specimen prepared by vibration has a more uniform initial stress distribution in the lateral direction.

In the specimens prepared by vibration, the fracture tends to propagate downward. This is probably due to the density gradient caused by the segregation of the particles during vibration.

Rodding tends to lock in lateral stresses. With increasing the magnitude of applied load, the influence of the locked-in stress is expected to decrease. The orientation of the two fractures in the specimens prepared by rodding tends to deviate from the vertical direction. This probably indicates the existence of the locked-in lateral stresses. At 10 *psi*, the fracture only curves slightly towards lateral direction. Consequently, the order of the

magnitude of the locked-in stresses is estimated to be ~ 10 *psi*.

The fractures generated in the vibrated specimens are thicker than those in the rodded specimens. This is probably due to the fact that the densities of the vibrated specimens are ~10% lower than those of the rodded specimen.

Table D.1 Comparison of fractures generated by different specimen preparation techniques

Vertical load	**Specimen Preparation Technique**	
psi	**Vibration**	**Rodding**
1	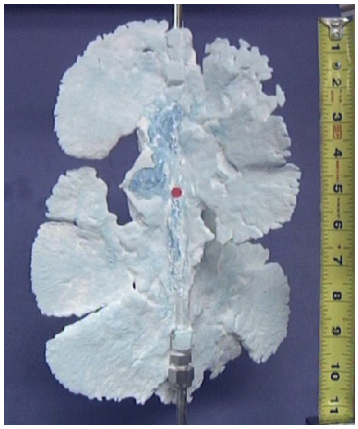	
	test 4	test 17
10		
	test 6	test 8

Although the vibration technique appears to produce specimens of higher quality, in this study rodding is necessary in some cases: (*i*) a specimen prepared in tri-axial cell cannot be vibrated since vibration could damage the rather delicate tri-axial cell; (*ii*) it is easier to achieve a very dense specimen with rodding than vibration. To increase the density by vibration, a loading apparatus is needed during vibration to apply a sufficient high surcharge for our large specimens. In addition, the vibration time may have to increase, which could aggravate the amount of particle segregation.

Summarizing, neither vibration nor rodding is necessarily a better technique to densify the particulate specimen.

APPENDIX E

TEST P7 WITH PRESSURE-CONTROLLED LATERAL BOUNDARY

The parameters of test P7 are listed in Table E.1. The photographs of the hydraulic fracture are presented in Figure E.1. The corresponding pressure curve is shown in Figure E.2. The results of the experiments are listed in Table E.2.

Table E.1 Parameters of test P7

Test		P7
Particulate materials		Silica flour
Relative Density	*%*	70
Densification Technique		Rodding
Lateral Boundary		Pressure-controlled
Scale		Large
Vertical Load	*psi*	10
Ratio of p_v / p_h		~2[(1)]
Fracturing Fluid		Joint compound
Injection Rate	*ml/s*	1.7
Injection Volume	*ml*	180

Note: (1) the specimen was overloaded with a ratio of ~3 for a short time.

Figure E.1 Fracture of test P7 viewed from different directions.

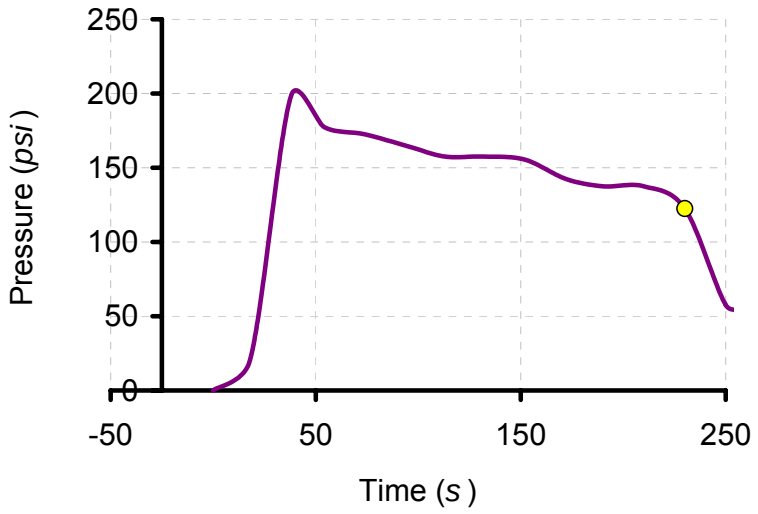

Figure E.2 Injection pressure curve of test P7.

Table E.2 Results of experiments with different applied loads

Test		P7
Peak Pressure	*psi*	197
Relative Volume Change	*%*	73
Average Density after Injection	*%*	71

APPENDIX F

TESTS L1, L2, AND L3 WITH FLUID LEAK-OFF

The parameters of tests L1, L2, and L3 are listed in Table F.1. The photographs of the hydraulic fractures obtained in these tests are presented in Figure F.1. The corresponding pressure curves are shown in Figure F.2. Some experimental results are given in Table F.2.

Table F.1 Parameters of tests L1, L2 and L3.

Test		L1	L2	L3
Particulate materials		Fine sand		
Condition of specimen		Oven dried	Fully-saturated and drained	
Relative Density	*%*	73		
Densification Technique		Vibration		Robbing
Lateral Boundary		Constrained		Pressure-controlled
Scale		Large		
Vertical Load	*psi*	10		40
Ratio of p_v / p_h		>1		2
Fracturing Fluid		Silicone sealant		
		White; regular viscosity	Clear; regular viscosity	Black, higher viscosity
Injection Rate	*ml/s*	1.7		
Injection Volume	*ml*	250	250	200

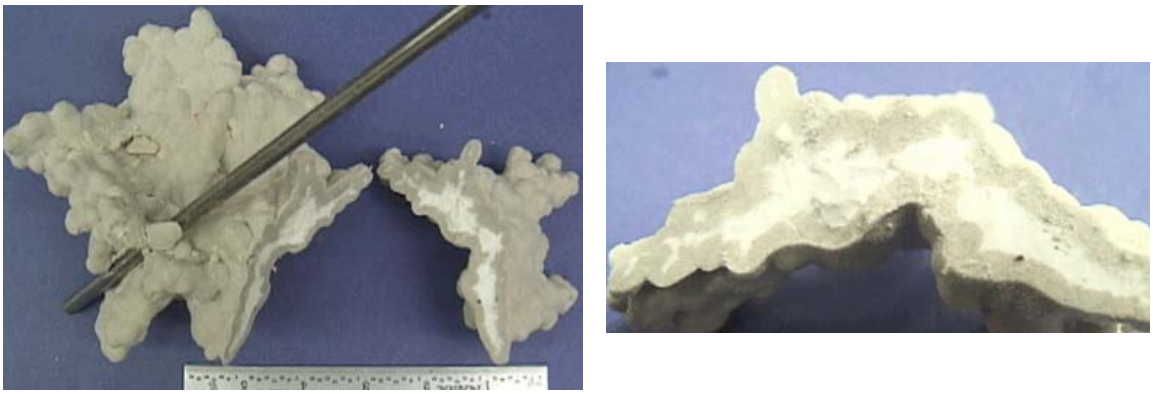

(a)

(b)

(c)

Figure F.1 Fractures generated in: (a) L1, (b) L2, and (c) L3 tests.

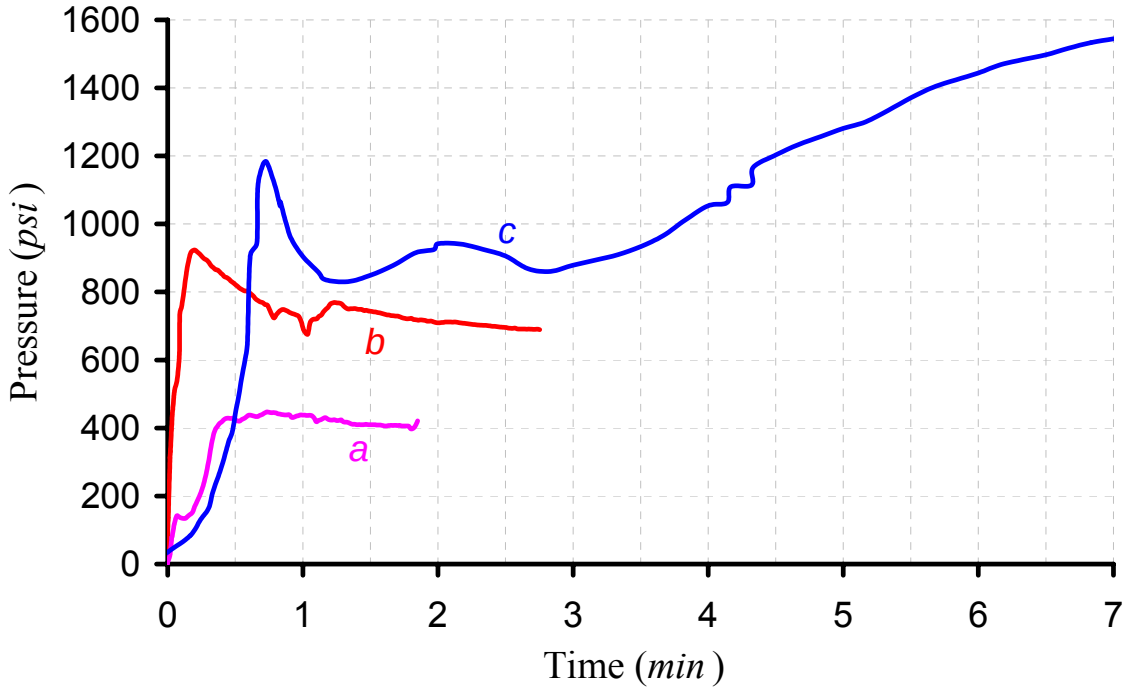

Figure F.2 Injection pressure curves measured in tests (a) L1, (b) L2, and (c) L3.

Table F.2 Results of tests L1, L2 and L3

Test		L1	L2	L3
Peak Pressure	*psi*	450	900	1200
Propagation Pressure	*psi*	400	700	n/a
Approximate Ratio of Leak-off to Fracture Thicknesses		1:1		2:1

APPENDIX G

TEST 11 WITH PATICULATE MATERIAL CLOSE TO FAILURE

An experiment is performed by injecting joint compound into silica flour with the specimen loaded to the point that is close to failure before the injection. Since silica flour has a residual friction angle of 38˚ (see Table 2.4), the stress ratio σ_1 / σ_3 at failure is 4.2 per Mohr-Coulomb criterion. This specimen is loaded with 60 *psi* vertical and 20 *psi* horizontal pressures. The initial load ratio of p_v / p_h is 3 before the injection. Because the injection pressure exceeded the pressure capacity of the available injection pump, the vertical and horizontal loads are reduced proportionally (i.e., keeping the constant ratio of 3) in small increments. The fluid is injected into the specimen at a vertical load of 5 *psi*. The parameters of the experiment are listed in Table G.1. The corresponding hydraulic fractures are presented in Figure G.1.

The fracture has an inclined orientation (Figure G.1a) and a star shape (Figure G.1b). The failure plane of the specimen was not clearly visible after the injection. It becomes more obvious after exerting a gentle lateral stress on the boundary of the specimen. This indicates that the material may have partially failed. The orientation and location of the fracture coincides with those of the observed failure plane after the experiment (Figure G.1c and Figure G.1d).

This experiment indicates that the initial stress state of the specimen that is close to failure may induce fracture aligned with the shear failure plane.

Table G.1 Parameters of experiment with the applied load ratio equal to three

Test		11
Particulate Material		Silica flour
Relative Density	*%*	87
Densification		Rodding
Lateral Boundary		Pressure controlled
Scale		Small
Vertical Load	*psi*	60 → 5
Ratio of p_v / p_h		*3*
Fracturing Fluid		Silicone sealant
Injection Rate	*ml/s*	0.5
Injection Volume	*ml*	20

(a)

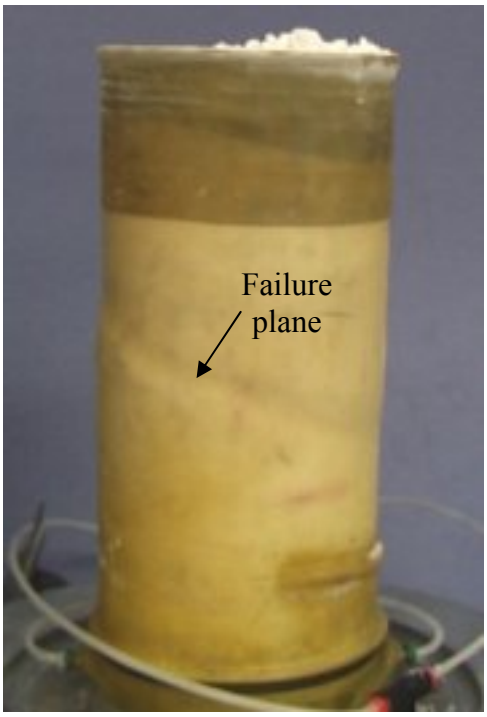

(c)

(b)

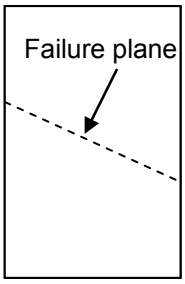

(d)

Figure G.1 (a) Side view and (b) top view of fracture sample, (c) failure plane observed after the specimen is disturbed during excavation, and (d) sketch of failure plane.

REFERENCES

[1] Al-Alusi, H. R., Compaction grouting: From practice to theory, *Grouting: Compaction/Remediation/Testing, Geotechnical Special Publication*, *66*, ASCE, New York, pp. 43-53, 1997

[2] Alsiny, A., Vardoulakis, I., and Dresher, A., Deformation localization in cavity inflation experiments on dry sand, *Geotechnique, 42*(3), 395-410, 1992

[3] Andersen, K. H., and Lunne, T. A., Method to determine conductor setting depth in silt-clay, *Publikasjon - Norges Geotekniske Institutt*, n 191, 173-186, 1994

[4] Andersen K. H., Lunne, T. A., Rawlings, C. G., and By, T. H., Hydraulic fracture as a criterion for conductor setting depth in silt-clay, *Proceedings of the 4th Canadian Conference in Marine Geotechnical Engineering, St. Johns*, *7*, 4-26, 1993

[5] Anderson, K. H., Rawlings, C. G., Lunne, T. A., and By, T. H., Estimation of hydraulic fracture pressure in silt-clay, *Canadian Geotechnical Journal, 31*(6), 817-828, 1994

[6] Anderson, T.L., *Fracture Mechanics; Fundamentals and Applications*, 2nd ed., CRC Press LLC, Boca Raton, FL. 688, 1995

[7] Atkins, P. W., *Physical Chemistry*, Oxford University Press, 1978

[8] Atkinson, J. H., Charles, J. A., and Mhach, H. K., Undrained hydraulic fracture in cavity expansion tests fracture, *XIII ICSMFE, New Delhi, India*, 1994

[9] Baars, S. V., Failure of cohesive granular materials, *Proceedings of the 9th International Conference on Fracture, Sydney, Australia*, 917-926, 1997

[10] Baguelin, F., Jezequel, J. F., Le Mee, E. and Le Mehaute, A., Expansion of cylindrical probes in cohesive soils, *Journal of the Soil Mechanics and Foundations Divisions, 98*(SM11), 1129-1143, 1972

[11] Baker, T. H. W. and Konrad, J. M., Effect of sample preparation on the strength of artificially frozen sand, Proceedings of the fourth international symposium on ground freezing, Japan, August 5-7, 1985

[12] Baligh, M. M., Cavity expansion in sands with curved envelopes, *Journal of the Geotechnical Engineering Division, 102*(GT11), 1,131-1,147, 1976

[13] Barker, C., Generation of anomalous internal pressures in source rocks and its role in driving petroleum migration, *Revue de l'Institut Francais du Petrole, 43*(3), 349-355, 1988

[14] Bertram, A., Kalthoff, J.F., Crack propagation toughness of rock for the range from low to very high crack speeds, *Key Engineering Materials*, Volumes. 251-252, 423-430, 2003

[15] Bird, R. B., Stewart W. E., and Lightfoot, E. N., *Transport phenomena*, 2nd ed., New York: J. Wiley, 895, 2002

[16] Bjerrum, L., Nash, J. K. T. L., Kennard, R. M., and Gibson, R. E., Hydraulic fracturing in field permeability testing, *Geotechnique*, *22*(2), 319-332, 1972

[17] Borden, R. H., and Ivanetich, K. B., Influence of fines content on the behavior of compaction grout, *Grouting: Compaction/ Remediation/Testing, Geotechnical Special Publication*, *66*, ASCE, New York, pp. 63-75, 1997

[18] Broek, D., *Elementary engineering fracture mechanics*, 2nd edition, Alphen aan den Rijn : Sijthoff & Noordhoff, 437, 1978

[19] Bui, H. D., and Paines, R., A re-examination of the pressure at the tip of a fluid-filled crack, *International Journal of Engineering Science, 20*, 1,215-1,220, 1982.

[20] Carter, J. P., Booker, J. R., and Yeung, S.K., Cavity expansion in cohesive frictional soils, *Geotechnique, 36*(3), 349-358, 1986

[21] Chadwick, P. The quasi-static expansion of a spherical cavity in metals and ideal soils, Q. J., Mech.. Appl. Math.. Part I, XII, 52-71, 1959

[22] Chang, H., Germanovich, L. N., Wu, R., Santamarina, J. C., and Dijk, P E, Hydraulic fracturing in cohesionless particulate materials, *Eos Trans. AGU*, 84*(46),* Fall Meet. Suppl., Abstract, H51B-03*,* 2003

[23] Chudnovsky, A., Saada, A.S., and Lesser, A.J., Micromechanisms of deformation in fracture of overconsolidated clays, *Canadian Geotechnique Journal*, *25*, 213-221, 1988

[24] Clark, P. E., Prediction of slurry convection in hydraulic fractures, *Journal of Petroleum Science and Engineering, 15*, 389-391, 1996.

[25] Clifton, R. J., and Abou-Sayed, A.S., On the mechanics of hydraulic fracturing, *Proceedings of the 9th U.S. National Congress of Applied Mechanics,* Cornell University, 443-451, 1982

[26] Clifton, R. J., Recent advances in the three dimensional simulation of hydraulic fracturing, *Developments in Mechanics, 13*, 311-319, 1985

[27] Corthay, J.E. II, Delineation of a massive seafloor hydrocarbon seep, overpressured aquifer sands, and shallow gas reservoirs, Louisiana Continental Slope, *Offshore Technology Conference, Annual Proceedings, 1*, 37-56, 1997

[28] Dai, X., and Borden, R. H., *The Change of In-situ Soil Conditions Induced by Compaction Grouting*, research report, Department of Civil Engineering, North Carolina State University, 1996

[29] Detournay, E., Propagation regimes of fluid-driven fractures in impermeable rocks*, International Journal of Geomechanics, Petroleum Geomechanics*, 4(1), 35-45, 2004

[30] Department of Energy*,* Hydraulic fracturing white paper*, Evaluation of*

Impacts to Underground Sources of Drinking Water by Hydraulic Fracturing of Coalbed Methane Reservoir, EPA 816-R-04-003*,* 2004

[31] Desroches, J., Detournay, E., Lenoach, B., Papanastasiou, P., Pearson, J.R.A., Thiercelin, M., and Cheng, A., The crack tip region in hydraulic fracturing, *Proceedings of the Royal Society of London, Series A: Mathematical, Physical and Engineering Sciences*, *447*, 39-48, 1994

[32] Dijk, P E, Chang, H., Germanovich, L. N., and Santamarina, J. C., Experiments on hydraulic fracturing in weakly cemented sediments, *Eos Trans. AGU*, 84*(46),* Fall Meet. Suppl., Abstract, H42F-1131*,* 2003

[33] Domanti, A. T. J., and Bridgwater, J., Surface fracture in axisymmetric paste extrusion: an experimental study, *Chemical Engineering Research and Design, Transactions of the Institute of Chemical Engineers, Part A, 78*(1), 68-78, 2000

[34] Dusseault, M. B, Bilak, R. A., and Rodwell, L. G., Disposal of dirty fluids using slurry fracture injection, Proceedings *SPE-EPA Drilling and Production Environmental Conference,* Dallas, March, SPE #37907, 1997

[35] Dusseault, M. B., and Simmons J. V., Injection-induced stress and fracture orientation changes, *Canadian Geotechnical Journal, 19*(4), 483-493, 1982

[36] Dusseault, M. B., and Bilak, R. A., Mitigation of heavy oil production environmental impact through large-scale slurry fracture injection of wastes, *SPE/ISRM Eurock,* Trondheim, Norway, 1998

[37] Dusseault, M. B., Bilak, R. A., Bruno M., and Rothenburg L., Disposal of granular solid wastes in the western Canadian sedimentary basin by slurry fracture injection, *University of Waterloo, Geomechanics Group Report*, 1994

[38] Eaton, L. F., Drilling through deepwater shallow water flow zones at Ursa, *SPE/IADC Drilling Conference, Amsterdam, Holland*, 1999

[39] Fang, H. Y., Cracking and fracture of soil, *Fracture Mechanics*, 102-117, 1994

[40] Fang, H. Y., Mikroudis, G. K., and Pamukcu, S., Fracture behavior of compacted fine-grained soils, *Fracture Mechanics: Perspectives and Directions (Twentiech Symposium), ASTM STP 1020,* edited by Wei, R. P. and Gangloff, R. P., American Society for Testing and Materials, Philadelphia, 659-667, 1989

[41] Gallavresi, F., Grouting improvement of foundation soils, *Grouting, Soil Improvement and Geosynthetics, 1, Geotechnical Special Technical Publication*, *30*, ASCE, New york, p. 1-38, 1992

[42] Geoserria website: http://www.geoserria.com, 2004

[43] Germanovich, L. N., Van Dyke, P. E., Chang, H. and Wu, R., Hydraulic fractures in particulate materials, *International Journal of Rock Mechanics and Mining Science*, 2005 (in press)

[44] Germanovich, L. N. and Astakhov, D. K., Stress-dependent permeability and fluid flow through parallel joints, *Journal of Geophysical Research - Solid Earth*, *109*(B9): Art. No. B09203, 2004a

[45] Germanovich, L. N. and Astakhov, D. K., Fracture closure in extension and mechanical interaction of parallel joints, *Journal of Geophysical Research - solid Earth*, *109*(B2): Art. No. B02208 FEB 24 2004b

[46] Germanovich, L. N., Astakhov, D. K., Mayerhofer, M. J., Shlyapobersky, J., and Ring, L.M. Hydraulic fracture with multiple segments I. Observations and model formulation, *International Journal of Rock Mechanics and Mining Sciences*, *34*(3-4), 471, 1997

[47] Germanovich, L. N., Ring, L. M., Astakhov, D. K., Shlyapobersky, J., Mayerhofer, M. J., Hydraulic fracture with multiple segments II. Effect of interaction, *International Journal of Rock Mechanics and Mining Sciences*, *34*(3-4), 472, 1997

[48] Germanovich, L. N, Astakhov, D. K., Shlyapobersky, J., Mayerhofer, M. J., Dupont, C., and Ring, L. M., Modeling multi-segmented hydraulic fracture in two extreme cases: no leak-off and dominating leak-off, *International Journal of Rock Mechanics and Mining Sciences*, *35*(4-5), 551-554, 1998

[49] Germanovich, L. N., Chang, H., Santamarina, J. C., and Corrigan, C., Fluid flow localization in particulate materials, Abstract of International Workshop on Bifurcations and Instabilities in Geomechanics, Minnesota, June 2-5, 2002

[50] Germanovich, L. N. and Lowell, R., Dike injection and the formation of megaplumes at ocean ridges, *Science*, *267*(5205), 1804, 1995

[51] Gidley, J. L., S. A. Holditch, D. E. Nierode, and Veatch, R. W*., Recent Advances in Hydraulic Fracturing*, Monograph, *12*, SPE Henry L. Doherty Series, First Printing, Henry L. Doherty Memorial Fund of AIME, Society of Petroleum Engineers, Richardson, Texas, 1989

[52] Gordeyev, Y. N., and Entov V. M., The pressure distribution around a growing crack, *Journal of Applied Maths. Mechs., 61*(6), 1,025-1,029, 1997

[53] Graf, E. D., Compaction Grout, 1992, *Grouting, Soil Improvement and Geosynthetics*, *1*, Geotechnical Special Technical Publication, 30, ASCE, New York, 275-287, 1992

[54] Grauls, D., Overpressures: causal mechanisms, conventional and hydromechanical approaches*, Oil and Gas Science and Technology, 54*(6), 667-678, 1999

[55] Haimson, B., Hydraulic fracturing in porous and non-porous rock and its potential for determining *in-situ* stresses at great depth, Ph.D. dissertation, University of Minnesota, 1968

[56] Haimson, B. and Fairhurst, C., Hydraulic fracturing in porous-permeable materials, *Journal of Petroleum Technology,* July, pp. 811-817, 1969

[57] Haimson, B. and Fairhurst, C., *In-situ* stress determination at great depth by

means of hydraulic fracture, *Proceedings of the 11th Symposium on Rock Mechanics,* AIME, 559-584, 1970

[58] Harison, J. A., Hardin, B. O., and Mahboub, K. Fracture toughness of compacted cohesive soils using a ring test, *Journal of Geotechnical Engineering*, *120*(5), 872-891, 1994

[59] Hill, R., *The Mathematical Theory of Plasticity*, Oxford University Press, 1950

[60] Hocking, G., Multiple participant proposal on azimuth control of hydraulic fractures in weakly cemented sediments, *Proposals to project*, Golder Associates Inc., 1995

[61] Hocking, G., Soil hydraulic fracturing, *Water Well Journal*, *50*(5), 70-72, 1996

[62] Holbrook, P., A simple closed form force balanced solution for pore pressure, overburden and the principal effective stresses in the Earth, *Marine and Petroleum Geology, 16*, 303-319, 1999

[63] Holtz, R. D., and Kovacs, W. D., *An Introduction to Geotechnical Engineering*, Prentice-Hall, Inc., New Jersey, 1981

[64] Horsrud, P., Risnes, R., and Bratli, R. K., Fracture initiation pressures in permeable poorly consolidated sands, *International Journal of Rock Mechanics, Mining Science and Geomechanics Abstract*, *19*, 255-266, 1982

[65] Howard, G. C., and Fast, C. R., *Hydraulic Fracturing,* American Institute of Mining, Metallurgical,and Petroleum Engineers, Inc., Monograph, Vol. 2, Henry L. Doherty Series, 1970

[66] Hubbert, M. K., and Willis, D. G., Mechanics of hydraulic fracturing, *Transactions of AIME, 210*, 153-166, 1957

[67] Huck, P. J., and Koerner, R. M., Acoustic emission monitoring of soil and rock grouting, *Acoustic Emissions in Geotechnical Engineering Practice, ASTM STP 750,* Philadelphia: American Society for Testing and Materials, 155-163, 1981

[68] Huckabee, P. T., Carbonate stimulation optimization using hydraulic fracturing field testing*, Society of Petroleum Engineers of AIME*, SPE 18, 224, 463-473, 1988

[69] Jaworski, G. W., Duncan, J. M., and Seed, H. B., Laboratory study of hydraulic fracturing, *ASCE Journal of Geotechnical Engineering*, *107*(GT6), 713-733, 1981

[70] Johnson, S., Cement and clay grouting of foundation: grouting with clay - cement grouts, *Journal of the Soil Mechanics and Foundations Division*, *ASCE*, Vol. 84, No. SM1, Proc. Paper 1545, 1545-1-1545-12, Feb. 1958

[71] Kim, S., *Mechanics of Catastrophic Failure of Soils*, Ph.D. dissertation, Georgia Institute of Technology, 2005

[72] Klein, A., and Polivka, M., Cement and clay grouting of foundation: The use of admixtures in cement grouts, *Journal of the Soil Mechanics and Foundations Division*, *ASCE*, Vol. 84, No. SM1, Proc. Paper 1547, 1547-1-1547-24, Feb. 1958

[73] Kravez, G. A., Cement and clay grouting of foundation: the use of clay in cement grouts, *Journal of the Soil Mechanics and Foundations Division*, *ASCE*, Vol. 84, No. SM1, Proc. Paper 1546, 1546-1-1546-30, Feb. 1958

[74] Ladanyi, B., Expansion of a cavity in a saturated clay medium, *Journal o f the Soil Mechanics and Foundations Division*, ASCE, V90, No. SM4, Proc. Paper 3577, 127-161, July, 1963.

[75] Lambe, T. W., *Soil testing for engineers*, Bitech Publishers Ltd, Canada, 165pp, 1991

[76] Lambe, T. W. and Whitman, R. V., *Soil mechanics*, John Wiley and Sons, 1968

[77] Lefebvre, G., Bozozuk, M., Philibert, A., and Hornych, P., Evaluating k_0 in champlain silt-clays with hydraulic fracture tests, *Canadian Geotechnical Journal,* 28, 365-377, 1991

[78] Lim, I. L., Johnston, I. W., and Choi, S. K., Mixed-mode fracture testing of soft rock, *Geotechnical Engineering of Hard Soils – Soft Rocks*, edited by Anagnostopoulos et al., Balkema, Rotterdam, 633-639, 1993

[79] Lim, I. L., Johnston, I. W., Choi, S. K., and Boland, J. N., Fracture testing of a soft rock with semi-circular specimens under three-point bending. Part 1 – Mode I, *Int. J. Rock Mech. Min. Sci. & Geomech. Abstr., 31*(3), 185-197, 1994

[80] Lo, K. W., Chu, K. H., and Tamilselvan, A fractured mechanical model for hard soil, *Geotechnical Engineering of Hard Soils – Soft Rocks*, 647-652, 1993

[81] Lo, K. Y., and Kaniare, K., Hydraulic fracture in earth and rock-fill dams, *Canada Geotechiques*, *27*, 496-506, 1990

[82] Luo, M., Baker, M. R., and LeMone, D. V., Distribution and generation of the overpressure system, eastern Delaware basin, western Texas and southern New Mexico, *AAPG (American Association of Petroleum Geologists) Bulletin, 78*(9), 1,386-1,405, 1994

[83] Mahmood, A., Mitchell, J.K., and Lindblom, Ulf, Effect of specimen preparation method on grain arrangement and compressibility in sand, *Soil Specimen Preparation for Laboratory Testing, ASTM STP 599*, American Society for Testing and Materials, 169-192, 1976

[84] Malachosky, E., Shannon, B.E., and Jackson, J.E., Offshore disposal of oil-based drilling fluid waste. An environmentally acceptable solution, *Proc First Int Conf Health Saf Environ Oil Gas Explor Prod*, 465-473, 1991

[85] Massarsch, K. R., New aspects of soil fracturing in silt-clay, *Journal of the*

Geotechnical Engineering Division, Proceedings of ASCE, *104*(GT8), 1,109-1,123, 1978

[86] Massarsch, K. R., and Broms, B. B., Fracturing of soil caused by pile driving in clay, *9th International Conference on Soil Mechanics and Foundation Engineering*, Tokyo, 1/40, 197-200, 1977

[87] Minton, R.C., Novel retrofit solution for oily cuttings slurrying and re-injection on the Ula platform, *Proceedings of the 1996 3rd International Conference on Health, Safety and Environment in Oil and Gas Exploration and Production*, 2, SPE 35951, 519-525, 1996

[88] Miura, S., and Toki, S., A sample preparation method and its effect on static and cyclic deformation-strength properties of sand, *Soils and Foundations*, Japanese Society of Soil Mechanics and Foundation Engineering, *22*(1), 61-77, 1982

[89] Morganstern, N. R., and Vaughan, P. R., Some observations on allowable grouting pressure, *Grouts and Drilling Muds in Engineering Practice,* London, Butterworths, 36-42, 1963

[90] Mori A., and Tamura, M., Hydrofracturing pressure of cohesive soils, *Soils and* Foundations, Japanese Society of Soil Mechanics and Foundation Engineering, *27*(1), 14-22, 1987

[91] Murdoch, L. C., A field test of hydraulic fracturing in glacial till, *Proceedings of the 15th Annual Reservoir Symposium,* Cincinnati, Ohio. 600/9-90-006, Washington, DC: US Environmental Protection Agency, 164-174, 1990

[92] Murdoch, L. C., Hydraulic fracturing of soil during laboratory experiments, Part I, Methods and observations, *Geotechnique*, *43*(2), 255-265, 1993a

[93] Murdoch, L. C., Hydraulic fracturing of soil during laboratory experiments, Part II, Propagations, *Geotechnique*, *43*(2), 267-276, 1993b

[94] Murdoch, L. C., Hydraulic fracturing of soil during laboratory experiments, Part III, Theoretical analysis, *Geotechnique, 43*(2), 277-287, 1993c

[95] Murdoch, L. C., Hydraulic Fracturing Techniques and Applications in Soils, presentation, University of Waterloo, Waterloo, Ontario, Canada, 1996

[96] Murdoch, L. C. and Slack, W. W., Forms of hydraulic fractures in shallow fine-grained formations, *Journal of Geotechnical and Geoenvironmental Engineering*, *128*(6), 479-487, 2002

[97] Murdoch, L. C., Mechanical Analysis of Idealized Shallow Hydraulic Fracture, *Journal of Geotechnical and Geoenvironmental Engineering*, *128*(6), 488-495, 2002

[98] Murdoch, L. C., Losonsky, G., Cluxton, P., Patterson, B., Klich, I., and Braswell, B., The feasibility of hydraulic fracturing of soil to improve remedial action, final report, 600/2-91-012, NTIS Report PB91-181818, p. 298. Washington, DC: US Environmental Protection Agency, 1991

[99] Murdoch, L. C., Schweisinger, T, Svenson, E, Germanovich, L, Using Changes in Fracture Aperture During the Interpretation of Hydraulic Well Tests, *Eos Trans. AGU*, 84*(46),* Fall Meet. Suppl., Abstract, H51H-06*,* 2003

[100] Nagel, N.B. and Strachan, K.J., Implementation of cuttings reinjection at the Ekofisk field, *SPE/International Society of Rock Mechanics in Petroleum Engineering Conference*, *1*, p 95-104, 1998

[101] Obrcian, V. "Determination of lateral pressures associated wit consolidation of granular soils", *Highway research Record 284, Highway Research Board*, 13-24, 1969

[102] Osborne, M. J., and Swarsbrick, R. E., Diagenesis in North Sea HPTT clastic reservoirs – consequences for porosity and overpressure prediction, *Marine and Petroleum Geology, 16*, 337-353, 1999

[103] Ostermeier, R. M., Pelletier, Winker, J. H., C. D., Nicholson, J. W., Rambow, F. H., and Cowan, K. M., Dealing with shallow-water flow in the deepwater Gulf of Mexico, *Proceedings of the Annual Offshore Technology Conference 1,* 75-86, 2000

[104] Owolabi, O. O., Okpobiri, G. A., and Obomanu, I. A., Prediction of abnormal pressures in the Niger Delta Basin using well logs, *Society of Petroleum Engineers of AIME,* SPE 21,575, 1990

[105] Palmer, A. C. and Mitchell, R. J., Plane-strain expansion of a cylindrical cavity in clay, *Stress-strain behavior of soil*, R. Parry, ed., Butterworth, London, England, 1972

[106] Palmer, A.C. and Rice, J.R., The growth of slip surfaces in the progressive failure of over-consolidated clay. *Proc. Roy. Soc., Lond. A*, *332*, 527-548, 1973

[107] Panah, A. K., and Yanagisawa, E., Laboratory studies on hydraulic fracturing criteria in soil, *Soils and Foundations*, Japanese Society of Soil Mechanics and Foundation Engineering, *29*(4), 14-22, 1989

[108] Papanastasiou, P., Hydraulic fracture closure in a pressure-sensitive elastoplastic medium, *International Journal of Fracture*, *103*(2), 149-161, 2000

[109] Papanastasiou, P., Influence of inelastic rock behaviour in hydraulic fracturing, *Int. J. Rock Mech. Min. Sci. & Geomech. Abstr., 30*(7), 1,241-1,247, 1993

[110] Papanastasiou, P., The influence of plasticity in hydraulic fracturing, *International Journal of Fracture,* 84, 61-79, 1997

[111] Paprocki, S. J. and Hodge, E. S., *Mechanical behaviour of materials under pressure*, edited by Pugh, H. Ll. D., London, 1971

[112] Park, J., A critical assessment of moist tamping and its effect on the initial and evolving structure of dilatant tri-axial specimens by, Doctoral Dissertation, Georgia Institute of Technology, 1999

[113] Ran, C., and J. J. K. Daemen, Fracture grouting with bentonite slurries, *Fracture Grouting*, 360-371, 1992

[114] Reed, A. D. and Dusseault M. B., Hydraulic fracturing of soil as an analogue to rock behavior, *International Journal of Rock Mechanics and Mining Science*, *34*(3-4), 897-906, 1997

[115] Reed, A. D., Hydraulic Fracturing in Non-Cohesive Soils, *Master thesis*, Department of Civil Engineering, University of Waterloo, Canada, 1996

[116] Rothbart, H.A., ed., Mechanical Design and System Handbook, McGraw Hill Book Company, Inc., New York, 21-5, 1964

[117] Rudnicki, J. W. and Rice, J. R., Conditions for the localization of deformation in pressure-sensitive dilatant materials, *Journal of the Mechanics and Physics of Solids*, 23(6), 371-394, 1975

[118] Saada, A.S., Chudnovsky, A., and Kennedy, M. A fracture mechanics study of stiff clays. *Proceedings of the 11th International Conference on Soil Mechanics and Foundation Engineering*, San Francisco, 2, 637-640, 1985.

[119] Saada, A.S., Liqun Liang,, and Bianchini, G.F., Fracture mechanics and plasticity in saturated clay, *Fracture Mechanics Applied to Geotechnical Engineering, Geotechnical Special Publication,* N 43, published by ASCE, New York, 1994

[120] Saasen, A., Bale, A., Corneliussen, R., Kristiansen, P. B.; and Oftedal, B., First cuttings injection operation worldwide in a subsea annulus: equipment and operational experience, *Proceedings - SPE Annual Technical Conference and Exhibition*, v Delta, SPE 48985, *Drilling and Completion*, 207-214, 1998

[121] Saasen, A., Tran, T. N.; Joranson, H., Meyer, E.; Gabrielsen, G., and Tronstad, A. E., Subsea re-injection of drilled cuttings - operational experience, *Proceedings of the Drilling Conference*, 1, 318-323, 2001

[122] Sahay, B., Geologging in oil and gas exploration, *Energy Sources, 8*(4), 331-354, 1986

[123] Santamarina, J. C., Klein, K. A., and Fam, M. A., *Soils and Waves: particulate materials behavior, characterization and process monitoring*, New York, J. Wiley & Sons, 488, 2001

[124] Saxena, A., *Nonlinear Fracture Mechanics for Engineers*, CRS Press, 472pp, 1998

[125] Schmertmann, J. H., and Henry, J. F., A design theory for compaction grouting, Grouting, Soil Improvement and Geosynthetics, 1, Geotechnical Special Technical Publication, 30, ASCE, New York, 215-228, 1992

[126] Sim, Y., Germanovich, L. N., and Vermilye, J. M., Effect of interaction on apertures of multisegmented natural veins, *Eos Trans. AGU*, 84*(46),* Fall Meet. Suppl., Abstract, H42F-1130, 2003

[127] Simonson, E. R., Abou-Sayed, A. S., and Clifton, R. J., Containment of

massive hydraulic fractures, *Society of Petroleum Engineers Journal,* 27-32, 1978

[128] Skjetne, E., Klov, T., and Gudmundsson, J. S., Experiments and modeling of high-velocity pressure loss in sandstone fractures*, Proceedings - SPE Annual Technical Conference and Exhibition: Reservoir Completion, 1*, 37-48, 1999

[129] Snyder, V. A., and Miller, R. D., Tensile strength of unsaturated soils, *Journal of the Soil Science Society of America,* 49, 58-65, 1985

[130] Soga, K., Au, S.K.A., Jafari, M.R., and Bolton, M.D, Laboratory investigation of multiple grout injections into clay *Geotechnique*, *54*(2), 81-90, 2004

[131] Swarbrick, R. E. and Schneider, F., Introduction to special issue on overpressure research*, Marine and Petroleum Geology*, 16(4), 301-302, 1999

[132] Tada, H., Paris, P. C, and. Irwin, G. R, *The Stress Analysis of Cracks Handbook,* 2nd ed., St. Louis: Paris Productions, 1985

[133] Talbot, J. R., The mechanics of cracking in embankment dams, *Fracture Mechanics Applied to Geotechnical Engineering*, 119-131, 1994

[134] Taylor, D. W., *Fundamentals of soil mechanics*, New York, Wiley, 1948

[135] Terzaghi, K., *Theoretical soil mechanics*, John Wiley and Sons, Inc., London, 1943

[136] Thallak, S., Holder, J., and Gray, K. E., The pressure dependence of apparent hydrofracture toughness, *Int. J. Rock Mech. Sci. & Geomech. Abstr., 30*(7), 831-835, 1993

[137] Upchurch, E. R., Near-wellbore halo effect resulting from tip screenout fracturing: its direct measurement and implication for sand control, *Proceedings - SPE Annual Technical Conference and Exhibition: Drilling and Completion,* 389-397, 1999

[138] U.S. Bureau of reclamation, *Earth Manual*, 2nd Ed., Denver, 810, 1974

[139] U.S. Environmental Protection Agency, Technology evaluation and applications analysis reports: University of Cincinnati/Risk Reduction Engineering Laboratory: Hydraulic Fracturing Technology. EPA/540/R-93/505, 1993

[140] Vaid, Y. P., and Negussey, D., Relative density of pluviated sand samples, *Soils and Foundations*, *24*(2), 101-105, 1984

[141] Vallejo, L. E., Shear stresses and the hydraulic fracturing of earth dam soils, *Soils and Foundations, Japanese Society of Soil Mechanics and Foundation Engineering*, *33*(3), 14-27, 1993

[142] Van Den Hoek, P. J., Van Den Berg, J. T. M., and Shlyapobersky, J., Theoretical and experimental investigation of rock dilatancy near the tip of a propagating hydraulic fracture, *Int. J. Rock Mech. Min. Sci. & Geomech.*

Abstr., 30(7), 1,261-1,264, 1993

[143] Veatch, R. W. Jr., Overview of current hydraulic fracturing design and treatment technology: Part 1, *Journal of Petroleum Technology, 35*(4), 677-687, 1983a

[144] Veatch, R. W. Jr., Overview of current hydraulic fracturing design and treatment technology: Part 2, *Journal of Petroleum Technology, 35*(5), 853-864, 1983b

[145] Vermeer P. A., and Borst R. de, Non-associated plasticity for soils, concrete and rock, HERON, *29*(3), 3-35, 1984

[146] Vesic, A. S., Cratering by explosives as an earth pressure problem, *Proceeding of the sixth international conference soil mechanics foundation engineering*, Montreal, Canada, 2, 427-431, 1965

[147] Vesic, A. S., Breakout resistance of objects embedded in ocean bottom, *Journal of the Soil Mechanics and Foundation Division,* ASCE, V97, No. SM9, Proc. Paper 8372, 1183-1206, September 1971

[148] Vesic, A. S., Expansion of cavities in infinite soil mass, *Journal of the Soil Mechanics and Foundations Division, ASCE, 98*(SM3), Proceedings Paper 8,790, 265-290, 1972

[149] Wang, S. W., Stevenson, V. M., Ohaeri, C. U., and Wotring, D. H., Analysis of overpressured reservoirs with a new material balance method, *Proceedings - SPE Annual Technical Conference and Exhibition: Reservoir Engineering*, *2*, 157-170, 1999

[150] Warner, J., Compaction grout: Rheology vs. effectiveness, *Grouting, Soil Improvement and Geosynthetics*, *1*, Geotechnical Special Technical Publication, 30, ASCE, New York, 229-239, 1992

[151] Warner, J., Compaction grouting mechanism – What do we know? *Grouting: Compaction/Remediation/Testing*, Geotechnical Special Publication, 66, ASCE, New York, 1-17, 1997

[152] Warner, J., Schmidt, N., Reed, J., Shepardson, D., Lamb, R. and Wong, S., Recent advances in compaction grouting technology, *Grouting, Soil Improvement and Geosynthetics*, *1*, Geotechnical Special Technical Publication, 30, ASCE, New York, 252-264, 1992

[153] Wawrzynek, P. A. and Ingraffea, A. R., *Interactive finite element analysis of fracture processes: an integrated approach,* Theoretical and Applied Fracture Mechanics, 8, 137-150, 1987

[154] Whittle, A. J., and Kavvadas, M. J., Formulation of MIT-E3 constitutive model for overconsolidated silt-clays, *Journal of Geotechnical. Engineering, 120*(1), 173-199, 1994

[155] Wu, R., *Mechanisms of Hydraulic fracturing in Geomaterials*, Ph.D. dissertation, Georgia Institute of Technology, 2005

[156] Yanagisawa, E., and Panah A. K., Two dimensional study of hydraulic

fracturing criteria in cohesive soils, *Soils and Foundations*, Japanese Society of Soil Mechanics and Foundation Engineering*, 34*(1), 1-9, 1994

[157] Yarema, S. Y., Analysis of cracked disk specimens, *Engineering Fracture Mechanic*s, 12(3), 365-375, 1979

[158] Yew, C. H., *Mechanics of Hydraulic Fracturing,* Houston, Gulf Publishing, 1997

[159] Yu, H. S. *Cavity Expansion Methods in Geomechanics,* Kluwer Academic Publishers, 2000

[160] Yu H. S. and Houlsby, G. T., A large strain analytical solution for cavity contraction in dilatant soils, *International Journal for Numerical and Analytical Methods in Geomechancis*, 19, 793-811, 1995

[161] Yu H. S. and Houlsby, G. T., Finite cavity expansion in dilatant soils: loading analysis, *Geotechnique*, *41*(2), 173-183, 1991

[162] Zoback, M. D., and Pollard, D. D., Hydraulic fracture propagation and the interpretation of pressure-time records of *in-situ* stress determinations. *Proceedings of the US symposium on Rock Mechanics, Reno*, Y. S. Kim, ed., 14-22, 1978